Ultimate Response of Stainless Steel Bolted Connections

By
Orhan Yapici

A thesis submitted to the University of Birmingham for
the degree of Doctor of Philosophy

Department of Civil Engineering, School of Engineering
University of Birmingham,
Edgbaston, B15 2TT, Birmingham, UK.

19 April 2021

List of Publications

The presented PhD study has led to a list of journal papers, conference papers and technical reports, as follows:

Journal papers

1- Yapici O., Theofanous M., Yuan H.X., Afshan S., Dirar S. (Submitted). Determination of fracture properties and explicit fracture modelling of stainless steel bolts in tension. Thin-Walled Structures.

2- Yapici O, Theofanous M, Yuan H, Skalomenos K, Dirar S. Experimental study of ferritic stainless steel bolted T-stubs under monotonic loading. Journal of Constructional Steel Research 2021;183:106761. https://doi.org/10.1016/j.jcsr.2021.106761.

3-Yapici O., Theofanous M., Dirar S., Yuan H.X., Skalomenos K.A. (Submitted) Numerical modelling of stainless steel bolted T-stubs in tension. Structures.

4-Yapici O., Theofanous M., Dirar S., Yuan H.X. (Submitted) Numerical modelling of the structural behaviour of ferritic stainless steel bolted T-stubs under tension. Engineering Structures.

Conference papers

1- Yapici O., Theofanous M., Dirar S., Yuan H.X. (Accepted). Behaviour of ferritic stainless steel bolted T-stubs under tension-Part 1: Experimental investigations. Eurosteel 2021, Sheffield, UK.

2- Yapici O., Theofanous M., Dirar S., Yuan H.X. (Accepted). Behaviour of ferritic stainless steel bolted T-stubs under tension-Part 2: Numerical investigations. Eurosteel 2021, Sheffield, UK.

Abstract

The use of stainless steels in structural applications has been steadily growing for decades with most research focusing on the structural behaviour of stainless steel members. However, the material behaviour of stainless steels has essential differences from that of carbon steel, as it exhibits significant strain hardening and an absence of a well-defined yield plateau. Moreover, the design provisions of EN 1993-1-8 (2005) which was originally developed for carbon steel joints are currently applicable to design of stainless steel connections with only minor modifications, thereby leading to unduly conservative strength predictions and hence inefficient design. To provide more efficient design rules, assess and improve the current design guidance for stainless steel connections, extensive experimental and numerical studies have been performed and are reported in this thesis.

Firstly, an experimental programme on the determination of fracture properties and explicit fracture modelling of stainless steel bolts in tension has been performed. A predictive equation relating the equivalent plastic strain at fracture initiation and stress triaxiality for A4-80 stainless steel bolts was obtained experimentally and utilised within the phenomenological fracture model for ductile metals available in the FE code ABAQUS. Subsequently, an advanced FE model was developed in which the fracture of the bolts was incorporated utilising a ductile damage model with a damage initiation criterion and fracture propagation parameters. The developed FE model was validated against available experimental data published in the literature and was shown to accurately predict the available ductility and overall response of stainless steel joints failing by bolt fracture under predominantly tensile load.

Subsequently, an experimental study on the ultimate behaviour of ferritic stainless steel bolted T-stubs under monotonic tension was carried out and 17 T-stubs employing a wide range of geometric configurations, which were designed to fail in a ductile mode were tested to failure. The obtained ultimate and plastic resistances with corresponding displacements and material characteristics including material anisotropy have been reported in detail. It was observed that the ferritic stainless steel T-stubs exhibit significant anisotropy and overstrength which can be defined as the ultimate over the plastic resistances. The effect of membrane action on the ultimate resistance of the T-stubs has been experimentally observed and quantified and a recently proposed predictive equation was assessed based on the obtained results. This immense strength reserve may be relied upon to mitigate progressive collapse under a column loss.

Following the experimental investigations on ferritic stainless steel bolted T-stubs, an advanced FE model was developed and validated against the available test data. The FE models predicted the ultimate and plastic forces, and failure modes very accurately and the full force-displacement curves of each test specimen were obtained. Moreover, an extensive parametric study was conducted to reveal the effect of different parameters on the ultimate response of the stainless steel T-stubs and the results are reported comprehensively.

Based on the obtained experimental and numerical results, the EN 1993-1-8 (2005) was assessed. It was concluded that the plastic resistance predictions of EN 1993-1-8 (2005) are overly conservative for austenitic and duplex stainless steel T-stubs, but satisfactory for ferritic stainless steel bolted T-stubs. This was attributed to the similarity of the strain-hardening characteristics between ferritic stainless steels and carbon steel, which are markedly inferior to those of the austenitic and duplex stainless steel grades. A recently proposed design formula for estimating the ultimate resistances of carbon steel bolted T-stubs was applied to the stainless steel T-stubs. It was concluded that the proposed formula can predict the ultimate resistances of stainless steel bolted T-stubs with a significant accuracy. Finally, conclusions have been made and future research suggestions are given in the final chapter of the thesis.

Acknowledgements

First of all, I would like to express my sincere gratitude to my supervisor, Dr Marios Theofanous, for his guidance, support and valuable contributions during the whole time of my PhD study, without his limitless guidance, and vision, my research cannot be accomplished. I also want to thank to my co-supervisors, Dr Samir Dirar and Dr Konstantinos Skalomenos for their sincere help and support.

I gratefully acknowledge the postgraduate scholarship and financial support received from Turkish Government. I would like to thank the all staff of the Structures Laboratory of the Department of Civil and Mechanical Engineering, University of Birmingham. My special thanks go to Mr David Price from the Material and Metallurgical Engineering Laboratory, University of Birmingham, for his kindness, valuable helps and supports during the challenging pandemic conditions in order to complete my coupon tests.

I would also like to send my sincere gratitude to my colleges and friends for their help and support throughout my all research in particular Sahin Gunes, Nurullah Yildiz, Kagan Sogut, Dr Georgios Kokosis and Dr Mohamed Elflah. I also acknowledge the valuable collaborations of Dr Huanxin Yuan from Wuhan University and Dr Sheida Afshan from University of Southampton.

I want to dedicate this accomplishment to memory of my father, Kadir Yapici, who no longer with us and my mother, Fadime Yapici whom I love so much. I also want to extend this respect and love to my brothers Burhan Yapici and Irfan Yapici who always believed in my ability and supported me unconditionally throughout my academic journey.

Most importantly, all my sincere gratitude and love go to my lovely wife Feyza Yapici whom I love more than anything in this world. You are the love and the most special gift of my life.

Table of Contents

List of Publications……………………………………………………………………......ii

Abstract……………………………………………………………………………………...iii

Acknowledgements…………………………………………………………………….......v

Table of Contents……………………………………………………………………….....vi

List of Figures…………………………………………………………………………......xi

List of Tables…...…………………………………………………………………………….xvii

Nomenclature…...…………………………………………………………………………….xxi

CHAPTER 1: Introduction……………………………………………………............1

1.1. Background…………………………………… ………………………………..........1

1.2. Aim and objectives...5

1.3. Methodology...6

1.4. Outline of the thesis 7

CHAPTER 2: Literature review …………………………………….……..…………........10

2.1. Introduction..10

2.2 Behaviour and design of bolted T-stubs...11

2.2.1. The Component Method..11

2.2.2. Past research on idealisation of tension zones of joints as T-stubs................13

2.2.3. Typical behaviour of T-stubs and ultimate resistance predictions................17

2.3. Previous studies on stainless steel connections...25

2.4. Literature review on material modelling and explicit fracture modelling of the stainless steel bolts..28

2.4.1. Material modelling..28

2.4.2. Fracture modelling of the bolts..29

2.5. Concluding remarks and knowledge gap...34

CHAPTER 3: Determination of fracture properties and explicit fracture modelling of stainless steel bolts in tension...……………………………..........37

3.1. Introduction...37

3.2. Experimental tests...38

3.2.1. Design of specimen geometry...38

3.2.2. Tensile tests and material properties...39

3.2.3. Stress triaxiality and fracture initiation...44

3.3. Numerical modelling of fracture..51

3.3.1. Axisymmetric FE model...52

3.3.2. 3D FE model..55

3.4. Case studies....58

  3.4.1. M20 bolt shank in tension....58

  3.4.2. M20 bolts under tension and shear....61

  3.4.3. Fracture of a threaded M16 bolt....64

  3.4.4. Simulation of stainless steel T-stub in tension....67

  3.4.5. Simulation of a moment resisting connection....69

3.5. Conclusions....72

CHAPTER 4: Experimental tests on ferritic stainless steel bolted T-stubs....74

4.1. Introduction....74

4.2. T-Stub test specimens....75

  4.2.1. Geometric configurations....75

  4.2.2. Material properties....78

4.3. Monotonic loading tests....85

  4.3.1. Setup and instrumentation....85

4.4. Results and discussions....88

  4.4.1. Failure modes....88

  4.4.2. Load-deformation response....92

  4.4.3. Load-strain response....94

4.4.4. Summary of the key results...98

4.4.5. Membrane action...99

4.5. Conclusions...101

CHAPTER 5: Numerical modelling of stainless steel bolted T-stubs...103

5.1. Introduction...103

5.2. FE modelling of austenitic and duplex stainless steel bolted T-stubs in tension......104

5.2.1. Modelling assumptions...104

5.2.2. Validation and discussion..110

5.2.3. Modelling of bolt fracture..122

5.3. Numerical modelling of ferritic stainless steel bolted T-stubs in tension....................127

5.3.1. Development of FE model..127

5.3.2. Material modelling and anisotropy..129

5.3.3. Modelling of fracture...131

5.3.4. Results and discussion..132

5.4. Parametric study...148

5.4.1. FE modelling and assumptions...148

5.5. Conclusions...150

CHAPTER 6: Design recommendations...153

6.1. Introduction..153

6.2. EN 1993-1-8 design provisions for the plastic resistance F_{pl} 154

    6.2.1. Assessment of EN 1993-1-8 for stainless steel T-stubs...............................155

    6.2.2. Design proposals for stainless steel T-stubs..160

6.3. Prediction of ultimate resistance force F_u..162

    6.3.1. Determination of overstrength...163

    6.3.2. Ultimate resistance predictions of stainless steel bolted T-stubs.................164

6.4. Conclusions...169

CHAPTER 7: Conclusions and suggestions for future research...171

7.1. Conclusions..171

7.2. Recommendations for future research...175

References..178

List of Figures

Figure 1.1: Stress-strain curves for typical stainless steel and carbon steel grades............................2

Figure 1.2: Examples of usage of stainless steel in construction...4

Figure 2.1: Components of an extended end plate beam-to-column joint.......................................13

Figure 2.2: Respective mechanical spring model of an extended end plate beam-to-column joint..13

Figure 2.3: Failure mechanisms of bolted T-stubs (Piluso *et al.*, 2001a)..17

Figure 2.4: Effect of β_{Rd} on the plastic collapse mechanisms of bolted T-stubs (EN 1993-1-8, 2005)...19

Figure 2.5: Yield line mechanisms of bolted T-stubs with one bolt row (Coelho, 2004)...20

Figure 2.6: Yield line mechanisms of bolted T-stubs with two bolt rows (Coelho, 2004)...21

Figure 2.7: Collapse mechanisms and relative kinematics models of T-stubs (extracted from Piluso *et al.*, 2001a)..22

Figure 2.8: The piecewise linear force deformation model for springs (Swanson and Leon, 2001)...23

Figure 2.9: Plastic mechanisms for the deformation capacity calculations of T-stubs (Beg *et al.* 2004)....24

Figure 2.10: Tri-linear assumption of load-deformation response of T-stubs (Elflah, 2018)....28

Figure 2.11: Stress-strain curve with progressive damage degradation (ABAQUS, 2013)....33

Figure 3.1: Notched specimens extracted from M10 A4-80 bolt shank....38

Figure 3.2: Tensile specimens approaching fracture....41

Figure 3.3: Force-displacement response of tested specimens....42

Figure 3.4: Stress-strain response of bolt material based on specimens SS0-1 and SS0-2....43

Figure 3.5: Typical axisymmetric FE model of the tested specimens....45

Figure 3.6: FE modelling of SS1 without accounting for fracture and determination of the point of damage initiation and corresponding equivalent plastic strain....46

Figure 3.7: Distribution of the stress triaxiality along the notched sections in axisymmetric FE models....47

Figure 3.8: Evolution of stress triaxiality with increasing strain and average stress triaxiality for each notched specimen....48

Figure 3.9: Equivalent plastic strain at fracture initiation as a function of stress triaxiality....50

Figure 3.10: Assessment of predictive equation (Song *et al.*, 2020) for true plastic strain at fracture $\bar{\varepsilon}_f^{pl}$....51

Figure 3.11: Comparison of the numerical force-displacement curves based on axisymmetric (2-D) model and the experimental curves..55

Figure 3.12: Close-up of test specimen and 3D FE model...56

Figure 3.13: Comparison of the numerical force-displacement curves with the experimental curves..57

Figure 3.14: Experimental (Song *et al.*, 2020) and numerical bolt elongation response for M20 A4-80 bolt..61

Figure 3.15: Numerical model of bolt subjected to tension and shear...62

Figure 3.16: Experimental and numerical bolt elongation response for M20 A4-80 bolts subjected to tension and shear..63

Figure 3.17: Geometric modelling of (a) axisymmetric and (b) 3-D FE models of an M16 A4-80 threaded bolt...65

Figure 3.18: Experimental and numerical bolt elongation response for threaded M16 bolt............66

Figure 3.19: Experimental and numerical bolt elongation response for smooth M16 bolt with effective cross-section..66

Figure 3.20: 3-D FE model for the bolted T-stub specimen S3 (Yuan *et al.*, 2019)..........................68

Figure 3.21: Experimental and numerical response of specimen S3 (Yuan *et al.*, 2019) for various modelling approaches...69

Figure 3.22: 3-D FE model of the stainless steel flush endplate connection tested by Elflah *et al.*, (2019)..70

Figure 3.23: Experimental and numerical response of flush end plate connection (Elflah *et al.*, 2019) for various modelling approaches...71

Figure 3.24: Experimental (Elflah *et al.*, 2019) and numerical failure mode of stainless steel flush end plate connection and closeup of bolt fracture..72

Figure 4.1: Geometric properties of a) single bolt row and b) double bolt row T-stubs..................77

Figure 4.2: Extracted coupons (a) and experimental set up (b)...79

Figure 4.3: Stress-strain response of the tested tensile coupons..80

Figure 4.4: Behaviour of 10mm thick coupons. a) Longitudinal splitting and b) Stress strain curves..81

Figure 4.5: Fracture of additional material coupons from the 10 mm plate.....................................83

Figure 4.6: Material behaviour of bolt coupons...85

Figure 4.7: Illustration of set up for a) single and b) double bolt row T-stubs and c) the picture of the experimental set up during testing...86

Figure 4.8: Strain gauge arrangements for the a) Single and b) double bolt row T-stubs.................87

Figure 4.9: Typical failure modes of T-stubs..89

Figure 4.10: Failure modes of the T-stub specimens..91

Figure 4.11: Load-deformation curves of the T-stub specimens..93

Figure 4.12: Load-strain curves for a) S2, b) D5, c) S5 and d) D11..97

Figure 4.13: The SG-1 load-strain curves for a) 5 mm and b) 10 mm flange thickness...................97

Figure 4.14: Overstrength as a function of parameter β..101

Figure 4.15: Overstrength as a function of parameter β’ considering preload...............................101

Figure 5.1: Geometric properties of T-stub specimens (Yuan *et al.*, 2019)..................................105

Figure 5.2: Geometric modelling assumptions for the bolt and the weld toe................................108

Figure 5.3: Force-displacement curves of the a) S4 and b) D2 specimens....................................115

Figure 5.4: Comparison of the stress distribution through the flange thickness

for explicit dynamic and static analysis...121

Figure 5.5: 3-D FE model for the T-stub specimens with threaded bolts......................................123

Figure 5.6: Experimental and numerical response of specimens a) S2, b) S3,

c) D2 and d) D7 for various modelling approaches...126

Figure 5.7: The developed FE model for the analyses..128

Figure 5.8: Numerical load-deformation curves with 3 and 4 elements through

the flange thickness of a) S2 and b) D1..133

Figure 5.9: The force-displacement curves and the failure modes of the specimens.....................136

Figure 5.10: Experimental and numerical failure modes of a) S1, b) D3, c) D5,

d) D6 and e) D11..140

Figure 5.11: The stress distribution through the flange plate thickness..145

Figure 5.12: The force-displacement curves of FE models with fracture model............................147

Figure 6.1: Theoretical relationship between F_{pl} and t_f^2 provided in EN 1993-1-8........................155

Figure 6.2: Relationships between F_{pl} and t_f^2 for parametric study..159

Figure 6.3: Definition of α in a bolted T-stub (Tartaglia *et al.,* 2020)...163

Figure 6.4: The overstrength ratio vs β relationship for parametric analysis.................................164

List of Tables

Table 3.1: Nominal geometric configuration of bolt specimens and associated stress triaxiality....39

Table 3.2: Key geometric measurements for each bolt specimen....40

Table 3.3: Material properties of stainless steel bolts....43

Table 3.4: Material parameters of the multistage material model (Hradil *et al.*, 2013) adopted for the stainless steel bolts....44

Table 3.5: Key fracture properties and average triaxiality....49

Table 3.6: Optimal values for the plastic displacement at fracture....56

Table 3.7: Optimal values for the plastic displacement at fracture for various bolt sizes....60

Table 4.1: Geometric configurations of the T-stubs (all dimensions are in mm)....76

Table 4.2: Material properties of the ferritic stainless steel plates....80

Table 4.3: Average stress values and anisotropy ratios....84

Table 4.4: Material properties of the stainless steel bolts....85

Table 4.5: Summary of the key test results....99

Table 5.1: Geometric dimensions of T-stub specimens (Yuan *et al.*, 2019). (All dimensions are in mm)....106

Table 5.2: Material properties of stainless steel plates and bolts (Yuan *et al.*, 2019)....................107

Table 5.3: Effect of modelling type and number of elements through the flange thickness on plastic resistance F_{pl}..111

Table 5.4: Effect of modelling type and number of elements through the flange thickness on displacement at plastic resistance Δ_{pl}...112

Table 5.5: Effect of modelling type and number of elements through the flange thickness on ultimate resistance F_u...112

Table 5.6: Effect of modelling type and number of elements through the flange thickness on displacement at ultimate resistance Δ_u..113

Table 5.7: Comparison of the mean values of Fu, FEM / Fu, Exp ratios for Type-3 and Type-4...116

Table 5.8: Comparison of the mean values of Δu, FEM / Δu, Exp ratios for Type-3 and Type-4...116

Table 5.9: Comparison of the mean values of Fpl, FEM / Fpl, Exp ratios for Type-3 and Type-4...116

Table 5.10: Comparison of the mean values of Δpl, FEM / Δpl, Exp ratios for Type-3 and Type-4...116

Table 5.11: Comparison of explicit dynamic procedure and static Riks analysis procedure..........118

Table 5.12: Optimal values for the plastic displacement at fracture for various bolt sizes............124

Table 5.13: Material properties of the ferritic stainless steel plates...130

Table 5.14: Material properties of the stainless steel bolts..131

Table 5.15: Experimental and numerical results for plastic resistance, ultimate resistance and displacement at ultimate resistance..138

Table 5.16: Numerical over experimental FE results for various material modelling assumptions...138

Table 5.17: Geometric dimensions of the specimens for the parametric study.............................148

Table 5.18: Parametric analysis results of stainless steel bolted T-stubs......................................149

Table 6.1 Comparison of plastic forces predicted by EN-1993-1-8 with test results....................156

Table 6.2 Comparison of the mean ratios of $F_{pl, EC3}$ / $F_{pl, Exp}$ for all three stainless steel grades...157

Table 6.3 Assessment of EN 1993-1-8 based on parametric study in Chapter 5 section 5.4..........158

Table 6.4: Assessment of proposed design formula by Yuan *et al.* (2020)...................................161

Table 6.5: Assessment of proposed design formula by Tartaglia *et al.* (2020) using available test data for austenitic and duplex stainless steel T-stubs..165

Table 6.6: The comparison of the predicted and experimental ultimate resistance forces for ferritic stainless steel bolted T-stubs...166

Table 6.7: Assessment of proposed design formula by Tartaglia *et al.* (2020) using parametric analysis results..168

Table 6.8: Summary of the ultimate resistance predictions by the predictive formula..................169

Nomenclature

β	Ratio between the flexural strength of the flanges and the axial strength of the bolts
ψ	Reduction factor applied to the bolts
b_{eff}	Effective width
CSM	Continuous Strength Method
d_w	Bolt head or washer diameter
δ	Vertical deformation of T-stubs, gap opening
D	Damage parameter
D_0	Initial dimeter of the bolt
D_{ult}	Diameter of the bolt after fracture
d_w	Diameter of the washer
E	Young’s modulus
ER	Elastic region
ε_f	Engineering plastic strain at fracture
ε_u	Engineering strain at ultimate stress
$\bar{\varepsilon}_{pl}$	Equivalent plastic strain
$\bar{\varepsilon}_f^{pl}$	Equivalent true plastic strain at fracture

$\bar{\varepsilon}_{pl,D}$	Equivalent true plastic strain at fracture initiation
F_{EC3}	Plastic resistance of the T-stubs predicted by EN 1993-1-8
F_{Rd}	Plastic resistance of the T-stubs in EN 1993-1-8
F_{pl}	Plastic resistance force
$F_{T,1}$	Resistance for failure mode 1 according to EN 1993-1-8
$F_{T,2}$	Resistance for failure mode 2 according to EN 1993-1-8
$F_{T,LD}$	Additional force due to the membrane action
ID	Initiation of damage
l_b	Bolt length
L	Length of the notched region
$L_{exten.}$	Length of the extensometer
λ	Ratio between n and m
$M_{f,Rd}$	Plastic resistance moment of the flanges in EN 1993-1-8
m	Distance between bolt and web
n	Strain hardening coefficient
$n_{0.2-1.0}$	Strain hardening coefficient between 0.2% and 1% proof stress
$n_{1.0-u}$	Strain hardening coefficient between 1% and ultimate stress

PEEQ	Equivalent plastic strain
R	Radius of circumferential notch
t_f	Flange thickness
t_w	Web thickness
u_f	Displacement at failure
η	Stress triaxiality
$\bar{\sigma}$	Undamaged stress
σ_{y0}	True stress at the onset of damage
$\sigma_{eq.}$	Von Mises stress
σ_H	Hydrostatic stress
σ_u	Engineering ultimate tensile stress
σ_0	Yield stress/end of elastic material response
$\sigma_{0.2}$	0.2% proof stress
$\sigma_{1.0}$	1% proof stress
TMCP	Thermal-Mechanical Controlled Processed

CHAPTER 1

Introduction

1.1. Background

Stainless steels are steel-chromium alloys that contain chromium in excess of 10.5 % by mass, with the actual content varying for different grades. Apart from chromium, stainless steels contain other alloying elements including carbon, nickel, silicon, copper, molybdenum, manganese, nitrogen and phosphorus (EN 10088-2, 2005). Based on their metallurgical structure and variation in chemical content, stainless steels are classified into five main families of grades, namely austenitic, ferritic, duplex, martensitic and precipitation hardening (Gardner, 2005). The austenitic, duplex and ferritic grades are the most common stainless steel types which are currently used in structural applications. Austenitic stainless steels have a content of 17–18% chromium and 8–11% nickel by mass and possess the highest corrosion resistance among all stainless steels. Duplex stainless steels consist of 21–23% chromium and 1.5–6.5% nickel and exhibit higher strength and wear resistance but lower ductility and corrosion resistance than austenitic stainless steels (Gardner, 2005; Baddoo, 2008). Ferritic stainless steels contain 11-30 % of chromium and have significant corrosion and heat resistance. The chromium content of stainless steels creates a self-healing thin surface layer of Cr_2O_3 by reacting with oxygen in the atmospheric environments which protects the underlying steel from corrosion.

In addition to their chemical compositions, the mechanical properties of stainless steels are important for their contribution to sustainable construction. The mechanical behaviour of stainless steel has essential differences from that of conventional carbon steel. In contrast to carbon steel, stainless steels have no sharp yield point as they do not possess a yield plateau and exhibit significant strain hardening. In addition, the ductility of austenitic and duplex stainless steels is considerably higher than the carbon steel which with a strain at fracture in the range of 50-60% and 30-40% respectively, whilst ferritic stainless steels have similar ductility levels to carbon steel. Figure 1.1 displays typical stress-strain responses representative of the three stainless steel families as well as the behaviour of an S275 carbon steel for comparison.

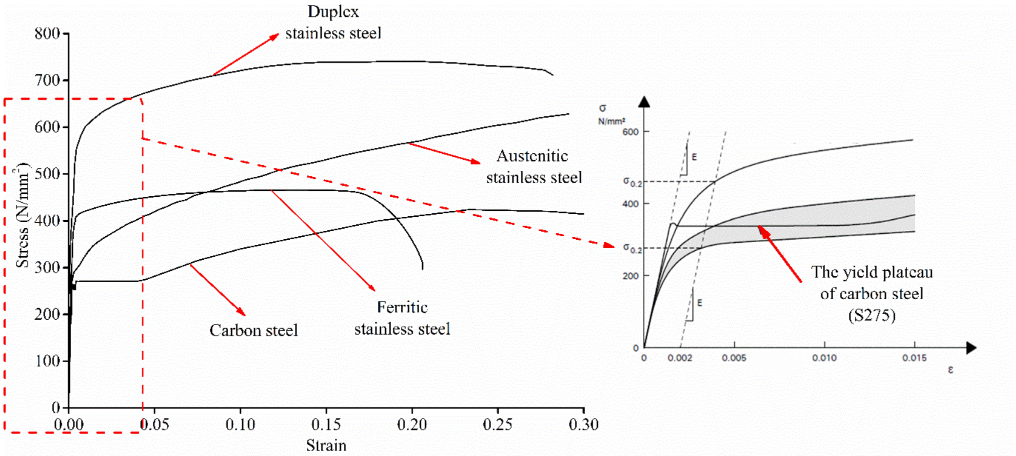

Figure 1.1: Stress-strain curves for typical stainless steel and carbon steel grades.

Due to their high corrosion resistance, superior strength and ductility and high recyclability, stainless steels are gaining popularity in the construction industry, particularly after the 1980`s due to the increased importance of sustainability (IISI, 2005; Rossi, 2014). In conjunction with development of the stainless steels market, new production and fabrication processes and developing design codes, the use of stainless steel in construction has been rapidly increasing (Baddoo, 2008; Gardner, 2005). Moreover, increasing demand for sustainability and their favourable cost when considered on a whole life basis, despite their high initial material cost, led to a growing interest to use of stainless steel as primary structural materials in construction industry (Gardner, 2005; Baddoo, 2008; Rossi, 2014).

Stainless steels have been used in many construction applications such as buildings and bridges for several years. The cladding of Chrysler building in New York, the Gateway arch in Missouri, the New Justice Palace in Anvers and the Glass Center in Lommel are the main examples of structures in which stainless steels have been used as a principal structural material (Figure 1.2). In addition to this, the Millennium footbridge in York, is a prime example of a bridge employing stainless steel as a main structural material, as shown in Figure 1.2(e). The Helix Bridge in Paddington train station, London, is another example of a recent stainless steel structure (Figure 1.2(f)).

The development of design codes based on experimental and numerical research has accelerated the wider use of stainless steel in construction industry. In 1968 the first American specifications related to design of structural stainless steel called “Specification for the Design of Light Gauge Cold-formed Stainless Steel Structural Members” (AISI, 1968) was introduced. It evolved later to the American SEI/ASCE 8-02 (2002) and AISC 27 (2013). The currently applicable structural design codes for stainless steel in Europe and Australia/New Zealand are EN 1993-1-4 (2015) and the Australian AS/NZS 4673 (2001) design code respectively. The design philosophy of stainless steel material in all international design standards is based on an assumed elastic-perfectly plastic material behaviour, to maintain consistency with carbon steel design standards and facilitate the transition from carbon steel to stainless steel design rules. However, not accounting for the actual material response of stainless steel and ignoring its significant strain-hardening has been shown to result in overly conservative ultimate resistance predictions and inefficient design particularly for structures employing stocky stainless steel cross-sections (Afshan and Gardner, 2013; Gardner and Theofanous, 2008).

(a) The Chrysler Building – New York, 1930 (b) The Gateway arch, Missouri, 1965.

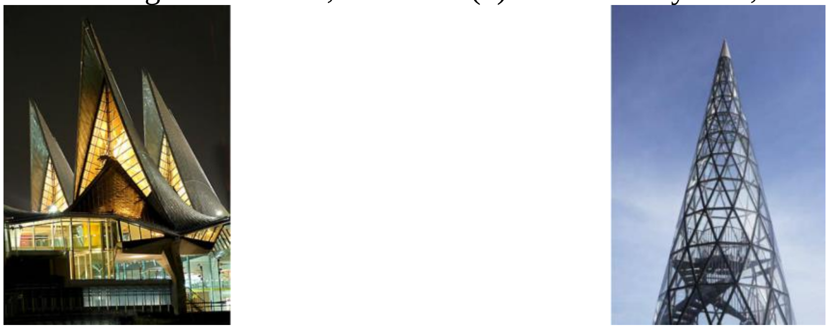

(c) New Justice Palace – Anvers, 2006 (d) Glass Center – Lommel, 2006

(e) The Millennium Bridge, York, UK, 2001 (f) The Helix Bridge, London, 2004

Figure 1.2: Examples of usage of stainless steel in construction.

Most research studies on stainless steel structures focus on cross-section or member response, whilst the studies on stainless steel connections have not received as much attention and the relevant published experimental and numerical research is very rare. The EN 1993-1-8 (2005), which was originally developed for carbon steel connections, is currently applicable to the design of stainless steel connections without proper research-based verification. The first ever experimental studies on stainless steel connections have been conducted by Elflah *et al.* (2019a; 2019b; 2019c), who reported experimental and numerical results on austenitic and duplex stainless steel beam-to-column moment resisting connections, and Yuan *et al.* (2019), who conducted an experimental study on austenitic and duplex bolted stainless steel T-stubs. The conducted research has concluded that the EN 1993-1-8 (2005) design rules lead to overly conservative predictions when applied to stainless steel connections and the design specifications should be improved and account for the pronounced strain-hardening of stainless steel. No studies on ferritic stainless steel connections have been reported to date. The intention of this research study is to fill in this gap and carry out experimental and numerical research on the ultimate response of the ferritic stainless steel bolted T-stubs, whilst it also focuses on the ultimate response and explicit fracture modelling of stainless steel bolts.

1.2. Aim and objectives

Over the past two decades a great deal of research has been devoted on the structural behaviour of stainless steel members resulting in revisions of the relevant structural stainless steel design guidance in accordance with available experimental tests. New design methods were developed in an attempt to reflect the actual material response and allow specifically for the pronounced strain-hardening exhibited by stainless steels. Contrary to the stainless steel members, their connections have received significantly less attention, and relevant design guidance is based on assumed analogies with carbon steel despite the differences in material response. The aim of this project is to enhance current understanding, assess and improve the current design guidance on stainless steel connections, so that it reflects the actual material, particularly for ferritic stainless steel connections, for which no experimental tests have been reported yet. To achieve this aim, the following objectives have to be met:

1) To determine the key material properties including material anisotropy of ferritic stainless steels and their effect on the response of stainless steel connections.

2) To quantify the strength and ductility of stainless steel bolts, the failure of which often limits the ultimate response of connections.

3) To develop a robust numerical modelling approach that can accurately simulate bolt fracture and identify relevant key material properties, currently lacking in the literature.

4) To expand the currently limited experimental database to include the behaviour of ferritic stainless steels which have not received significant attention despite their favourable price compared to the more expensive austenitic and duplex grades.

5) To develop a robust numerical analysis framework that can accurately simulate the behaviour of stainless steel connections including their ultimate response under extreme loading.

6) To use the developed tools to conduct parametric studies and assess currently available design predictions for the capacity of stainless steel connections as well as develop novel ones if needed.

1.3. Methodology

The purpose of this research is to study the ultimate response of stainless steel bolted connections and to assess the reliability of the current design guidance of EN 1993-1-8 by comparing the predicted design resistances with the experimental and numerical results generated in this research study. The adopted methodology consists of two main parts: Experimental testing and advanced numerical modelling. Experimental testing on both material coupons and structural connections was conducted using a tensile testing machine in the Civil Engineering Laboratory of the University of Birmingham. The employed instrumentation to monitor and record key response characteristics included LVDTs, strain gauges and a data acquisition system. It should be noted that due to the nature of structural connections, where material fracture is often a governing failure mode, material characterisation studies was more extensive than in most similar studies including a comprehensive experimental study on stainless steel bolt material under various levels of stress triaxiality.

The advanced numerical modelling using the general-purpose FE software ABAQUS (2013) was based on material models developed on the basis of the previously conducted material characterisation studies and in the first instance aimed to numerically replicate the experimental results. Upon successful validation, extensive FE studies were conducted that allowed the effect of key parameters on the main response characteristics to be determined, thus generating a large number of structural performance data. The EN 1993-1-8 (2005) was assessed using the experimental and numerical data in terms of ultimate resistance. The efficiency and accuracy of the equivalent T-stub idealisation for stainless steel connection design was highlighted and reported comprehensively to develop accurate and effective design rules for stainless steel bolted connections.

1.4. Outline of the thesis

In this chapter, a comprehensive overview of stainless steel material has been presented including its chemical composition, mechanical behaviour, usage in construction industry and available international design standards. A brief summary has been reported on the research studies conducted on stainless steel member and connection design to date. The aim and objectives of this research project have been specified.

In Chapter 2, a literature review of existing studies on both carbon steel and stainless steel connections which are relevant to this research study is given. The existing design philosophy of stainless steel connections is explained comprehensively. A review on material modelling and fracture modelling of stainless steel bolts is also included.

Chapter 3 focuses on a novel experimental study on stainless steel bolts in order to quantify the available ductility of the bolts and to enable the explicit fracture modelling of stainless steel bolts in tension. Tensile tests on specimens machined from A4-80 bolts with predefined geometries yielding a wide range of stress triaxialities are carried out and the development of an advanced numerical model validated against the obtained results are reported. The generated numerical model is shown to be capable to predict the behaviour of the tested specimens including the initiation and propagation of fracture, thus enabling the explicit incorporation of bolt fracture into the numerical modelling of bolted connections utilising well-established damage mechanics concepts.

An experimental study on the ultimate behaviour of stainless steel bolted connections is reported in detail in Chapter 4. The experimental study includes 17 ferritic stainless steel bolted T-stubs under monotonic tension for which the plastic resistance, deformation capacity and failure mechanism are obtained and further utilised to assess the existing design method in EN 1993-1-8 (2005). To obtain the material characteristics of the ferritic stainless steel T-stubs and the connecting bolts, tensile coupon tests were conducted, and the material anisotropy exhibited by ferritic stainless steel is quantified in Chapter 4. Furthermore, a previously not observed failure mode of tensile coupons extracted from structural ferritic stainless steels is documented and discussed.

In Chapter 5 an advanced numerical study on stainless steel bolted T-stubs is described. Considering the previously tested T-stubs, a comprehensive numerical study is conducted and the developed FE model validated against the available test data. Moreover, the developed FE model is utilised for numerical modelling of ferritic stainless steel T-stubs and validated against the experimental results which are reported in Chapter 4. Key simulation strategies regarding the modelling of bolt geometry and overcoming numerical instabilities are compared and contrasted. Following the determination of material properties in the longitudinal, transverse and diagonal direction, the effect of allowing for anisotropy in the FE simulations is investigated and modelling recommendations for its inclusion in FE models are made.

Chapter 6 reports the design recommendations on stainless steel connections with the assessment of current design codes. In addition to the estimation of the plastic resistance, utilised in conventional structural design, the prediction of the ultimate resistance of T-stubs, which may be relied upon in extreme cases such as a column loss analysis under a robustness scenario is studied. A recently developed predictive equation to determine the ultimate resistance of carbon steel T-stubs is adapted for use in ferritic stainless steel T-stubs. The proposed equation is validated against all available experimental and numerical results on stainless steel bolted T-stubs including those reported herein and others extracted from the literature.

Finally, the main findings of this research study including an overview of the potential contributions to stainless steel design codes are summarised in Chapter 7. Recommendations on numerical modelling and design of stainless steel connections are made and potential future research is proposed.

CHAPTER 2

Literature review

2.1. Introduction

A comprehensive review of published research pertinent to this project is presented and discussed in this chapter. Past research on the structural behaviour of conventional carbon steel bolted T-stub connections is summarized and the relevant design provisions of the European specification of EN 1993-1-8 (2005) is demonstrated. Afterwards, all available experimental and numerical test data on various types of stainless steel connections are reported in detail. Subsequently, existing research on the modelling of material and fracture in the numerical studies of steel joints is discussed. Finally, concluding remarks are presented and knowledge gaps are identified. Further discussions of existing studies on the relevant topics are appropriately included in the relevant chapters of the thesis.

2.2. Behaviour and design of bolted T-stubs

In spite of the essential differences in the mechanical behaviour of carbon steel and stainless steel and particularly the significant strain-hardening characteristic in stainless steel which was shown to lead to overly conservative design, EN 1993-1-8 (2005), originally developed for the design of carbon steel joints, it is also currently applicable to stainless steel joints with some minor modifications. The expressions which are used to calculate the ultimate strength of the T-stubs for each failure mode can be used for stainless steel joints and there are no special design rules given in EN 1993-1-4+A1 (2015). The overall response of the joints can be evaluated by combining the load-deformation response of idealised components assumed to represent the behaviour of the key parts of a joint, within the so-called component method.

2.2.1. The Component Method

The most effective and accurate method for determining the behaviour of moment resisting connections is the use of full-scale experimental testing accompanied by numerical models. Full-scale testing provides reliable data for the behaviour of the connections, but it is expensive and the obtained data such as measurements of displacements, strains and forces cannot be easily extended to other joint configurations beyond the tested ones. However, tests provide accurate knowledge for the response of connections in order to validate numerical models, which can then be utilised to predict the response of joints that have not been tested.

Nethercot and Zandonini (1989) provide a comprehensive background to the methods of prediction of joint behaviour. The component method is adopted by current design provisions as a simple, effective and reliable analytical model (Jaspart, 1991; Weynard *et al.*, 1996). The main philosophy of the component method is based on predicting the stiffness and strength of the basic components that constitute the connection and combining them to determine the overall behaviour of the joint. Explicit design equations for each component are provided in EN 1993-1-8 (2005). Consequent to establishing the response of each component, the response of the joint is assembled in compliance with the provisions of EN 1993-1-8 (2005). Mainly, the component method follows three stages: (1) identification of the joint components, (2) determination of the stiffness and strength of the components and (3) assembly of the joint response using the established response of the constituent components. In this method, connections can be divided into three main different regions namely the tension zone, the compression zone and the shear zone in which the source of deformations can be specified by different components. An example of the commonly adopted joint components for an extended end plate beam-to-column joint is shown in Figure 2.1, where the associated critical components are identified. Moreover, a respective mechanical spring model for an extended end plate beam-to-column joint is depicted in Figure 2.2, in order to determine the strength and stiffness of the critical components. The failure of the joint coincides with failure of the weakest constituent spring of the respective mechanical model of the joint. Since the components of the column flange in bending, end plate in bending and bolts in tension can be idealized with equivalent T-stubs, the mechanism of establishing the stiffness, strength and post limit behaviour for T-stubs is reported hereafter.

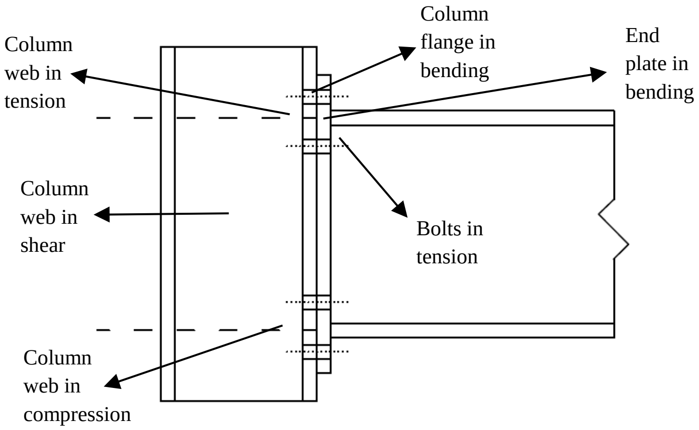

Figure 2.1: Components of an extended end plate beam-to-column joint.

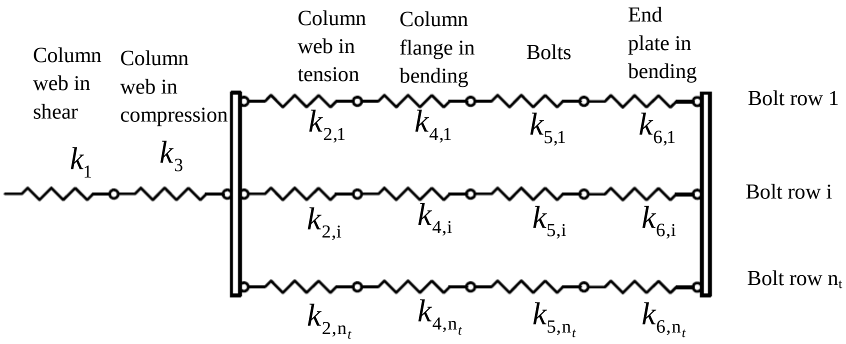

Figure 2.2: Respective mechanical spring model of an extended end plate beam-to-column joint.

2.2.2 Past research on idealisation of tension zones of joints as T-stubs

Steel bolted beam-to-column connections are commonly idealised as an assembly of simplified components, with the tension zone of the connections, typically encompassing columns flange in bending, end plate in bending and/or angle cleats in bending, usually idealised an equivalent T-stub in tension (Zoetemeijer, 1974, Packer and Morris, 1977, Mann and Morris, 1979, Yee and Melchers, 1986, Zoetemeijer, 1990, Nair *et al.*, 1974, Thornton, 1985, Kato and McGuire, 1973). Zoetemeijer (1974) reported a comprehensive experimental and analytical study and developed yield line models for the tension zone of connections using T-stub specimens. Based on a series of tests, some criteria and analytical formulations have been proposed by Zoetemeijer (1990) for the determination of the strength and deformation capacity of such connection.

Further studies have been conducted by various researchers focussing on T-stub connections instead of whole connections to determine the resistance of this basic connection (Yee and Melchers, 1986, Nair *et al.*, 1974, Thornton, 1985, Kato and McGuire, 1973). Faella *et al.* (1995;1996b) and Weynand *et al.* (1996) have conducted studies on the stiffness and strength of T-stubs and proposed some predictive equations. Additionally, Faella *et al.* (1996a;1998), Jaspart and Maquoi (1995) have studied the effect of the preload level on the behavior of the T-stub and concluded that preloading affects the stiffness but not the strength of the T-stubs. Furthermore, Faella *et al.* (2000) have taken into account the influence of moment shear interaction on the plastic resistance of the T-stubs and have represented analytical expressions for each collapse mechanism. They determined the initial stiffness of T-stubs using a flexible beam model ignoring the effect of prying forces. Comprehensive studies on the determination of the initial stiffness of a T-stub in order to evaluate the elastic response of the connections have been conducted by Aggerskov (1976;1977). Afterwards, Jaspart (1991) has adopted the same approach with a minor modification and determined the location of the prying forces according to the relative stiffness of the bolts and flanges and preload level. To provide practical design, Jaspart (1997) proposed a new approach in which bolt deformations are explicitly considered.

Since the determination of the nonlinear response of the T-stubs is very complex due to geometrical and material nonlinearities as well as due to the effect of the varying contact conditions on the emerging prying forces, various approaches have been proposed in the literature to simplify the determination of the nonlinear behaviour of the T-stubs by Jaspart (1991), Faella and co-workers (2000;2001a;2001b) and Swanson (1999). Beg *et al.* (2004) have proposed a method for determining the deformation capacity of single T-stubs. The proposed model predicts the deformation capacity of T-stubs considering fracture elongation of the bolts, the ultimate strain of the steel and the geometrical configuration of the connection. Coelho (2004) developed a beam model to characterize the nonlinear behaviour of the T-stubs and validated it with the experiments. The main conclusions of these studies and details of each model are summarized in the next section. Swanson and Leon (2000;2001) have studied the nonlinear behaviour of T-stub connections and proposed a spring model to determine key response characteristics of the T-stubs such as strength, ductility and stiffness. They concluded that the current design equations provide conservative strength predictions for the flanges and bolts (Swanson and Leon, 2000). Based on this experimental study, a stiffness model was proposed for the T-stub components and extensively calibrated against test results (Swanson and Leon, 2001). The model was based on a spring theory which takes into account the deformations of the bolts, the bending of the flanges, the elongation of the T-stem and local deformations of the T-stem and of the beam flange due to bearing of the bolts and proposed a piecewise linear force - displacement relationship model to characterize the behaviour of each spring (Swanson and Leon, 2001). The model was shown to lead to accurate predictions of the T-stub structural behaviour when compared with the experimental results.

An experimental and analytical research was carried out to investigate the essential parameters which affect the behaviour of T-stub assemblies with welded plates. The investigated parameters included the geometric configurations of the T-stubs, the material grade of the bolt and bolt diameter, the steel material grade, the existence or absence of transverse stiffeners and the weld throat thickness (Coelho *et al.*, 2004). It was reported that some of the test specimens collapsed due to the early cracks in the vicinity of the weld toe. Because of the changes in the material behaviour of the heat affected zone of the welded T-stubs, many specimens collapsed prematurely. It was concluded that as the weld thickness increases the deformation capacity reduces and the resistance increases. Moreover, the transverse stiffeners were found to increase the stiffness and resistance and reduce the ductility of T-stub connections (Coelho *et al.*, 2004).

Moreover, Coelho *et al.* (2006a; 2006b) have studied the nonlinear behaviour of T-stubs within the framework of the component method with numerical and experimental investigations. In addition to the three basic failure mechanisms, four additional failure mechanisms were proposed according to ultimate conditions and all possible failure modes and parameters that affect the ductility of the T-stubs were reported (Coelho *et al.*, 2006b). An analytical procedure was proposed to characterize the force-displacement behaviour of the T-stubs and was implemented to provide moment rotation response of the joint in line with the component method. The model has been validated against experiments conducted with bolted extended end plate connections. It was concluded that the proposed analytical model can predict the rotational behaviour of the joints with significant accuracy (Coelho *et al.*, 2006a).

2.2.3. Typical behaviour of T-stubs and ultimate resistance predictions

Essential failure mechanisms of T-stubs in tension were determined as bolt failure and plastification of the flange plate and yield line theory has been used to determine suitable effective length formulation which is used for the calculation of ultimate load of each failure mechanism (Zoetemeijer, 1974). Zoetemeijer (1974) applied a simple plastic hinge theory and introduced an effective width formulation for each collapse mechanism of T-stubs using yield line theory. The possible failure mechanisms of the T-stubs have been represented in Figure 2.3. The type-1 failure mechanism was described by the development of four plastic hinges where two plastic hinges were situated along the bolt axis and the other two plastic hinges located along the flange to web junction. In type-2 mechanism, two plastic hinges are formed at the flange to web junction and the mechanism is triggered by the failure of bolts prior to the formation of plastic hinges along the bolt axis. Type-3 failure mechanism consists only of bolt failure prior to the formation of any plastic hinges.

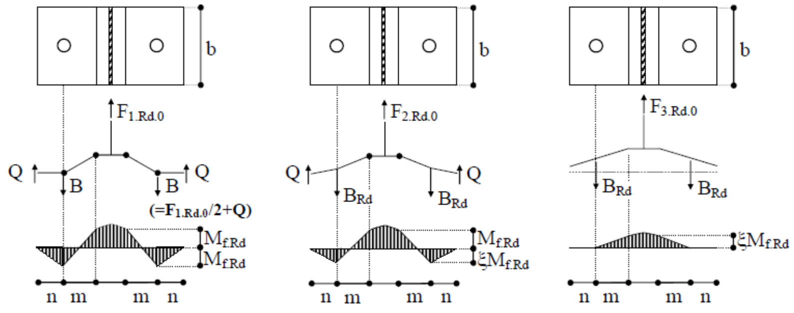

(a) Type-1: $\left(\beta_{Rd} \le \frac{2\lambda}{2\lambda+1}\right)$.

(b) Type-2 ($\xi \le 1.0$): $\left(\frac{2\lambda}{2\lambda+1} < \beta_{Rd} \le 2\right)$.

(c) Type-3 ($\xi \le 1.0$): $(\beta_{Rd} > 2)$.

Figure 2.3: Failure mechanisms of bolted T-stubs (Piluso *et al.*, 2001a).

The plastic resistance of the T-stubs, F_{Rd}, for each failure mode can be computed using the equilibrium equations considering the relevant plastic collapse mechanisms. F_{Rd} is determined as the minimum value of the three failure modes considered, $F_{Rd} = \min(F_{1,Rd}, F_{2,Rd}, F_{3,Rd})$, and the resistance corresponding to each failure mode can be calculated by the equations given below. The plastic resistance of the flanges, $M_{f,Rd}$ is given in Equation 2.4 where b_{eff} is the effective width, t_f is the flange thickness $f_{y,f}$ is the yield stress of the flange, the parameter of "m" is the distance between the bolt axis and the plastic hinge, "n" is distance between the bolt axis and the edge of the T-stub.

$$F_{1,\mathrm{Rd}} = \frac{4M_{f,Rd}}{m} \tag{2.1}$$

$$F_{2,\mathrm{Rd}} = \frac{2M_{f,Rd} + 2B_{Rd}n}{m+n} \tag{2.2}$$

$$F_{3,\mathrm{Rd}} = 2B_{Rd} \tag{2.3}$$

$$M_{f,Rd} = \frac{t_f^2}{4} f_{y,f} b_{eff} \tag{2.4}$$

According to EN 1993-1-8 (2005), the ratio between the flexural strength of the flanges and the axial strength of the bolts, β_{Rd}, can be used to predict the prevailing collapse mode, as shown in Figure 2.4, where λ is the ratio between n and m.

$$\beta_{Rd} = \frac{2M_{f,Rd}}{B_{Rd}m} \tag{2.5}$$

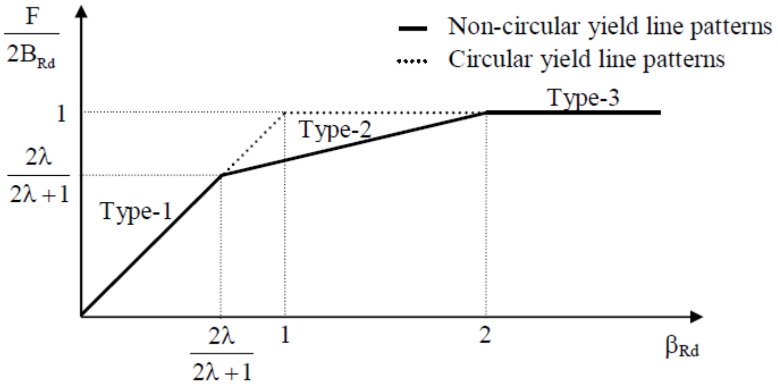

Figure 2.4: Effect of β_{Rd} on the plastic collapse mechanisms of bolted T-stubs (EN 1993-1-8, 2005).

In addition to this, Faella *et al.* (2000) have taken into account the effect of moment shear interaction on the plastic resistance of the T-stubs and have represented analytical expressions for each collapse mechanism. Expressions for type-1 and type-2 given below, type-3 mechanism is not affected by moment shear interaction.

$$F_{1,Rd} = \frac{8}{3}\left(\frac{m}{t_f}\right)^2 \left[\sqrt{1+\frac{3}{\left(m/t_f\right)^2}} - 1\right]\frac{M_{f,Rd}}{m} \tag{2.6}$$

$$F_{2,Rd} = \frac{16}{3}\left(\frac{m}{t_f}\right)^2 (1+\lambda)\left[\sqrt{1+\frac{3}{4}\,\frac{(2\lambda/\beta_{Rd})+1}{\left(m/t_f\right)^2(1+\lambda)^2}} - 1\right]\frac{M_{f,Rd}}{m} \tag{2.7}$$

Furthermore, Jaspart (1991) proposed an alternative expression for type-1 mechanism in order to take into account the effect of bolt geometry, where d_w is the bolt head, nut or washer diameter.

$$F_{1,Rd} = \frac{(32n-2d_w)M_{f,Rd}}{8mn-d_w(m+n)} = \frac{32\lambda m-2d_w}{8\lambda m-d_w(1+\lambda)}\,\frac{M_{f,Rd}}{m} \tag{2.8}$$

The effective width, b_{eff}, which is involved in the expressions for the plastic resistance, is not a physical length and it can be defined as the length of the flange which contributes to convey the load effectively. Zoetemeijer (1974) has represented a concept for effective width calculations of bolted T-stubs with considering all possible yield lines. Three possible yield line mechanisms can be defined for one bolt row T-stubs such as circular ($b_{eff,1}= 2\pi m$), non-circular ($b_{eff,2}= 4m+1.25e$) and beam pattern ($b_{eff,3}= b$) (Figure 2.5). The effective width can be determined as $b_{eff} = \min (b_{eff,1}, b_{eff,2}, b_{eff,3})$ and the parameter of *e* is defined as distance between the bolt axis and the tip of the flanges.

For the T-stubs with more than one bolt, the effective width can be determined as the minimum length determined for each of the five cases which are represented in Figure 2.6. The effective width can be calculated for five cases $b_{eff,1}= 2\pi m$ (Figure 2.6a), $b_{eff,2}= 4m+1.25e$ (Fig. 5b), $b_{eff,3}= b$ (Fig. 5c), $b_{eff,4}= \pi m+0.5p$ (Fig. 5d), $b_{eff,5}= 2m+0.625e+0.5p$ (Fig. 5e), respectively. The effective width can be determined as $b_{eff} = \min (b_{eff,1}, b_{eff,2}, b_{eff,3}, b_{eff,4}, b_{eff,5})$ and the *p* parameter corresponds to pitch of the bolts.

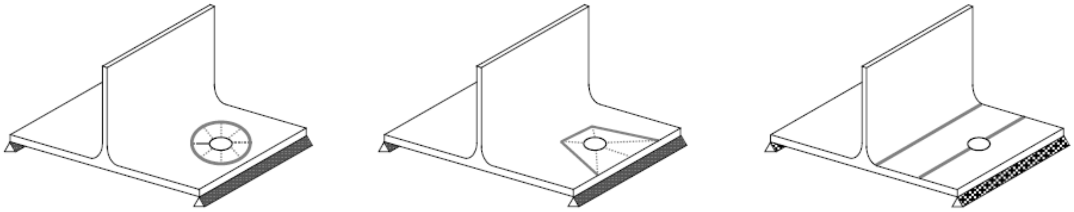

(a) Circular pattern. (b) Non-circular pattern. (c) Beam pattern.

Figure 2.5: Yield line mechanisms of bolted T-stubs with one bolt row (Coelho, 2004).

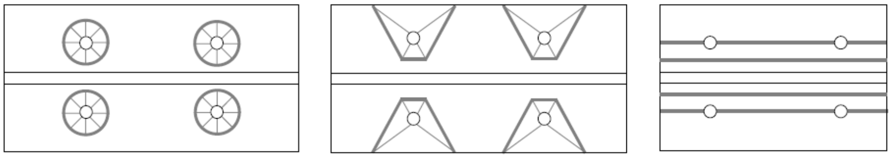

(a) Circular pattern. (b) Non-circular pattern. (c) Beam pattern.

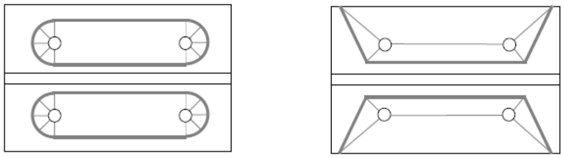

(d) “Circular” pattern. (e) “Non-circular” pattern.

Figure 2.6: Yield line mechanisms of bolted T-stubs with two bolt rows (Coelho, 2004).

In addition to determination of plastic resistance of T-stubs, several studies have been conducted to predict the full load-deformation response of T-stubs in tension. In the previously mentioned study by Piluso *et al.*, (2001a), a fundamental method to evaluate the plastic deformation capacity of T-stubs in which corresponding moment curvature diagram has been used to calculate the plastic deformation of the flange and the proposed model has been validated by experimental work (Piluso *et al.*, 2001b). The presented method was based on the assumption that the ratio between the flexural resistance of the flanges and the axial resistance of the bolts is the determining factor for specifying each failure mode given in Figure 2.7a. Plastic rotations have been calculated for the developed kinematic mechanism which is given in Figure 2.7b. The force displacement relationship was determined as a multilinear curve which consists of four branches that correspond to yielding point, the point of initial hardening, maximum load point and ultimate load point for each failure mode. Swanson and Leon (2001) proposed an alternative method in which nonlinear material properties have been used, plastic hinges in the flanges have been employed and the stiffness of the bolts has been assumed to vary as a function of the applied loads. The bolts have been modelled as a spring at the nearest edge of the bolt shank to the web plate and the spring has a piecewise linear force deformation behaviour described in Figure 2.8. The approach required various checks on whether the bolt force or the flange internal stress limit is achieved first and based on an incremental method. It is also stated that predictions of strength and deformation capacity of the flange are not always provided accurately due to uncertainties regarding strain hardening parameters and bolt ductility (Swanson and Leon, 2001).

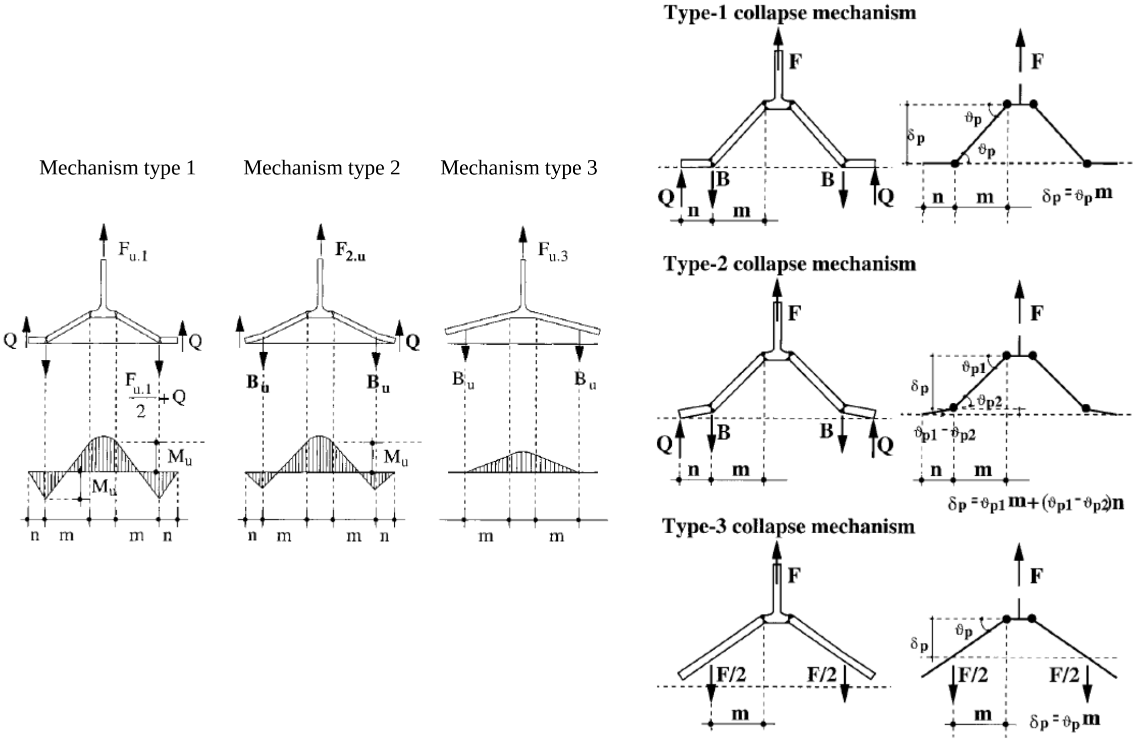

(a) Collapse mechanisms and moment diagrams (b) Kinematics of collapse mechanisms

Figure 2.7: Collapse mechanisms and relative kinematics models of T-stubs (extracted from Piluso *et al.*, 2001a).

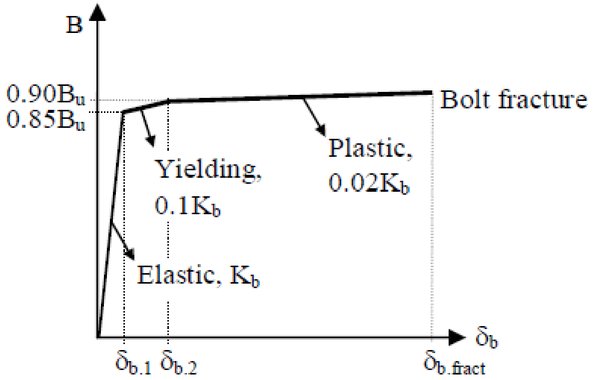

Figure 2.8: The piecewise linear force deformation model for springs (Swanson and Leon, 2001).

Beg *et al.* (2004) proposed analytical expressions for the deformation capacity of T-stubs for three possible failure modes (Figure 2.9). The approach was based on ultimate strain (ε_u) of the steel T-stub that can be reached in bending and it was assumed as 0.2 in their research. They assumed that all deformation is concentrated at which the plastic hinges occurred and the plastic hinge length is equal to the flange thickness. The following expressions (Eqs. 2.9-2.11) were proposed for the ultimate displacement correspond to all three possible failure modes where l_b is the bolt length and k is an empirical factor varies between 1 to 5.

Mode 1: $$\delta_u = 2.\varepsilon_u.m \tag{2.9}$$

Mode 2: $$\delta_u = 0.1 l_b\,(1+k(\frac{m}{n})) \tag{2.10}$$

Mode 3: $$\delta_u = 0.1 l_b \tag{2.11}$$

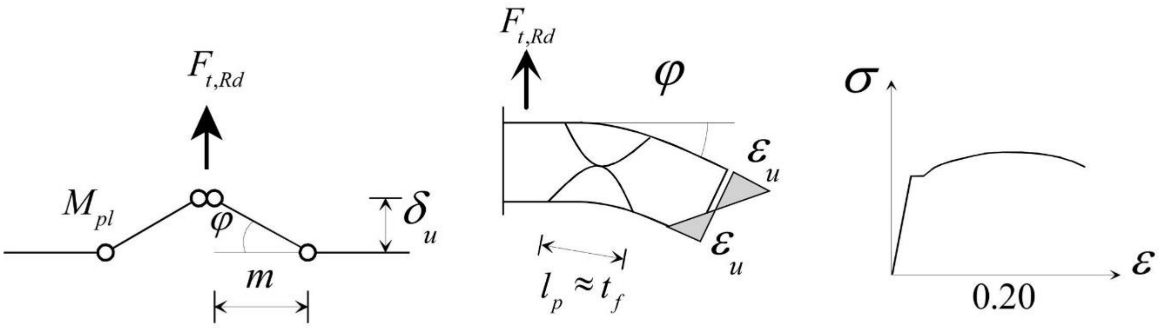

(a) Deformation capacity δu for Mode 1

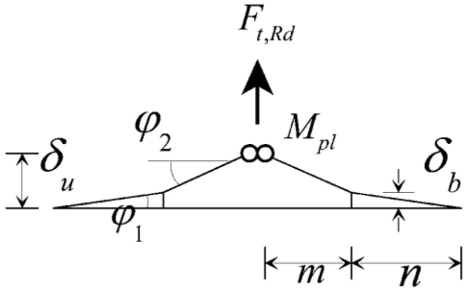

(b) Deformation capacity δu for Mode 2

Figure 2.9: Plastic mechanisms for the deformation capacity calculations of T-stubs (Beg *et al.* 2004).

Moreover, the influence of the bending actions in bolts on ultimate performance of the T-stubs is another point of view that should be properly taken into account since it was reported that the bolts on the T-stub joints are actually subjected to combined bending and tension actions (Nair *et al.*, 1974; Zhu *et al.*, 2017; Anwar *et al.*, 2019). Consequently, several analytical approaches have been proposed which include the effect of bending actions in the bolts by Stamatopoulos and Ermopoulos (2010), Abidelah *et al.* (2014) and Bao *et al.* (2019). In addition, the gap openings between the flange and connected plates triggered by the bending, develop membrane actions on the flange of the T-stubs which induce additional shear force into the bolts (Baniotopoulos 1994;1995; Baniotopoulos *et al.*, 1994; Baniotopoulos and Abdalla, 1995; Mistakidis *et al.*, 1997;1998; Kontoleon *et al.*, 1999; Kontoleon and Baniotopoulos, 2000; Latour and Rizzano, 2012;

Latour *et al.*, 2014; Francavilla *et al.*, 2015; Ribeiro *et al.*, 2015;2016; Faralli *et al.*, 2018; Santos *et al.*, 2020). To properly include the membrane actions into the calculations, Tartaglia *et al.* (2020) recently proposed equations to estimate the ultimate resistance of the T-stub under large deformations. It was stated that the membrane actions occurred in the flange in bending may affect quantifying the available ductility of T-stubs and have a vital role in seismic and robustness scenarios. The proposed expressions by Tartaglia *et al.* (2020) are presented in Chapter 6 in which ultimate resistances of stainless steel bolted T-stubs are predicted by the proposed methodology and a comprehensive discussion of the results is reported.

2.3. Previous studies on stainless steel connections

The majority of published studies that lead to the creation of stainless steel design codes have primarily focused on structural member behaviour, yet studies on stainless steel connections are limited. Errera *et al.* (1974) reported the first experimental study on stainless steel bolted and welded joints in which the design equations for the attaining the strength of austenitic stainless steel lap joints proposed by Winter (1956) were validated. Subsequently, experimental behaviour of ferritic stainless steel lap joints in single and double shear was examined by Van der Merwe (1987). In line with the results of the 36 tests on austenitic, duplex and ferritic stainless steel bolted lap joints which have been carried out by Ryan (1999), Buchair *et al.* (2008) and Salih *et al.* (2010; 2011; 2013) performed comprehensive parametric studies and validated their developed numerical models. The net section failure (Salih *et al.*, 2010), bearing failure (Salih *et al.*, 2011) and response of gusset plate connections (Salih *et al.*, 2013) have been extensively examined and it was concluded that the predictions of the valid European design recommendations EN 1993-1-4 (2006) are significantly conservative. Additionally, Kim and Kuwamura (2007; 2011) and Kim *et al.*

(2008) reported numerical studies on austenitic stainless steel joints in single shear and the numerical models were validated against the test results by Kuwamura and Isozaki (2002). More recently, a comprehensive experimental study was conducted by Talja and Torkar (2014) in which ferritic stainless steel bolted and screwed lap joints have been utilised. It was reported that design guidance which was developed for carbon steel was also valid for the ferritic stainless steel lap joints with a minor modification of requiring an extra reduction factor of 0.9 for block tearing of bolted connections and load bearing of screwed connections. Furthermore, 100 lap joints have been tested in single shear (Cai and Young, 2014a) and 49 tests were performed on austenitic and lean duplex stainless steel lap joints in single and double shear (Cai and Young, 2014b).

Bouchaïr *et al.* (2008), have investigated numerically the ductility and ultimate behaviour of stainless steel bolted T-stubs. The resistance predictions for stainless steel T-stubs according to EN 1993-1-8 (2005) were very conservative and it was also stressed that extensive numerical and experimental researches should be conducted to confirm these conclusions. The pioneered experimental studies on stainless steel bolted T-stubs in tension were reported by Yuan *et al.* (2019), who conducted 27 experimental tests on austenitic and duplex stainless steel T-stubs. It was concluded that the existing design rules defined in EN 1993-1-8 (2005) provide overly conservative strength predictions for stainless steel bolted T-stubs (Yuan *et al.*, 2019). Elflah *et al.* (2019a; 2019b), have examined the behaviour of stainless steel moment resisting connections as well as stainless steel blind-bolted connections (Elflah *et al.*, 2019c) with experimental and numerical studies. It was reported that the design provisions of EN 1993-1-8 (2005), which specify design rules for carbon joints, that are also applicable for stainless steel joints (EN 1993-1-4+A1, 2015), can predict the stiffness of the joints sufficiently but provides significantly conservative predictions for the strength (Elflah *et al.*, 2019a; 2019b; 2019c). Moreover, the structural behaviour of the moment resisting connections was investigated by three-dimensional FE model and the stiffness and resistance predictions were reported comprehensively, and proposed model validated using the experimental results (Elflah *et al.*, 2019b). Recently, Wang *et al.* (2019), Bu *et al.* (2019), Song *et al.* (2019), Gao *et al.* (2020) and Yuan *et al.* (2020a) conducted experimental and numerical studies on the behaviour of stainless steel connections and reported similar conclusions.

The reason behind the conservatism of EC3 design methodology on stainless steel components have been referred to the neglecting the significant strain hardening exhibited by stainless steel members in the design guidance in which the maximum stress is limited to the nominal yield stress (Gardner and Theofanous, 2008; Afshan and Gardner, 2013). In order to include the strain hardening into the design procedure, the Continuous Strength Method (CSM) was developed which utilises a bilinear elastic-linear hardening material response (Gardner and Nethercot, 2004; Ashraf *et al.*, 2006; Gardner 2008; Gardner and Theofanous, 2008; Afshan and Gardner, 2013; Liew and Gardner, 2015). For the case of a T-stub under tension, the exploitation of strain-hardening is mainly limited by material ductility and the CSM allows a rational exploitation of strain-hardening in the design procedure considering a bilinear elastic-linear hardening representation of the material response. Elflah (2018) utilised the CSM to estimate the full load-deformation behaviour of stainless steel T-stubs by a trilinear curve which is shown in Figure 2.10. The ultimate point (F_u, δ_u) of the load-deformation curve was calculated based on the Eqs. (2.9-2.11) which were proposed by Beg *et al.* (2004) and it was reported that the proposed approach provided accurate estimations for plastic force resistance. The ultimate loads and corresponding deformations were obtained less accurately for the ones especially failing in mode 1. The experimental force-deformation curves were replicated successfully by the proposed approach.

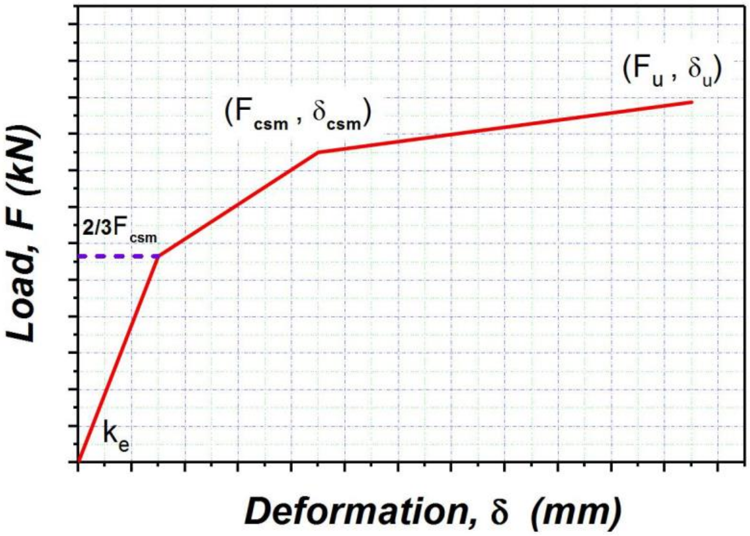

Figure 2.10: Tri-linear assumption of load-deformation response of T-stubs (Elflah, 2018).

2.4. Literature review on material modelling and explicit fracture modelling of the stainless steel bolts

2.4.1. Material modelling

Stainless steel is generally characterized by a rounded stress-strain behaviour and it does not exhibit a sharp yield point. For the materials which do not have any clear yield point, various material models have been proposed in the literature. The Ramberg-Osgood model (Ramberg and Osgood, 1943) is the well-known fundamental material model in the literature. Mirambell and Real (2000) modified these expressions in order to fit well the observed behaviour of some materials at higher stress levels. Subsequently, Rasmussen *et al.* (2003) revised this model for austenitic, ferritic and duplex stainless steels. Gardner and Nethercot (2004a; 2004b; 2004c) carried out both tension and compression tests of flat coupons and proposed modifications to the Ramberg-Osgood relationship for square and rectangular hollow sections. Moreover, Rasmussen's material model was extended by Quach *et al.* (2008) into the three stage material model. Hradil *et al.* (2013) proposed a generalized multistage model for nonlinear metallic materials.

2.4.2. Fracture modelling of the bolts

Connections between members are arguably the most critical part of a steel structure since they are subjected to high localized strength and ductility demands and high stress concentrations. The structural behaviour of connections is commonly determined using the component method which is given in EN 1993-1-8 (2005) and must reflect the design assumptions in terms of stiffness, strength and ductility. In the design of bolted connections, bolts are required to carry tension, shear or a combination thereof, with little regard to their ductility. Bolt failure is a priori considered a brittle failure mode, which is to be avoided by ensuring that other parts of the joint deform plastically prior to the bolts reaching their failure load.

In several experimental studies on structural steel (Coelho *et al.*, 2004), high strength steel (Coelho *et al.*, 2006) and stainless steel (Elflah *et al.*, 2019; Gao *et al.*, 2020) beam-to-column connections, failure was in most cases ultimately triggered by bolt fracture in the tension zone of the connections. Experimental tests on stainless steel T-stubs revealed that failure was always triggered by bolt fracture due to the high ductility and pronounced strain-hardening of the plate material allowing significant plastic deformations and stresses significantly higher than the nominal yield strength to be reached (Yuan *et al.*, 2019;2020). A combination of bolt fracture and/or plate fracture has been observed in tested structural steel T-stubs (Coelho *et al.*, 2004), whilst plate fracture dominated the response of both TMCP and quenched and tempered high strength steel T-stubs (Zhao *et al.*, 2016). Hence, depending on the relative strength and ductility of the bolts and the connected parts, bolt fracture or plate fracture may lead to overall failure.

Due to the significance of the structural behaviour of the bolts for the overall connection performance, several studies have investigated the structural performance of bolts and bolt-nut assemblies to determine their strength and characterise their failure mode. The loading regimes considered, include monotonic (Grismsmo *et al.*, 2016) and cyclic tensile loading (D`Aniello *et al.*, 2016), tension and shear loading during and after exposure to fire (Shasheena *et al.*, 2020), as well as high strain rate tensile loading (Fransplass *et al.*, 2011), whilst studies on the behaviour of bolts subjected to various combinations of tension and shear have also been reported for both high strength steel (Li *et al.*, 2020) and stainless steel bolts (Song *et al.*, 2020).

In the aforementioned studies (Grismsmo *et al.*, 2016; D`Aniello *et al.*, 2016; Shasheena *et al.*, 2020; Fransplass *et al.*, 2011), the identified failure modes of the bolts included shear and tensile fracture for bolts subjected to shear and tension respectively, as well as thread stripping of the bolt or the nut for bolt-nuts assemblies subjected to tension. It was concluded that the number of the threads in the grip length has a significant effect on the response of the bolts. Among the three possible failure modes, tensile fracture is considered more ductile as it follows the development of necking and allows significant inelastic deformations to develop. The effect of the failure mode of the bolts on the overall connection ductility has been highlighted in full-scale tests on moment resisting connections under quasi-static and impact loading (Culache *et al.*, 2017), as well as under cyclic loading (Yidu *et al.*, 2019), where bolt failure due to thread stripping was shown to result in significantly lower energy dissipation compared to bolt failure involving bolt necking and fracture.

Replacing high strength steel bolts with stainless steel ones was shown to increase the strength and ductility of the connections significantly, as stripping failure mode was observed for the majority of the high strength steel bolts, whereas a ductile fracture following necking of the bolt shank has been reported for the stainless steel bolts (Culache *et al.*, 2017).

In addition to the experimental studies, several numerical studies on bolts and bolted connections have been reported. Most studies, focus on capturing the plastic response of the material without explicit modelling of fracture, which is inferred based on comparisons of the obtained plastic strain against the material strain at fracture (Gao *et al.*, 2020; Yuan *et al.*, 2019; Yidu *et al.*, 2019; Salih *et al.*, 2010; Elflah *et al.*, 2019). This is by far the easiest modelling approach and suffices for ultimate strength predictions. However, this approach cannot accurately capture the behaviour beyond the utlimate strength of the modelled components and cannot provide accurate predictions for the deformation at fracture and the available ductility. Furthermore, assuming that fracture depends only on plastic strain is incorrect as the effect of stress triaxiality is ignored. To accurately simulate the post-ultimate response, the effect of fracture initiation and subsequent damage accumulation, which macroscopically manifests itself as material softening and strain localisation, needs to be accounted for. Some modelling approaches are discussed hereafter.

Analytical micromechanical modelling work (Rice and Tracey, 1969; Gurson, 1977; Tvergaard and Needleman, 1984) attributed ductile fracture of metals to the growth and coalescence of microscopic voids and established that the void growth is an exponential function of stress triaxiality (Rice and Tracey, 1969). Kanvinde and Deierlein (2007) tested standard and circumferentially notched material coupons and derived experimentally the parameters of the exponential relantionship (Rice and Tracey, 1969) between stress triaxiality and a fracture index which they termed void growth index. They subsequently used this index as a fracture criterion to predict fracture of steel plates with reduced section. A combination of the void growth index and miner's rule was applied by Jia and Kuwamura (2014) to predict fracture of steel flat coupons of various steel grades. In both studies (Kanvinde and Deierlein, 2007; Jia and Kuwamura, 2014) localised fracture was inferred based on obtained strain values from FE analysis.

Wierzbicki *et al.* (2005) carried out a comparative assessment of seven fracture models available in commercial FE codes and discussed their accuracy, ease of application and required number of tests to calibrate them. Furthermore, Bao and Wierzbicki (2004) conducted detailed studies on the determination of the fracture locus of previously uncracked bodies. Based on a series of tests on aluminium specimens of various geometries encompassing a wide range of stress triaxialities, they determined -1/3 as the limiting triaxiality value below which fracture cannot occur (Bao and Wierzbicki, 2005) and they calibrated a fracture model covering negative, low and high triaxialities (Bao and Wierzbicki, 2004). Their model was later improved upon to include the effect of the Lode angle (Bai and Wierzbicki, 2008). It should be noted that the methodology developed by Wierzbicki and coworkers utilises innovative tests in conjunction with FE modelling to derive and calibrate fracture models that associate cracking with the stress and strain state in a material that can be utilized to predict the formation of ductile cracks. Crack propagation is not covered, as was shown by Bao (2003), where the Bao and Wierzbicki (2004) model accurately predicted crack formation in a notched beam sbjected to three-point bending but could not replicate the observed crack propagation response correctly.

In parallel with the development of micromechanical models predicting fracture initiation, phenomenological models based on continuum damage mechanics concepts and suitable for numerical implementation have also been developed (Lemaitre, 1985; Chaboche, 1987) and implemented. Pavlovic *et al.* (2013) successfully modelled the shear fracture of steel bolts and shear studs using the "damage for ductile metals" material behaviour available in ABAQUS (2013), which is schematically depicted in Figure 2.11. In their model they utilised experimentally derived stress-strain curves to define the material response up to the attainment of the ultimate tensile stress (σ_{y0} in Figure 2.11) , whilst an iterative procedure was proposed to continue the curve beyond the ultimate tensile stress (dotted curve). Damage initiation was defined in terms of the equivalent plastic strain ε_0^{pl} which was assumed to be an exponential function of the stress triaxiality, in accordance with Rice and Tracey (1969). The exact form of the exponential function was based on earlier experimental work on austenitic steels (Trattnig *et al.*, 2008). Finally, damage evolution was defined in terms of equivalent plastic displacement following a trial and error approach to obtain a good agreement with the exprimental results. As expected a strong mesh dependancy of the damage evolution parameters was observed.

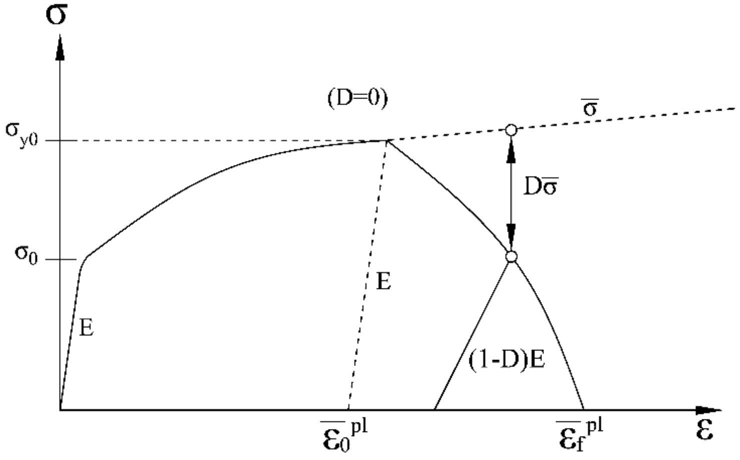

Figure 2.11: Stress-strain curve with progressive damage degradation (ABAQUS, 2013).

More recently, Song *et al.* (2020) complemented their extensive experimental study on austenitic stainless steel bolts subjected to combined shear and tension with a proposed numerical simulation methodology to predict fracture. Their work mixes continuous damage mechanics concepts with the research findings by Bao and Wierzbicki (2004) and Bao (2003) on the effect of stress triaxiality on the fracture locus of some aluminium alloys. Contrary to the approach followed by Pavlovic *et al.* (2013), Song *et al.* (2020) assumed that damage initiation (i.e. fracture initiation) is proportional to the reciprocal of the stress triaxiality, in line with Bao and Wierzbicki (2004) and Bao (2003). Furthermore, despite incorporating damage evolution in their material model, they also account for the post ultimate stress-strain response using the modified weigthed average method (MWA) based on the seminal work of Ling (1996). Ling's method relies on the identification of a lower and upper bound for the post-necking stress strain response and the determination of suitable weighting factors for them so that a post-ultimate stress-strain response that yields a close agreement with experimental data can be generated. The developed model is shown to work reasonably well in most cases, but, as will be shown in Chapter 3, the proposed material properties for fracture initiation are not in accordance with experimental results reported in Chapter 3. In Chapter 3, a predictive equation for damage initiation for Grade A4-80 stainless steel bolts as well as a consistent modelling methodology within the framework of continuum damage mechanics is provided by experimental tests on notched specimens.

2.5. Concluding remarks and knowledge gap

In this chapter, a literature review on experimental and numerical investigations of carbon steel bolted T-stubs was presented and the design provisions of EN 1993-1-8 (2005) for the design of carbon steel and stainless steel bolted T-stubs were summarised. Past experimental and numerical research on stainless steel connections as well as isolated bolted T-stubs have been reviewed. Additionally, literature review on material modelling and explicit modelling of stainless steel bolt fracture was extensively reported. It was concluded that the studies on stainless steel T-stubs in the literature focused primarily on austenitic and duplex stainless steel grades, while the structural performance of ferritic stainless steel T-stub connections has not been studied to date. Ferritic stainless steels display lower ductility and strain-hardening than austenitic and duplex grades but, as all stainless steels, lack a yield plateau. Therefore, their material behaviour is in between that of carbon steel and austenitic stainless steel. Hence it is not clear whether current design provisions of EN 1993-1-8 (2005) for carbon steel joints are suitable for ferritic stainless steel joints or whether novel design methods, such as those recently proposed for austenitic and duplex stainless steel joints by Gao *et al.* (2020) should be adopted instead. Therefore, experimental and numerical investigations of ferritic stainless steel bolted T-stubs in tension will fill the gap in the literature and behave as complementary to recently published research in which only austenitic and duplex stainless steel bolted T-stubs were considered (Yuan *et al.*, 2019; 2020a, Gao *et al.*, 2020). Experimental characterisation of the behaviour of ferritic stainless steel bolted T-stubs in tension will assess the applicability of current design rules provided in EN 1993-1-8 (2005), which were originally derived for and based on the response of carbon steel joints. The reported studies in Chapters 4-6 provide extensive basis for the development of new design methodologies and validation of current design rules for stainless steel bolted T-stubs.

Moreover, based on literature review on explicitly modelling of bolt fracture, it was concluded that the studies on explicitly modelling of stainless steel bolt fracture within the framework of continuum damage mechanics are very limited. Most studies, focus on capturing the plastic response of the material without explicit modelling of fracture, which is inferred based on comparisons of the obtained plastic strain against the material strain at fracture (Gao *et al.*, 2020; Yuan *et al.*, 2019; Yidu *et al.*, 2019; Salih *et al.*, 2010; Elflah *et al.*, 2019). This simplified approach provides sufficient ultimate strength predictions however cannot accurately capture the behaviour beyond the utlimate strength of the modelled components and cannot provide accurate predictions for the deformation at fracture and the available ductility due to the neglecting the effect of stress triaxiality. In order to accurately simulate the post-ultimate response, the effect of fracture initation and subsequent damage propagation have to be considered. Therefore, the experimental and numerical studies reported in Chapter 3 are an important step towards the development of advanced FE model which can accurately predict the fracture and available ductility of stainless steel bolts within the framework of continuum damage mechanics concept.

CHAPTER 3

Determination of fracture properties and explicit fracture modelling of stainless steel bolts in tension

3.1. Introduction

Bolt fracture often limits the ultimate strength and deformation capacity of bolted connections and leads to overall joint failure. Therefore, the prediction of structural collapse under extreme loads necessitates the incorporation of a reliable fracture model that reflects the observed structural response of bolts. This chapter reports a comprehensive experimental and numerical study into the structural behaviour, ductility and fracture characteristics of Grade A4-80 stainless steel bolts, which are commonly used as fasteners in bolted connections. Tensile tests on six duplicate smooth notched specimens machined from A4-80 bolts covering a wide range of stress triaxialities were performed and the obtained results were used to develop an equation relating the plastic strain at fracture initiation to the stress triaxiality. 2D axisymmetric and 3D advanced finite element models were calibrated against the experimental results and damage propagation parameters were defined for various mesh densities. The developed numerical models are shown to replicate the observed experimental behaviour of the tested bolts, including the initiation and propagation of fracture, and those collected from the literature. In addition, based on the conducted research herein a journal paper was submitted for publication to Thin-Walled Structures journal.

3.2. Experimental tests

3.2.1. Design of specimen geometry

A total of 12 tensile tests has been conducted on specimens machined from the shank of M10 A4-80 bolts. For all specimens the initial diameter of 10 mm was reduced to 6 mm to allow testing to failure in the available 50kN capacity machine. Two tests were carried out on standard unnotched specimens to obtain the material response, and a further 10 tests on specimens incorporating smooth circumferential notches yielding five different levels of stress triaxiality. Duplicate tests were conducted for each level of triaxiality to ensure consistency and repeatability of the results. Figure 3.1 depicts an illustration of the notched specimen geometry and the 10 notched specimens.

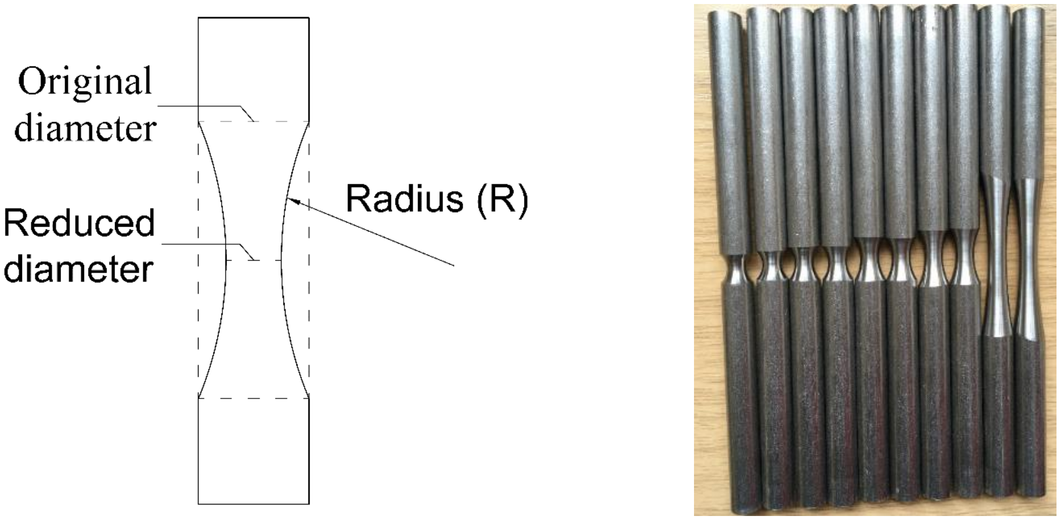

(a) Illustration of specimen geometry (b) Notched specimens prior to testing

Figure 3.1: Notched specimens extracted from M10 A4-80 bolt shank.

The selection of the notch radius R was based on predictive equations linking the notch radius with stress triaxiality η, which is defined as the ratio of hydrostatic stress σ_H over the von Mises stress $\sigma_{eq.}$. The classical Bridgman (1964) equation (Equation 3.1) and a more refined version of it (Equation 3.2) (Bai *et al.*, 2009), which was shown to better predict triaxiality, were considered. The predicted stress triaxialities for the adopted notch radii R are reported in Table 3.1, where nominal specimen geometry is reported. It should be noted that the values for stress triaxiality η predicted by both equations are significantly lower than the actual ones, which are later on determined based on FE analysis.

$$\eta = \left(\frac{\sigma_H}{\sigma_{eq.}}\right) = \frac{1}{3} + ln\left(\frac{r}{2R} + 1\right) \tag{3.1}$$

$$\eta = \left(\frac{\sigma_H}{\sigma_{eq.}}\right) = \frac{1}{3} + \sqrt{2}ln\left(\frac{r}{2R} + 1\right) \tag{3.2}$$

Table 3.1: Nominal geometric configuration of bolt specimens and associated stress triaxiality.

Specimen designation	Initial diameter (mm)	Reduced diameter (mm)	Notch radius R (mm)	Predicted stress triaxiality Equation (3.1)	Predicted stress triaxiality Equation (3.2)
SS0	10	6	-	0.33	0.33
SS1	10	6	160	0.34	0.35
SS2	10	6	20	0.41	0.44
SS3	10	6	12	0.45	0.50
SS4	10	6	8	0.51	0.58
SS5	10	6	6	0.56	0.65

3.2.2. Tensile tests and material properties

All tests have been conducted using a universal tensile testing machine under displacement control with slow applied displacement rates appropriate for quasi-static material response. The smooth (unnotched) specimens were tested according to the provisions of BS EN ISO 6892-1 (2009). In Table 3.2, the measured minimum diameter at the reduced cross-section prior to testing D_0 and the final measured diameter after fracture D_{ult} are reported, together with the measured length of the notched region, the length of the extensometer over which deformations were measured and the applied loading rate. The values of D_0 and D_{ult} are utilised to obtain the true plastic strain at fracture $\bar{\varepsilon}_f^{pl}$ of the tested specimens according to Equation 3.3, which is also reported in Table 3.2. The ultimate tensile stress, determined by dividing the maximum recorded force by the initial cross-sectional area of the smallest cross-section, is also reported and a significant increase is observed with increasing triaxiality. Figure 3.2 depicts Specimens SS0-1 (smooth coupon), SS3-1 (coupon with a notch radius of 12 mm) and SS5-1 (specimen with notch radius of 6 mm) during testing just prior to fracture.

$$\bar{\varepsilon}_f^{pl} = 2\ln\left(\frac{D_0}{D_{ult}}\right) \tag{3.3}$$

Table 3.2: Key geometric measurements for each bolt specimen.

Specimen	D_0 (mm)	$D_{ult.}$ (mm)	Length of notched region(L) (mm)	$L_{exten.}$ (mm)	Loading rate (mm/min)	True plastic strain at fracture $\bar{\varepsilon}_f^{pl}$	Ultimate tensile stress (MPa)
SS0-1	6.07	2.7	-	60	0.37	1.62	727
SS0-2	6.06	2.59	-	60	0.37	1.70	726
SS1-1	6.09	2.8	48.44	50	0.25	1.55	749
SS1-2	6.09	2.82	48.44	50	0.25	1.54	744
SS2-1	6.1	3.02	17.03	20	0.15	1.41	779
SS2-2	6.09	2.95	17.23	20	0.15	1.45	783
SS3-1	6.1	2.98	13.12	20	0.15	1.43	808
SS3-2	6.07	2.99	13	20	0.15	1.42	819
SS4-1	6.08	3.18	10.11	20	0.15	1.30	855
SS4-2	6.04	3.17	10.11	20	0.15	1.29	862
SS5-1	6.03	3.21	8.9	20	0.15	1.26	891
SS5-2	6.04	3.45	8.9	20	0.15	1.12	883

(a) smooth coupon SS0-1 (b) notched coupon SS3-1 (c) notched coupon SS5-1

Figure 3.2: Tensile specimens approaching fracture.

The obtained force-displacement response is depicted in Figure 3.3 for all tested specimens. The reported elongation has been determined based only on the notched region of the specimens; the elongation of the non-notched part of the specimens recorded by the extensometer has been eliminated assuming a linear elastic material response. In all cases the duplicate specimens are shown to give almost identical results, with the exception of specimens SS0-1 and SS0-2, where a noticeable difference in the recorded ultimate deformations can be observed. The smooth specimens are shown to possess far higher ductility compared to the notched ones as they are able to maintain their strength throughout large plastic deformations, whilst, with increasing stress triaxiality, the maximum recorded force increases and failure occurs at lower deformations. It is important to note that the apparent gain in strength of the specimens with high stress triaxiality is purely due to the prevailing stress conditions and this overstrength is accurately predicted by FE analysis using the material properties obtained from SS0-1 and SS0-2 for all specimens. A similar behaviour was observed by Song *et al.* (2020), where threaded bolts outperformed unthreaded ones in terms of ultimate tensile stress but displayed lower ductility, presumably due to the effect of increased stress triaxiality of the threaded bolts.

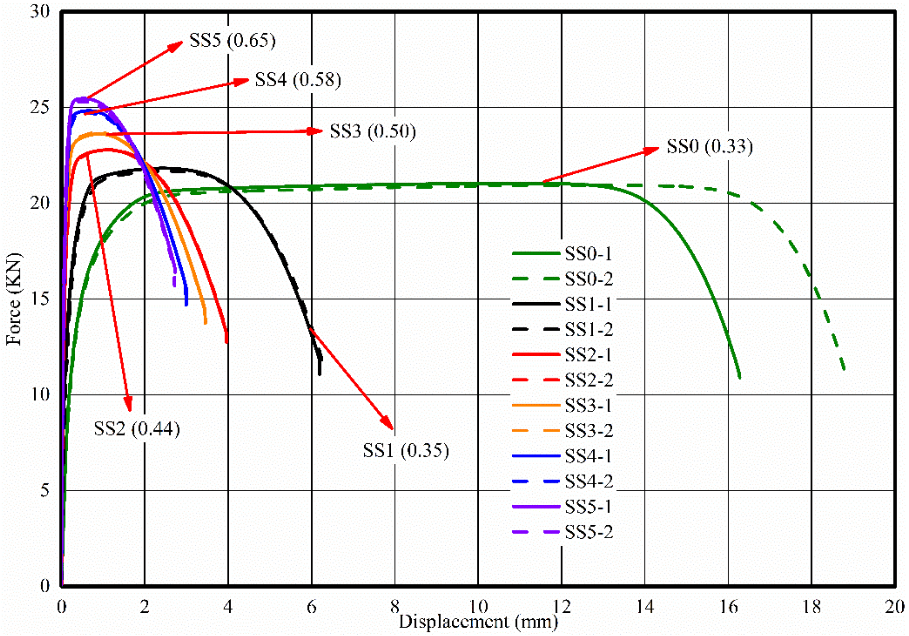

Figure 3.3: Force-displacement response of tested specimens.

The results of the two smooth specimens SS0-1 and SS0-2 are further utilised to obtain the stress-strain response of the bolt material and derive an analytical approximation of it. The engineering stress is obtained by dividing the recorded force by the initial cross-sectional area and is plotted against the engineering strain recorded by the extensometer. The resulting plot is shown in Figure 3.4. Both bolt specimens display identical response up to the attainment of the ultimate tensile stress, whereafter SS0-1 is seen to degrade and fail at lower strain than its duplicate counterpart. Contrary to most types of stainless steels, A4-80 bolt material is shown to display very low strain-hardening with the stress level remaining virtually unchanged and an almost linear region with a small slope following the initially curved response. Key material properties such as the Young's modulus E, the 0.2% and 1% proof strengths $\sigma_{0.2}$ and $\sigma_{1.0}$, respectively, the ultimate tensile stress

σ_u, the strain at the ultimate tensile stress ε_u and the strain at fracture ε_f are reported in Table 3.3. The reported values for Young's modulus, ultimate tensile stress and strain at fracture are similar to the ones reported by Gao *et al.* (2020), Yuan *et al.* (2019; 2020a) and Song *et al.* (2020) for the same nominal bolt material. None of the reported tests reached the 800 MPa nominal ultimate tensile stress of the bolt material.

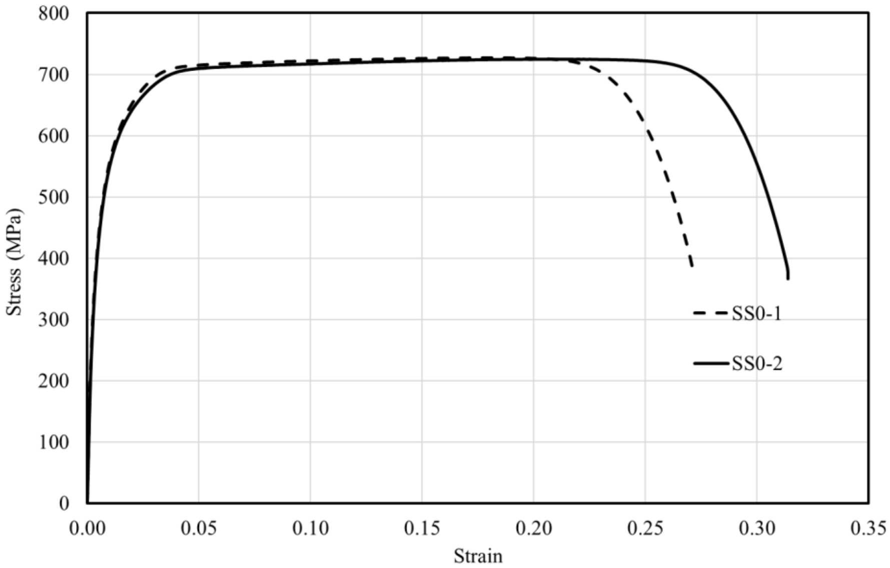

Figure 3.4: Stress-strain response of bolt material based on specimens SS0-1 and SS0-2.

Table 3.3: Material properties of stainless steel bolts.

Specimen	E (MPa)	$\sigma_{0.2}$ (MPa)	$\sigma_{1.0}$ (MPa)	σ_u (MPa)	ε_u (%)	ε_f (%)
SS0-1	185000	410	600	727	0.19	0.27
SS0-2	178821	396	592	726	0.21	0.31

Having obtained the bolt material behaviour, an analytical model approximating the recorded stress-strain response is sought. Customarily, a variant of the Ramberg-Osgood model is employed to describe the response of materials displaying gradual yielding. In this paper, a three-stage model is employed as it is shown to provide the best fit to the obtained response (Quach *et al.*, 2008). The first stage of the model is the traditional Ramberg-Osgood model (Ramberg and Osgood, 1943) and is valid up to the $\sigma_{0.2}$, the second stage is an extension of the original Ramberg-Osgood model providing a curved fit to the response up to $\sigma_{1.0}$ (Gardner and Nethercot, 2004) and the third stage provides a fit from $\sigma_{1.0}$ till the σ_u (Hradil *et al.*, 2013). The necessary material parameters to define the analytical approximation are given in Table 3.4 and are based on the average material response displayed by SS0-1 and SS0-2. The strain-hardening coefficients n, $n_{0.2,1.0}$ and $n_{1.0,u}$ were determined such that a good fit to the experimental curve can be obtained. This model is also used to extend the stress-strain curve beyond the ultimate tensile stress, as discussed in Section 3.3.

Table 3.4: Material parameters of the multistage material model (Hradil *et al.*, 2013) adopted for the stainless steel bolts.

E (MPa)	$\sigma_{0.2}$ (MPa)	$\sigma_{1.0}$ (MPa)	σ_u (MPa)	ε_u (%)	n	$n_{0.2,1.0}$	$n_{1.0,u}$
181911	403	596	726.5	0.2	4	4	11

3.2.3. Stress triaxiality and fracture initiation

During testing of the notched specimens, the stress triaxiality changes both across the cross-section and with increasing strain (Bao *et al.*, 2004; Bao, 2003; Schafer *et al.*, 2000) as the geometry of the notch and hence the prevailing local stress state along it changes. The FE software ABAQUS has been utilised to obtain the distribution of stress triaxiality across the minimum cross-section of the specimens and determine the location of its maximum value and how it changes during loading. An axisymmetric model was generated using the average measured dimensions of each set of duplicate specimens and the material model defined by the parameters reported in Table 3.4. The resulting stress-strain curve was converted into true stress-logarithmic plastic strain format as required by ABAQUS. A typical axisymmetric model with the applied boundary conditions and prescribed displacement is shown in Figure 3.5. The 4-noded bilinear axisymmetric quadrilateral element CAX4R with reduced integration and hourglass control was utilised to discretise the model. A nonlinear static analysis incorporating both geometric and material nonlinearity was conducted. A mesh convergence study was conducted, and a mesh size of 0.2 mm was found to provide a converged solution at a small computational cost. As the purpose of this analysis was to obtain stress triaxiality prior to damage initiation, no material damage was defined and the material curve was extended well beyond the recorded strain at fracture. Figure 3.6 depicts the experimental response of specimens SS1-1 and SS1-2 and the corresponding numerical curve which does not consider material damage. Damage initiation is assumed to occur at the load increment at which the numerical curve deviates from the experimental one.

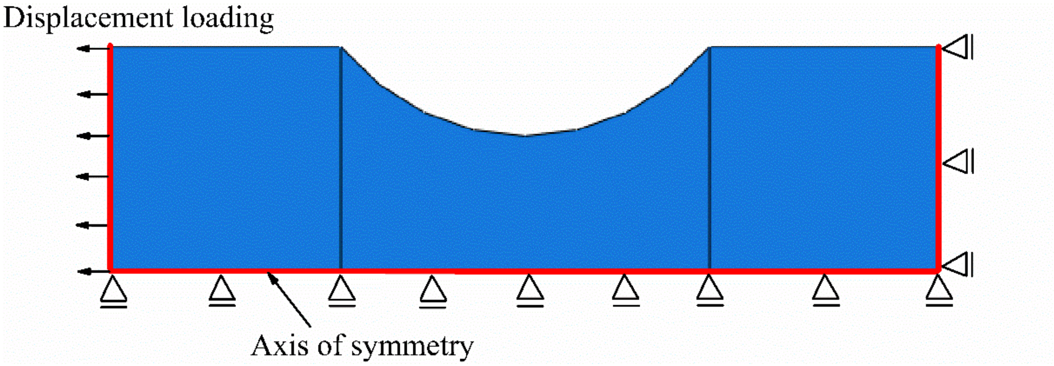

Figure 3.5: Typical axisymmetric FE model of the tested specimens.

The resulting stress triaxiality distribution along the mid-section of the model has been obtained and is reported in Figure 3.7 at two discrete load levels: at the beginning of the loading prior to any yielding occurring denoted as ER (elastic region) and at the attainment of the maximum experimental load denoted as ID (initiation of degradation). For the unnotched specimens, the triaxiality value remains constant at 0.333 throughout the cross-section at all load levels, whilst, with increasing initial triaxiality values a pronounced increase in the stress triaxiality is observed with increasing loading. The right end of each curve corresponds to the surface of the notched sections. It can be observed that the peak stress triaxiality increases when the radius of the notch decreases as expected. Furthermore, the peak stress triaxiality occurs at the centre of the sections and it decreases smoothly along the radius of notched section.

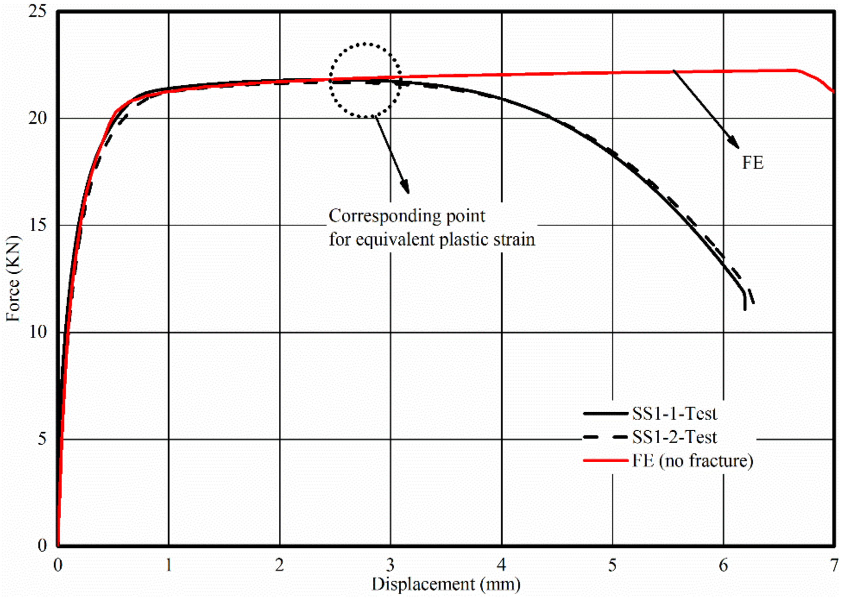

Figure 3.6: FE modelling of SS1 without accounting for fracture and determination of the point of damage initiation and corresponding equivalent plastic strain.

Ductile crack initiation mainly follows two patterns i.e. surface cracks and centre cracks. In addition, the specimens with a large notch radius rupture due to the propagation of centre cracks. The occurrence of fracture initiates with necking, followed by the formations of micro voids and coalescence of micro voids to form a crack and terminates with the shear cracks. The findings reported herein accord well with the attained experimental results. The location of peak stress triaxiality corresponds well with the crack initiation location monitored in the experiments, where a softening material response was observed in the absence of surface cracking. The stress triaxiality values at the centre of the specimens (r=0) appear to be the highest at both load levels considered. Similarly, the equivalent plastic strain, henceforth denoted as PEEQ, also reaches its highest value at this location. Thus, it can be concluded that fracture initiates at the centre of the specimens. This is an important observation, given that machining of the bolts with a lathe to obtain the final specimen geometry is expected to only locally affect the material response on the surface of the specimens, with the material in the centre remaining virtually undisturbed. Hence it can be supported that the obtained results for the machined specimens are valid to characterise the fracture of the bolt material.

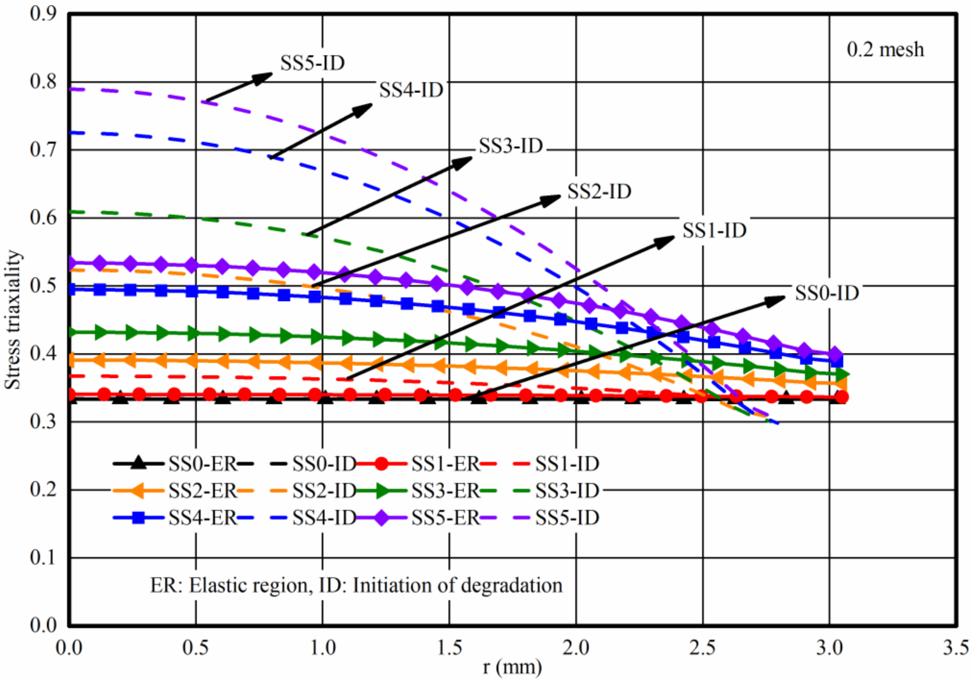

Figure 3.7: Distribution of the stress triaxiality along the notched sections in axisymmetric FE models.

Having obtained the triaxiality distribution along the specimens’ mid-section, a representative average triaxiality value is sought for each specimen. For the smooth specimens, this representative value is 1/3, whilst for the notched specimens, where a change in triaxiality is observed with increasing loading, the triaxiality value at the centre of the specimen is plotted against the corresponding PEEQ for all analysis increments (i.e. from the onset of loading until the attainment of the maximum experimental force), as shown in Figure 3.8. The average triaxiality value is obtained as the area under the curve normalised by the PEEQ at the maximum force, in accordance with the procedure described by Bao and Wierzbicki (2004) and Bao (2003).

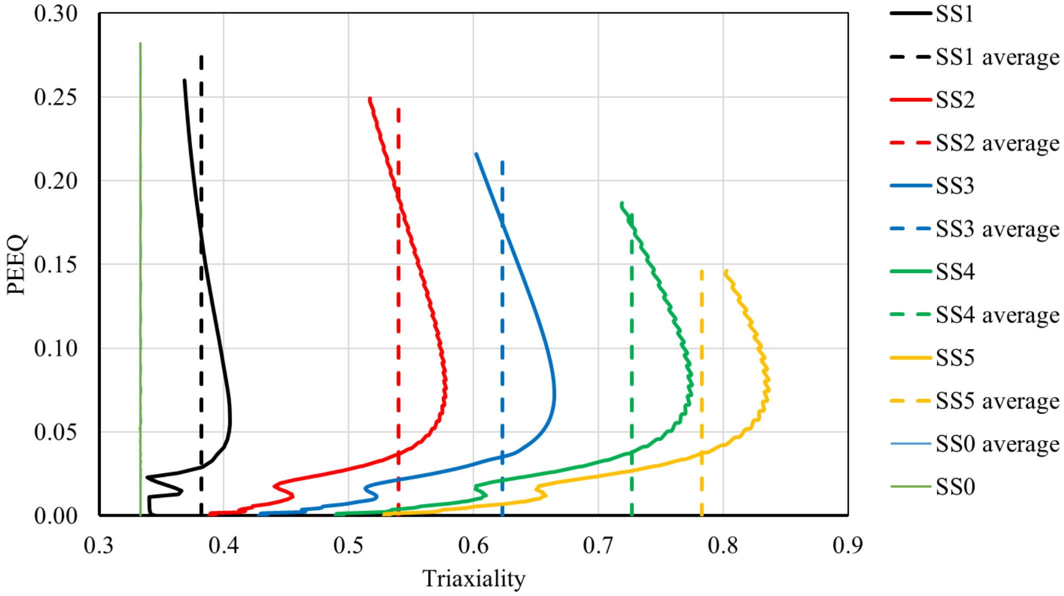

Figure 3.8: Evolution of stress triaxiality with increasing strain and average stress triaxiality for each notched specimen.

The average stress triaxiality values as well as the equivalent plastic strain at fracture initiation $\varepsilon_{pl,D}$ and the true plastic strain at fracture ε_f are reported in Table 3.5 for all tested specimens. As expected, the plastic strain at fracture initiation $\varepsilon_{pl,D}$ decreases with increasing stress triaxiality. The average stress triaxiality values range from 0.33 to 0.78 and are significantly higher than the predicted values based on Equations (3.1) and (3.2). An exponential function (Equation (3.4)), has been determined that provides a best fit to the obtained results, as shown in Figure 3.9. Equation (3.4) predicts on average 99% of $\varepsilon_{pl,D}$ with a coefficient of variation of 0.07. For comparison, the exponential function utilised by Pavlovic *et al.* (2013) for the determination of the fracture initiation strain of Grade 8.8 bolts is also included, highlighting the significant differences of the two materials in terms of their fracture characteristics. Equation (3.4) is utilised in the next section to define the equivalent plastic strain at fracture initiation as a function of the stress triaxiality and can be considered a material property characterising the fracture initiation of A4-80 bolts. It should be noted that since no damage and hence no softening response was incorporated in the developed numerical models, there is no mesh dependency of the derived Equation (3.4).

$$\varepsilon_{pl,D} = 0.46e^{-1.33\eta} \tag{3.4}$$

Table 3.5: Key fracture properties and average triaxiality.

Specimen	Predicted triaxiality Equation (3.2)	Actual average triaxiality η	Equivalent plastic strain at fracture initiation $\varepsilon_{pl,D}$	Predicted equivalent plastic strain at fracture initiation by Equation (3.4)	True plastic strain at fracture $\bar{\varepsilon}_f^{pl}$
SS0-1	0.33	0.33	0.282	0.295	1.62
SS0-2	0.33	0.33	0.282	0.295	1.70
SS1-1	0.35	0.38	0.274	0.277	1.55
SS1-2	0.35	0.38	0.274	0.277	1.54
SS2-1	0.44	0.54	0.247	0.224	1.41
SS2-2	0.44	0.54	0.247	0.224	1.45
SS3-1	0.50	0.62	0.216	0.201	1.43
SS3-2	0.50	0.62	0.216	0.201	1.42
SS4-1	0.58	0.73	0.185	0.175	1.30
SS4-2	0.58	0.73	0.185	0.175	1.29
SS5-1	0.65	0.78	0.146	0.162	1.26
SS5-2	0.65	0.78	0.146	0.162	1.12

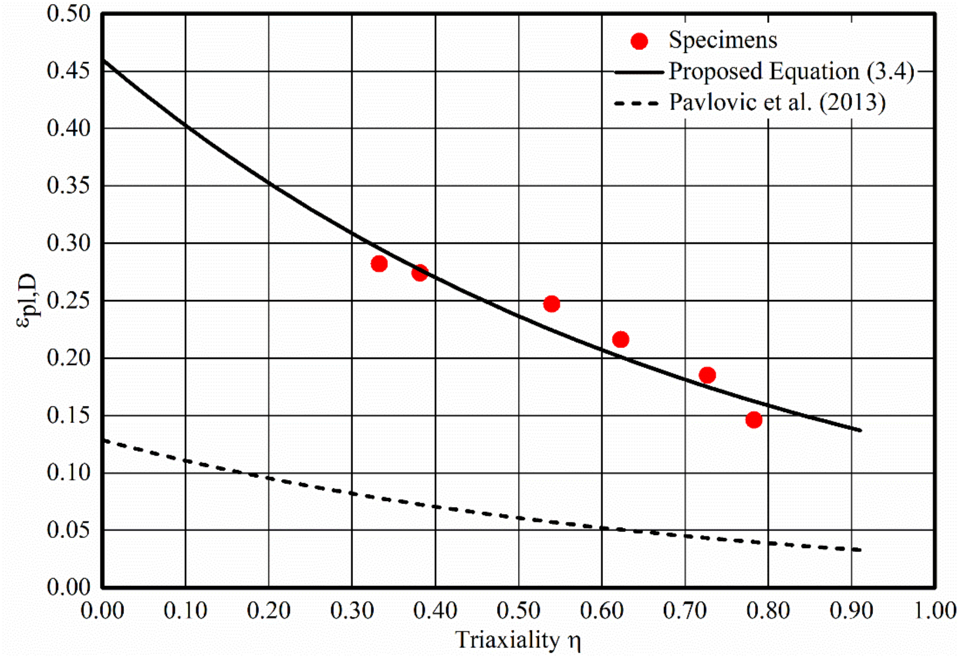

Figure 3.9: Equivalent plastic strain at fracture initiation as a function of stress triaxiality.

Finally, Equation (3.5) proposed by Song *et al.* (2020) for the prediction of the true plastic $\bar{\varepsilon}_f^{pl}$ strain at fracture (Equation (3.5)), which is based on the study by Bao and Wierzbicki (2004), is assessed against the results reported in Table 3.5. Although the predicted strains are used by Song *et al.* (2020) for the initiation of damage accumulation, in essence they are strains at fracture, since they already incorporate significant material degradation as earlier discussed. Hence Equation (3.5) is assessed against the experimentally obtained ε_f values. It can be clearly observed in Figure 3.10 that Equation (3.5) does not agree at all with the experimentally obtained values particularly for small to medium stress triaxialities, whilst the agreement improves for stress triaxialities above 0.6. The predicted strains are in all cases higher with discrepancies in excess of 80% for stress triaxiality equal to 0.33.

$$\bar{\varepsilon}_f^{pl} = \frac{2.94(\frac{1}{3})}{\eta} \tag{3.5}$$

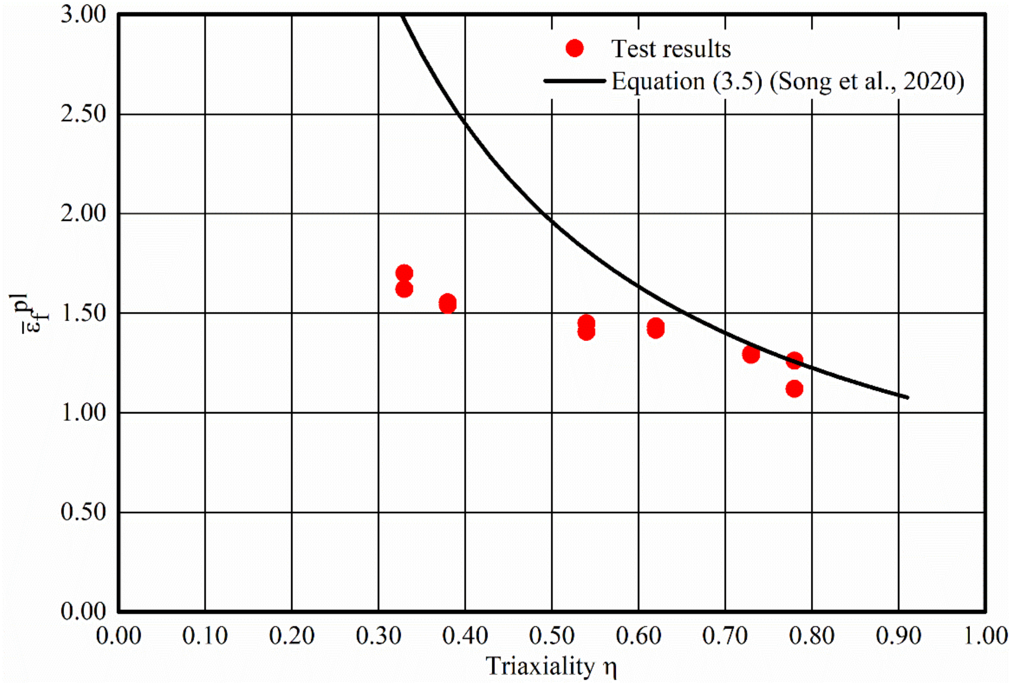

Figure 3.10: Assessment of predictive equation (Song *et al.*, 2020) for true plastic strain at fracture $\bar{\varepsilon}_f^{pl}$.

3.3. Numerical modelling of fracture

Having determined a relationship between the equivalent plastic strain at fracture initiation and the stress triaxiality, an advanced FE model incorporating damage initiation and evolution is developed and validated against the experimental response of the tested specimens. The developed numerical model is capable to predict the behaviour of the tested specimens including the initiation and propagation of fracture and is utilised hereafter to predict the structural response of bolted connections collated from the literature. Both an axisymmetric and a 3D model are considered, as discussed below.

3.3.1. Axisymmetric FE model

The developed axisymmetric model is identical to the one described in Section 3.2.3 for the determination of the average triaxiality η and the equivalent plastic strain at fracture initiation $\varepsilon_{pl,D}$ in terms of the employed element type, applied boundary conditions and material modelling prior to damage initiation. Von Mises plasticity coupled with isotropic hardening is defined based on the material properties defined in Table 3.4, whilst the response of the material incorporates a damage initiation criterion, in the form of equivalent plastic strain at damage/fracture initiation as a function of the stress triaxiality, which has been defined according to Equation (3.4) and a damage evolution law. Once the fracture initiation criterion specified in Equation (3.6) is met, i.e. once the critical equivalent plastic strain for the prevailing stress triaxiality is reached at an integration point, the material response changes from undamaged von Mises plasticity to damaged plasticity. To this end a scalar damage variable D is introduced which effectively degrades the undamaged material response, shown in Figure 3.6 as a red line, and allows the experimental curve to be traced. Material damage manifests itself as softening of the material response and as degradation of the elastic stiffness. The damage parameter varies from 0 prior to damage initiation to 1 which correspond to the complete loss of material strength and stiffness. The damage evolution can be defined based on effective plastic displacement at or energy dissipated during the damage process. In this study, the damage evolution law was defined based on the effective displacement at failure and was assumed to be linear.

$$\int \frac{d\varepsilon_{pl}}{\varepsilon_{pl,D}(\eta)} = 1 \tag{3.6}$$

It is well known that numerical instabilities arise when softening material response is considered. To this end, the explicit dynamics solver ABAQUS/EXPLICIT (2013) was employed to perform the nonlinear analyses. Quasi-static response was achieved by specifying a slow displacement rate and checking that the kinetic energy was smaller than 2% of the internal energy throughout the analysis with the exception of the first few increments as was successfully done in similar studies involving damage propagation (Manos *et al.*, 2014). Furthermore, softening material behaviour is known to be accompanied by pronounced mesh dependency (Crisfield and Wills, 1988). A uniform mesh of 4-noded bilinear axisymmetric quadrilateral CAX4R elements with reduced integration and hourglass control was adopted to discretise the bolts within the length of the extensometer. The mesh sizes considered were 0.5 mm and 0.2 mm. The corresponding effective plastic displacement at failure value was determined based on comparing the FE results with the experimental ones for various values of the displacement at failure. The best agreement was obtained for a displacement value of 1.1 mm and 0.7 mm for the 0.5 mm and the 0.2 mm mesh sizes, respectively. Subsequent mesh refinement necessitated the use of smaller values for the displacement at failure without offering any improvement in the quality of the obtained results. Hence a mesh size of 0.2 mm is deemed fine enough for the developed FE models.

The resulting numerical force-displacement curves are plotted together with the experimental curves in Figure 3.11 for all tested specimens. It can be observed that the experimental curves were accurately replicated using the developed FE model with axisymmetric elements. The proposed damage initiation and propagation models can accurately predict the experimental response throughout the full range of stress triaxialities considered. Both the 0.2 mm and the 0.5 mm mesh sizes give a remarkably close agreement with the experimental results in all cases. The finer mesh seems to more accurately capture the curvature of the post-ultimate response of the curves, owing to the more elements used over which damage accumulates and hence a more gradual manifestation of damage. It is important to note that the proposed material model necessitates only the calibration of a single damage propagation parameter for a given mesh size, whilst the triaxiality dependence of the damage initiation is mesh independent and valid for the bolt material considered.

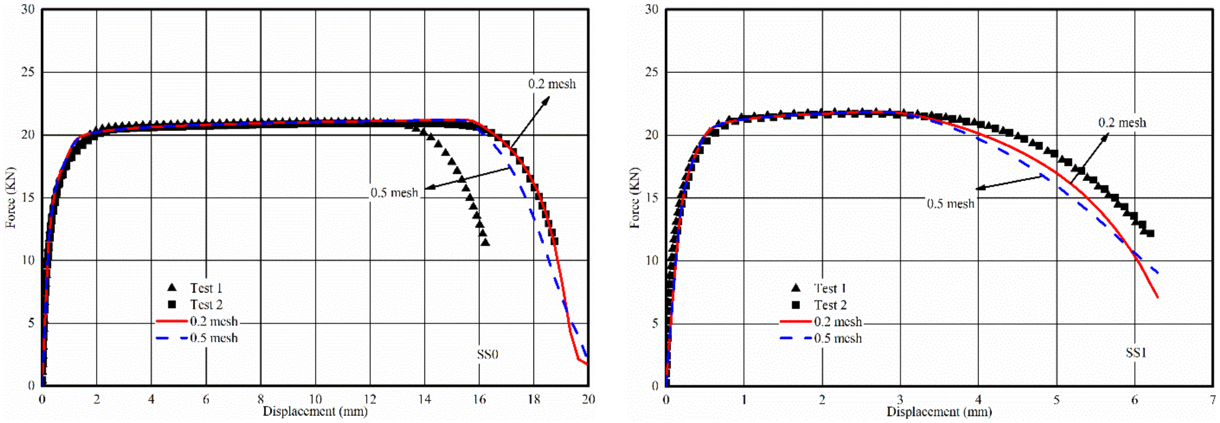

(a) SS0 (b) SS1

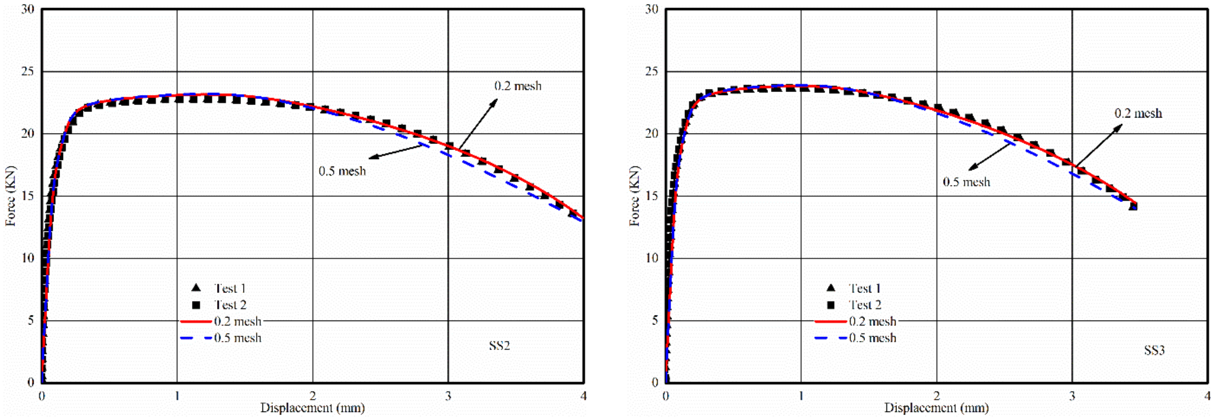

(c) SS2 (d) SS3

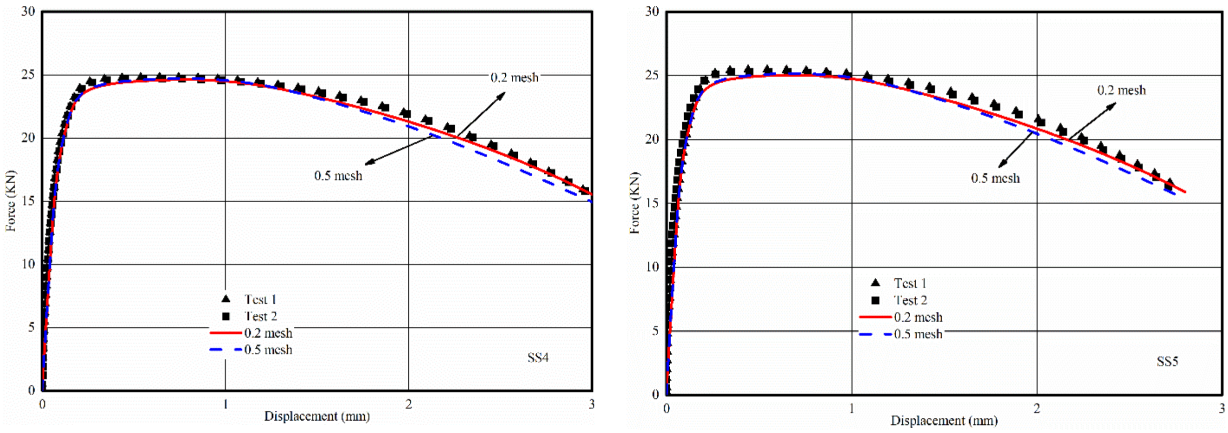

(e) SS4 (f) SS5

Figure 3.11: Comparison of the numerical force-displacement curves based on axisymmetric (2-D) model and the experimental curves.

3.3.2. 3D FE model

In addition to the axisymmetric model, a 3D FE model was also developed to demonstrate the effectiveness of the proposed damage modelling approach in realistic 3D representation of bolted connections. The measured geometry of the specimens was discretised using 8-node C3D8R linear brick elements with reduced integration and hourglass control, as shown in Figure 3.12. All other modelling assumptions, including the adopted material model and the fracture initiation criterion as well as the analysis type were identical to the ones adopted in the axisymmetric model. Calibration of the damage parameter for two uniform mesh sizes was conducted and optimal agreement with the experimental results was obtained for a plastic displacement at fracture of 0.55 mm and 0.26 mm for the 0.5 mm and the 0.2 mm mesh size respectively. In Table 3.6 the optimal displacement at fracture values are summarised for axisymmetric and 3D models for both mesh sizes considered.

Figure 3.13 depicts the obtained numerical curves alongside the experimental ones. For ease of comparison, the numerical response obtained both from axisymmetric and 3D models is shown.

Again, an almost perfect agreement between the numerical and experimental results was obtained in all cases, with the fine mesh capturing the post-ultimate response slightly better. Furthermore, it can be seen that the axisymmetric model and the 3D model offer identical results, albeit at much different computational cost.

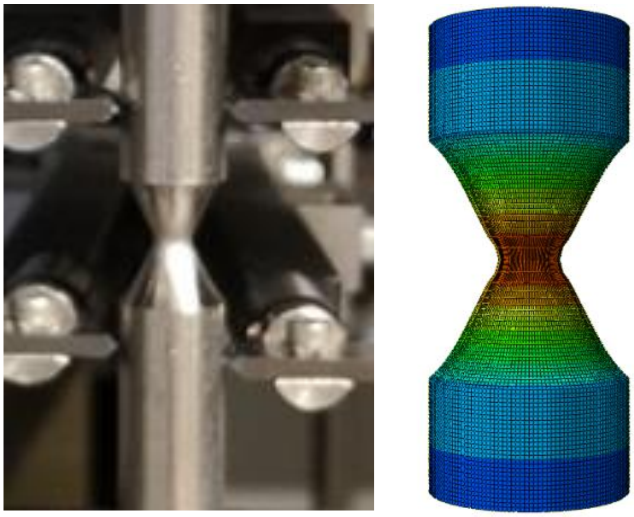

Figure 3.12: Close-up of test specimen and 3D FE model.

Table 3.6: Optimal values for the plastic displacement at fracture.

mesh size (mm)	u_f (mm) for axisymmetric model	u_f (mm) for 3D model
0.5	1.10	0.55
0.2	0.70	0.26

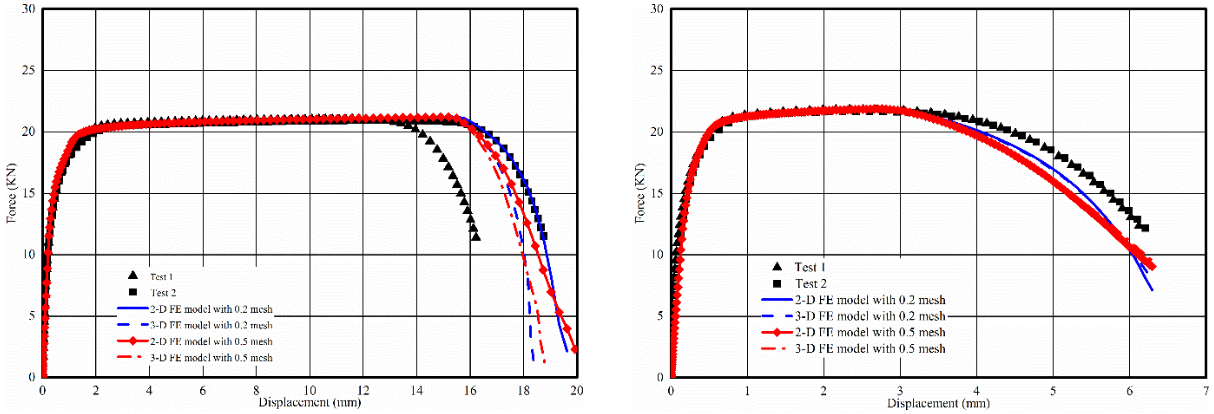

(a) SS0 (b) SS1

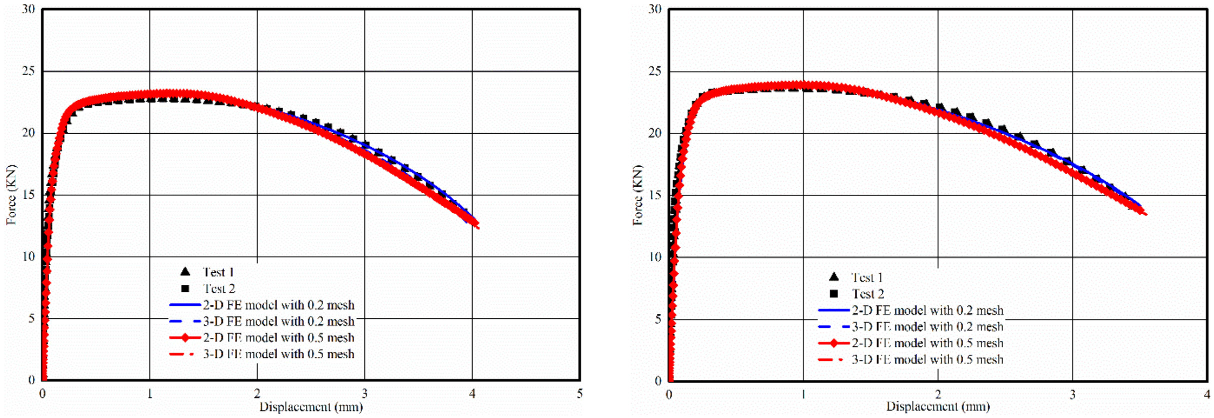

(c) SS2 (d) SS3

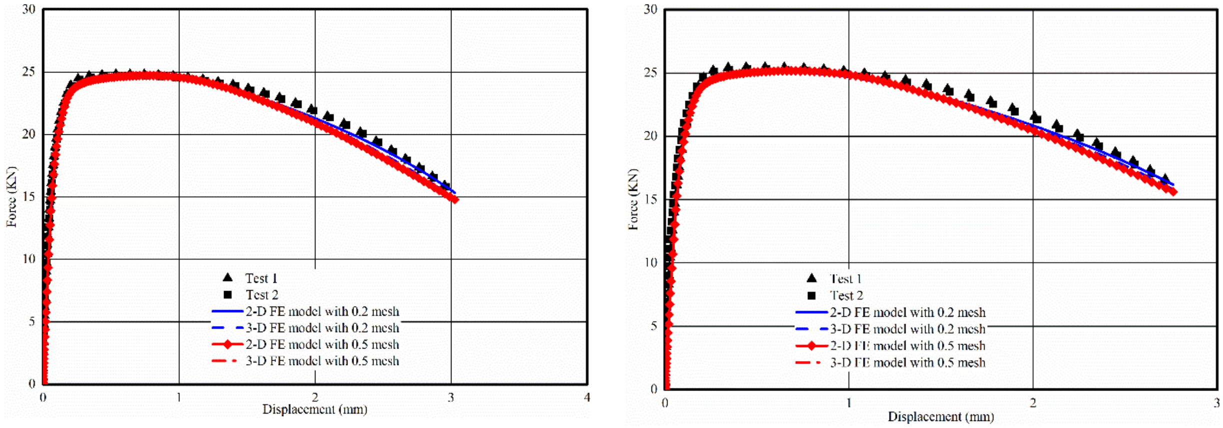

(e) SS4 (f) SS5

Figure 3.13: Comparison of the numerical force-displacement curves with the experimental curves.

3.4. Case studies

In order to show the validity of the proposed fracture model, the numerical model previously described is utilised herein to simulate the structural behaviour of four experimental tests reported in the literature employing M20 and M16 bolts in Grade A4-80. These include a series of tests on stainless steel A4-80 bolts subjected to tension and/or shear was recently reported by Song *et al.* (2020), the behaviour of a fully threaded bolt in tension (Elflah *et al.*, 2019), the behaviour of a bolted T-stub specimen tested to failure (Yuan *et al.*, 2019) and the behaviour of a moment resisting connection (Elflah *et al.*, 2019) the failure of which was triggered by bolt fracture. All models were analysed using ABAQUS/Explicit to overcome the convergence issues associated with softening material response (Manos *et al.*, 2014; Crisfield *et al.*, 1988) and utilised mass scaling to speed up the analysis time.

3.4.1. M20 bolt shank in tension

An M20 bolt in Grade A4-80 was tested under tension and the full load-elongation curve of the bolt as well as the corresponding numerical prediction were reported by Song *et al.* (2020). This test is also simulated herein utilising the previously presented numerical modelling approach. As earlier discussed, axisymmetric and 3-D models were shown to offer almost identical predictions for bolts in tension, albeit at markedly different computational costs. For efficiency, an axisymmetric FE model is developed herein to determine the force-displacement curve of the bolt. The geometry, boundary conditions and applied loading for the axisymmetric model are identical to the ones shown in Figure 3.5, whilst the geometric modelling of the bolt introduced a gradually decreasing cross-section from 20.1 mm at the end to 20 mm at mid-length to trigger failure at the desired location. Given the similarity of the material properties reported by Song *et al.* (2020) with the ones reported herein in Table 3.4 for this bolt grade, particularly for the σ_u and ε_u, the three-stage Ramberg-Osgood model was adopted to define the undamaged material response up to a true plastic strain value of 2.0, adopting the Young's modulus, $\sigma_{0.2}$ and σ_u values reported by Song *et al.* (2020). Equation (3.4) was employed to define the equivalent plastic strain at fracture initiation as a function of stress triaxiality.

Particular attention was paid to the employed mesh size given the pronounced mesh dependency of the damage parameter defining fracture propagation. In Section 3.3.1, two mesh sizes, namely 0.5 mm and 0.2 mm, were employed to mesh the 6 mm smooth bolt coupons, resulting in a uniform mesh with 12 and 30 elements through the thickness, respectively. To maintain consistency when analysing this geometrically identical structure, a uniform mesh was employed for the M20 bolt with the same number of elements through its thickness, thus resulting in mesh sizes of 1.67 mm and 0.67 mm for the coarse and the fine mesh size, respectively. It is well known that the length of the necking area of round coupons is proportional to the square root of the cross-sectional area, which is used to define the gauge length based on which the strain at fracture is determined (BS EN ISO 6892-1, 2009). Hence the necking area over which strain and damage localisation occurs, is expected to be proportional to the diameter of the bolt, and the employed uniform mesh size of 1.67 mm and 0.67 mm for the M20 bolt is expected to result in the same number of elements over the damage localisation region as the mesh sizes 0.5 mm and 0.2 mm for the 6 mm smooth bolt coupon. The optimal displacement at fracture u_f for the two mesh sizes reported in Table 3.6 is updated for the equivalent mesh sizes corresponding to M16 and M20 bolts in Table 3.7. Although not entirely correct, this easy to apply reasoning can provide fast and reasonably accurate estimates of the optimal damage parameter when modelling different bolt sizes, provided that the optimal displacement at fracture value has been determined for one bolt size.

Figure 3.14 depicts the obtained numerical results using the herein proposed model for the two mesh sizes (0.67 mm and 1.67 mm) alongside the experimental curve (Song *et al.*, 2020). The corresponding numerical curve reported by Song *et al.* (2020) is identical and indistinguishable from the experimental curve, given that the modified weighted average approach (Ling, 1996) was adopted by Song *et al.* (2020) to define the post-necking material behaviour such that the resulting numerical force-displacement curve is identical to the experimental one. The numerical curves based on the damage mechanics approach proposed in this paper, can be seen to replicate the experimental response quite accurately, with both mesh sizes resulting in identical responses up to the fracture initiation as expected, but the model with the finer mesh more closely replicating the experimental response.

Table 3.7: Optimal values for the plastic displacement at fracture for various bolt sizes.

Diameter of model (mm)	mesh size (mm)	u_f (mm) for axisymmetric model	u_f (mm) for 3D model
6	0.5	1.10	0.55
	0.2	0.70	0.26
16	1.33	2.93	1.47
	0.53	1.87	0.69
20	1.67	3.67	1.83
	0.67	2.33	0.87

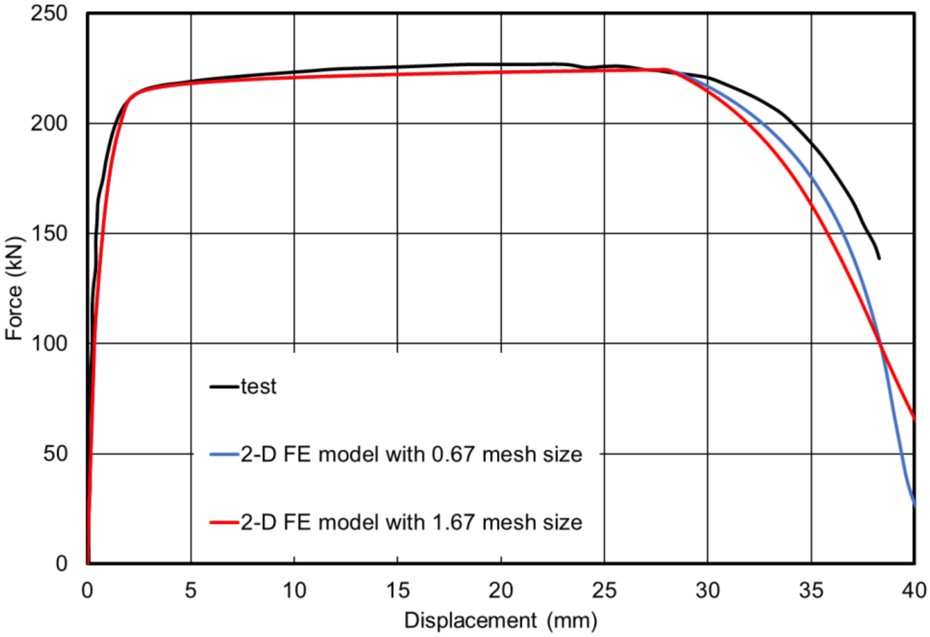

Figure 3.14: Experimental (Song *et al.*, 2020) and numerical bolt elongation response for M20 A4-80 bolt.

3.4.2. M20 bolts under tension and shear

Having demonstrated the ability of the proposed fracture model to accurately capture the experimentally determined force-displacement behaviour of an M20 bolt in tension, it is attempted to expand the scope of application to bolts subjected to combined tension and shear. To this end, two experimental tests on A4-80 bolts loaded at 30^0 and 45^0 with respect to the bolt axis, which failed by combined shear and tension in the shank are utilised (Song *et al.*, 2020). The FE model of the specimen loaded at a 30^0 inclination with respect to the bolt axis is shown in Figure 3.15, where the discretisation of the overall model and the mesh refinement of the bolt are shown. Due to the nature of the problem a 3D model was generated. A uniform mesh size of 0.67 mm with a displacement at fracture of 0.87 mm was employed in the expected failure region, whilst a coarser mesh was employed in the remaining model to save computational time. Contact was explicitly modelled using the embedded general contact algorithm, assuming hard contact in the normal direction and frictionless contact in the tangential direction.

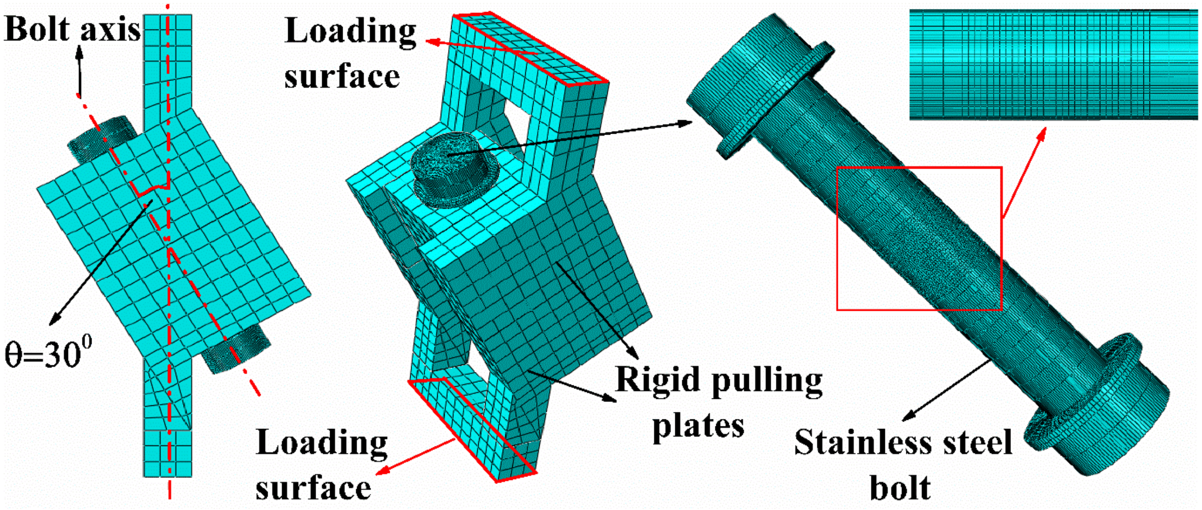

Figure 3.15: Numerical model of bolt subjected to tension and shear.

Figure 3.16 (a) and 3.16 (b) show the obtained results together with the corresponding experimental and numerical curves reported by Song *et al.* (2020) for the 30^0 and the 45^0 specimens, respectively. The model by Song *et al.* (2020) significantly underpredicts the displacement at which fracture initiation occurs presumably because it does not accurately predict the strain at fracture initiation. Although a coarser mesh than that employed by Song *et al.* (2020) was used, the model proposed herein approximates reasonably well the experimental results, thus highlighting the validity of the proposed model. It should be noted that Equation (3.4), which relates the equivalent plastic strain at fracture initiation to the stress triaxiality was calibrated based on experimental results with stress triaxialities in excess of 0.33, whereas combined shear and tension generally leads to lower triaxiality values. Nonetheless, Equation (3.4) seems to provide a good estimate for the equivalent plastic strain at the onset of damage even for triaxialities below the values considered for its calibration.

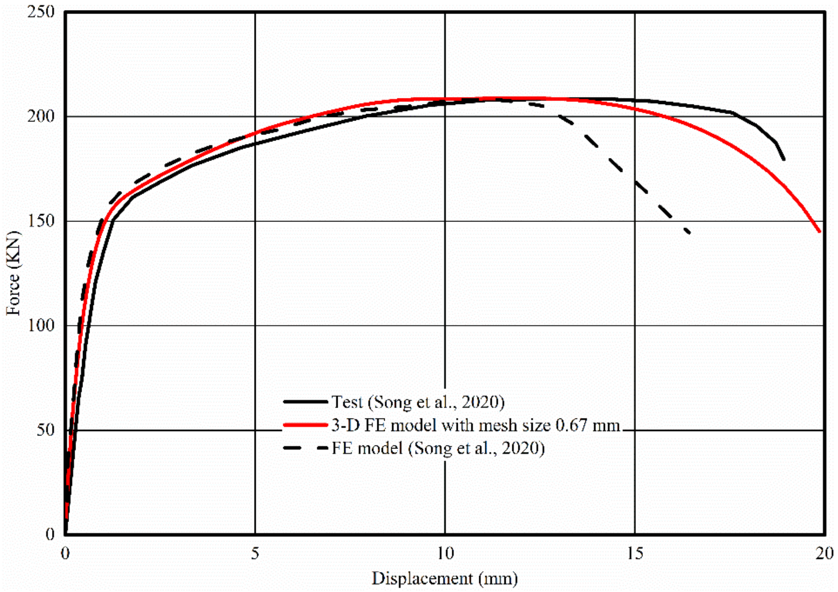

(a) 30^0 test

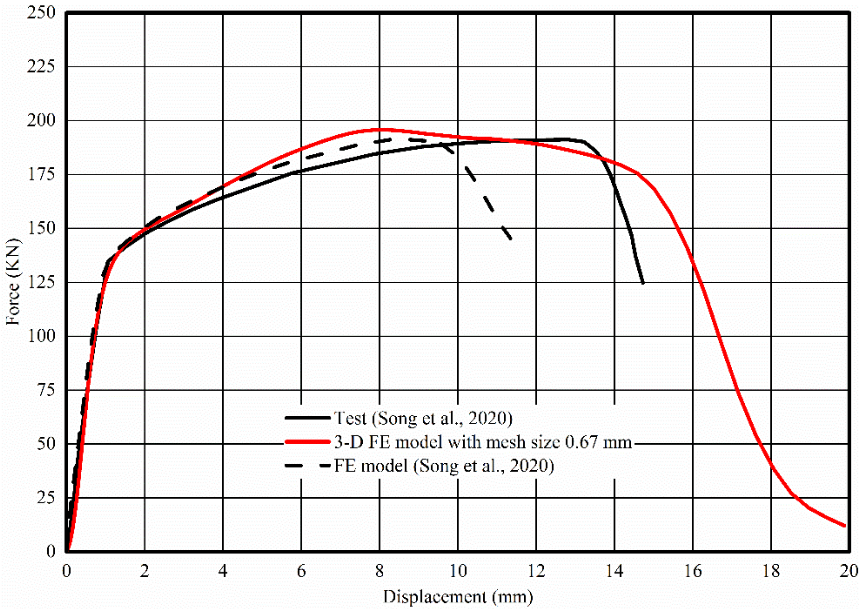

(b) 45^0 test

Figure 3.16: Experimental and numerical bolt elongation response for M20 A4-80 bolts subjected to tension and shear.

3.4.3. Fracture of a threaded M16 bolt

An M16 threaded bolt in Grade A4-80 was tested under tension as part of a wider study on bolted stainless steel moment resisting connections and the full load-elongation curve of the bolt were reported by Elflah *et al.* (2019). An axisymmetric and a 3-D FE model were developed herein and for both models the proposed fracture model was utilised to obtain the force-displacement curve. The geometry, boundary conditions and applied loading for the axisymmetric and 3-D models are shown in Figure 3.17. The dimensions of the bolt threads were based on the idealisation of M16 bolts with a 2.0 mm pitch reported in ISO 68-1 (1998). To account for the reduced cross-sectional area when the thread is assumed to be axisymmetric, the cross-sectional area of the shaft was reduced such that minimum cross-sectional area is equal to the stress area of the bolt (157 mm^2), in line with the approach followed by Song *et al.* (2020). The material model was created based on the reported Young's modulus value (Elflah *et al.*, 2019), but using the three-stage Ramberg-Osgood model (Hradil *et al.*, 2013) and the material properties reported in Table 3.4. This was done, because the reported material properties by Elflah *et al.* (2019) were based on a test on a threaded bolt, which inadvertently includes the effects of the threaded geometry and hence of the triaxiality on the material response. The resulting stress-strain response was converted into true stress-logarithmic plastic strain format and stress-strain pairs up to 2.0 true plastic strain were provided. This value was deemed sufficient to obtain the full material response including complete material failure. In order to incorporate the fracture into the numerical models, the proposed damage initiation model defined by Equation (3.4) and the plastic displacement at failure values reported in Table 3.7 were considered.

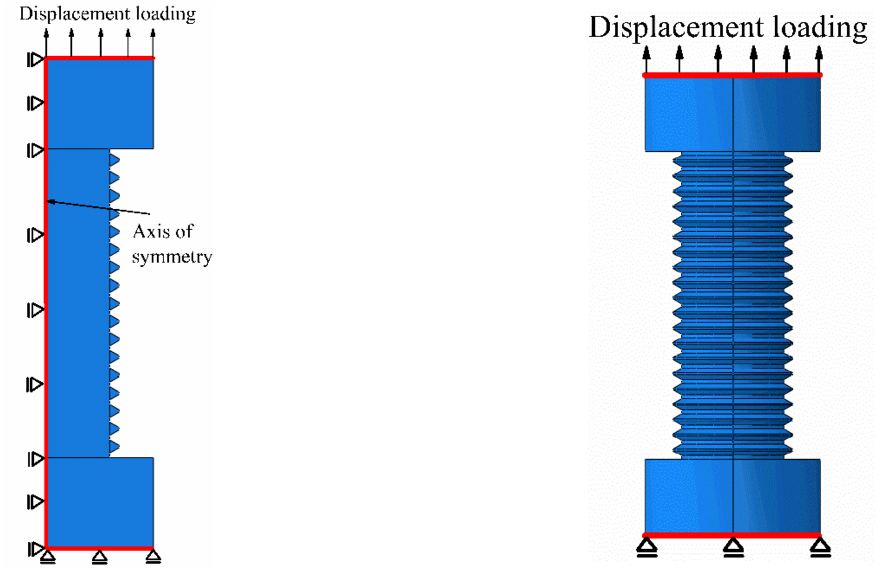

(a) (b)

Figure 3.17: Geometric modelling of (a) axisymmetric and (b) 3-D FE models of an M16 A4-80 threaded bolt.

The obtained numerical force-displacement response for the axisymmetric and the 3-D FE models is illustrated in Figure 3.18 for a mesh size of 0.53 mm together with the experimental curve. For comparison purposes, a 3-D FE model that does not incorporate material damage is also included. Overall, the full load-deformation behaviour of the bolt is accurately replicated, particularly by the axisymmetric mesh. Some discrepancies are to be expected, given that the material law was based on the strain-hardening exponents proposed in the present study.

In the preceding analysis the existence of the threads was explicitly modelled for both the axisymmetric and the 3-D model. This however increases the complexity and computational cost of the analysis. An attempt has been made to simulate the bolt as a smooth 3-D cylinder with an effective area equal to the stress area of the threaded bolt. In this analysis the only simplification is the elimination of the threads, which changes the stress triaxiality values on the shank-thread interface of the bolts. The resulting numerical force-deformation curves are shown in Figure 3.19

for the same mesh size and fracture properties as the ones used in the models where the threads were included. It can be observed that excluding the threads from the analysis leads to an overestimation of the bolt ductility due to the artificial reduction of the stress triaxiality and the resulting increase in the equivalent plastic strain for damage initiation.

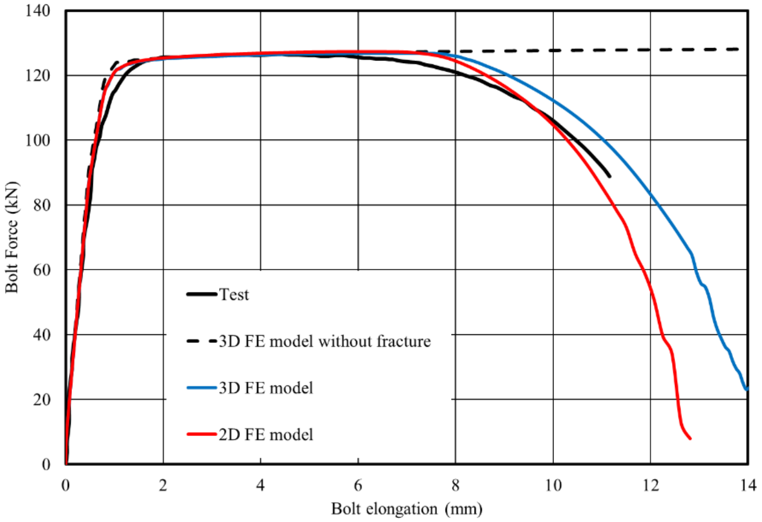

Figure 3.18: Experimental and numerical bolt elongation response for threaded M16 bolt.

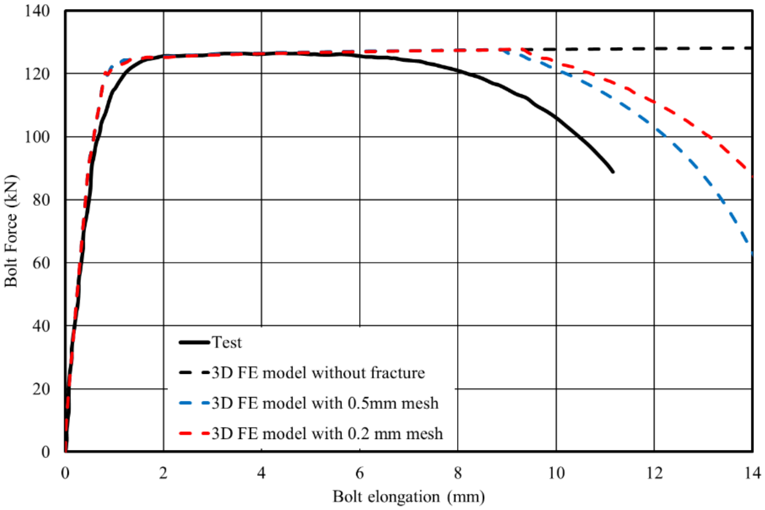

Figure 3.19: Experimental and numerical bolt elongation response for smooth M16 bolt with effective cross-section.

3.4.4. Simulation of stainless steel T-stub in tension

The experimental test on a stainless steel T-stub in tension S3 reported by Yuan *et al.* (2019), is simulated herein using the reported measured geometry and material properties. It should be noted that the material properties reported by Yuan *et al.* (2019) are based on cylindrical coupons machined from bolts belonging to the same batch as the bolts used in the tests and are hence considered representative of the bolt behaviour free from any effects of the geometry on the structural response. In the FE model, half of the T-stub was explicitly modelled, as shown in Figure 3.20, due to the symmetry of the T-stub in terms of geometry, applied load, boundary conditions and observed response. Since the existence of the fillet welds affects the exact location of the yield lines of the flange near the web, the geometry of the fillet welds was explicitly modelled. The thick steel plate to which the specimen was bolted was also explicitly modelled as shown in Figure 3.20. The bolt head and nut were modelled as cylindrical instead of hexagonal discs. All parts were discretized with the eight-node linear brick element of C3D8R and the bolt was meshed with a uniform mesh of size 0.5 mm. Surface to surface contact, with finite sliding was assumed for all contact surfaces thus enabling finite slip to be simulated. The penalty friction method is adopted to simulate tangential behaviour with a friction coefficient of 0.3, whilst hard contact is assumed for normal behaviour. The model was loaded with a prescribed displacement at the top of the web of the T-stub, while all degrees of freedom of the bottom side of the reaction plate was restrained to provide reaction to the applied loading.

In order to assess the effect of explicitly modelling the threads of the bolt on the structural response, two bolt geometries were considered, one with threads and one with a smooth cylindrical surface with an effective diameter such that the area of the simulated bolts equals the stress area of the threaded bolts. For both bolt geometries the proposed fracture model defined via Equation (3.4) and the plastic displacement at failure given in Table 3.7 for various mesh sizes was explicitly incorporated in the models. For comparison, a model including the threaded bolt but not allowing for fracture was also analysed. Finally, a similar model without fracture but with a stress-strain response truncated at an effective plastic strain value of 0.33, in line with the reported strain at fracture by Yuan *et al.* (2019), was also analysed to assess the ability of simplified material models without fracture to assess the ultimate response of bolts. A similar approach was successfully employed by Elflah *et al.* (2019).

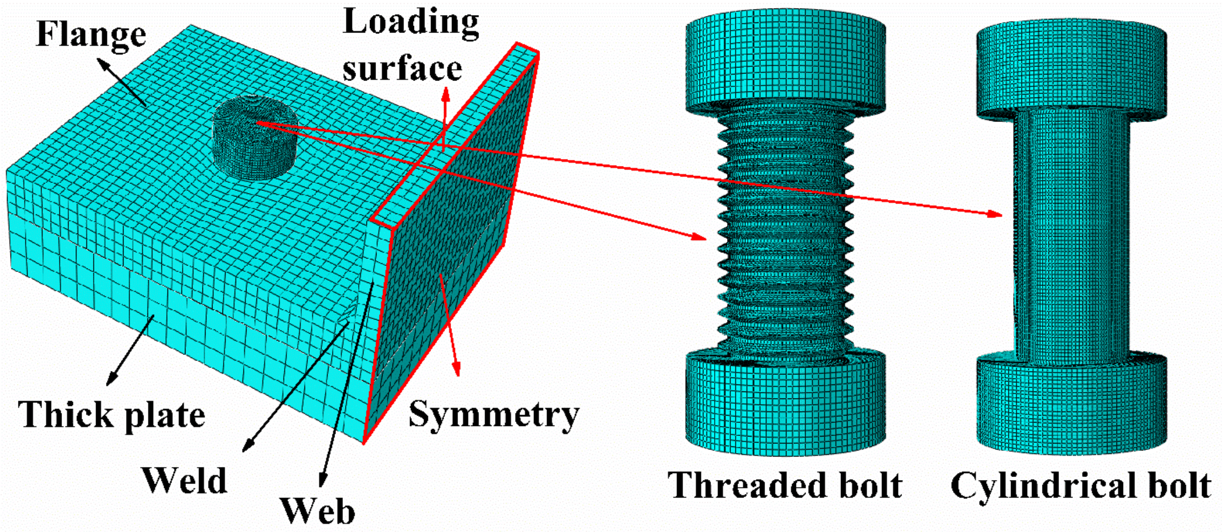

Figure 3.20: 3-D FE model for the bolted T-stub specimen S3 (Yuan *et al.*, 2019).

Figure 3.21 shows the experimental force-displacement response together with the numerical ones for the four modelling approaches employed. As expected, extending the material response curve beyond the strain at fracture without allowing for damage leads to an overestimation of the behaviour with the numerical curve continuing to increase at a constant slope. Truncating the material behaviour at the strain at fracture provides a simplified means to model the ultimate strength of the bolt as the relevant curve starts dropping at approximately the displacement at which the maximum force was obtained. The available ductility however is not accurately captured, because the numerical curve does not drop fast enough. Both numerical models explicitly considering fracture are shown to accurately capture the deformation at which fracture occurs, with the model including the bolt threads providing a close agreement to the experimental response.

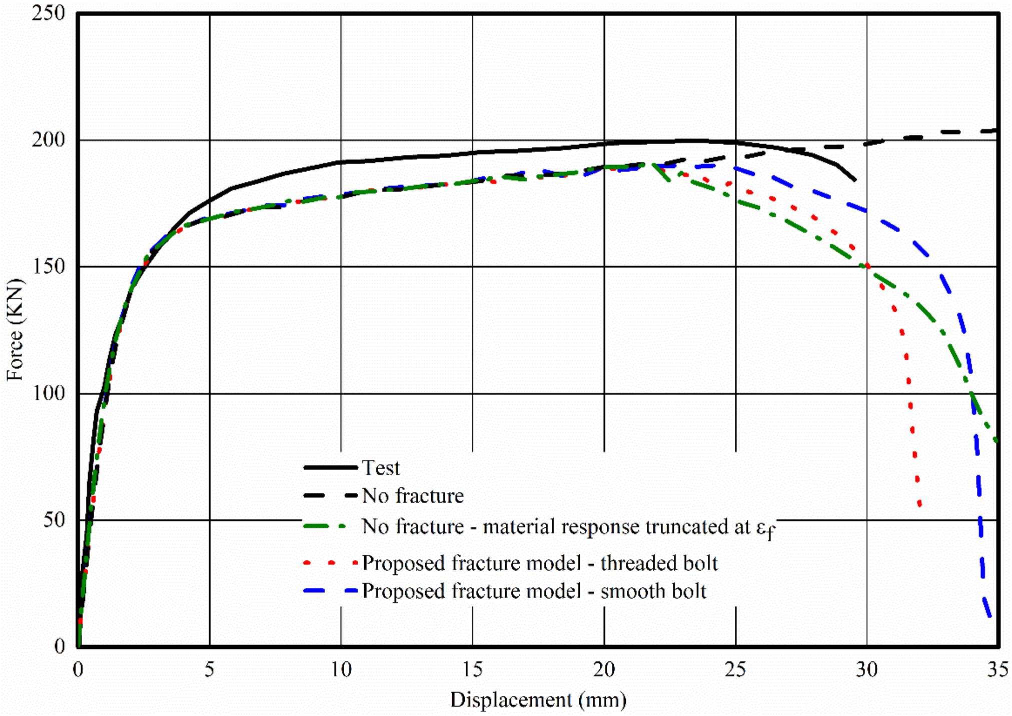

Figure 3.21: Experimental and numerical response of specimen S3 (Yuan *et al.*, 2019) for various modelling approaches.

3.4.5. Simulation of a moment resisting connection

A final case study is considered to demonstrate the ability of the proposed fracture model for A4-80 bolts to simulate the response of bolted connections. The flush end plate connection tested by

Elflah *et al.* (2019), which failed by bolt fracture is simulated using the proposed fracture model. The modelling strategy is identical to the one reported by Elflah *et al.* (2019), with the only difference being in the simulation of the bolt response. Two modelling approaches regarding modelling of the bolt threads were considered with both models allowing for material damage initiation and propagation. Two further models that do not include material degradation were also considered, one with the full material response up to a true plastic strain of 2.0 and the other with a material response truncated at 0.31. The material model is based on the properties reported in Table 3.4 and the fracture model proposed herein. The meshed model is shown in Figure 3.22. All models utilised a mesh size of 0.53 mm for the bolt with a corresponding displacement at fracture of 0.69 mm.

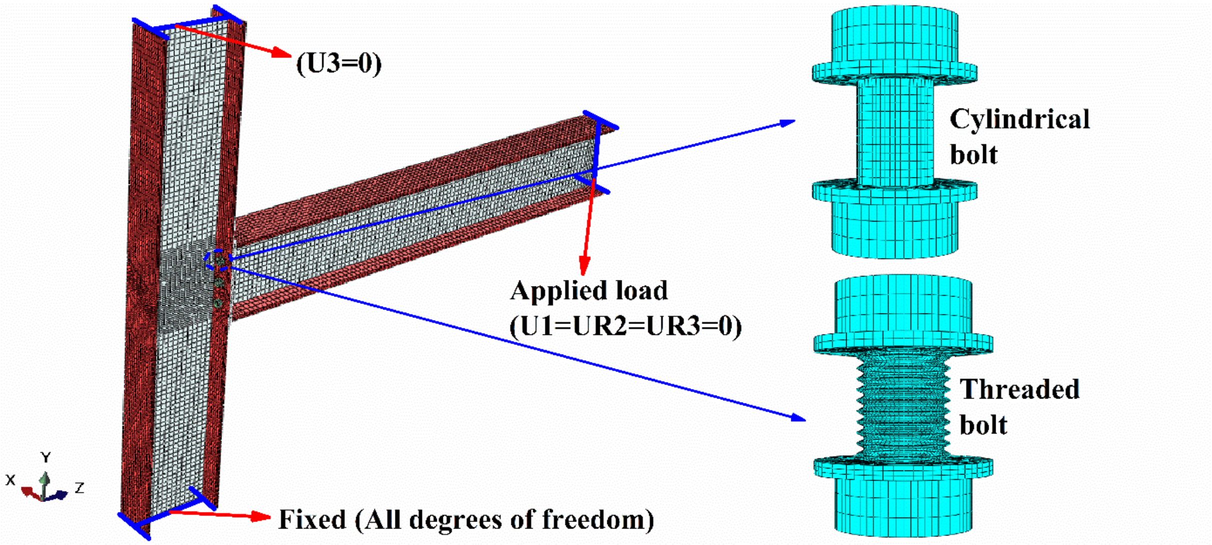

Figure 3.22: 3-D FE model of the stainless steel flush endplate connection tested by Elflah *et al.*, (2019).

Figure 3.23 shows the obtained numerical moment-rotation curves alongside the experimental one for the four analysis cases considered. It can be seen that explicitly allowing for material damage is essential to accurately capture the available ductility of the connection, whilst, a simplified approach based on truncating the stress-strain curve at the strain at fracture leads to satisfactory strength prediction but inaccurate assessment of the ultimate displacement at fracture. Figure 3.24 shows the experimental and numerical failure mode for the simulated connection accounting for both material damage and the presence of threads. Both the location and the shape of the predicted fracture are mimicking very well the experimental observations, thus verifying the adequacy of the proposed fracture modelling approach.

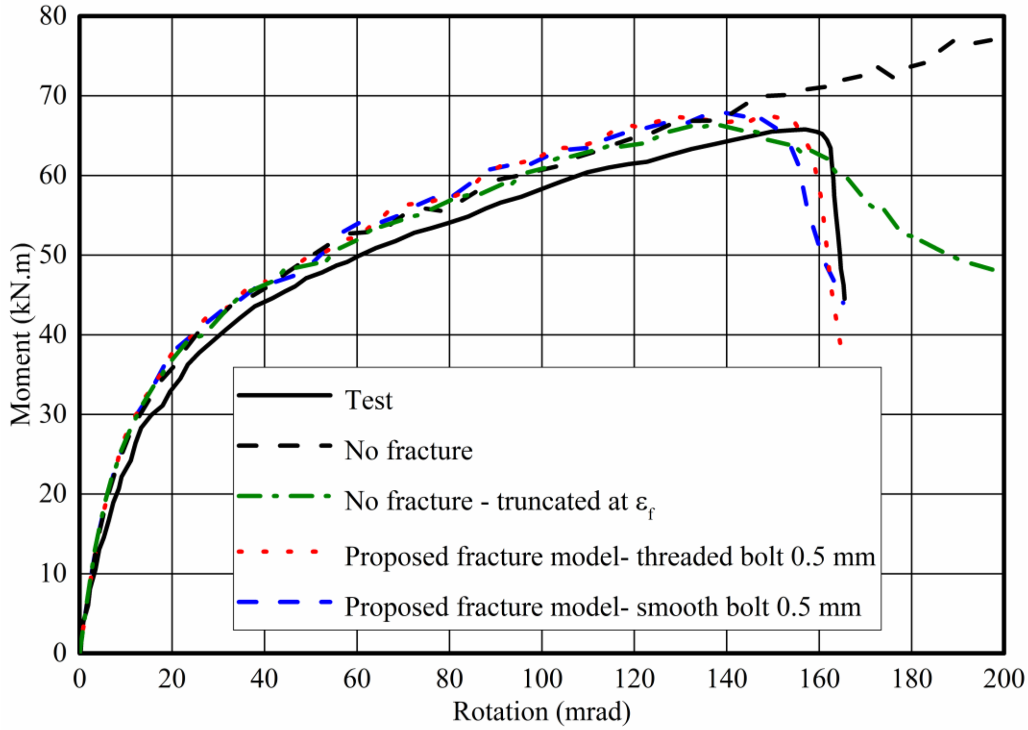

Figure 3.23: Experimental and numerical response of flush end plate connection (Elflah *et al.*, 2019) for various modelling approaches.

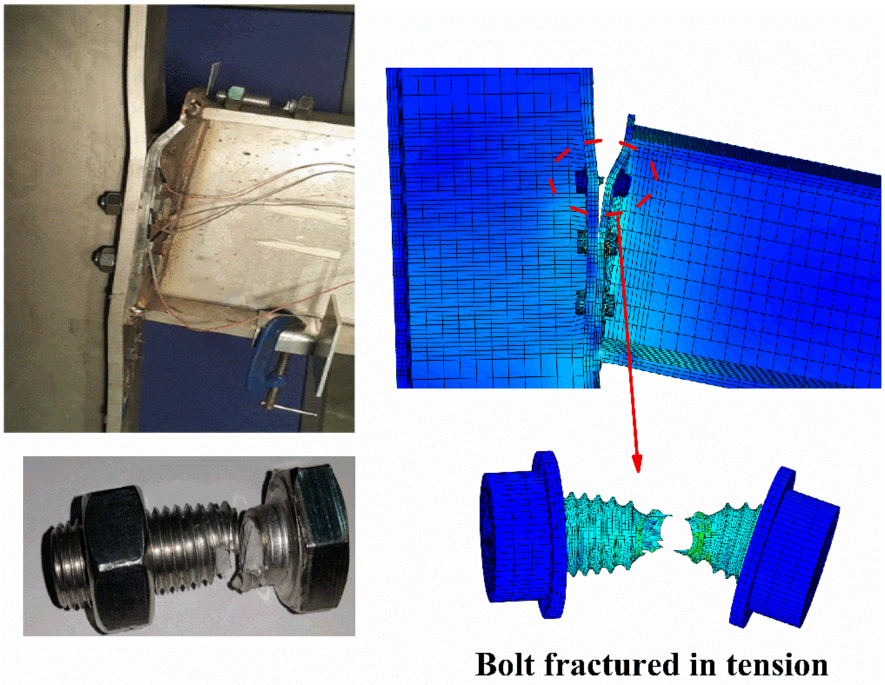

Figure 3.24: Experimental (Elflah *et al.*, 2019) and numerical failure mode of stainless steel flush end plate connection and closeup of bolt fracture.

3.5. Conclusions

In this study, the structural behaviour and fracture characteristics of A4-80 stainless steel bolts were investigated comprehensively using a combination of experimental tests and numerical modelling. In order to determine the relationship between the plastic strain at fracture initiation and stress triaxiality as well as to quantify the strain at fracture, tensile specimens with various circumferential notches, yielding a range of stress triaxialities, were machined from A4-80 stainless steel bolts and tested in tension. The measured force-displacement curves and the key material and fracture properties for all tested bolts were reported herein. Both the strain at fracture and the maximum recorded force were observed to highly depend on the stress triaxiality of the specimens. Therefore, it is recommended that for threaded bolts, the bolt material properties should be determined from tensile tests on smooth specimens, machined from threaded bolts, to eliminate the effect of stress triaxiality which may be significant for bolts with fine thread pitch. Comparisons with existing predictive models for fracture initiation developed for carbon steel bolts (Pavlovic *et al.*, 2013) showed that the A4-80 stainless steel bolts possess much higher ductility, and hence their fracture initiates at comparatively higher effective plastic strains throughout the triaxiality range considered. Furthermore, the measured true plastic strain at facture showed that a recently proposed predictive model for A4-80 stainless steel bolts (Song *et al.*, 2020) overpredicts the strain at fracture considerably, particularly in the triaxiality range between 0.33 and 0.6. A newly calibrated equation relating the strain at fracture initiation with the stress triaxiality, suitable for incorporation into numerical models accounting for bolt fracture, was established and its accuracy was demonstrated.

An advanced numerical model which can predict the behaviour of stainless steel bolts including the initiation and propagation of fracture was developed and validated against bolt test results. A single damage variable in the form of the plastic deformation at failure in conjunction with a linear material degradation model was shown suitable to numerically replicate the experimental response for both axisymmetric and 3-D FE models. The value of this damage parameter was calibrated for 2 mesh sizes for axisymmetric and 3-D models and has been reported herein. An excellent agreement between numerical and experimental results was obtained for all modelled specimens. Finally, the developed fracture modelling approach was shown to accurately predict the experimental response of bolts subjected to pure tension and a combination of tension and shear, the T-stub in pure tension as well as the full moment-rotation response of a flush end plate connection, which ultimately failed by bolt fracture.

CHAPTER 4

Experimental tests on ferritic stainless steel bolted T-stubs

4.1. Introduction

Research on the behaviour of stainless steel T-stubs focused primarily on austenitic and duplex stainless steel grades, whilst the structural performance of ferritic stainless steel connections has not been studied to date. Ferritic stainless steels exhibit lower ductility and strain-hardening than austenitic and duplex grades but, as all stainless steels, lack a yield plateau. Therefore, their material behaviour is in between that of carbon steel and austenitic stainless steel. Hence it is not clear whether current design provisions (EN 1993-1-8, 2005) for carbon steel joints are suitable for ferritic stainless steel joints or whether novel design methods should be developed instead. Therefore, a project studying the structural behaviour of ferritic stainless steel connections is reported in this chapter. An experimental program consisting of 17 ferritic stainless steel bolted T-stubs under monotonic tension was carried out for disclosing the resistance, deformation capacity and failure mechanism which were further used to assess the existing design method in EN 1993-1-8 (2005). This chapter reports in detail the first ever set of tests on ferritic stainless steel bolted T-stubs. The research reported herein has been submitted for publication to the Journal of Constructional Steel Research. Additionally, a conference paper based on the conducted research was submitted and accepted for oral presentation at the Eurosteel 2021 conference.

4.2. T-Stub test specimens

4.2.1. Geometric configurations

Two T-stub configurations were tested, one employing a single bolt row and one employing two bolt rows. The bolt spacing and the end and edge distances of each specimen were selected within the spacing requirements of EN 1993-1-8 9 (2005) with some cases being close to the minimum spacing, end and edge distances to ascertain the effect of bolt spacing on the failure mode of specimens for which membrane effects were significant. The geometry of the tested T-stub specimens is reported in Table 4.1, where n is the distance between the free edge and bolt centre line, t_f is the flange thickness, h_f is the fillet weld size and m is the distance between bolt centre and the web less $0.8h_f$. All symbols are defined in Figure 4.1, where the geometric configuration of the tested specimens is schematically depicted.

All specimens were bolted to very stocky T-stubs which remained virtually undeformed during testing. The choice of a rigid reaction T-stub was preferred over symmetric back-to-back specimens in order to produce comparable results with similar studies on stainless steel T-stubs (Yuan *et al.*, 2019; 2020), which also employed rigid reaction T-stubs. Furthermore, connecting a relatively thin T-stub specimen to a rigid one allows membrane actions to develop in the specimen at high deformations and leads to increased shear forces and bending moments in the bolts (Tartaglia *et al.*, 2020). All bolts were M16 in Grade A4-80 in 18 mm clearance holes and were hand tightened, as previous studies (Yuan *et al.*, 2019; 2020) revealed that bolt preloading only affects the joint stiffness and leaves strength unaffected. Given that all stainless steel grades have similar Young's moduli to one another and to carbon steel, the stiffness of the ferritic T-stubs is not expected to differ from that of T-stubs in other stainless steel or carbon steel grades. Hence bolt preloading is not considered in this study.

Table 4.1: Geometric configurations of the T-stubs (all dimensions are in mm).

Type	Specimen	n	m	b_f	b_1	b_2	b	t_f	t_w	h_f
S	S1	25	75	220	50	-	100	4.88	10	6
	S2	50	50	220	50	-	100	4.88	10	6
	S3	75	25	220	50	-	100	4.88	10	6
	S4	25	75	220	50	-	100	10	10	6
	S5	50	50	220	50	-	100	10	10	6
	S6	75	25	220	50	-	100	10	10	6
D	D1	30	70	220	50	140	240	4.88	10	6
	D2	50	50	220	50	140	240	4.88	10	6
	D3	30	70	220	75	90	240	4.88	10	6
	D4	50	50	220	75	90	240	4.88	10	6
	D5	30	70	220	100	40	240	4.88	10	6
	D6	50	50	220	100	40	240	4.88	10	6
	D7	30	70	220	50	140	240	10	10	6
	D8	50	50	220	50	140	240	10	10	6
	D9	30	70	220	75	90	240	10	10	6
	D10	50	50	220	75	90	240	10	10	6
	D11	30	70	220	100	40	240	10	10	6

The ferritic stainless steel T-stubs were fabricated by fillet welding two hot-rolled plates in Grade EN 1.4003 at a right angle. For all specimens, a 10 mm thick plate was used for the T-stub web, whilst 2 nominal thickness sizes, 5 mm and 10mm, were employed for the flanges. The variation in flange thickness in conjunction with the variation in bolt spacing was intended to produce a range of failure modes, with the focus lying primarily on T-stubs failing in mode 1, which is accompanied by significant plastic deformation of the T-stub, thus allowing the effect of material on the structural response of the T-stubs to be studied.

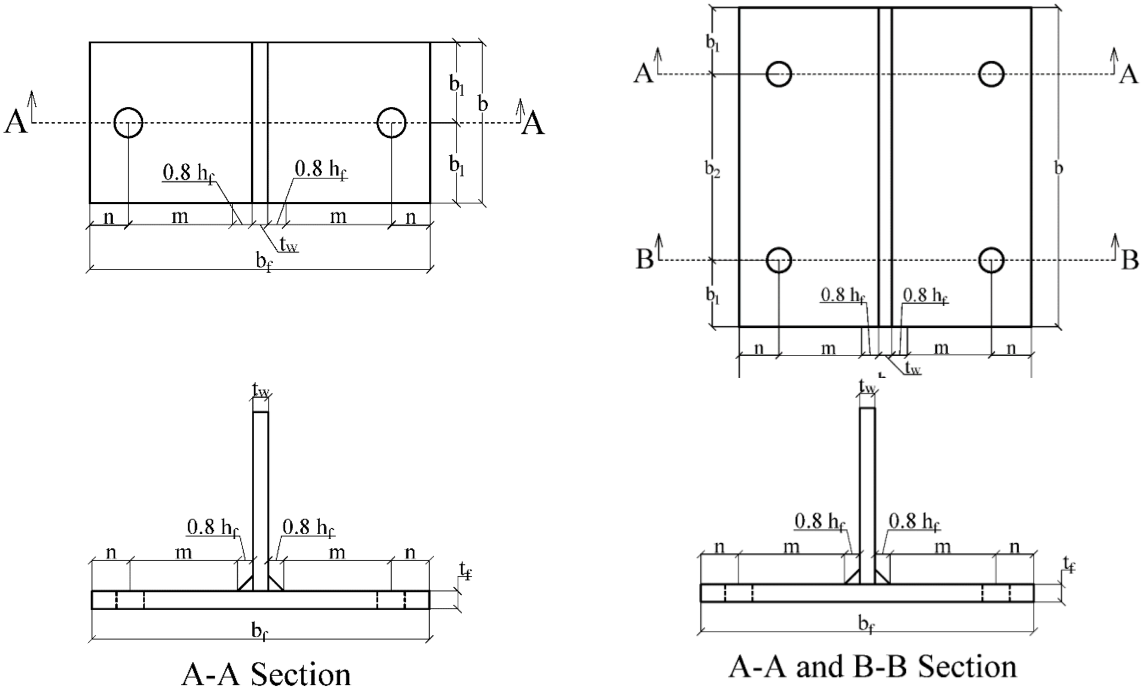

(a) (b)

Figure 4.1: Geometric properties of a) single bolt row and b) double bolt row T-stubs.

It should be noted that all T-stubs had a pronounced uplift of their free edges parallel to the welded web, due to the weld shrinkage causing bowing of the flanges. Hence the edges of the T-stubs were not in contact with the rigid T-stub unless the bolts were overtightened to cause plastic deformation sufficient to eliminate the initial gap. In all cases the maximum gap between the specimens' free edges and the rigid reaction T-stub was less than 8 mm (8% of the T-stub half-width) and is not expected to have had any significant effect on the global response of the T-stubs (Tartaglia *et al.*, 2020).

4.2.2. Material properties

To facilitate the analysis of the experimental results and allow future numerical simulations to be conducted, the material properties of the T-stub specimens and the bolts are required. Material coupons were extracted from the ferritic stainless steel plates and tested in tension to failure. It is well-known that ferritic stainless steels exhibit anisotropy having a higher nominal yield strength in the transverse direction than in the rolling direction, whilst a variation in other key material properties such the ultimate tensile stress and the strain at fracture with changing loading direction relative to the rolling direction is also observed (Manninen, 2010; Becque and Rasmussen, 2009a; Rossi, 2010a). Since in the vicinity of bolt holes connections are subjected to complex stress fields, the material response in different orientations is would be required to accurately define an anisotropic plasticity model in subsequent numerical modelling (Becque and Rasmussen, 2009b; Rossi, 2010b).

To quantify anisotropy, coupons were extracted in three different directions from the plates that were used for the fabrication of the specimens, namely along the longitudinal, transverse and diagonal directions. The longitudinal rolling direction of the plate is indicated as L, the transverse direction is termed T, and the diagonal direction which is at a 45° angle to the rolling direction is designated as D. Two identical coupons were extracted via water jet cutting for each direction as shown in Figure 4.2a. The coupons were tested under strain control (Figure 4.2b) with an applied strain rate of 0.007%/s up to the 0.2% proof stress $\sigma_{0.2}$ and a strain rate of 0.025%/s until fracture, in accordance with BS EN ISO 6892-1 (2009). The obtained material properties are reported in Table 4.2, where E_0 is the initial Young's modulus, $\sigma_{0.2}$, $\sigma_{1.0}$ and $\sigma_{2.0}$ are the 0.2%, 1% and 2% proof stresses, respectively, σ_u is the ultimate tensile stress, ε_u is the strain at the ultimate tensile stress and ε_f is the plastic strain at fracture.

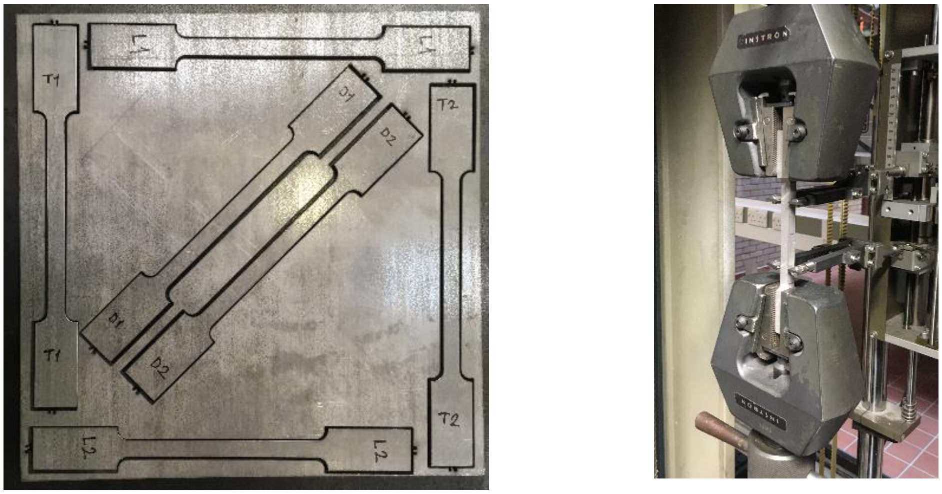

(a) (b)

Figure 4.2: Extracted coupons (a) and experimental set up (b).

The obtained stress-strain curves for the 5mm and 10 mm thick plates are shown in Figure 4.3. As expected, the material response strongly depends on the direction of loading relative to the rolling direction, with transverse coupons having a higher nominal yield strength $\sigma_{0.2}$ and ultimate tensile stress σ_u and a lower strain at fracture ε_f than the longitudinal ones, whilst the coupons extracted in the diagonal direction exhibit a response in-between that of the transverse and the longitudinal coupons. A further important observation relates to the markedly different response that the thick (10 mm) coupons exhibit compared to the thin ones (5 mm). As shown in Figure 4.3, the 10 mm coupons display a much earlier loss of strength, inferior strain-hardening characteristics at low strains and an apparent higher ductility than the 5 mm ones.

Table 4.2: Material properties of the ferritic stainless steel plates.

#	Thickness (mm)	Width (mm)	E (Mpa)	$\sigma_{0.2}$ (Mpa)	$\sigma_{1.0}$ (Mpa)	$\sigma_{2.0}$ (Mpa)	σ_u (Mpa)	ε_u (%)	ε_f (%)
L1-10	10.05	8.32	185602	278.2	297.4	322.3	438.8	22.4	35.6
L2-10	10.05	8.2	192626	280.3	300.2	325.8	443.7	22.6	33.3
T1-10	10.05	7.32	185578	302.0	324.6	351.6	465.8	15.8	-
T2-10	10.05	8.17	208388	294.7	318.0	344.5	460.0	18.0	27.8
D1-10	10.05	8.36	177549	285.1	304.5	329.3	438.8	19.4	35.6
D2-10	10.05	8.24	206639	283.8	302.4	327.4	438.3	20.1	36.7
L1-5	4.88	8.3	197849	339.8	369.3	380.4	427.1	17.0	31.9
L2-5	4.88	8.3	210683	334.3	365.3	376.8	425.5	17.3	30.6
T1-5	4.88	8.31	183028	408.0	424.0	434.4	466.0	13.4	18. 1
T2-5	4.88	8.2	202963	409.9	426.2	436.8	468.2	12.1	-
D1-5	4.88	8.21	189723	374.5	390.8	400.1	437.5	17.0	25.0
D2-5	4.88	8.25	178527	376.1	389.4	398.6	435.7	16. 3	25.0

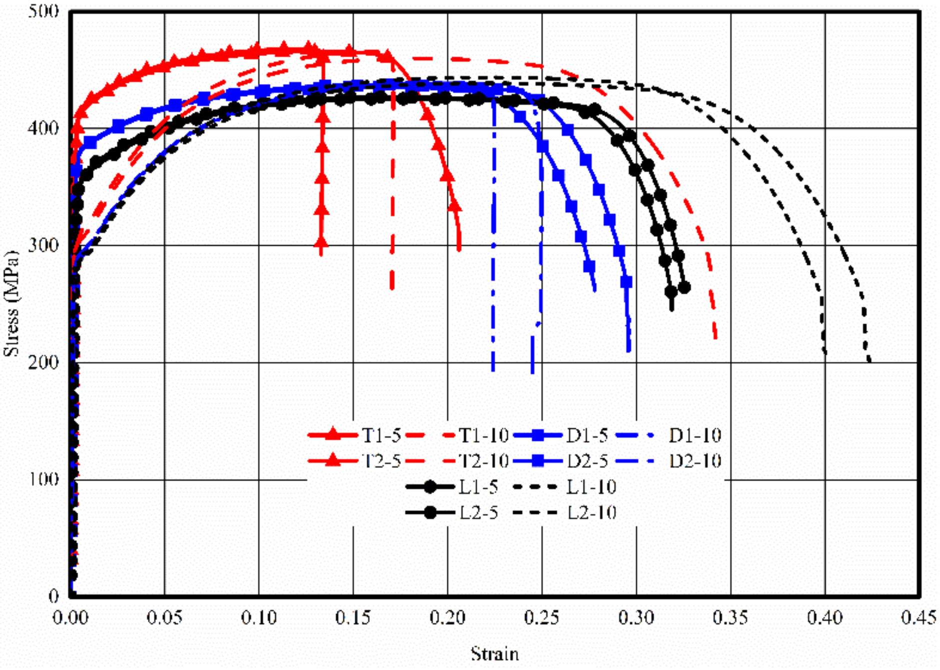

Figure 4.3: Stress-strain response of the tested tensile coupons.

Visual inspection of the failure modes revealed that all six coupons extracted from 10 mm plate exhibited a distinct longitudinal crack parallel to the applied load prior to the formation of necking, as shown in Figure 4.4a. This distinct longitudinal crack, also called longitudinal splitting or delamination fracture has been often observed in thick tensile specimens (Verma *et al.*, 2017; Guo *et al.*, 2002). Its formation is attributed to the increased constraint and accompanying increased out of plane stresses observed in thicker specimens which precipitate growth and coalescence of voids to cause delaminations which alleviate the out-of-plane stresses prior to the formation of the main crack (Verma *et al.*, 2017; Guo *et al.*, 2002). It should be noted that no longitudinal splitting was observed in tests on hot-rolled austenitic (Yuan *et al.*, 2019; Elflah *et al.*, 2019; Gardner *et al.*, 2016) and duplex (Yuan *et al.*, 2019) stainless steel tensile coupons with thicknesses up to 12 mm thus revealing the different fracture characteristics of ferritic stainless steels. Moreover, all previous experimental tests on ferritic stainless steel tensile coupons considered smaller thicknesses varying between 1.13 and 6 mm (Bock *et al.*, 2015; Manninen, 2010; Rossi, 2010).

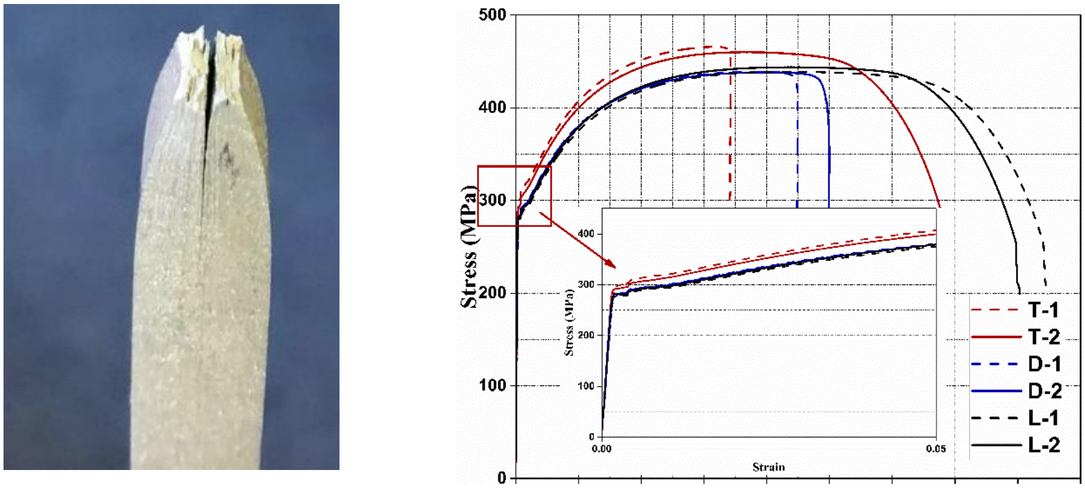

(a) (b)

Figure 4.4: Behaviour of 10mm thick coupons. a) Longitudinal splitting and b) Stress strain curves.

An alternative explanation for the observed failure mode of the thicker specimens relates to the potential existence of a material imperfection within the thicker plates which might have led to the development of the longitudinal crack. In any case, the material response of any specimen should not depend on the geometry of the specimen and should not be affected by imperfections not typical of the material studied, otherwise its applicability is limited. Furthermore, the material response obtained for the 10 mm thick specimens as reported in Table 4.2 inherently contains the effect of the observed longitudinal crack and is hence considered not to be representative of the material response of T-stubs, which are primarily subjected to bending stresses and hence the thickness of the material under tension is significantly less than 10 mm even when high membrane stresses develop.

To determine whether the obtained response of the 10 mm thick plates is indeed due to longitudinal splitting and to eliminate its effect on the obtained material response, additional material coupon tests were performed. Two additional coupons, one in the longitudinal direction and one in the transverse direction were extracted from the 10 mm thick plates via water jetting through the thickness in such a way that the larger dimension of the coupons coincided with the thickness of the plate (10 mm) and the smaller dimension of the coupons was set equal to 3 mm. Hence, any pre-existing crack within the thickness of the plate would also be present in the extracted coupons. No diagonal coupons were extracted. The two additional coupons were tested to failure according to the provisions of BS EN ISO 6892-1 (2009). Figure 4.5 depicts the two tested coupons after fracture. No longitudinal splitting was observed in either coupon, as can be observed in Figure 4.5, where a detail of the longitudinal coupon after fracture is also shown. Hence it was concluded that there were no pre-existing cracks in the 10 mm thick plate and the previously observed longitudinal splitting was due to the geometry of the coupon.

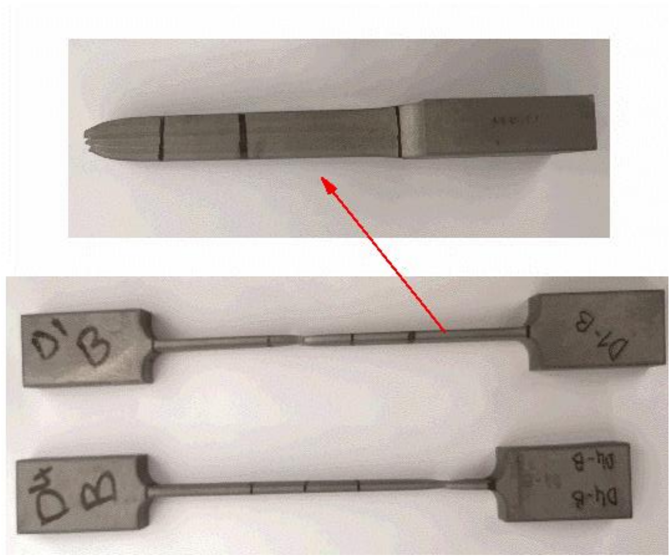

Figure 4.5: Fracture of additional material coupons from the 10 mm plate.

In Table 4.3 the obtained material results from the six 5 mm thick specimens are averaged for each of the three directions considered and reported together with the material properties from the two 10 mm thick specimens deemed representative of the material response. The anisotropy ratio r, defined as the ratio of the 0.2% proof stress in a particular direction over the 0.2% proof stress in the rolling direction is also reported as a means to quantify the observed material anisotropy. The material exhibited a 0.2% proof stress in the transverse direction 21% and 7% higher than that in the longitudinal direction for 5 mm and 10 mm coupons, respectively. Other studies on cold-formed sheet ferritic material reported anisotropy ratio in the range of 10% (Manninen, 2010) - 15% (Becque and Rasmussen, 2009). Hence hot-rolled ferritic stainless steel seems to be more anisotropic than ferritic sheet material. Since it is not always known which the rolling direction of a plate is, the experimental results of the rolling direction L which possess the lowest $\sigma_{0.2}$ values are adopted in the remainder of the paper as the representative material properties for comparisons with design predictions. A similar recommendation regarding adopting the longitudinal material properties for strength predictions was proposed for ferritic stainless steel members (Cashell and Baddoo, 2014).

Table 4.3: Average stress values and anisotropy ratios.

Specimen	Direction	E (MPa)	$\sigma_{0.2}$ (MPa)	$\sigma_{1.0}$ (MPa)	σ_u	Anisotropy ratio r	ε_u (%)	ε_f (%)
5 mm thick plate	LT	204266	337.1	367.3	426.3	1.00	17.2	31.3
	TT	192996	409.0	425.1	467.1	1.21	12.8	18.1
	DT	184125	375.3	390.1	436.6	1.11	16.7	25.0
10 mm thick plate	LT	185060	286.0	301.0	431.1	1.00	17.0	34.3
	TT	210132	304.5	324.1	438.0	1.07	10.5	19.0

In addition to the material behaviour of the plates comprising the T-stubs, the material behaviour of the bolts used to connect the specimens to the rigid reaction T-stub need to be determined. To this end, two smooth cylindrical coupons were machined from A4-80 stainless steel bolts and tested to failure. Both the bolts used for coupon extraction and the ones used in the assembly of the specimens were of the same grade and were ordered from the same supplier, however the length of the bolts used for coupon extraction was longer to allow adequate gripping length in the machine. Key material properties were averaged and are reported in Table 4.4. The obtained stress-strain curves are shown in Figure 4.6.

Table 4.4: Material properties of the stainless steel bolts.

Bolt Specimen	E (MPa)	$\sigma_{0.2}$ (MPa)	$\sigma_{1.0}$ (MPa)	σ_u (MPa)	ε_u (%)	ε_f (%)
1	185000	410	600	727	0.19	0.27
2	179000	400	590	726	0.21	0.31

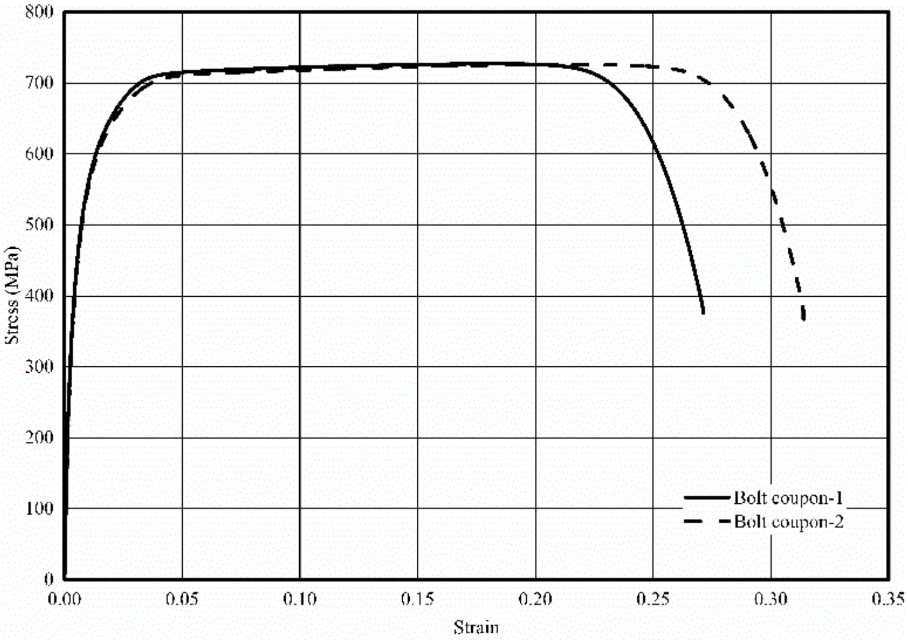

Figure 4.6: Material behaviour of bolt coupons.

4.3. Monotonic loading tests

4.3.1. Setup and instrumentation

All specimens were tested using a tensile testing machine in the Civil Engineering Laboratory of the University of Birmingham. The flange of the T-stub specimens was bolted to a rigid T-stub which was fixed to the machine grips, whilst the web of the T-stubs was connected to the testing machine via the configuration of plates schematically shown in Figure 4.7a and Figure 4.7b for single and double bolt row specimens, respectively. The Figure 4.7c depicts the experimental setup during testing, where part of the employed instrumentation is also depicted. The rigid T-stub, the support plates and their bolt configurations were over-designed in order to remain elastic and were hence reused for all tests.

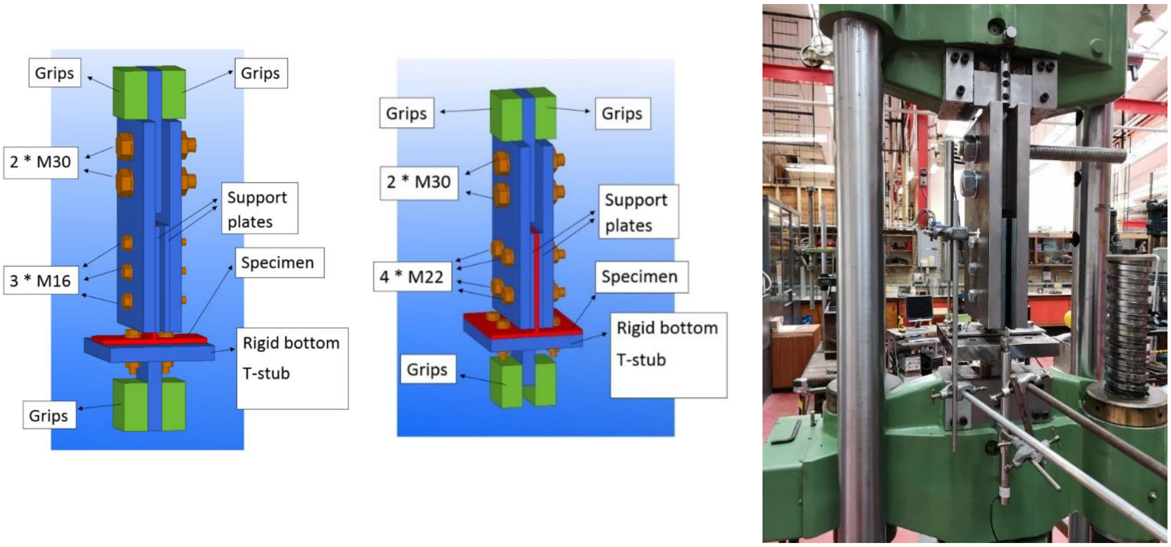

(a) (b) (c)

Figure 4.7: Illustration of set up for a) single and b) double bolt row T-stubs and c) the picture of the experimental set up during testing.

The specimens were loaded using displacement control with a constant loading rate of 0.5 mm/min to ensure static response and negligible strain rate effects. The loading process was terminated once a clear drop of the applied load was observed, which was triggered by either fracture of the bolts or cracking of the T-stubs, as later discussed.

The employed instrumentation consisted of two LVDTs monitoring the vertical deflection of the T-stub specimen at the web location and at the location of the bolt rows, and strain gauges affixed at specific locations of the flange of the specimens. The location of the strain gauges was selected so that the evolution of strains and hence the plastic deformations of the flanges of the T-stubs could be monitored in order to deduce the formation of plastic hinges. The adopted strain gauge arrangements for the single and double bolt row specimens are shown in Figure 4.8. Different strain gauge arrangements were adopted for the single and double bolt row T-stubs as depicted in Figure 4.8, with strain gauges along the length of the T-stub at different locations intended to capture any variation in strains between the bolt location and the specimen end. The failure mode of each specimen was determined using the data obtained from the strain gauges as well as by visual inspection. All deflections and strains were recorded at 2 seconds intervals.

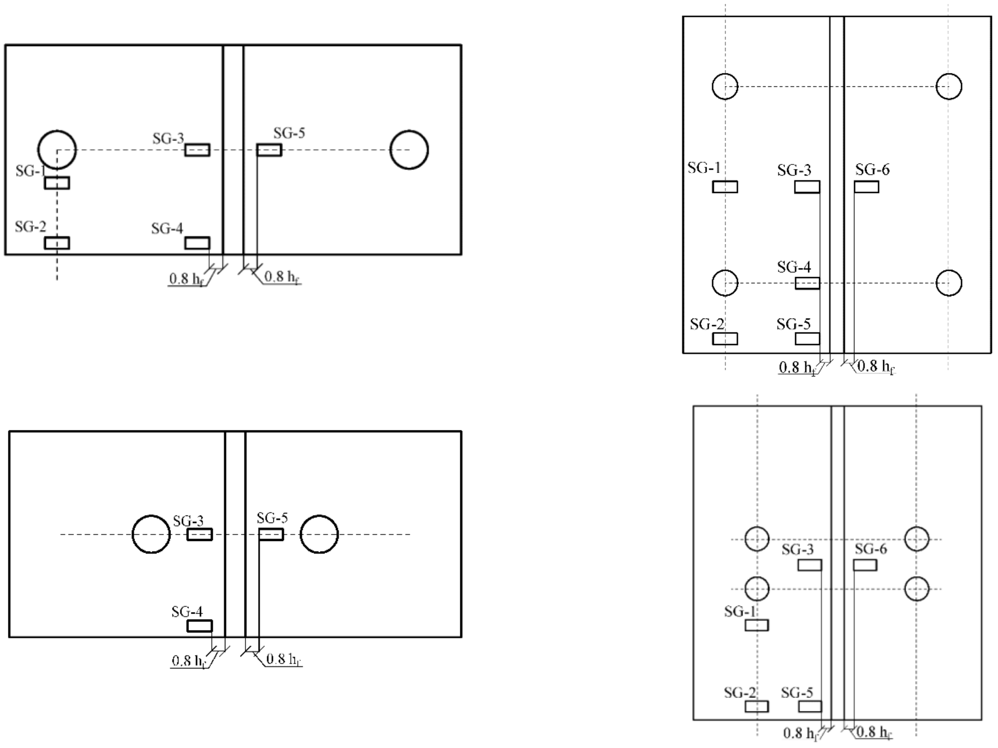

(a) (b)

Figure 4.8: Strain gauge arrangements for the a) Single and b) double bolt row T-stubs.

4.4. Results and discussions

4.4.1. Failure modes

The three failure modes typically encountered in T-stubs in tension according to EN 1993-1-8 (2005) are depicted in Figure 4.9. Type 1 failure mode corresponds to yielding of the flange and the formation of four plastic hinges prior to bolt fracture. Type 2 failure is characterized by the development of two plastic hinges at the flange to web junction followed by bolt fracture, whilst when bolt fracture precedes the formation of plastic hinges in the flange, the failure modes is said to be type 3. These failure modes refer to T-stubs being subjected primarily to bending stresses, with no significant membrane actions. However, bolting a T-stub on a rigid support may lead to the development of significant membrane actions at high deformations provided that the T-stub material is ductile enough to undergo significant plastic deformations and the bolts are strong enough to anchor the tension field developed at high deformations to the rigid support. Both of these conditions were met in the present study and most of the specimens (particularly the 5mm thick ones) reached loads far beyond the ones corresponding to their plastic resistance due to the development of membrane actions.

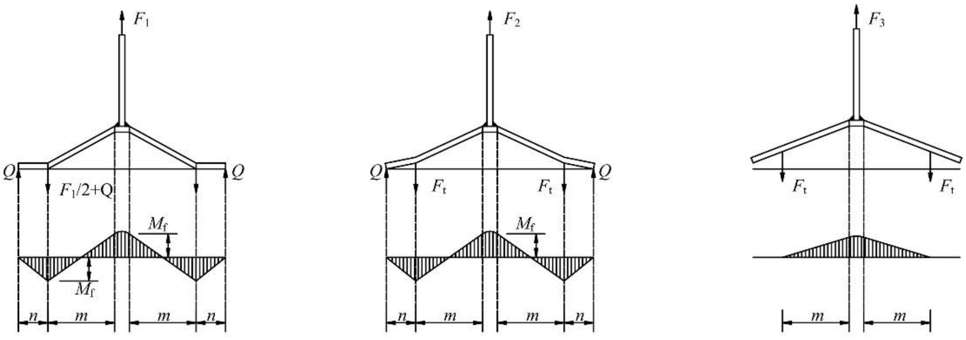

(a) Type-1 (b) Type-2 (c) Type-3

Figure 4.9: Typical failure modes of T-stubs.

The failure modes of the tested specimens are shown in Figure 4.10. All specimens displayed significant plastic deformations of varying degree depending on the employed bolt arrangement and flange thickness. Plastic deformations of the flanges were followed by significant plastic deformations of the bolts in tension and bending. The tests were terminated when a marked drop in load was noted, which was caused by the fracture initiation in either the bolts or the T-stubs. During testing of specimen D8 the testing machine unexpectedly stopped working before the specimen failed. However, the plastic resistance was determined from obtained force-deformation curve of D8.

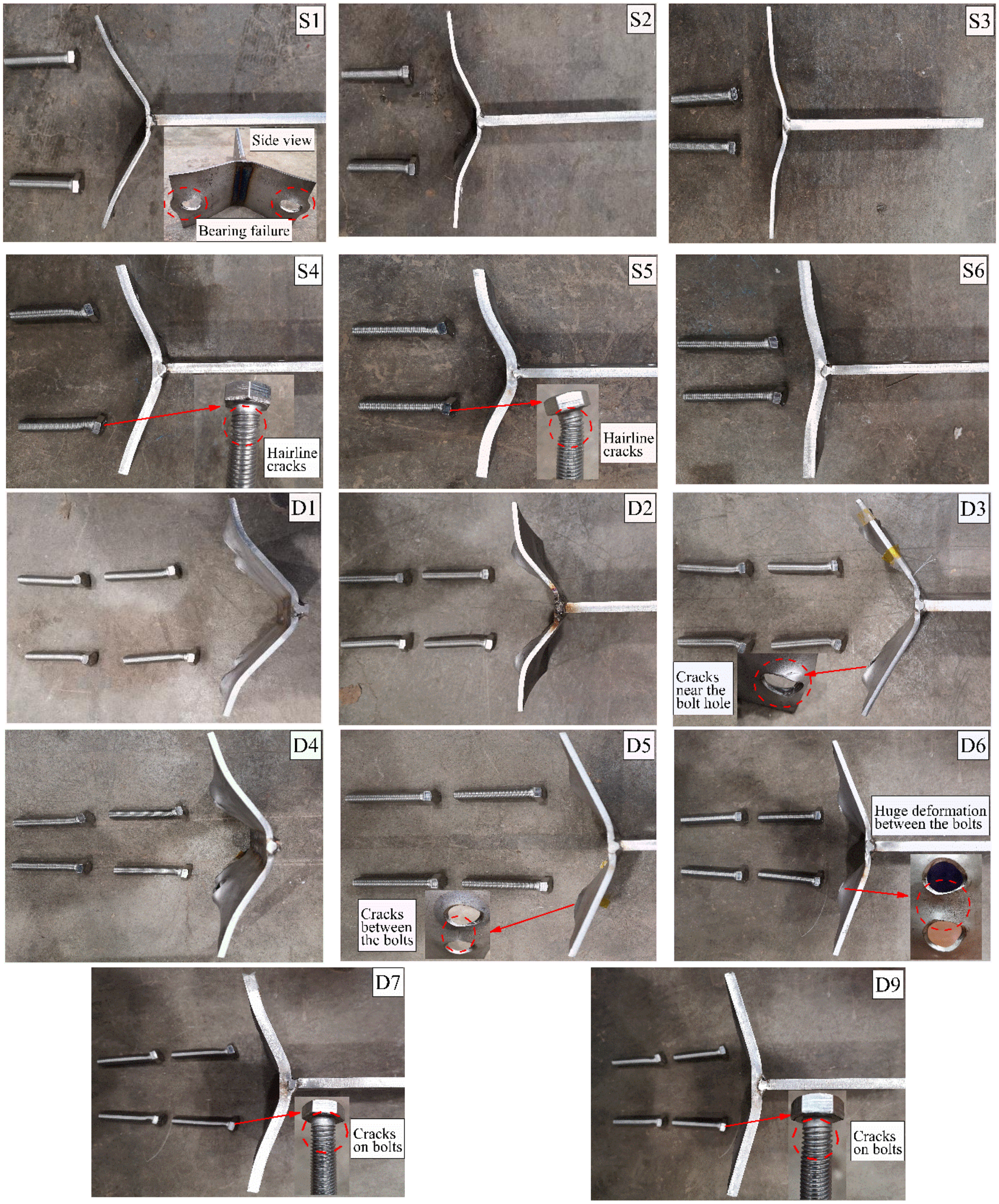
S1
Side view
Bearing failure
S2
S3
S4
Hairline cracks
S5
Hairline cracks
S6
D1
D2
D3
Cracks near the bolt hole
D4
D5
Cracks between the bolts
D6
Huge deformation between the bolts
D7
Cracks on bolts
D9
Cracks on bolts

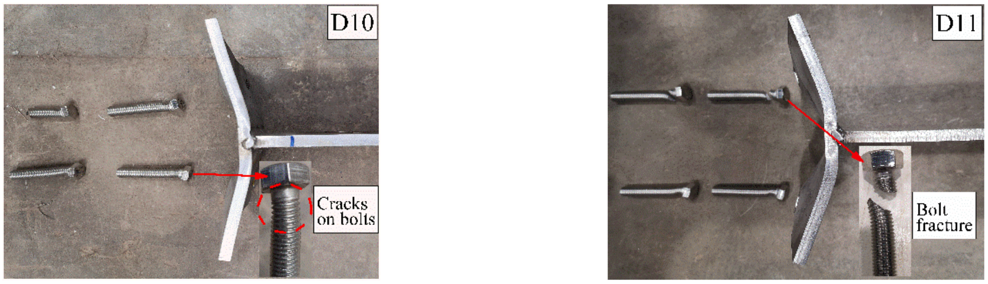

Figure 4.10: Failure modes of the T-stub specimens.

In Figure 4.10, it can be clearly seen that specimen S1 ultimately failed by bearing of the bolt holes of the T-stub flange against the bolts, due to its small end distance (25 mm). At small deformations where bending action dominated the response four plastic hinges developed and subsequently bearing failure occurred at very high deformations. The deformed shape of S1 does not exhibit the characteristic plastic hinges developed at the location of the bolt holes due to the subsequently developed membrane action. Specimens S2 and S3 display a typical type 1 failure mode with the four plastic hinges clearly visible. Similarly, specimens S4-S6 exhibited the formation of four plastic hinges followed by hairline cracks on the bolt surface failure ultimately occurred at lower overall deformations.

The thin specimens D1-D6 employ two bolt rows and failed after the development of four plastic hinges in their flanges. Specimens D5 and D6 which employed a small distance between the bolts (40 mm) ultimately failed by the formation of cracks in the plate in-between the bolt holes thus demonstrating the significance of bearing of the plates when membrane actions develop. D3 failed by cracking of the plate material at the location of the bolt hole. Specimens D1, D2 and D4 exhibited significant plastic deformation of the bolt hole and a partial penetration of the bolt and washer through the elongated bolt hole which caused a partial loss of contact between the bolts and the specimens and an accompanying drop in the applied force. The thicker specimens D7 and D9-

D11 also developed 4 plastic hinges and moderate membrane action but ultimately failed by cracking or fracture of the bolts.

4.4.2. Load-deformation response

The recorded load-deflection curves are depicted in Figure 4.11, where the design predictions of EN 1993-1-8 (2005) for failure modes 1 and 2 are also depicted as horizontal red and blue lines respectively, with all safety factors set to unity. All specimens display an initial linear response followed by a drop in stiffness and a knee region corresponding to the attainment of the plastic resistance of the joint, whereafter a second linear curve follows.

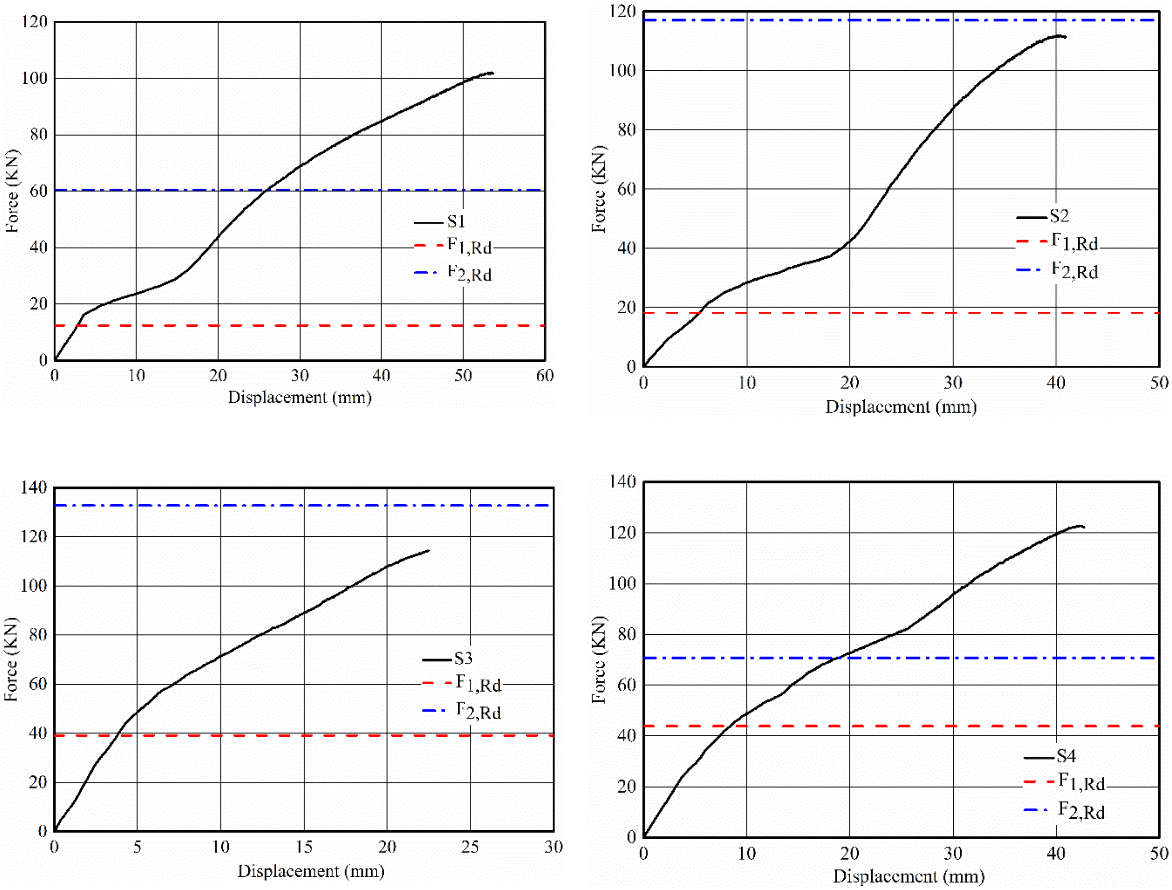

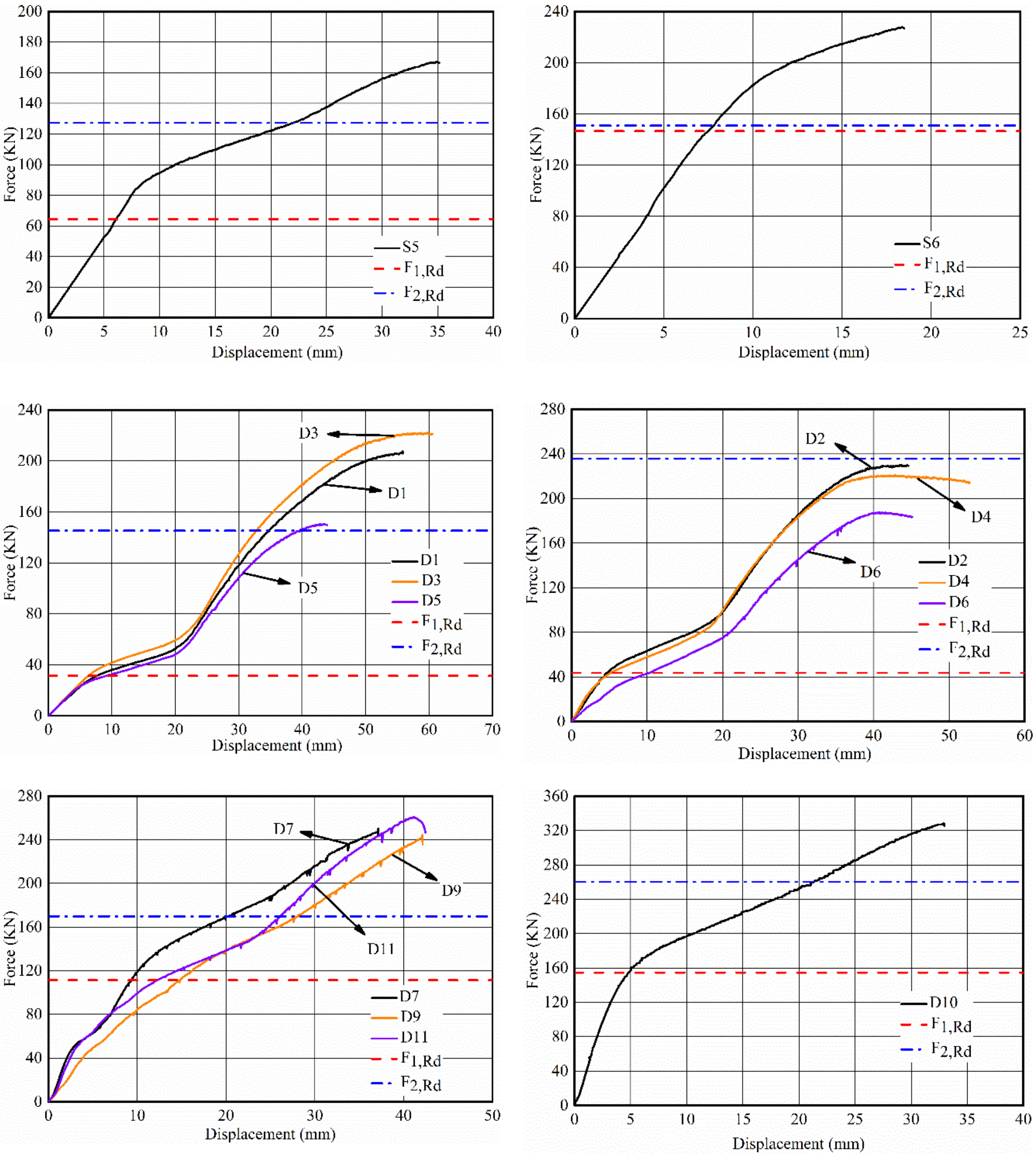

Figure 4.11: Load-deformation curves of the T-stub specimens.

It is worth noting that all specimens except S3, S6, D7-D11 display a third region in their load-deflection curve following the second linear region, which is seen to be stiffer than the second linear region. This gain in stiffness relates to the change of the load carrying mechanism of the T-stubs at high deformations from primarily flexural to primarily tensile, due to the development of membrane action in the deformed flanges. Similar observations have been made by Elflah *et al.* (2019) and Yuan *et al.* (2019) for moment resisting joints and T-stubs respectively. This change in response only occurs when the flexural stiffness of the flanges is small (small thickness, large m values) and the bolts are stiff and strong enough to accommodate large inelastic deformations of the T-stubs and anchor the developing membrane stresses, which cause a combination of tension and shear in the bolt.

As previously discussed, in Figure 4.10, it can be clearly seen that specimens S1 and D1 ultimately fail by bearing of the T-stub plate; hairline cracks were observed at the interface with the bolts. The marked bearing deformations of the plate ends lead to a gradual loss of stiffness of the third branch of the recorded load-deflection curves depicted in Figure 4.11. For specimens with smaller end distances n, loss of stiffness is caused by extensive yielding and elongation of the bolt holes and gradual loss of contact between the bolt head and the plate. It is noted that specimens D5 and D6 ultimately failed by fracture of the flange due to the strain concentration between the bolt holes. The main reason for that is that the selected bolt distance was the minimum allowed by EN 1993-1-8 (2005), hence bearing resistance was compromised.

4.4.3. Load-strain response

The load-strain curves for specimens S2, S5, D5 and D11 are shown in Figure 4.12. The curves obtained for S2 and D5 are typical of test specimens in which significant membrane actions developed, whilst specimens S5 and D11 did not exhibit membrane actions since they had a higher flange thickness.

Figures 4.12a and 4.12b report the obtained load vs strain behaviours for specimens S2 and D5, respectively. For each of the two specimens, two characteristic strain gauge readings are reported, one close to the web of the T-stub and one at a distance n from the end (i.e. at the location of the bolt holes). As expected, for both specimens, the strain gauge close to the web records tensile strains, which begin to increase significantly at a load level close to the $F_{pl, Exp}$ thus indicating excessive yielding corresponding to the formation of a plastic hinge. At higher load levels and higher deformations corresponding to the transition of the T-stub response from primarily flexural to primarily tensile, the tensile strains increase less abruptly.

Similarly, the strain gauges at a distance *n* from the free end record compressive strains which begin to increase significantly as $F_{pl, exp}$ is approached and continue to increase until a load level corresponding to the beginning of the third distinct branch of the load deflection curves. Thereafter, a reduction in the rate of increase of the recorded compressive strains occurs followed by a reduction of the compressive strains themselves. These observations are consistent with the development of membrane actions in the flanges of the T-stub. For example, with regard to specimen D5, strain gauge 1 and strain gauge 5 record almost equal but opposite in sign strains which begin to increase more rapidly at a load level approximately 20 kN, which corresponds to the beginning of the transition region between the initial linear and the second linear branch of the load-deflection curve of specimen as shown in Figure 4.11. The slope of the load strain curve remains constant until a load level of approximately 50 kN, whereupon the slope decreases. This load levels correspond to the beginning of the third branch of the load-deflection response. When the ultimate load is reached the compressive strains are clearly seen to decrease, presumably due to the development of membrane action throughout the T-stub flanges. Similar conclusions can be made for S2, the strain gauge readings for SG-1 expeditiously increases at the load level of plastic resistance and at the beginning of third branch in force-displacement curve the slope of the strain readings start to decrease. This trend was not observed for the S5 and D11, the force-strain curves of the SG-1 remains zero until the force level that corresponds to the plastic resistance however the SG-5 curve increases until the plastic resistance force which means the formation of plastic hinges at near the web-to-flange connection and remains constant until the ultimate load is reached. The SG-1 curve keeps increasing till the ultimate load is reached which shows that the membrane actions were not appeared for S5 and D11.

The normalised force-strain curves of SG-1 for all 5 mm and 10 mm flange thickness are depicted in Figure 4.13 in which the force values normalised by the respective ultimate forces obtained from tests are also reported. As shown in Figure 4.13a, when the applied load reaches 70 % of the ultimate load for S1, S2, D5 and D6, the strain readings begin to decrease significantly till the ultimate load is reached. Likewise, D2 and D4 exhibit a sudden drop when the 35% of the ultimate capacity is achieved and the curves become almost flat with a slight decreasing slope. Moreover, D1 and D3 increase until the 65-70 % of the ultimate load level and stabilize following slightly decreased slope. All these findings are supported by the force-displacement curves which have three distinct branches caused by the membrane actions represented in Figure 4.11. On the other hand, for specimens with 10 mm thick flanges the SG-1 strain readings start increasing followed by the formation of the first plastic hinges near the web-to-flange junction and no significant membrane actions can be observed. This observation is in line with the discussion on the load-deflection response.

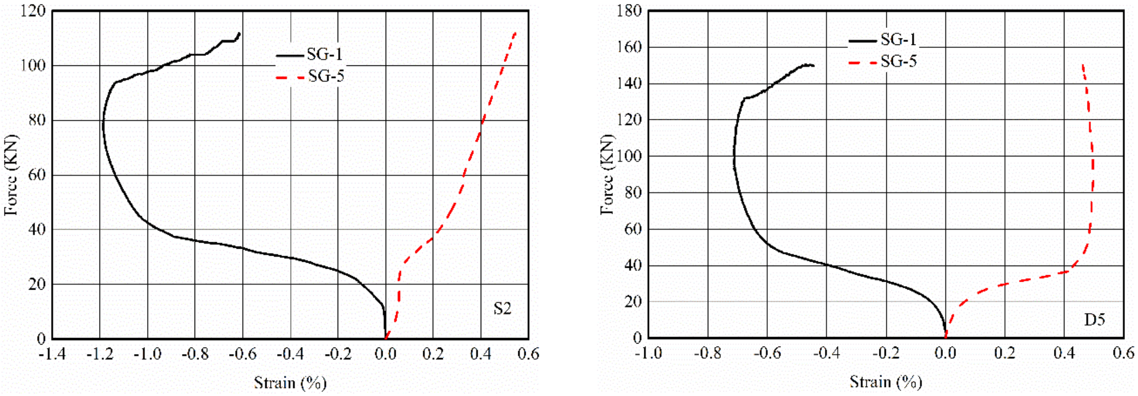

(a) Specimen S2

(b) Specimen D5

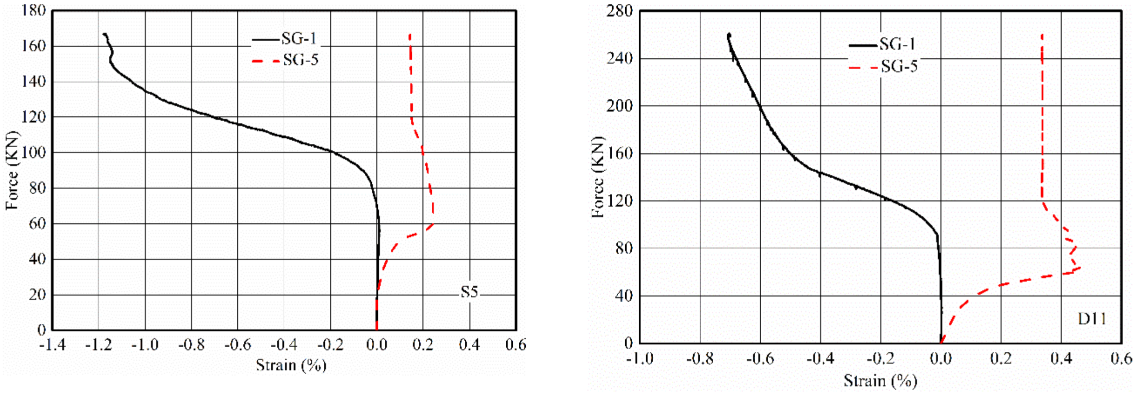

(c) Specimen S5

(d) Specimen D11

Figure 4.12: Load-strain curves for a) S2, b) D5, c) S5 and d) D11.

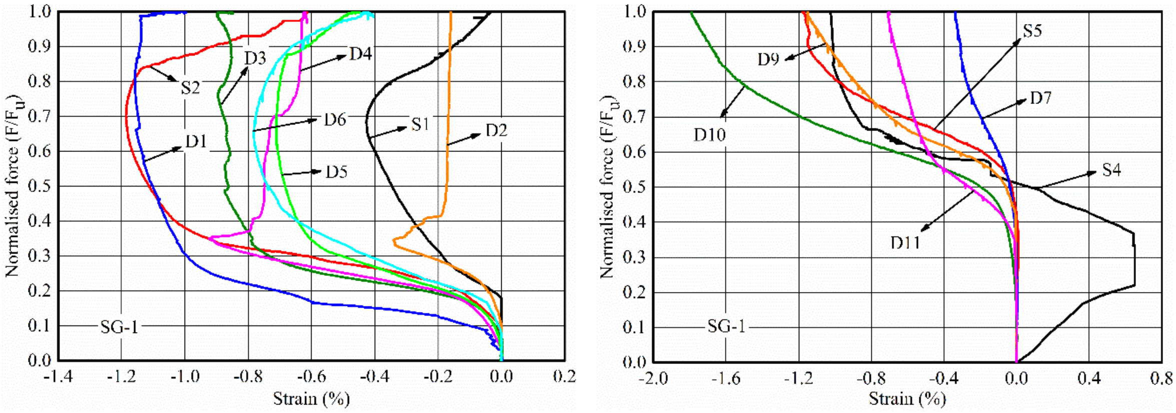

(a) 5 mm flange thickness

(b) 10 mm flange thickness

Figure 4.13: The SG-1 load-strain curves for a) 5 mm and b) 10 mm flange thickness.

4.4.4. Summary of the key results

Table 4.5 summarizes the experimentally obtained plastic resistance of the tested specimens $F_{pl,}$ and the ultimate resistance $F_{u,exp}$. The plastic resistance F_{pl} is determined as the intersection between the initial linear part of the curve and the tangent to the second linear region (Elflah *et al.*, 2019). As expected, specimens with smaller m distances display a higher stiffness and plastic resistance F_{pl}, e.g. S3 and S6 have a markedly higher stiffness and plastic resistance than S1, S2 and S3, S4, respectively. Similar observations can be made for the double bolt row T-stubs.

The comparison of the deformation capacity of the double bolt row specimens D1 and D2 demonstrates that when the bolt distance m increases, the deformation capacity increases substantially. Similar conclusions can be drawn for D9 and D10 which have 10 mm flange thickness. Moreover, the effect of bolt distance along the web plate (b_2) on the deformation capacity of the T-stubs is not significant. When the results of the double bolt row specimens D1, D3 and D2, D4 compared to each other it can be concluded that the deformation capacity and the ultimate resistance of the specimens are not changing significantly.

Likewise, the deformation capacity of 10 mm specimens of D7, D9 and D11are not affected by the change of distance b_2. On the other hand, the results of the D5 specimen which has the same geometric properties with the D1 and D3 except for the bolt spacing b_2 which is much lower than others, shows that D5 has lower deformation capacity and significantly lower ultimate resistance when compared to D1 and D3. It can be concluded that when the distance between bolts along the web plate (b_2) is very low, strains accumulate in a relatively small area and cause fracture of the flange plates as observed in specimens D5 and D6. The ultimate resistance of all specimens F_u remains unaffected by the change of the adopted *m* and *n* values, whilst the distance between the bolts b_2 seems to be an influential parameter for both the ultimate resistance and ductility.

Table 4.5: Summary of the key test results.

Specimen	Failure mode	F_{pl}	F_u	Δ_u	F_u/F_{pl}	β
S1	1	16.8	102.1	54.0	6.1	0.08
S2	1	22.3	111.8	41.0	5.0	0.11
S3	1	47	114.3	22.5	2.4	0.23
S4	1	48	122.7	42.2	2.6	0.23
S5	1	93.5	167.0	34.9	1.8	0.46
S6	1	188	227.7	18.4	1.2	0.92
D1	1	31	207.5	55.8	6.7	0.08
D2	1	46	229.9	43.5	5.0	0.11
D3	1	37.5	222.1	59.7	5.9	0.09
D4	1	40	220.8	42.8	5.5	0.10
D5	1	29	150.5	43.0	5.2	0.07
D6	1	36	187.5	41.2	5.2	0.09
D7	1	127	249.9	37.2	2.0	0.31
D8	1	180	-	-	-	0.44
D9	1	105	244.2	42.1	2.3	0.26
D10	1	170	328.1	32.9	1.9	0.41
D11	1	92	260.9	41.1	2.8	0.22

4.4.5. Membrane action

The presence of membrane action in the behaviour of thin T-stubs is evident both in the obtained load-deformation response as well as from the observations regarding the evolution of strains. Table 4.5 allows a quantification of membrane actions by dividing the ultimate force at failure F_u by the respective plastic resistance F_{pl} of each specimen. The obtained ratios are plotted against the parameter β, defined as the ratio of plastic resistance of the T-stub for mode 1 failure over the resistance of the bolts (Piluso *et al.*, 2001a; 2001b; Tartaglia *et al.*, 2020) in Figure 4.14. A value of β equal to 2 corresponds to mode 3 failure, whilst mode 1 failure occurs when $\beta<2(n/m)/[1+2(n/m)]$ and mode 2 for values in-between. To facilitate comparisons with the behaviour of other stainless steel grades, Figure 4.14 includes the test results reported herein as well as test results on austenitic and duplex stainless steel T-stubs reported by Yuan *et al.* (2019; 2020).

As expected, the lower the value of β, the higher the overstrength ratio F_u/F_{pl}, which is attributable to membrane effects. Overstrength values up to 6.7, 4.4 and 2.67 times the plastic resistance can be observed recorded for ferritic, austenitic and duplex stainless steel, respectively. The correlation between overstrength and β seems to be strong as is the trend displayed in Figure 4.14. It may be observed that the ferritic stainless steel T-stubs display a higher F_u/F_{pl} ratio than their austenitic and duplex counterparts. This is attributed to the high preload forces applied to many of the austenitic and duplex T-stubs, which lead to an earlier bolt failure and hence smaller membrane effects compared to T-stubs in the snug tight condition. This can be observed in Figure 4.15, where the same data are plotted but the effect of preload has been considered in the determination of parameter $\beta^{'}$, by subtracting the applied preload from the bolt strength. This effectively shifts the datapoints corresponding to a high applied preload towards the right and results all three grades exhibiting similar response.

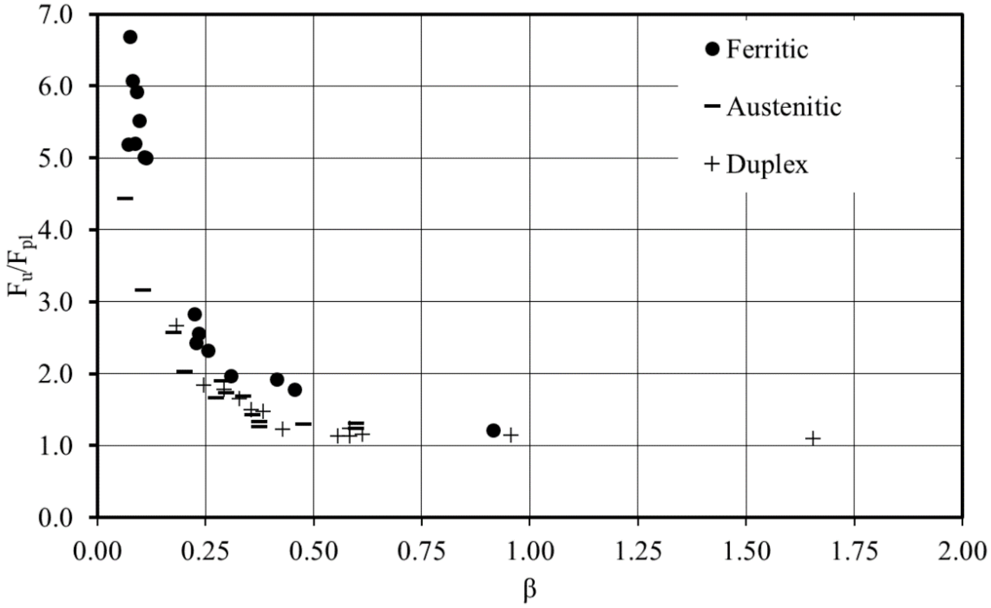

Figure 4.14: Overstrength as a function of parameter β.

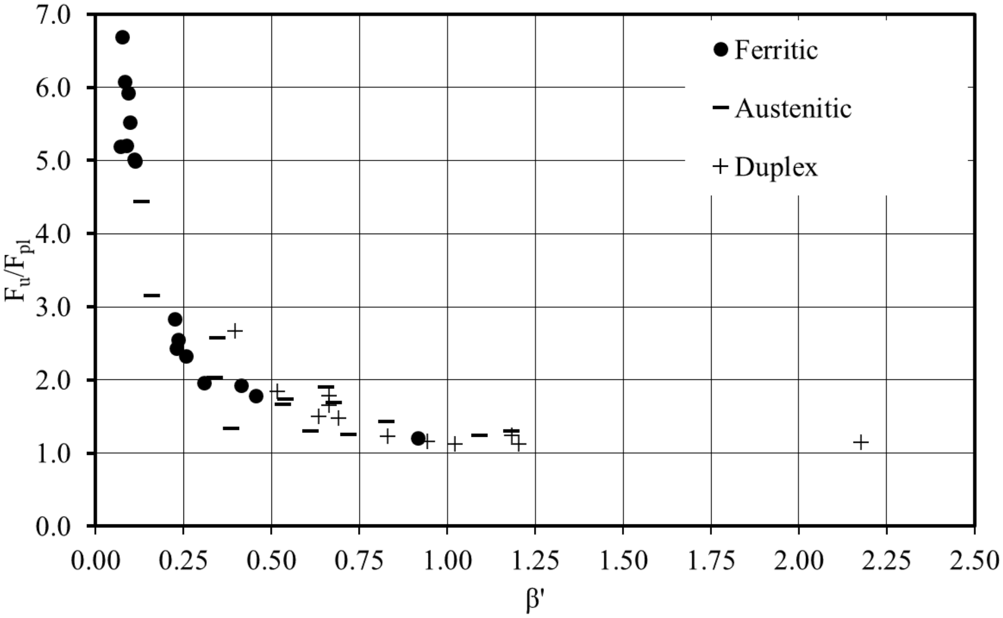

Figure 4.15: Overstrength as a function of parameter β' considering preload.

4.5. Conclusions

A comprehensive experimental study on the structural behaviour of stainless steel bolted T-stubs fabricated from EN 1.4003 ferritic stainless steel grade is reported herein. The experimental configurations considered included both single and double bolt rows bolted T-stubs and have been assembled with A4-80 stainless steel bolts. In order to determine the material characteristics of the T-stubs and the connecting bolts, tensile coupon tests were performed, and the material anisotropy exhibited by ferritic stainless steel has been quantified. The ultimate resistance, plastic deformation capacity and failure mode of each T-stub were obtained and reported.

It was found that the ferritic stainless steel exhibited significantly high anisotropy. The nominal yield strength in transverse direction is 21% and 7% larger than the yield strength in longitudinal direction for 5 mm and 10 mm thickness, respectively. Initial material tests on the 10 mm thick material revealed an unexpected response involving longitudinal splitting which affects the obtained results. It is evidenced by additional coupon tests with thinner coupons that the longitudinal splitting is related to thickness of the coupons.

Furthermore, the ultimate resistance of the specimens was obtained and the effects of bolt distances on the response of the T-stubs have been discussed. All specimens exhibited significant overstrength. The ratio of the ultimate over the plastic resistance $F_{u,\ Exp}/F_{pl,\ Exp}$ ranged from 1.21 to 6.69 thus indicating significant reserve capacity inherent in ferritic stainless steel connections failing in mode 1. Since large deformations are required to mobilise membrane actions, it is not practical to consider this over strength in conventional design, but it may be beneficial to mitigate progressive collapse in an extreme event and can hence enhance robustness.

CHAPTER 5

Numerical modelling of stainless steel bolted T-stubs

5.1. Introduction

In the first part of Chapter 5 (section 5.2), a numerical study which builds upon a previous experimental research on bolted austenitic and duplex stainless steel T-stubs in tension conducted by Yuan *et al.* (2019) is reported in detail. The development and validation of an advanced FE model able to predict the overall behaviour, failure modes and fracture mechanisms of bolted T-stubs in tension is reported in detail and key modelling assumptions are highlighted and discussed. Key simulation strategies regarding the explicit modelling of bolt geometry and fracture and overcoming numerical instabilities are discussed and recommendations on best modelling practices are made.

In the second part of Chapter 5 (section 5.3), following the experimental study on EN 1.4003 ferritic stainless steel T-stubs in tension reported in Chapter 4, the development and validation of an advanced FE model that can predict the overall behaviour and failure modes of ferritic stainless steel bolted T-stubs subjected to tension is reported. A comprehensive discussion on modelling strategies of bolt geometry is reported and suggestions on overcoming numerical instabilities are made. Following the determination of material properties in the longitudinal, transverse and diagonal direction reported in Chapter 4, the effect of allowing for anisotropy in the FE simulations is investigated and modelling recommendations for its inclusion in FE models are made. Moreover, the effect of bolt end and edge spacing on the joint plastic resistance, ultimate capacity, ductility as well as overall response is comprehensively discussed by inspecting the stress distribution through the plate thickness at various locations along the T-stub, thus revealing both the flexural and the membrane component of the load transfer mechanism. The numerical results are validated against the experimental results reported in Chapter 4 in terms of predicted plastic and ultimate resistance, ductility and obtained failure modes. A parametric study utilising the developed FE model is performed and analysis results in terms of plastic and ultimate resistance are reported in detail. The results of the parametric studies reported in this Chapter are utilized in Chapter 6 where predictive equations for the quantification of membrane action and the ultimate strength of T-stubs are assessed against all relevant experimental and numerical results, either collated or generated as part of this thesis.

5.2. FE modelling of austenitic and duplex stainless steel bolted T-stubs in tension

5.2.1. Modelling assumptions

The geometric configurations of the specimens tested by Yuan *et al.* (2019) are defined in Table 5.1 and Figure 5.1 for single-row and double-row T-stub connections. These tests are numerically replicated herein.

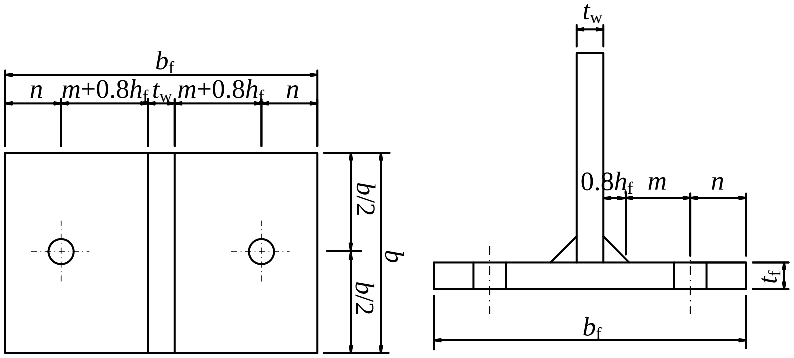

(a) T-S

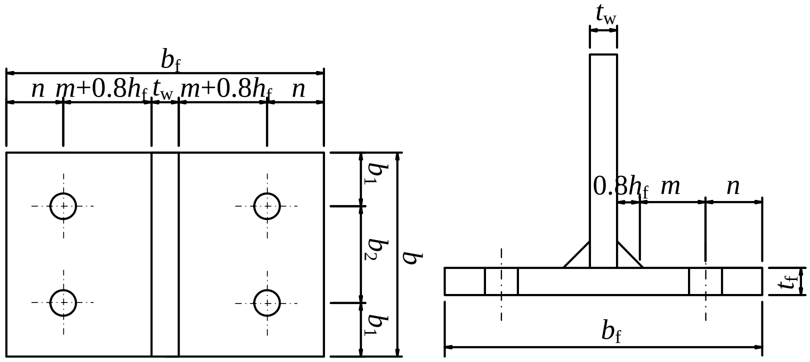

(b) T-D

Figure 5.1: Geometric properties of T-stub specimens (Yuan *et al.*, 2019).

The T-stub specimens were manufactured by welding two hot-rolled stainless steel plates to one another. Two nominal plate thicknesses (8 mm and 12 mm), two different bolt diameters (12 mm and 16 mm) and two different bolt configurations (single bolt row TS-S and double bolt row TS-D) with various bolt spacings are considered. It should be noted that a third bolt configuration employing 4 bolts per row was also considered by Yuan *et al.* (2019), but this is beyond the scope of this project. The measured geometric properties of each specimen are represented in Table 5.1

in which d_b corresponds the nominal bolt diameter and h_f is the fillet weld size. Other geometric symbols included in Table 5.1 are defined in Figure 5.1. The fillet weld size h_f is specified as 5 mm and 6 mm for a plate thickness of 8 mm and 12 mm, respectively.

Table 5.1: Geometric dimensions of T-stub specimens (Yuan *et al.*, 2019). (All dimensions are in mm)

Type	Specimen	Material	Bolt	d_b	n_1	n_2	n	m	b_1	b_2	b	b_f	$t_f = t_w$	h_f
TS-S	S1	EN 1.4301	A4-70	16	-	-	50	50.2	-	-	120	222	11.85	6
	S2	EN 1.4301	A4-80	12	-	-	35	65.2	-	-	120	222	11.85	6
	S3	EN 1.4462	A4-80	16	-	-	50	50.2	-	-	90	222	12.58	6
	S4	EN 1.4462	A4-80	12	-	-	50	53.0	-	-	120	222	7.72	5
	S5	EN 1.4462	A4-80	16	-	-	50	53.0	-	-	90	222	7.72	5
	S6	EN 1.4301	A4-80	12	-	-	50	53.0	-	-	120	222	7.85	5
	S7	EN 1.4462	A4-80	16	-	-	50	53.0	-	-	120	222	7.72	5
	S8	EN 1.4301	A4-70	16	-	-	50	50.2	-	-	90	222	11.85	6
	S9	EN 1.4301	A4-80	12	-	-	35	65.2	-	-	120	222	11.85	6
TS-D	D1	EN 1.4301	A4-70	16	-	-	50	50.2	40	70	150	222	11.85	6
	D2	EN 1.4301	A4-80	12	-	-	35	65.2	40	70	150	222	11.85	6
	D3	EN 1.4462	A4-70	16	-	-	35	68.0	40	70	150	222	7.72	5
	D4	EN 1.4462	A4-70	16	-	-	35	65.2	40	70	150	222	12.58	6
	D5	EN 1.4462	A4-70	16	-	-	50	50.2	40	70	150	222	12.58	6
	D6	EN 1.4301	A4-80	16	-	-	35	65.2	40	70	150	222	11.85	6
	D7	EN 1.4301	A4-80	12	-	-	35	65.2	28	54	110	222	11.85	6
	D8	EN 1.4301	A4-80	12	-	-	35	65.2	40	70	150	222	11.85	6

The material properties of the stainless steel T-stubs and the connecting bolts are adopted from the study conducted by Yuan *et al.* (2019) and are given in Table 5.2. The standard von Mises yield criterion with isotropic hardening is employed to simulate the plastic behaviour of the T-stubs. The material behaviour beyond the nominal yield stress $\sigma_{0.2}$ is approximated by the 3 stage Ramberg-Osgood expression (Quach *et al.*, 2008).

Accurate geometric modelling of the specimens may lead to overly high computational cost. The bolts contain a threaded part, which is tedious to model explicitly and necessitates the adoption of a very fine mesh locally to accurately discretise it, as discussed in Chapter 3. In addition to the high number of elements, modelling the threaded part may also lead to a low stable time increment in quasi-static explicit dynamic analyses, thus further increasing computational time. An additional question relates to the need to explicitly model the weld toe at the flange-to-web junction of the T-stubs, or whether simulating the effect of welding via tying to one another the degrees of freedom of the welded parts over the weld toe region suffices.

Table 5.2: Material properties of stainless steel plates and bolts (Yuan *et al.*, 2019).

Stainless steel plates and bolts	Plate thickness or nominal bolt diameter (mm)	v	E_0 (MPa)	$\sigma_{0.01}$ (MPa)	$\sigma_{0.2}$ (MPa)	$\sigma_{1.0}$ (MPa)	σ_u (MPa)	ε_u (%)	ε_f (%)	n
EN 1.4301	7.85	0.257	180700	191.4	291.7	338.9	706.0	-	62.9	7.1
EN 1.4301	11.85	0.258	182800	184.7	280.4	319.1	719.6	-	57.7	7.2
EN 1.4462	7.72	0.207	188700	296.5	551.4	614.5	738.4	19.3	33.0	4.8
EN 1.4462	12.58	0.226	184000	227.8	464.6	552.8	705.3	23.3	37.4	4.2
A4-70	12	-	175400	273.8	522.6	667.1	758.1	8.5	36.5	4.6
A4-70	16	-	173000	283.8	484.6	622.7	732.7	26.0	44.9	5.6
A4-80	12	-	184500	271.5	553.9	710.4	794.0	5.9	29.7	4.2
A4-80	16	-	175300	300.7	524.4	682.3	765.4	9.8	33.4	5.4

To determine an optimal modelling strategy four types of numerical models with different levels of complexity were considered. In the first model, a cylindrical bolt with a diameter such that its cross-sectional area is equal to the nominal stress area of the threaded bolt is used. This approach leads to larger clearance between the bolt and the bolt hole and hence different contact conditions. In the second model, the diameter of the unthreaded part of the bolt is considered, in order to maintain the same clearance between the bolt and the bolt hole, but material from the central part of the bolt is removed so that its cross-sectional area matches the nominal cross-sectional area of the threaded bolt. The resulting geometry of the bolt is bounded by two concentric cylinders. For each of the two models for the bolt, two variations of modelling the weld toe are considered, one where the weld toe is explicitly modelled with triangular elements and one where it is omitted and only a tie constraint is applied. The generated numerical models are named Type-1, Type-2, Type-

3 and Type-4, as outlined in Figure 5.2.

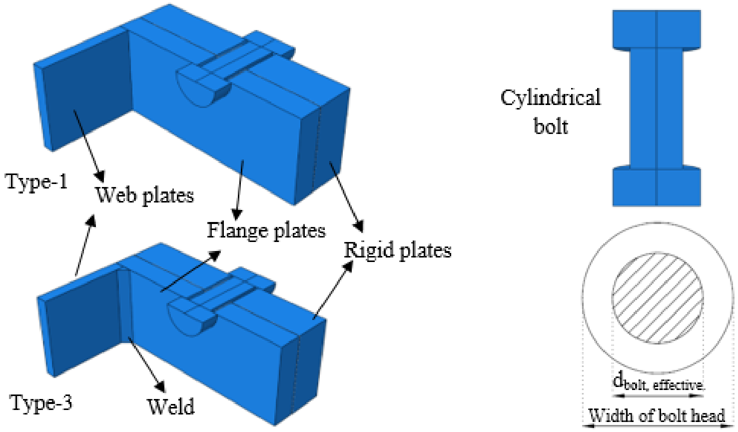

(a) Type 1 and Type-3

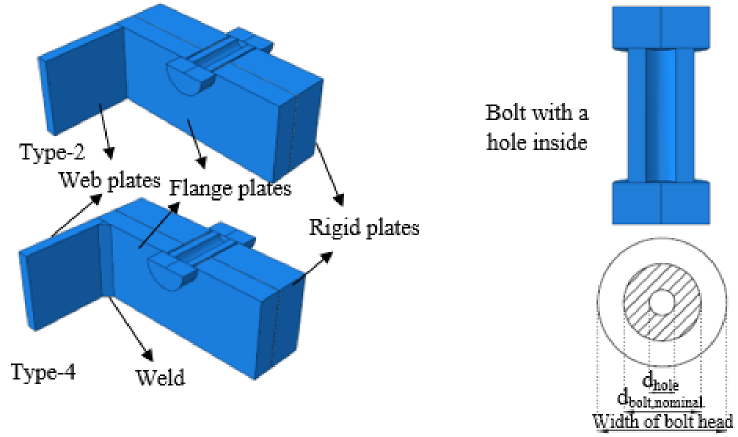

(b) Type 2 and Type-4

Figure 5.2: Geometric modelling assumptions for the bolt and the weld toe.

Three dimensional nonlinear finite element analysis is carried out to determine the ultimate strength and the corresponding displacement of the T-stubs using ABAQUS (2013). To minimise computational time without compromising accuracy, the symmetry of the model in terms of geometry, applied load, boundary conditions and structural response is exploited. Hence one quarter of the T-stub is modelled and appropriate boundary conditions are applied along the planes of symmetry. In line with the conducted tests, the T-stub models are attached via bolts to a reaction rigid T-stub with a 20 mm thickness, which is discretised with rigid elements with all its degrees of freedom being fixed. Surface to surface contact is defined between bolt shank and bolt hole, bolt head and flange, bolt head and rigid T-stub and T-stub and rigid reaction T-stub. The contact behaviour for each contact pair is assumed hard in the normal direction hence eliminating any penetration and finite sliding with a friction coefficient of 0.25 is assumed in the tangential direction thus allowing the changing contact conditions to be traced as the analysis progresses.

To obtain an optimal mesh for the subsequent numerical studies, the effect of the employed element type and mesh size on the obtained results were investigated. Both the T-stub and the bolts were discretised with a uniform mesh with a characteristic element size equal to either 1/3 or 1/4 of the flange thickness, as earlier studies (Elflah *et al.*, 2019 (b)) showed that at least three linear elements are required through the thickness of a plate in bending to obtain accurate results. Moreover, the performance of linear and quadratic elements was compared with the 8-noded reduced integration continuum solid elements C3D8 and the 20-noded reduced integration continuum solid elements C3D20R being employed.

For each of the resulting four meshes (2 element types and 2 mesh sizes) two analysis types were considered. Initially, a static Riks analysis (Abaqus, 2013), which is a variant of the classic arc-length method was conducted, which resulted in long computational times and in some cases loss of convergence. To reduce computational time a quasi-static explicit dynamic analysis was also attempted. For the explicit dynamic analysis, a mass scaling factor of 10^{-4} was increase the stable time increment and reduce computational time; in all cases it was ensured that the kinetic energy of the model was below 2% of its internal energy thus resulting in a quasi-static response. The results for the 2 analysis types are compared hereafter for each of the 4 modelling strategies employed for the modelling of the bolts and the weld toes, as well as for the different mesh densities and element types considered.

5.2.2. Validation and discussion

5.2.2.1. Modelling of bolt and weld toe

For each of the four types of geometric modelling considered for the simulation of the bolt geometry and the weld toe, as defined in Figure 5.2, the plastic and ultimate resistance and corresponding displacement values obtained from the static Riks analysis are presented in Tables 5.3-5.6. Only the models employing linear continuum elements have been considered herein to assess the effect of modelled geometry for the weld toes and bolts on the obtained response. To facilitate a direct comparison with the experimental values, the reported results are normalised by the corresponding experimental ones. As expected, the scatter of the numerical over experimental displacements (Tables 5.4 and 5.6) is considerably higher than that observed for the plastic and ultimate force predictions shown in Tables 5.3 and 5.5 respectively. This is attributed to the high sensitivity of the experimental stiffness on existing imperfections and applied level of preload. Hence, the experimental displacements are less suitable to assess the quality of the numerical results and only the plastic resistance F_{pl} and ultimate resistance F_u are considered hereafter.

In Table 5.5 it can be seen that the mean value of the numerical over the experimental ultimate resistance ratio $F_{u, FEM}/ F_{u, Exp}$ obtained for type-2 and type-3 models is 1.00 for both mesh densities considered (i.e. with 3 and 4 elements through the flange thickness) with a coefficient of variation (COV) of 0.06 and 0.07, respectively. The mean value of $F_{u, FEM}/ F_{u, Exp}$ ratios for the type-4 model were determined as 1.02 and 1.03 for the mesh configurations with 3 and 4 elements. Hence it can be concluded that both mesh densities lead to similar levels of accuracy in terms of the ultimate resistance F_u. From the mean values of the numerical over the experimental plastic resistance ratios $F_{pl,FEM}/ F_{pl,Exp}$ shown in Table 5.3 it can be concluded that the best predictions are obtained by type-3 and type-4 models, thus indicating the importance of explicitly modelling the weld toe geometry. The numerical analysis results using four elements along the flange thickness show only slightly lower coefficient of variation values in terms of ultimate force. Overall it can be concluded that as long as the modelled bolt has a cross-sectional area equal to the effective area of the threaded bolt used in the tests, reasonably accurate results can be obtained. In the remainder of this chapter only Type-3 and Type-4 models are considered.

Table 5.3: Effect of modelling type and number of elements through the flange thickness on plastic resistance F_{pl}.

		Type-1	Type-2	Type-3	Type-4	Type-1	Type-2	Type-3	Type-4
		3 elements through flange thickness				4 elements through flange thickness			
Specimens	$F_{pl,\ Exp}$ (KN)	$F_{pl,FEM}/F_{pl,Exp}$	$F_{pl,FEM}/F_{pl,Exp}$	$F_{pl,FEM}/F_{pl,Exp}$	$F_{pl,FEM}/F_{pl,Exp}$	$F_{pl,FEM}/F_{pl,Exp}$	$F_{pl,FEM}/F_{pl,Exp}$	$F_{pl,FEM}/F_{pl,Exp}$	$F_{pl,FEM}/F_{pl,Exp}$
S1	159	0.77	0.78	0.79	0.82	0.79	0.81	0.82	0.86
S2	92	0.83	0.85	0.83	0.85	0.85	0.85	0.85	0.90
S3	187	0.82	0.82	0.84	0.84	0.83	0.84	0.86	0.86
S4	101	0.82	0.82	0.82	0.86	0.82	0.86	0.87	0.89
S5	87	0.77	0.76	0.84	0.82	0.83	0.83	0.90	0.90
S6	66	0.73	0.73	0.76	0.77	0.76	0.73	0.80	0.82
S7	106	0.82	0.78	0.88	0.80	0.86	0.79	0.92	0.87
S8	134	0.75	0.78	0.81	0.84	0.80	0.79	0.78	0.87
S9	91	0.84	0.86	0.84	0.86	0.86	0.86	0.86	0.91
D1	216	0.73	0.79	0.84	0.83	0.76	0.82	0.85	0.88
D2	157	0.74	0.76	0.78	0.78	0.78	0.80	0.83	0.83
D3	96	0.93	0.90	0.97	0.93	1.01	0.94	1.01	0.99
D4	262	0.76	0.75	0.82	0.78	0.79	0.78	0.82	0.82
D5	338	0.77	0.78	0.82	0.83	0.81	0.81	0.85	0.86
D6	154	0.77	0.71	0.81	0.77	0.81	0.78	0.89	0.88
D7	105	0.79	0.76	0.88	0.82	0.89	0.82	0.93	0.90
D8	154	0.75	0.77	0.80	0.80	0.80	0.82	0.84	0.85
Mean		0.79	0.79	0.83	0.82	0.83	0.82	0.86	0.88
COV		0.06	0.06	0.06	0.05	0.07	0.06	0.06	0.05

Table 5.4: Effect of modelling type and number of elements through the flange thickness on displacement at plastic resistance Δ_{pl}.

		Type-1	Type-2	Type-3	Type-4	Type-1	Type-2	Type-3	Type-4
		3 elements through flange thickness				4 elements through flange thickness			
Specimens	$\Delta_{pl,Exp}$ (mm)	$\Delta_{pl, FEM}/\Delta_{pl,Exp}$	$\Delta_{pl, FEM}/\Delta_{pl,Exp}$	$\Delta_{pl, FEM}/\Delta_{pl,Exp}$	$\Delta_{pl, FEM}/\Delta_{pl,Exp}$	$\Delta_{pl, FEM}/\Delta_{pl,Exp}$	$\Delta_{pl, FEM}/\Delta_{pl,Exp}$	$\Delta_{pl, FEM}/\Delta_{pl,Exp}$	$\Delta_{pl, FEM}/\Delta_{pl,Exp}$
S1	1.15	1.22	1.13	1.04	1.13	1.13	1.22	1.22	1.26
S2	1.2	1.08	1.13	1.08	1.08	1.04	1.13	1.08	1.13
S3	1.3	1.23	1.23	1.23	1.23	1.15	1.15	1.15	1.15
S4	2.25	1.11	1.00	1.00	1.00	1.00	1.07	1.00	1.04
S5	1.6	1.00	1.13	1.03	1.03	1.09	1.09	1.13	1.09
S6	0.9	1.11	1.11	1.06	1.11	1.11	1.06	1.11	1.11
S7	1.1	1.73	2.18	1.82	2.00	1.91	1.64	1.91	1.73
S8	0.85	0.94	1.29	1.29	1.41	1.41	1.41	1.35	1.47
S9	2.8	0.46	0.48	0.46	0.46	0.45	0.48	0.46	0.48
D1	0.9	1.06	1.11	1.11	1.11	1.00	1.06	1.06	1.11
D2	1.25	0.88	0.88	0.88	0.88	0.88	0.88	0.96	0.88
D3	0.5	4.20	4.00	4.20	4.00	4.80	4.50	4.00	4.00
D4	0.6	2.67	2.67	2.75	2.75	2.67	2.67	2.50	2.67
D5	1.0	1.25	1.25	1.20	1.25	1.35	1.40	1.25	1.35
D6	0.5	1.50	1.60	1.30	1.60	1.60	1.70	1.30	1.60
D7	0.9	0.89	0.78	1.00	0.89	1.00	0.89	1.00	0.89
D8	3.2	0.34	0.34	0.34	0.34	0.34	0.34	0.38	0.34
Mean		1.33	1.37	1.34	1.37	1.41	1.39	1.34	1.37
COV		0.67	0.64	0.67	0.64	0.73	0.68	0.62	0.62

Table 5.5: Effect of modelling type and number of elements through the flange thickness on ultimate resistance F_u.

		Type-1	Type-2	Type-3	Type-4	Type-1	Type-2	Type-3	Type-4
		3 elements through flange thickness				4 elements through flange thickness			
Specimens	$F_{u,Exp}$ (KN)	$F_{u,FEM}/F_{u,Exp}$	$F_{u, FEM}/F_{u,Exp}$	$F_{u, FEM}/F_{u,Exp}$	$F_{u, FEM}/F_{u,Exp}$	$F_{u, FEM}/F_{u,Exp}$	$F_{u, FEM}/F_{u,Exp}$	$F_{u, FEM}/F_{u,Exp}$	$F_{u, FEM}/F_{u,Exp}$
S1	200.2	0.95	0.95	0.98	0.95	0.95	0.94	0.98	0.96
S2	106.8	0.96	0.94	0.95	1.01	0.98	0.97	0.96	1.02
S3	198.4	0.95	0.96	0.98	0.98	0.96	0.97	1.00	0.98
S4	108.9	0.95	1.02	0.97	1.03	0.95	1.01	0.98	1.03
S5	161.6	1.06	1.04	1.08	1.07	1.04	1.04	1.06	1.07
S6	104.3	0.91	1.00	0.95	1.04	0.95	1.00	0.97	1.04
S7	175.2	0.81	0.87	0.85	0.90	0.80	0.87	0.85	0.90
S8	188	0.99	0.99	1.01	0.99	0.98	0.98	1.00	1.00
S9	108.9	0.94	0.93	0.93	0.99	0.96	0.95	0.94	1.00
D1	367.5	1.01	1.00	1.03	1.02	1.01	0.99	1.02	1.00
D2	179.1	1.00	1.04	1.02	1.06	0.98	1.04	1.00	1.07
D3	260.9	1.11	1.13	1.15	1.16	1.13	1.13	1.14	1.15

D4	312.5	1.06	1.04	1.08	1.07	1.07	1.04	1.06	1.06
D5	382.5	0.94	0.95	0.97	0.98	0.94	0.94	0.97	0.97
D6	306.6	1.05	1.02	1.05	1.04	1.05	1.02	1.07	1.05
D7	174.3	1.00	1.04	1.02	1.06	1.00	1.04	1.03	1.07
D8	181.6	0.99	1.02	1.01	1.05	0.97	1.02	0.99	1.05
Mean		0.98	1.00	1.00	1.02	0.98	1.00	1.00	1.03
COV		0.07	0.06	0.07	0.06	0.07	0.06	0.06	0.05

Table 5.6: Effect of modelling type and number of elements through the flange thickness on displacement at ultimate resistance Δ_u.

		Type-1	Type-2	Type-3	Type-4	Type-1	Type-2	Type-3	Type-4
		3 elements through flange thickness				4 elements through flange thickness			
Specimens	$\Delta_{u,Exp}$ (mm)	$\Delta_{u, FEM}/\Delta_{u,Exp}$	$\Delta_{u, FEM}/\Delta_{u,Exp}$	$\Delta_{u, FEM}/\Delta_{u,Exp}$	$\Delta_{u, FEM}/\Delta_{u,Exp}$	$\Delta_{u, FEM}/\Delta_{u,Exp}$	$\Delta_{u, FEM}/\Delta_{u,Exp}$	$\Delta_{u, FEM}/\Delta_{u,Exp}$	$\Delta_{u, FEM}/\Delta_{u,Exp}$
S1	31.8	1.214	1.084	1.166	0.975	1.191	1.080	1.174	1.029
S2	23.9	0.788	0.903	0.827	0.823	0.822	0.862	0.843	0.853
S3	21.5	0.978	0.933	0.887	0.871	0.947	0.928	0.887	0.868
S4	19.7	1.040	1.046	0.921	0.968	0.971	1.036	0.901	0.949
S5	29.2	1.284	1.286	1.192	1.233	1.272	1.235	1.172	1.229
S6	26	0.966	0.981	0.947	0.968	1.108	1.089	1.101	0.971
S7	28.9	0.845	0.893	0.838	0.831	0.854	0.867	0.840	0.846
S8	27.3	1.414	1.262	1.358	1.136	1.387	1.258	1.368	1.199
S9	25	0.753	0.863	0.791	0.787	0.786	0.824	0.806	0.815
D1	28.7	1.426	1.392	1.396	1.345	1.537	1.491	1.435	1.422
D2	22.5	1.161	1.050	1.072	1.035	1.108	1.142	1.023	1.049
D3	33.6	1.273	1.365	1.295	1.330	1.368	1.385	1.345	1.355
D4	25.4	1.622	1.545	1.600	1.557	1.724	1.583	1.506	1.552
D5	26	1.181	1.190	1.173	1.111	1.224	1.208	1.159	1.096
D6	31.4	1.280	1.234	1.230	1.247	1.311	1.278	1.297	1.254
D7	25.8	1.165	1.124	1.098	1.076	1.193	1.192	1.177	1.105
D8	25.3	1.032	0.934	0.953	0.921	0.985	1.015	0.910	0.933
Mean		1.144	1.129	1.105	1.076	1.170	1.153	1.112	1.090
COV		0.209	0.184	0.210	0.201	0.226	0.194	0.200	0.200

5.2.2.2. Effect of element type

The numerical analyses discussed previously exhibited the necessity of including the geometry of the weld toes in the numerical models. In this section, the results obtained from Type-3 and Type-4 models discretised with linear elements are compared to those obtained using quadratic elements to assess the effect of element type on the obtained response. For both element types two mesh densities were considered as previously discussed. The experimental and numerical force-displacement curves for specimens S4 and D2 are shown in Figure 5.3 to demonstrate the effect of the employed element type. The numerical models employing quadratic elements exhibit an almost identical behaviour to that of the models employing linear elements up to the attainment of the ultimate resistance. However, for the models with quadratic elements, it was observed that after the ultimate load was reached, the force drop was sharper.

The comparison of the mean and COV values of the plastic and ultimate resistance ratios are given in Tables 5.7 and 5.9. For completeness, the ratios for the corresponding displacements are given in Tables 5.8 and 5.10, respectively. The data considered for these tables are the same as previously (Tables 5.3-5.6) but for brevity only the average values and COV of the key response parameters are reported. It can be concluded that the effect of using quadratic elements instead of linear ones elements on the ultimate and plastic force predictions is not significant. In terms of ultimate displacements, quadratic elements provide slightly better and more consistent results. Additionally, the Type-3 numerical model using a cylindrical bolt exhibits better results in terms of ultimate force values and it provides simpler and faster solution. Given the simplicity of modelling a cylindrical bolt with an effective diameter, only Type-3 model is considered hereafter. Furthermore, due to the close agreement of the response of the models with 3 elements through the flange thickness with the experimental one and the significant savings in computational time, 3 elements through the thickness are adopted.

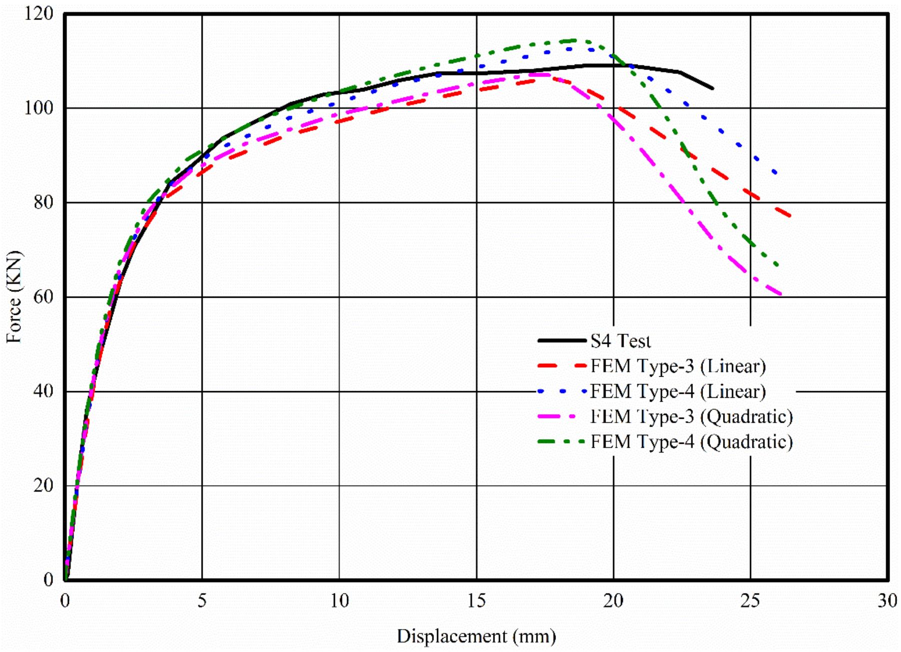

(a)

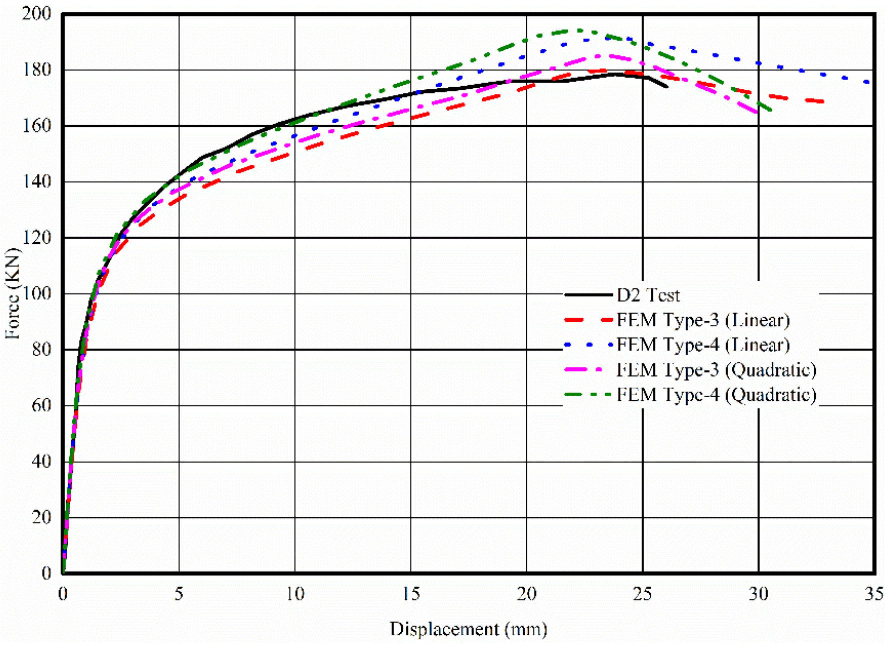

(b)

Figure 5.3: Force-displacement curves of the a) S4 and b) D2 specimens.

Table 5.7: Comparison of the mean values of $F_{u,\,FEM}$ / $F_{u,\,Exp}$ ratios for Type-3 and Type-4.

	Type-3				Type-4			
	3 elements through flange thickness		4 elements through flange thickness		3 elements through flange thickness		4 elements through flange thickness	
	Linear mesh	Quadratic mesh	Linear mesh	Quadratic mesh	Linear mesh	Quadratic mesh	Linear mesh	Quadratic mesh
	$F_{u,\,FEM}/F_{u,Exp}$	$F_{u,\,FEM}/F_{u,Exp}$	$F_{u,\,FEM}/F_{u,Exp}$	$F_{u,\,FEM}/F_{u,Exp}$	$F_{u,\,FEM}/F_{u,Exp}$	$F_{u,\,FEM}/F_{u,Exp}$	$F_{u,\,FEM}/F_{u,Exp}$	$F_{u,\,FEM}/F_{u,Exp}$
Mean	1.00	1.01	1.00	1.00	1.02	1.03	1.03	1.03
COV	0.07	0.06	0.06	0.06	0.06	0.05	0.05	0.05

Table 5.8: Comparison of the mean values of $\Delta_{u,\,FEM}$ / $\Delta_{u,\,Exp}$ ratios for Type-3 and Type-4.

	Type-3				Type-4			
	3 elements through flange thickness		4 elements through flange thickness		3 elements through flange thickness		4 elements through flange thickness	
	Linear mesh	Quadratic mesh	Linear mesh	Quadratic mesh	Linear mesh	Quadratic mesh	Linear mesh	Quadratic mesh
	$\Delta_{u,\,FEM}/\Delta_{u,Exp}$	$\Delta_{u,\,FEM}/\Delta_{u,Exp}$	$\Delta_{u,\,FEM}/\Delta_{u,Exp}$	$\Delta_{u,\,FEM}/\Delta_{u,Exp}$	$\Delta_{u,\,FEM}/\Delta_{u,Exp}$	$\Delta_{u,\,FEM}/\Delta_{u,Exp}$	$\Delta_{u,\,FEM}/\Delta_{u,Exp}$	$\Delta_{u,\,FEM}/\Delta_{u,Exp}$
Mean	1.11	1.08	1.11	1.08	1.08	1.04	1.09	1.04
COV	0.21	0.19	0.20	0.19	0.20	0.18	0.20	0.17

Table 5.9: Comparison of the mean values of $F_{pl,\,FEM}$ / $F_{pl,\,Exp}$ ratios for Type-3 and Type-4.

	Type-3				Type-4			
	3 elements through flange thickness		4 elements through flange thickness		3 elements through flange thickness		4 elements through flange thickness	
	Linear mesh	Quadratic mesh	Linear mesh	Quadratic mesh	Linear mesh	Quadratic mesh	Linear mesh	Quadratic mesh
	$F_{pl,FEM}/F_{pl,Exp}$	$F_{pl,FEM}/F_{pl,Exp}$	$F_{pl,FEM}/F_{pl,Exp}$	$F_{pl,FEM}/F_{pl,Exp}$	$F_{pl,FEM}/F_{pl,Exp}$	$F_{pl,FEM}/F_{pl,Exp}$	$F_{pl,FEM}/F_{pl,Exp}$	$F_{pl,FEM}/F_{pl,Exp}$
Mean	0.83	0.89	0.86	0.88	0.82	0.90	0.88	0.89
COV	0.06	0.07	0.06	0.05	0.05	0.06	0.05	0.04

Table 5.10: Comparison of the mean values of $\Delta_{pl,\,FEM}$ / $\Delta_{pl,\,Exp}$ ratios for Type-3 and Type-4.

	Type-3				Type-4			
	3 elements through flange thickness		4 elements through flange thickness		3 elements through flange thickness		4 elements through flange thickness	
	Linear mesh	Quadratic mesh	Linear mesh	Quadratic mesh	Linear mesh	Quadratic mesh	Linear mesh	Quadratic mesh
	$\Delta_{pl,\,FEM}/\Delta_{pl,Exp}$	$\Delta_{pl,\,FEM}/\Delta_{pl,Exp}$	$\Delta_{pl,\,FEM}/\Delta_{pl,Exp}$	$\Delta_{pl,\,FEM}/\Delta_{pl,Exp}$	$\Delta_{pl,\,FEM}/\Delta_{pl,Exp}$	$\Delta_{pl,\,FEM}/\Delta_{pl,Exp}$	$\Delta_{pl,\,FEM}/\Delta_{pl,Exp}$	$\Delta_{pl,\,FEM}/\Delta_{pl,Exp}$
Mean	1.34	1.35	1.34	1.34	1.37	1.36	1.37	1.36
COV	0.67	0.63	0.62	0.64	0.64	0.65	0.62	0.64

5.2.2.3. Effect of analysis type

In this section, the results obtained using the static Riks analysis procedure are compared with those obtained when a quasi-static explicit dynamic analysis is used. Table 5.11 summarizes the mean value of the $F_{pl,\ FEM}$/ $F_{pl,\ Exp}$ and $F_{u,\ FEM}$/ $F_{u,\ Exp}$ ratios obtained from a static Riks analysis with 3 linear or 3 quadratic elements through the flange thickness as well as the corresponding results from a quasi-static explicit dynamic analysis with 3 linear elements through the flange thickness. It should be noted that quadratic elements are not supported for explicit analysis (ABAQUS, 2013). It can be seen that, the mean value of the $F_{pl,\ FEM}$/ $F_{pl,\ Exp}$ ratio was obtained equal to 0.86 for the dynamic explicit analysis which is much better than the one corresponding to the static Riks analysis with a linear mesh and slightly lower than static analysis with quadratic elements. Moreover, the mean values of the $F_{u,\ FEM}$/ $F_{u,\ Exp}$ ratio for the explicit dynamic analysis was 1.00, which is equal to that of the static Riks analysis with linear elements. Furthermore, the coefficient of variation was for the explicit dynamic analysis was 0.06, slightly lower than the respective value for the Riks analysis with linear elements which was 0.07. Hence, it can be concluded that using the explicit dynamic analysis procedure with the modelling type-3 provides the closest and most consistent agreement to the experimentally determined ultimate resistance, whilst the plastic resistance is also well-predicted, albeit slightly lower on average compared to the Riks analysis with 3 quadratic elements through the flange thickness. Bearing in mind the significant savings in computational cost associated with using explicit dynamic analysis, this analysis type is adopted in subsequent numerical studies throughout this project.

Table 5.11: Comparison of explicit dynamic procedure and static Riks analysis procedure.

	Type-3			Type-3		
	3 elements through flange thickness			3 elements through flange thickness		
	Linear	Quadratic	Explicit	Linear	Quadratic	Explicit
	$F_{pl,FEM}$/ $F_{pl,Exp}$	$F_{pl,FEM}$/ $F_{pl,Exp}$	$F_{pl,FEM}$/ $F_{pl,Exp}$	$F_{u,FEM}$/ $F_{u,Exp}$	$F_{u,\ FEM}$/ $F_{u,Exp}$	$F_{u,\ FEM}$/ $F_{u,Exp}$
Mean	0.83	0.89	0.86	1.00	1.01	1.00
COV	0.06	0.07	0.06	0.07	0.06	0.06

A significant numerical result that cannot be obtained experimentally is the distribution of normal stresses throughout the depth of the T-stub flange at the attainment of the plastic resistance F_{pl} as well as at the ultimate resistance F_u. This stress distribution through the thickness in conjunction with the corresponding bolt force can be utilised to determine the failure mode of the T-stub as demonstrated by Yuan *et al.* (2020). The stress distribution curves through the thickness were obtained for the thinnest and thickest flange thickness of the single and double bolt rows for each material grades considered (i.e. a total of 8 models) and are presented in Figure 5.4. The stress distribution through the flange thickness is reported at three cross-sections along the length of the T-stubs, at the end of the fillet weld as shown in the relevant figures. The selected locations include the location of the bolt, middle of the T-stub and the end of the T-stub. The reported normal stresses have been normalised by the longitudinal nominal yield stress $\sigma_{0.2}$ and are plotted on the x-axis against the through thickness locations at which they occur, which are plotted on the y-axis. For each of the three locations along the length of the T-stub sections where the stress values are reported, two load levels were considered, namely the load corresponding to the plastic resistance of the T-stub $F_{pl,\ FE}$ and the ultimate load $F_{u,\ FE}$ with the stress distribution curves are denoted with solid and dotted lines, respectively.

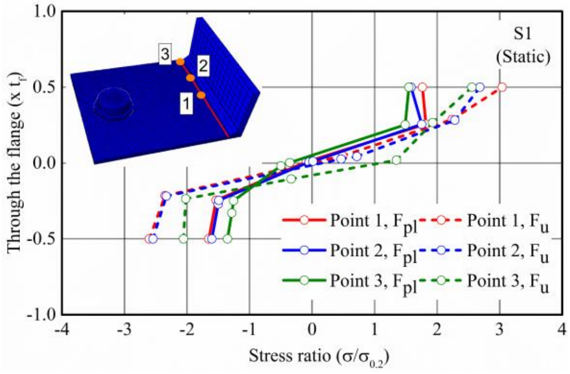

a) S1 Static Riks with quadratic mesh

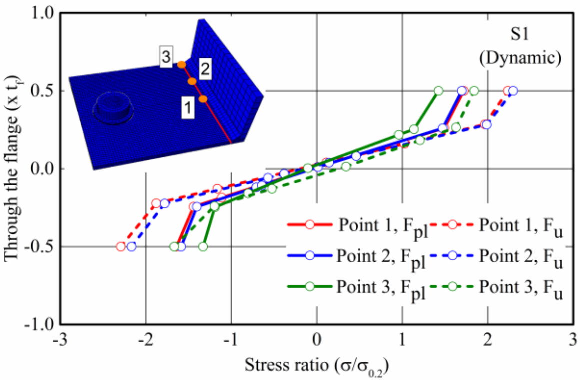

b) S1 Dynamic explicit

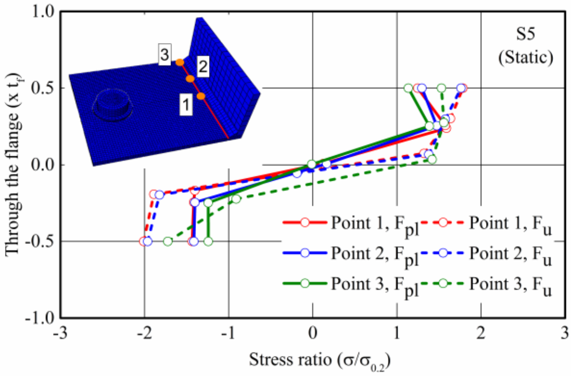

c) S5 Static Riks with quadratic mesh

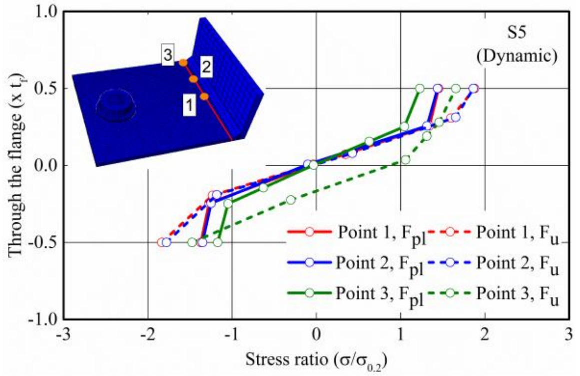

d) S5 Dynamic explicit

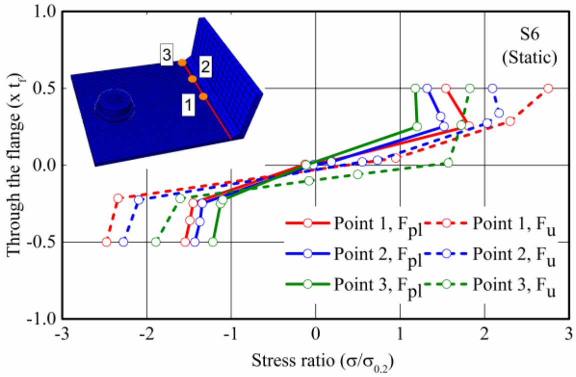

e) S6 Static Riks with quadratic mesh

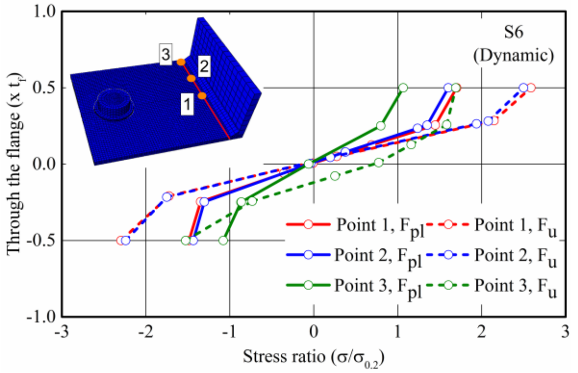

f) S6 Dynamic explicit

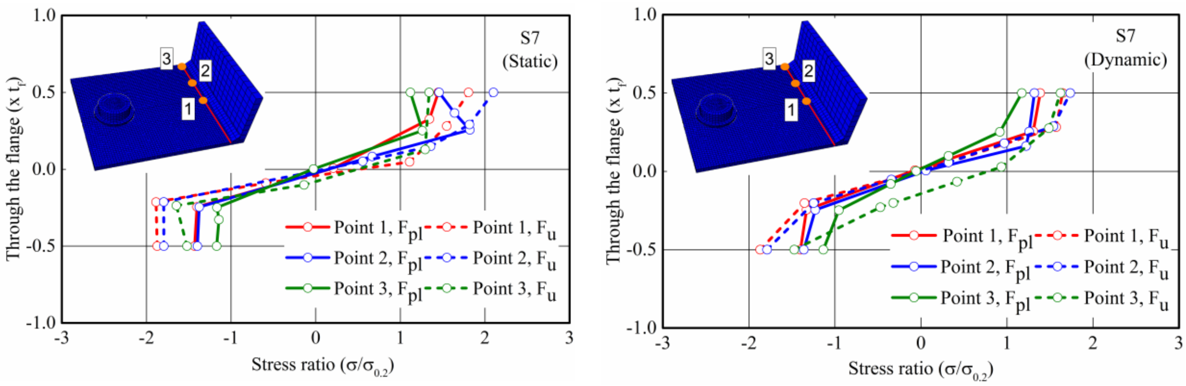

g) S7 Static Riks with quadratic mesh

h) S7 Dynamic explicit

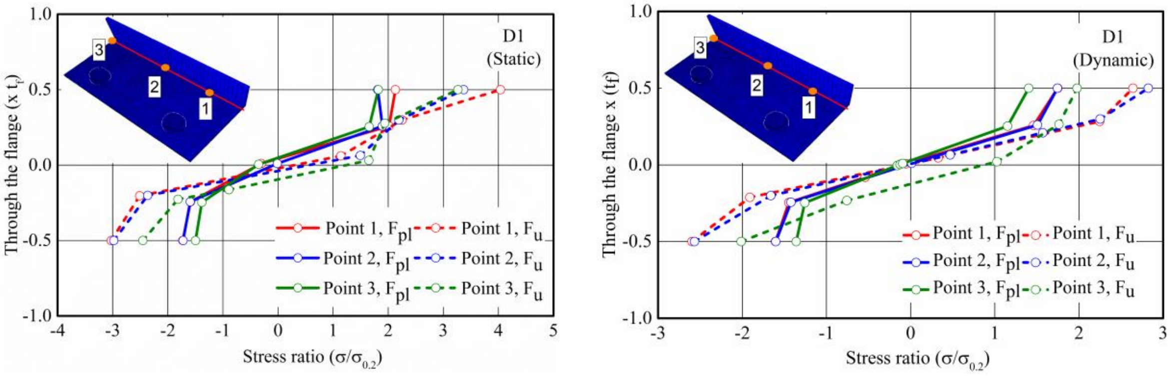

i) D1 Static Riks with quadratic mesh

j) D1 Dynamic explicit

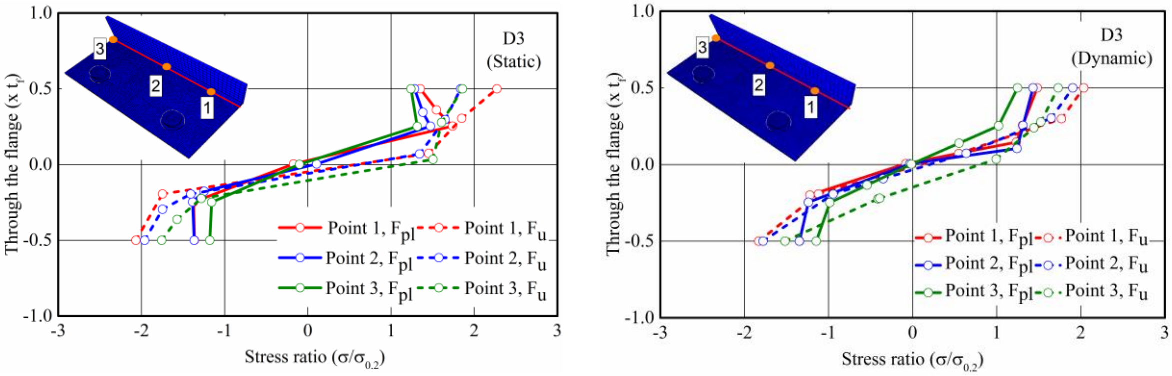

k) D3 Static Riks with quadratic mesh

l) D3 Dynamic explicit

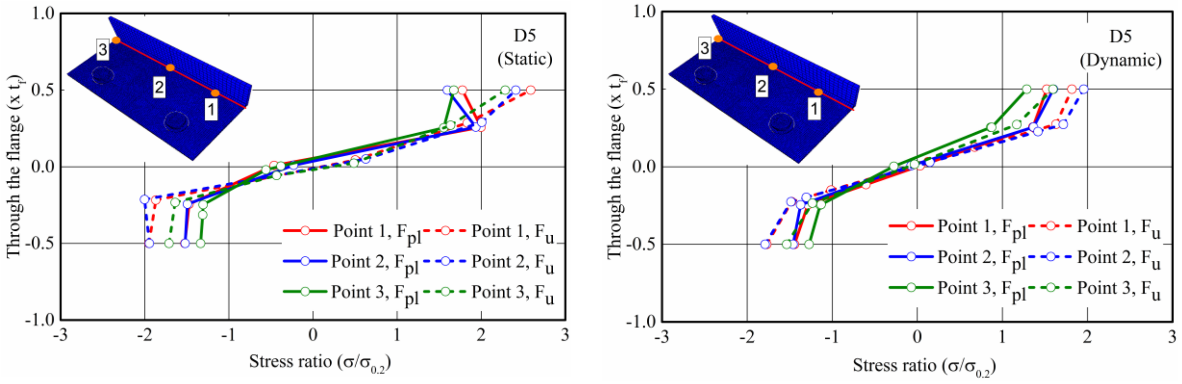

m) D5 Static Riks with quadratic mesh

n) D5 Dynamic explicit

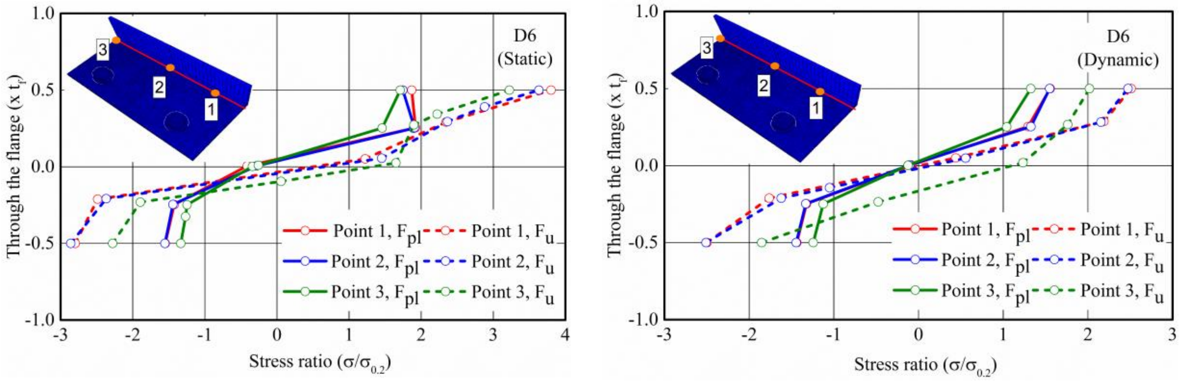

o) D6 Static Riks with quadratic mesh

p) D6 Dynamic explicit

Figure 5.4: Comparison of the stress distribution through the flange thickness for explicit dynamic and static analysis.

The EN 1993-1-8 (2005) assumes that the derivation of strength which corresponds to Type-1 failure mode is based on rigid plastic analysis in which rigid plastic material response is considered. This assumption is suitable for materials with a well-defined yield plateau, however for stainless steels which exhibit a gradual loss of stiffness and significant strain hardening this assumption becomes questionable. Hence, the attainment of stress distribution through the flange thickness at the load level which corresponds to the plastic resistance of the T-stub can provide valuable insight into the true stress-distribution at plastic resistance, which can be compared to the assumed one. In Figure 5.4, it can be observed that stress distribution in all locations are symmetric for all models.

In all models, the T-stub section at the bolt location experiences higher stress values (red curves) compared to the other sections, whilst the lowest stress values were observed at the free ends of the T-stubs (green curves) with the intermediate locations (blue curves) being in-between depending on the bolt arrangement. The stress distributions obtained from the static Riks and dynamic explicit procedures at the attainment of the plastic resistance are very similar. Moreover, at the ultimate load level the stress distributions slightly differ and the normalised stress ratios are marginally larger for the static Riks analysis. Overall, it is concluded that the dynamic explicit analysis procedure can accurately simulate the stress distribution through the flange thickness and qualitatively similar results are obtained regardless of the employed type of analysis.

5.2.3. Modelling of bolt fracture

In the experimental study conducted by Yuan *et al.* (2019), all T-stubs failed due to bolt fracture. Incorporation of a bolt fracture model into the FE models can provide accurate predictions of the available ductility of the joints, as discussed in Chapter 3. Therefore, the bolt fracture model reported in Chapter 3 for stainless steel bolts in Grade A4-80 is utilised in this part of the study to predict the behaviour of tested stainless steel bolted T-stubs including the initiation and propagation of fracture and is validated against the test results. Given the high computational cost associated with explicit modelling bolt fracture, particularly when the bolt geometry is accurately modelled (i.e. including the threads of the bolt), an objective of this analysis is to assess whether the extra computational cost is justified by the obtained accuracy of the response or whether a cheaper means to assess fracture, more suitable for parametric studies, could be utilised instead.

Equation (5.1) defines the equivalent plastic strain at fracture initiation as a function of stress triaxiality, as discussed in Chapter 3.

$$\bar{\varepsilon}_{pl,D} = 0.46e^{-1.33\eta} \tag{5.1}$$

ABAQUS/Explicit was used in all models incorporating fracture to overcome the convergence issues associated with softening material response (Crisfield and Wills, 1988). All boundary conditions and contact definitions remain unchanged as in the previous sections FE models and 3 elements are employed through the T-stub flange. The bolt geometry was explicitly modelled (including the threads). Symmetry was utilised and hence half of the T-stub was explicitly modelled, as shown in Figure 5.5. The ductile damage option was activated and the selected displacement at failure values are based on the selected mesh sizes as reported in Table 5.12. The actual values are based on the relevant values reported in Chapter 3, modified to maintain the same ratio of mesh size over displacement at fracture.

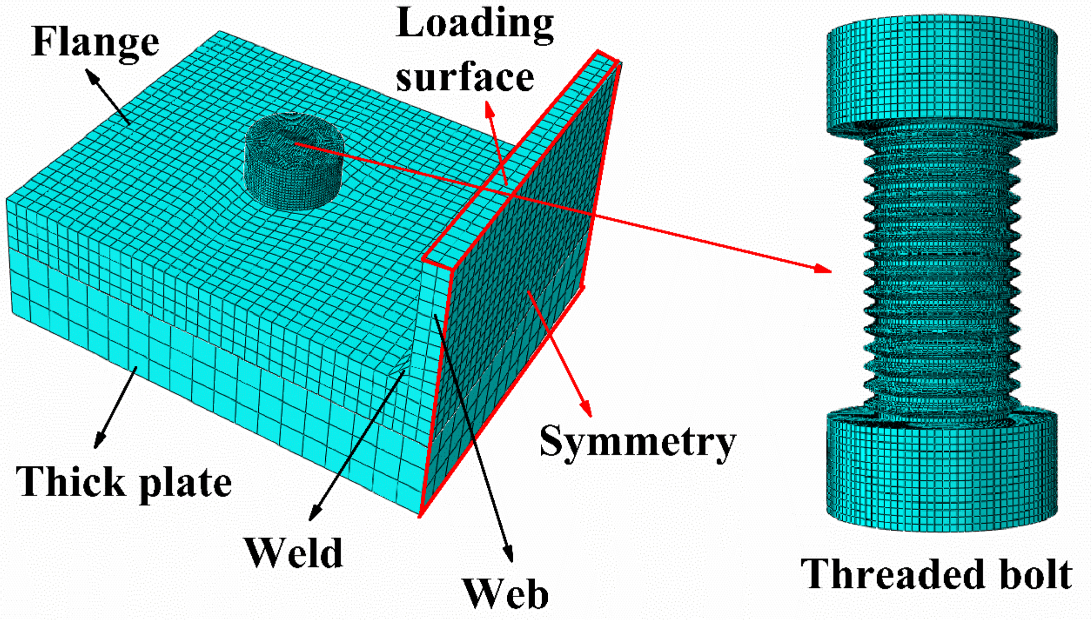

Figure 5.5: 3-D FE model for the T-stub specimens with threaded bolts.

Table 5.12: Optimal values for the plastic displacement at fracture for various bolt sizes.

Diameter of bolt (mm)	Mesh size (mm)	u_f (mm) for 3D model
12	0.34	0.44
16	0.47	0.61

The obtained numerical force-displacement curves for four representative T-stubs are presented in Figure 5.6 together with the experimental curves. Two modelling approaches were considered; in the first approach, the material response was incorporated until a true plastic strain value of 2.00 (i.e. far beyond the expected fracture strain) together with the fracture model discussed in Chapter 3. The second approach does not incorporate a fracture model but assumes that the stress-strain curve is truncated at the plastic strain at fracture as obtained from coupon tests (Table 5.2), thereby leading to a loss of strength with increasing bolt elongation as the true stress value remains constant whilst the bolt cross-sections is thinning due to the incompressibility of the plastic deformation.

For all 4 T-stubs considered, the developed FE model in which the proposed fracture model was incorporated can accurately capture the deformation at which the fracture occurs. Moreover, truncating the material behaviour at the strain at fracture provides a reasonable representation of the experimental response up to deformations slightly smaller than the deformation at ultimate force, but the near-peak and post-peak response cannot be accurately captured. The incorporation of the proposed fracture model into the developed FE model, provides accurate predictions for the available ductility and fracture of the stainless steel bolted T-stubs in tension, albeit at high computational cost.

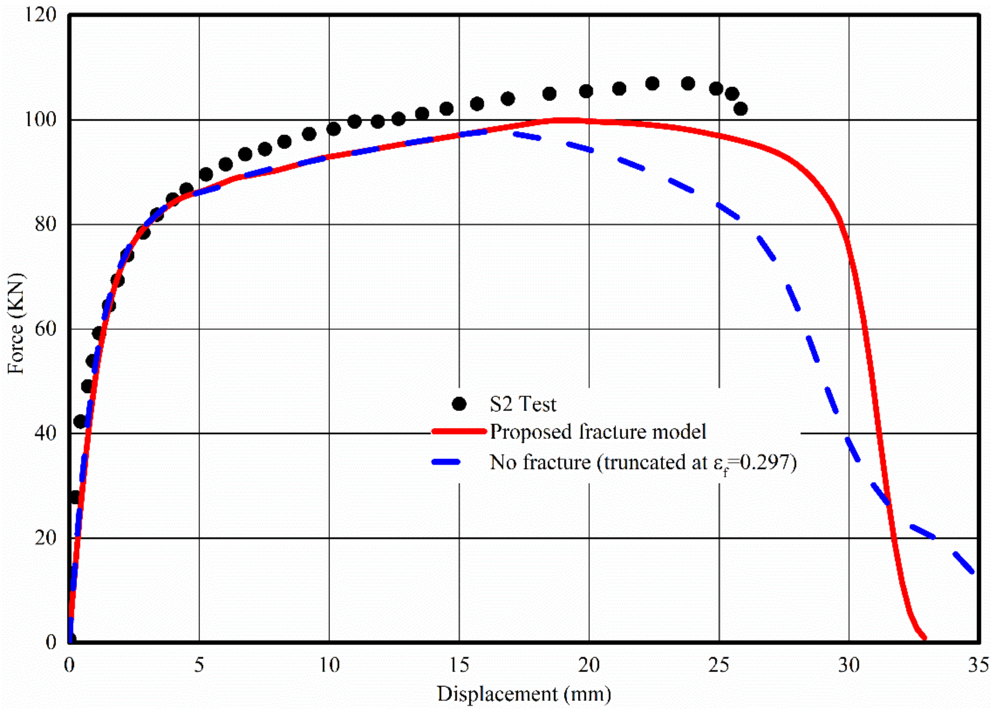
Force (KN)
0
20
40
60
80
100
120
Displacement (mm)
0
5
10
15
20
25
30
35
● S2 Test
Proposed fracture model
No fracture (truncated at ε_f=0.297)

a) S2

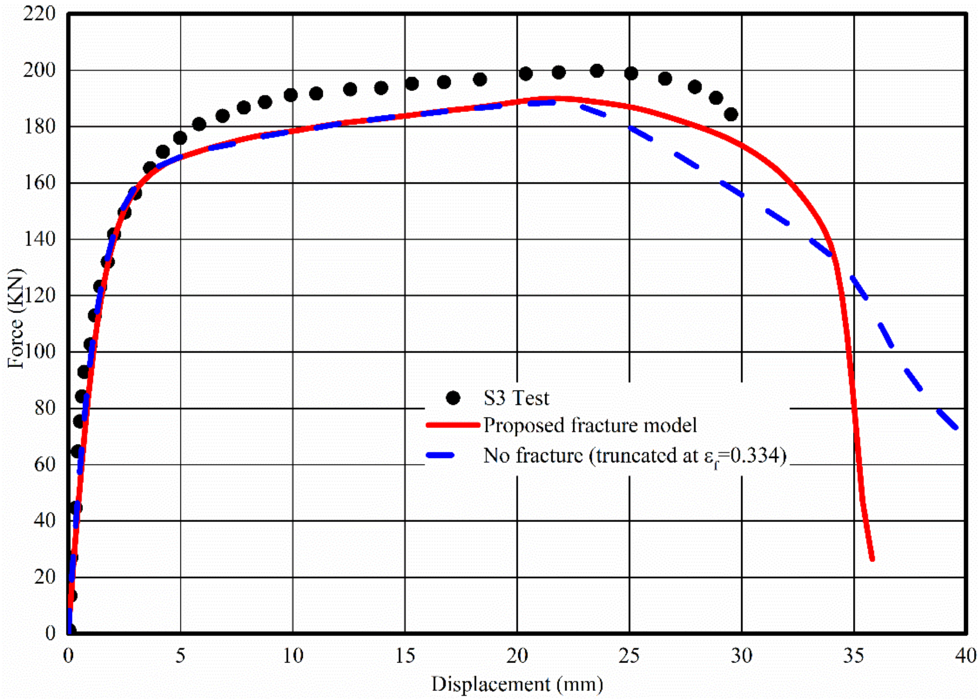
Force (KN)
0
20
40
60
80
100
120
140
160
180
200
220
Displacement (mm)
0
5
10
15
20
25
30
35
40
● S3 Test
Proposed fracture model
No fracture (truncated at ε_f=0.334)

b) S3

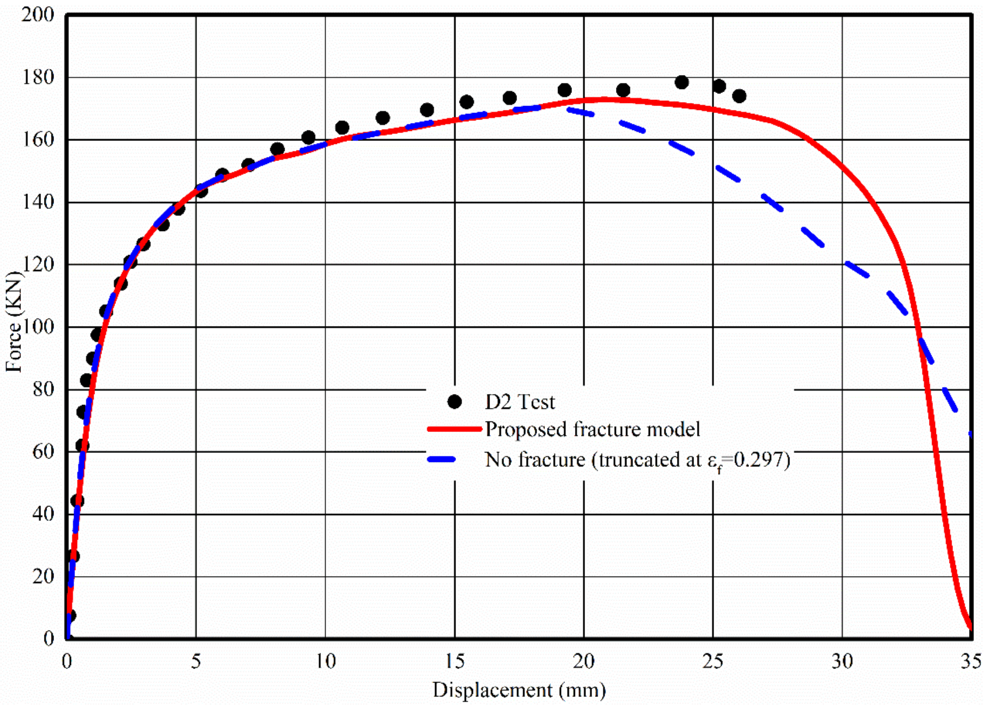

c) D2

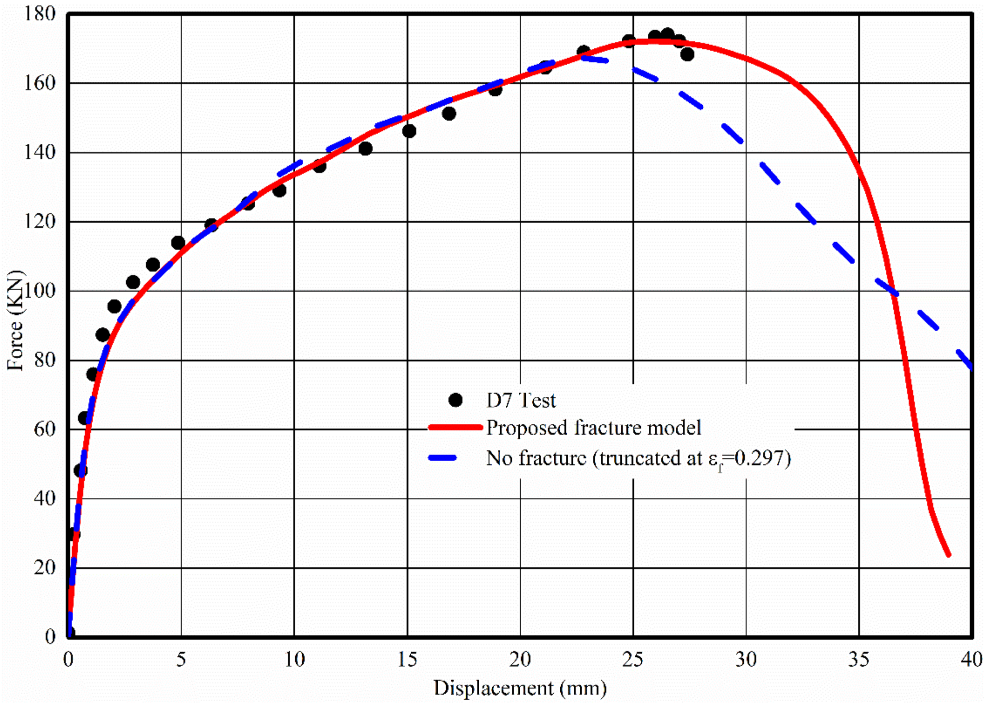

d) D7

Figure 5.6: Experimental and numerical response of specimens a) S2, b) S3, c) D2 and d) D7 for various modelling approaches.

5.3. Numerical modelling of ferritic stainless steel bolted T-stubs in tension

5.3.1. Development of FE model

Following the numerical modelling of the tests conducted by Yuan *et al.* (2020), the tests on the ferritic T-stubs reported in Chapter 4 have also been numerically simulated. Overall the same modelling assumptions as the ones stated in section 5.2 were made, however the pronounced material anisotropy of ferritic stainless steels prompted additional studies into the explicit modelling of material anisotropy. For completeness, the modelling assumptions made for the ferritic stainless steel T-stubs are reiterated herein.

Because of the symmetry of the modelled T-stub in terms of geometry, applied load, boundary conditions and observed response, with respect to two planes, only a quarter of the T-stubs was explicitly modelled, as shown in Figure 5.7, using the measured geometry reported in Chapter 4. The 30 mm thick steel plate to which the specimens were bolted was also explicitly modelled as shown in Figure 5.7. The same modelling assumptions which were given in section 5.2 were adopted herein.

To reduce computational cost, the threaded geometry of the bolt shank was simplified in the simulations as a cylindrical surface with an effective diameter such that the area of the simulated bolts equals the stress area of the threaded bolts, whilst the bolt heads and nuts were modelled as cylindrical instead of hexagonal discs. This modelling simplification of the bolt geometry has been shown to yield good results without compromising accuracy (Swanson *et al.*, 2002; Elflah *et al.*, 2019; Wang *et al.*, 2010), however as discussed previously it may not accurately represent the post-ultimate behaviour. Furthermore, the bolt head, bolt nut and washers were simplified as cylinders and were tied to the bolt shank as is customarily done when simulating bolts (Swanson *et al.*, 2002; Elflah *et al.*, 2019; Wang *et al.*, 2010; Liu *et al.*, 2012; Massimo *et al.*, 2014). No bolt preload was applied, given that in the tests the bolts were hand-tightened to obtain the snug-tight condition.

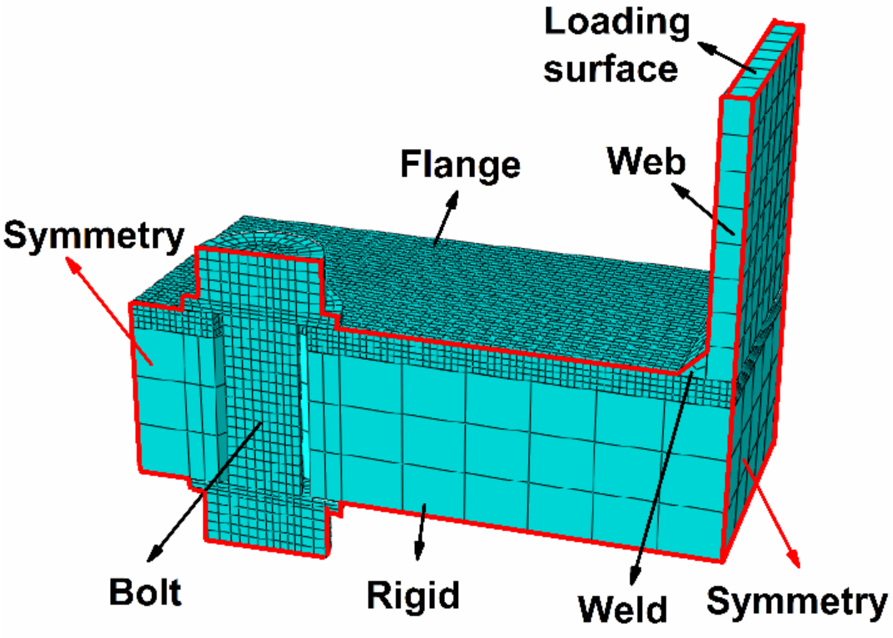

Figure 5.7: The developed FE model for the analyses.

Surface to surface contact, with finite sliding was assumed for all contact surfaces, namely bolt shank to bolt hole, bolt head to flange, bolt head to rigid plate are modelled thus enabling large slip to be simulated. The penalty friction method is adopted to simulate tangential behaviour, whilst hard contact is assumed for normal behaviour. The selected coefficient of friction was 0.3 and lies within the values of 0.2-0.33 recommended in the literature for steel, stainless steel and aluminium connections (Elflah *et al.*, 2019; Wang *et al.*, 2010; Liu *et al.*, 2012; Massimo *et al.*, 2014; De Matteis *et al.*, 2000; Wang and Wang, 2016). Symmetry conditions with respect to two planes of symmetry were applied. The model was loaded via a prescribed displacement at the top of the web of the T-stub, whilst all degrees of freedom of the bottom side of the thick elastic plate was restrained to provide reaction to the applied loading.

Due to the highly nonlinear behaviour of the model, brought about by the contact among its various parts, convergence difficulties emerged when a nonlinear static procedure was employed. To speed up the analysis and overcome the convergence difficulties, a quasi-static explicit dynamic analysis was employed as the selected analysis type based on the analysis assumptions given in section 5.2 regarding the mass scaling.

5.3.2. Material modelling and anisotropy

The nonlinear material properties of the stainless steel T-stubs and the bolts were modelled using the three stage Ramberg-Osgood model (Quach *et al.*, 2008). The material parameters for the ferritic stainless steel plates determined from tensile coupon tests as reported in Chapter 4 were adopted herein. Likewise, the material properties of the stainless steel bolts reported in Chapter 3 were adopted.

The standard von Mises yield criterion with isotropic hardening is conventionally employed to simulate the plastic behaviour of metals subjected to monotonic loading. In order to incorporate the material anisotropy in the numerical analysis, material properties in the longitudinal, transverse and diagonal directions are required. In Table 5.13, the average nominal yield strength values as determined in Chapter 4, are reported for each direction. The anisotropy ratio, defined as the ratio of the 0.2% proof stress in a particular direction over the 0.2% proof stress in the rolling/longitudinal direction is also reported as a means to quantify the observed material anisotropy. The material exhibited a 0.2% proof stress in the transverse direction 21% and 7%

higher than that in the longitudinal direction for 5 mm and 10 mm coupons, respectively. The anisotropy ratio values determined herein for the ferritic stainless steel plates is very similar to those found in the literature as discussed in Chapter 4. Hill's (1953) yield potential is adopted as the yield criterion in the numerical models which account the material anisotropy. In order to establish the yield function considering the anisotropy, six anisotropic yield stress ratios have to be defined. The six anisotropic yield stress ratios have been calculated using stress values reported for the 5 mm coupon tests as R11=1, R22=1.21, R33=R12=1.11, R13=R23=1 and for the 10 mm coupon tests as R11=1, R22=1.07, R33=R12=1.02, R13=R23=1. The effects of anisotropy on the obtained results are assessed in the next section. In Table 5.14, the material properties for two smooth cylindrical coupons which were machined from A4-80 stainless steel bolts are reported.

Table 5.13: Material properties of the ferritic stainless steel plates.

Coupon thickness	Direction	E_0	$\sigma_{0.2}$	$\sigma_{1.0}$	$\sigma_{2.0}$	σ_u	ε_f	m	n	Anisotropy
10 mm	LT	189114	279.3	298.8	324.1	441.3	0.35	2.8	20	1.00
10 mm	TT	196983	298.4	321.3	348.1	462.9	0.10	2.8	25	1.07
10 mm	DT	192094	284.5	303.5	328.4	438.6	0.36	2.8	16	1.02
5 mm	LT	204266	337.1	367.3	378.6	426.3	0.32	2.8	6.3	1.00
5 mm	TT	192996	409.0	425.1	435.6	467.1	0.18	2.8	12	1.21
5 mm	DT	184125	375.3	390.1	399.4	436.6	0.25	2.8	13	1.11

Table 5.14: Material properties of the stainless steel bolts.

#	E (MPa)	$\sigma_{0.2}$ (MPa)	$\sigma_{1.0}$ (MPa)	σ_u (MPa)	ε_u (%)	$n_{0-0.2}$	$n_{0.2-1.0}$	$n_{1.0-u}$
1	185000	410	600	727	0.19	4	4	11
2	178821	396	592	726	0.21	4	3	11

5.3.3. Modelling of fracture

As observed in the experimental tests, all T-stubs with a 5 mm thickness ultimately failed due to fracture of the ferritic T-stubs, in the vicinity of the bolt holes, whilst the bolts exhibited pronounced plastic deformation but no fracture due to the employed small thickness of the T-stub specimens compared to the bolt strength. Since no fracture characterisation studies were conducted for the ferritic stainless steel material, the fracture of the plates could not explicitly simulated in the analysis. In the absence of relevant material parameters, a simplified approach was followed, according to which fracture of the T-stub flange was not explicitly modelled but was indirectly defined based on the longitudinal plastic strain at fracture ε_f given in Table 5.13. Hence, the T-stubs were assumed to fail when the equivalent plastic strain obtained from the analysis reached ε_f, at which point the analysis was discontinued. For models considering anisotropy, the average value of the strain at fracture obtained for the 3 directions (i.e. longitudinal, trnasverse and diagonal) was adopted as the strain limit of the material. An indirect modelling of fracture based on strain values was successfully employed in similar studies investigating the fracture of stainless steel plates (Salih *et al.*, 2010), as well as fracture of bolts in T-stubs (Yuan *et al.*, 2019; Coelho *et al.*, 2006b) and moment resisting connections (Elflah *et al.*, 2019a; Gao *et al.*, 2020). A similar approach incorporating a damage initiation criterion but no damage propagation is attempted and discussed in Seciton 5.3.4.3.

5.3.4. Results and discussion

5.3.4.1. Validation of the FE models

The developed FE models were utilised to simulate the ferritic stainless steel bolted T-stubs tests and the obtained numerical results were validated against the test data reported in Chapter 4. For each of the tested specimens, three analyses with different assumed material responses for the T-stubs were conducted to assess the effect of incorporating material anisotropy in the simulations. In two of the analyses isotropic material response was assumed; the longitudinal material properties were adopted for the first case and the transverse ones for the second, whilst the third analysis explicitly incorporated anisotropy via Hill's yield potential.

For all three analyses conducted, at least 3 solid elements through the flange thickness were adopted to capture the flexural deformations. The adequacy of the selected mesh density is verified by comparing the results obtained for a typical T-stub with 1 bolt row (S2) and a typical T-stub with 2 bolt rows (D1), as shown in Figure 5.8. Similar results were obtained for the rest of the T-stub regardless of the assumed material properties. In line with the previously modelled austenitic and duplex stainless steel T-stubs, 3 elements through the thickness lead to an excellent replication of the experimental results of the ferritic T-stubs as well.

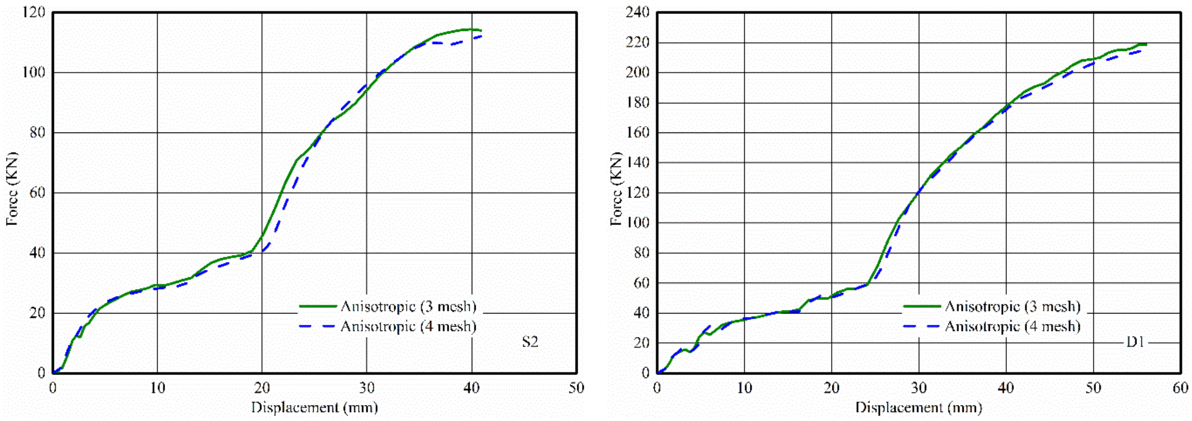

(a) (b)

Figure 5.8: Numerical load-deformation curves with 3 and 4 elements through the flange thickness of a) S2 and b) D1.

The comparison between the FE predictions and the test results in terms of the overall force-deformation curves and the failure modes of the specimens are presented in Figure 5.9. It can be observed that the numerically predicted load-deformation curves are in close agreement with the experimental ones. The anisotropic FE models significantly improve the accuracy of the predictions, as evidenced by the load-displacement curves especially for the models of specimens S1, S2, D2, D3 and D6 with respect to the experimental response. For the rest of the specimens it seems the models employing isotropic material response with longitudinal material properties display the closest agreement with the test results. It should be noted that there is a discrepancy in the prediction of the initial stiffness of specimen S3 and ultimate force of S6, as the experimental stiffness appears significantly lower than the numerically predicted one for S3 and the experimental ultimate force is considerably higher than the numerically predicted ultimate force. These are attributed to a 3 mm gap between the ends of the T-stub and the rigid plate to which it was bolted due to welding induced thermal distortion of the specimen, which led to a delay in the development of the prying forces. This effect was not properly reflected in the FE models however Tartaglia *et al.* (2020) examined the influence of constructional imperfections i.e. misalignment of the web and flange bowing namely non-perpendicularity between the web and flange due to the initial curve and concluded they have no significant effect on the predicted strength of the T-stubs.

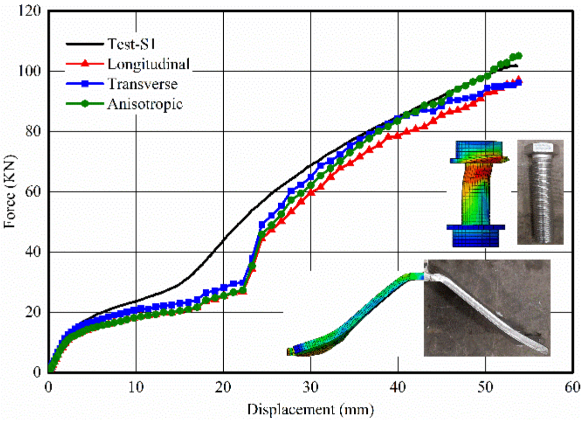

(a) S1

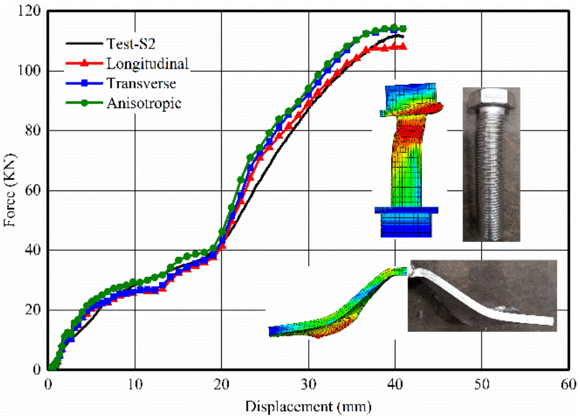

(b) S2

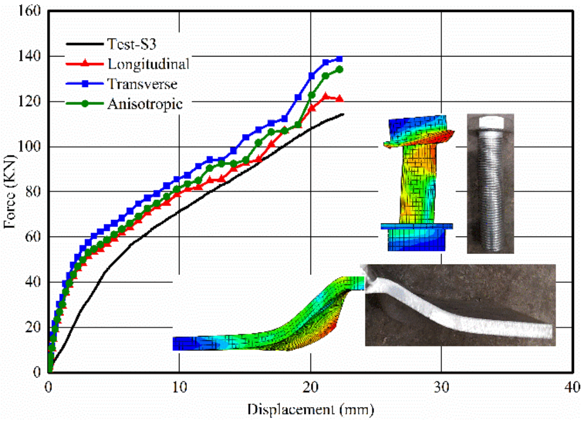

(c) S3

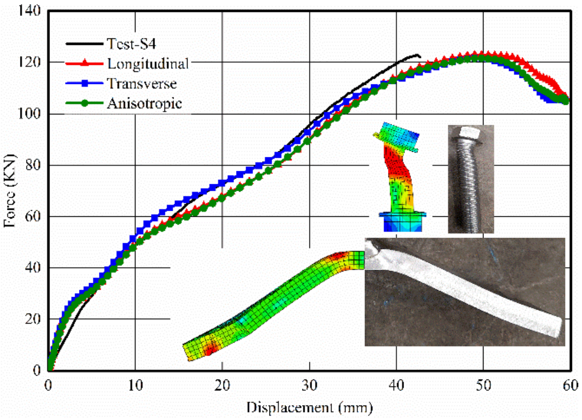

(d) S4

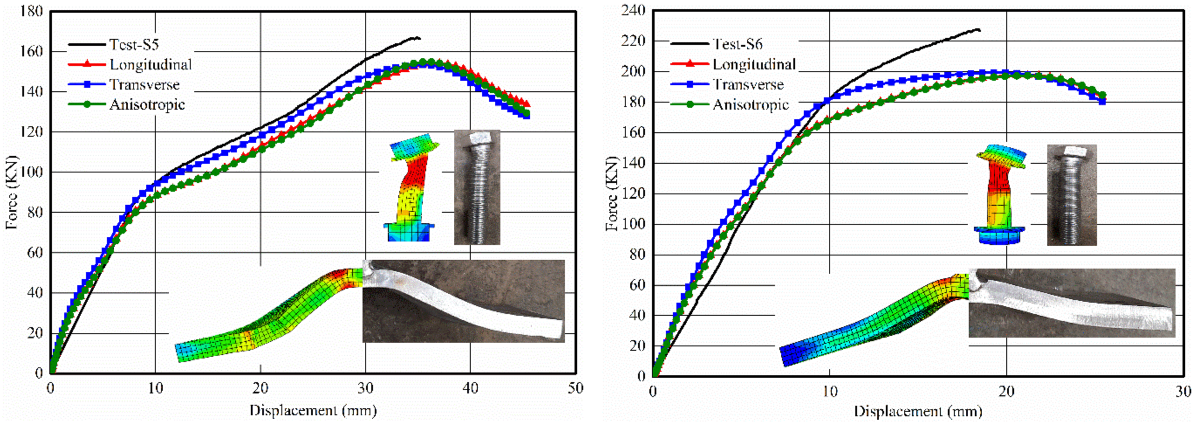

(e) S5 (f) S6

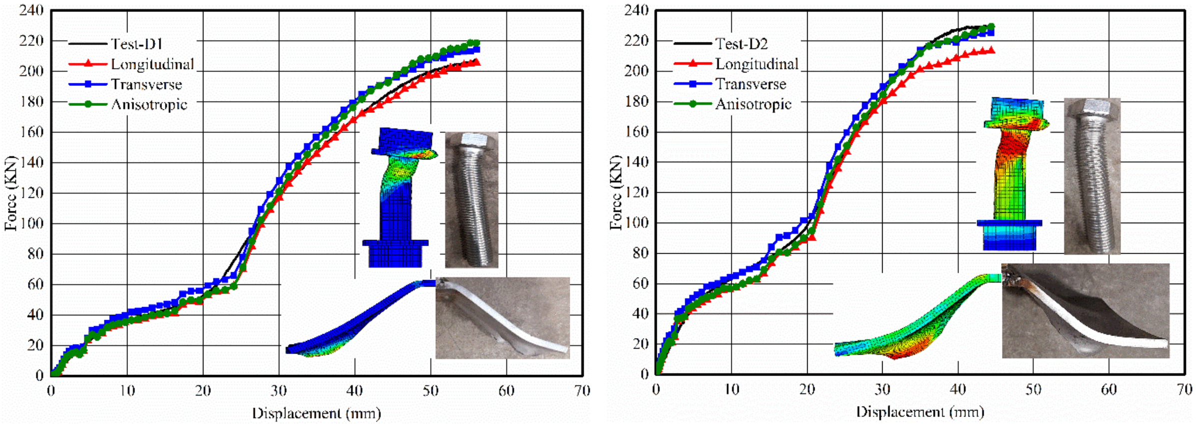

(g) D1 (h) D2

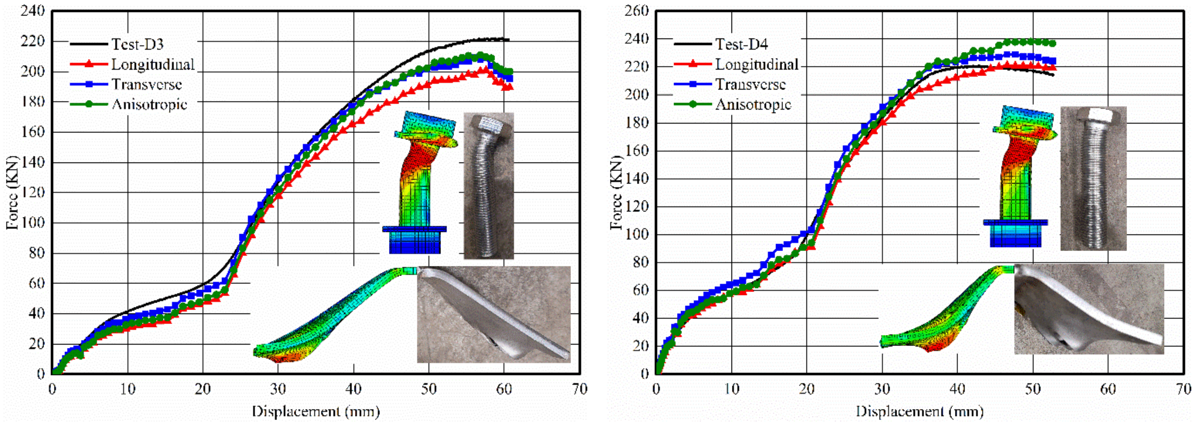

(i) D3 (j) D4

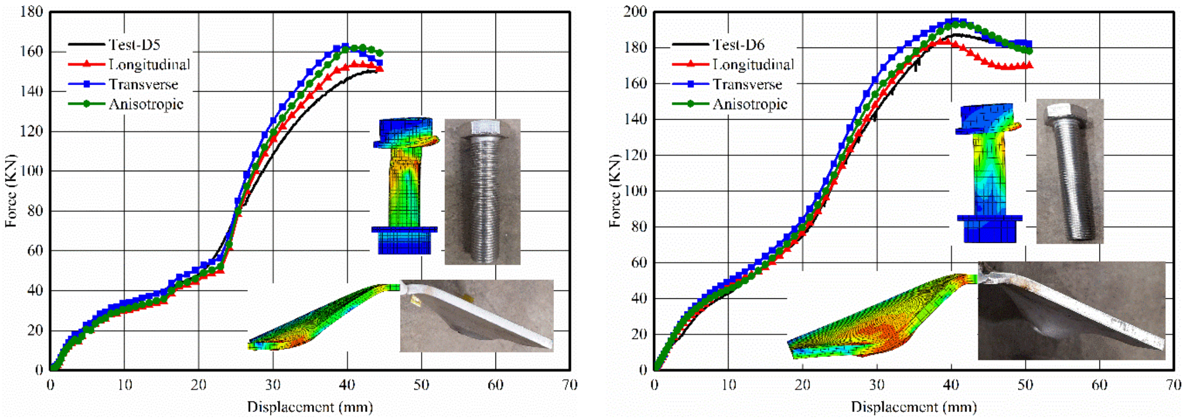

(k) D5

(l) D6

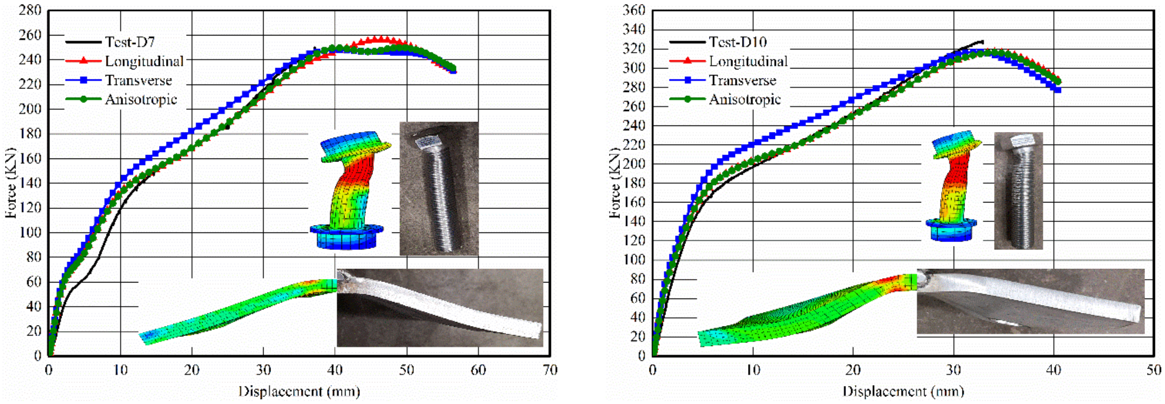

(m) D7

(n) D10

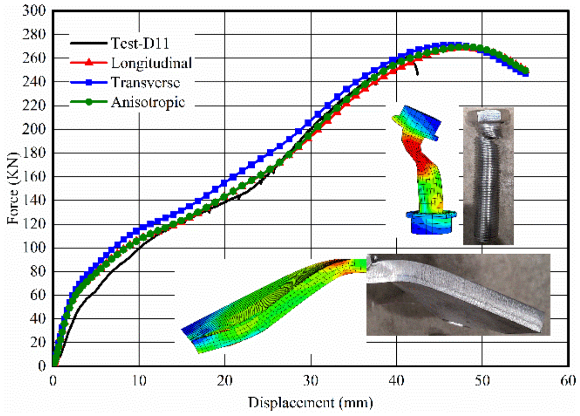

(o) D11

Figure 5.9: The force-displacement curves and the failure modes of the specimens.

The numerically predicted plastic and ultimate resistances F_{pl} and F_u for all T-stubs, as well as the displacement at ultimate resistance Δ_u are reported in Table 5.15 for all three material modelling assumptions. The ratios of the corresponding numerical over experimental ratios are reported in Table 5.16. The average values of the numerical over experimental plastic resistance ratios $F_{pl,FE}$ / $F_{pl,Exp}$ are 0.93, 1.05 and 0.96 with coefficients of variation (COV) of 0.07, 0.08 and 0.06 for the FE models assuming isotropic longitudinal, isotropic transverse and anisotropic material response respectively. In terms of the ultimate load, the corresponding ratios are 0.97, 1.01 and 1.01 with COV of 0.05, 0.08 and 0.08, respectively. The respective mean ratios of the numerical over experimental displacement at ultimate load ratios $\Delta_{u,FE}$ / $\Delta_{u,Exp}$ are 1.05, 1.03 and 1.07 with COV of 0.09, 0.07 and 0.10.

Hence it can be concluded that accounting for material anisotropy when modelling ferritic stainless steel T-stubs is necessary to obtain accurate FE predictions of the structural response. This is expected since in the vicinity of the bolt holes, T-stubs are subjected to a multi-axial stress state hence the behaviour of the material in all directions needs to be considered in the numerical model. If data on material anisotropy are not available, the longitudinal material properties should be adopted to ensure conservative strength predictions.

Table 5.15: Experimental and numerical results for plastic resistance, ultimate resistance and displacement at ultimate resistance.

#	Test results			FE results								
				Longitudinal			Transverse			Anisotropic		
	$F_{Pl,Exp}$ (kN)	$F_{u,Exp}$ (kN)	$\Delta_{u,Exp}$ (mm)	$F_{Pl,FE}$ (kN)	$F_{u,FE}$ (kN)	$\Delta_{u,FE}$ (mm)	$F_{Pl,FE}$ (kN)	$F_{u,FE}$ (kN)	$\Delta_{u,FE}$ (mm)	$F_{Pl,FE}$ (kN)	$F_{u,FE}$ (kN)	$\Delta_{u,FE}$ (mm)
S1	16.8	102.1	54.0	14.5	97.1	53.8	16.0	96.3	53.8	15.0	96.3	53.8
S2	22.3	111.8	41.0	20.0	108.0	39.9	21.0	114.1	40.9	23.0	114.1	39.9
S3	47.0	114.3	22.5	46.0	122.0	21.1	53.0	138.9	22.2	47.0	138.9	22.2
S4	48.0	122.7	42.2	45.0	122.8	49.8	51.0	121.6	49.0	47.0	121.5	49.8
S5	93.5	167.0	34.9	81.0	154.2	37.0	88.0	153.5	35.4	82.0	154.9	36.3
S6	188.0	227.7	18.4	166.0	197.8	21.2	184.0	199.4	19.3	167.0	197.3	21.2
D1	31.0	207.5	55.8	29.5	205.7	56.1	33.5	214.4	56.1	30.0	214.4	55.3
D2	46.0	229.9	43.5	40.0	213.3	44.4	49.5	225.4	44.4	44.5	225.4	44.4
D3	37.5	222.1	59.7	31.2	200.9	57.6	34.0	209.2	56.1	32.2	209.2	56.8
D4	40.0	220.8	42.8	37.0	221.2	46.6	46.3	229.0	47.7	39.8	229.0	49.7
D5	29.0	150.5	43.0	27.0	153.6	40.9	32.2	162.8	39.8	28.0	162.8	42.1
D6	36.0	187.5	41.2	33.0	183.1	38.5	41.0	195.1	40.6	36.0	192.8	41.6
D7	127.0	249.9	37.2	128.0	256.2	46.4	136.0	248.0	40.6	127.0	249.9	49.0
D10	170.0	328.1	32.9	178.0	316.7	34.1	198.0	316.9	32.0	177.0	316.2	34.1
D11	92.0	260.9	41.1	93.0	268.7	48.1	98.0	271.2	46.4	92.0	269.6	48.1

Table 5.16: Numerical over experimental FE results for various material modelling assumptions.

#	Longitudinal			Transverse			Anisotropic		
	$F_{Pl,FE}$ / $F_{Pl,Exp}$	$F_{u,FE}$ / $F_{u,Exp}$	$\Delta_{u,FE}$ / $\Delta_{u,Exp}$	$F_{Pl,FE}$ / $F_{Pl,Exp}$	$F_{u,FE}$ / $F_{u,Exp}$	$\Delta_{u,FE}$ / $\Delta_{u,Exp}$	$F_{Pl,FE}$ / $F_{Pl,Exp}$	$F_{u,FE}$ / $F_{u,Exp}$	$\Delta_{u,FE}$ / $\Delta_{u,Exp}$
S1	0.86	0.95	1.00	0.95	0.94	1.00	0.89	0.94	1.00
S2	0.89	0.96	0.97	0.94	1.02	1.00	1.03	1.02	0.97
S3	0.98	1.06	0.93	1.12	1.22	0.99	1.00	1.22	0.99
S4	0.93	1.00	1.18	1.06	0.99	1.16	0.98	0.99	1.18
S5	0.87	0.93	1.06	0.94	0.92	1.02	0.88	0.93	1.04
S6	0.88	0.87	1.15	0.98	0.88	1.05	0.88	0.87	1.15
D1	0.95	0.99	1.01	1.08	1.03	1.01	0.97	1.03	0.99
D2	0.87	0.93	1.02	1.08	0.98	1.02	0.97	0.98	1.02
D3	0.83	0.90	0.96	0.91	0.94	0.94	0.86	0.94	0.95
D4	0.93	1.00	1.09	1.16	1.04	1.11	0.99	1.04	1.16
D5	0.93	1.02	0.95	1.11	1.09	0.93	0.96	1.09	0.98
D6	0.92	0.98	0.93	1.14	1.04	0.99	1.00	1.03	1.01
D7	1.01	1.02	1.25	1.08	0.99	1.09	1.00	1.00	1.32
D10	1.04	0.96	1.04	1.16	0.96	0.97	1.04	0.96	1.04
D11	1.01	1.03	1.18	1.06	1.04	1.12	1.00	1.03	1.18
Average	0.93	0.97	1.05	1.05	1.01	1.03	0.96	1.01	1.07
COV	0.07	0.05	0.09	0.08	0.08	0.07	0.06	0.08	0.10

In addition, in all cases, the T-stubs failed in mode 1 with the formation of 4 yield lines and significant plastic deformation. In the failure modes shown in Figure 5.9, the flexural deformations of the flanges are not pronounced since the photos were taken at the end of the test and the membrane action developed in the T-stub flanges dominates the observed plastic deformation. A close-up of the failure modes of specimens S1, D3, D5, D6 and D11 are shown in Figure 5.10 where the numerically obtained equivalent plastic strain at the end of the analysis is also depicted for these specimens. The specimen S1 ultimately failed by bearing of the T-stub flange plate since at high deformations the bolts anchoring the membrane action of the T-stub flanges were subjected to high levels of shear forces. In specimen D3, the initiation of a crack is clearly seen at the bolt hole due to high levels of plastic strain, whilst D5 and D6 ultimately failed by fracture of the flange in-between the bolts due to the strain concentration between the bolt holes. Specimen D11 failed by the fracture of the bolts and the strain concentration of the bolts in the FE model agree well with the tested T-stub. All these failure types were accurately predicted by the developed FE models where the locations of accumulation of plastic strain coincides with the location where the cracks were observed during the tests.

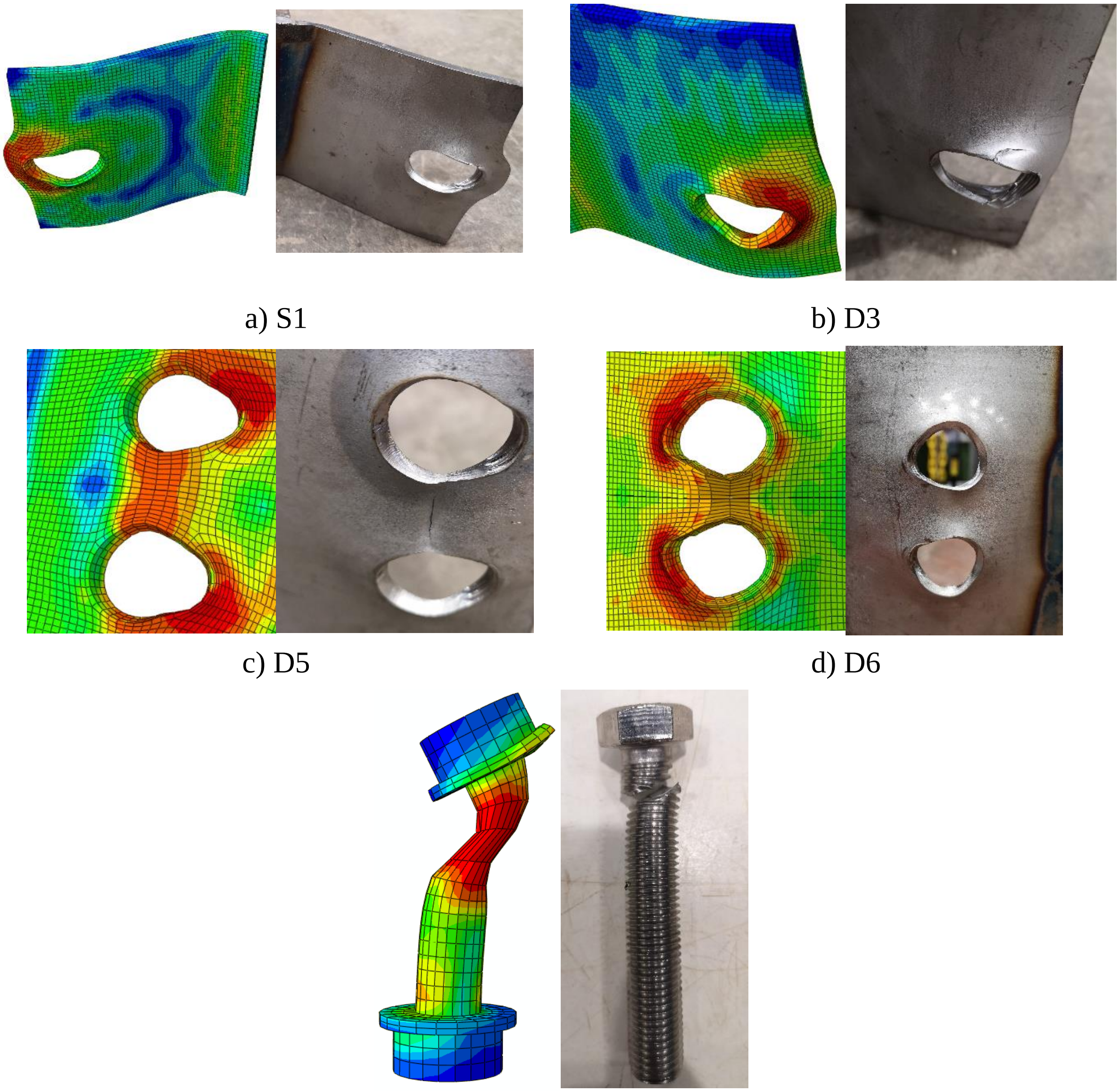

a) S1

b) D3

c) D5

d) D6

e) D11

Figure 5.10: Experimental and numerical failure modes of a) S1, b) D3, c) D5, d) D6 and e) D11.

5.3.4.2. Stress distribution through the flange thickness

Having demonstrated the ability of the FE models to replicate the experimentally observed response, the validated models are utilised to extract valuable information regarding the stress distribution through the flange thickness at specific load levels. In Figure 5.11, the stress distribution through the flange thickness is reported at three sections along the length of the T-stubs, at the end of the fillet weld as shown in the relevant figures. The selected locations include the middle of the T-stub, the end of the T-stub and the location of the bolt. The reported normal stresses are oriented perpendicular to the web, have been normalised by the longitudinal $\sigma_{0.2}$ and are plotted on the x-axis, whilst the through thickness locations at which they occur are on the y-axis. For each of the three locations along the length of the T-stub sections where the stress values are reported, two load levels are considered, namely the load corresponding to the plastic resistance of the T-stub $F_{pl,FE}$ and the ultimate load $F_{u,FE}$ with the stress distribution curves are denoted with solid and dotted lines, respectively. It should be noted that to obtain local stress values with a sufficient accuracy, the models from which the stress distributions were extracted employed 4 elements through the thickness, despite, as earlier stated, three elements through the thickness suffice to obtain an accurate prediction of the global response of the T-stubs.

In Figure 5.11, for all models, it can be observed that at the attainment of F_{pl} the stress distributions in all locations are symmetric with equal and opposite stress values occurring at the top and bottom nodes of the T-stubs, thus confirming that the main load carrying mechanism up to the attainment of the plastic resistance of the section is bending. In all models, the T-stub section at the bolt location experiences higher stress values (red curves) compared to the other sections, whilst the lowest stress values are observed at the free ends of the T-stubs (green curves) with the intermediate locations (blue curves) being in-between depending on the bolt arrangement. In models with large distances between the bolt axis and the T-stub web (large m values) like the models for specimens D3 and D5, the edge of the T-stub experiences significantly lower stresses, which are predominantly elastic, whilst at the same load level the sections at the bolt axis are subjected to inelastic stresses at or above the nominal yield stress. For models D2 and D4 a more uniform stress distribution at the plastic load level can be observed along the T-stubs. For all models, at the attainment of the plastic resistance of the T-stub, the maximum recorded stress is approximately 25% higher than the nominal yield stress, a value that corresponds to the ultimate tensile stress in the longitudinal direction as reported in Chapter 4. In a recent study on austenitic and duplex stainless steel T-stubs (Yuan *et al.*, 2020) the respective value was 100% higher than the nominal yield stress, due to the significantly more favourable strain-hardening characteristics that these grades exhibit compared to ferritic stainless steel.

An interesting observation can be made with regards to the stress distribution at the ultimate load (dotted curves in Figure 5.11). In all cases the dotted lines shift to the right and a clear asymmetry emerges; the T-stubs are no longer working predominantly in flexure; they are carrying simultaneously bending moment and tension due to membrane action. Hence the neutral axis of the sections can be seen to have moved towards the bottom (compression side) of the T-stub. This observation confirms the change of the load transfer mechanism form flexural to membrane at high deformations.

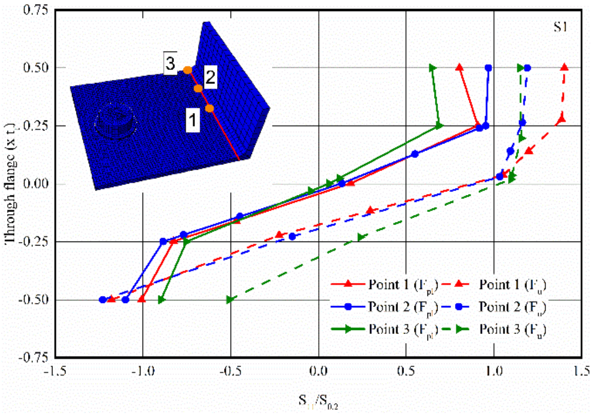

(a) S1

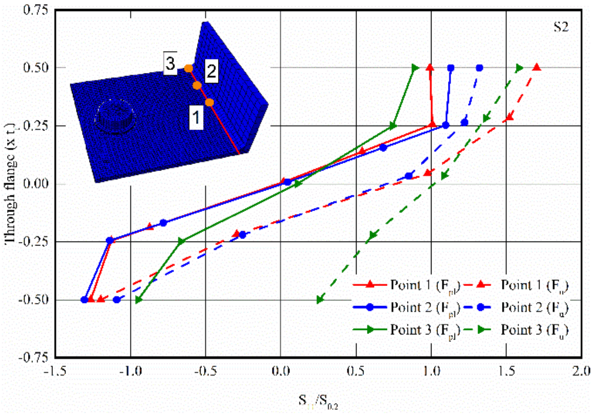

(b) S2

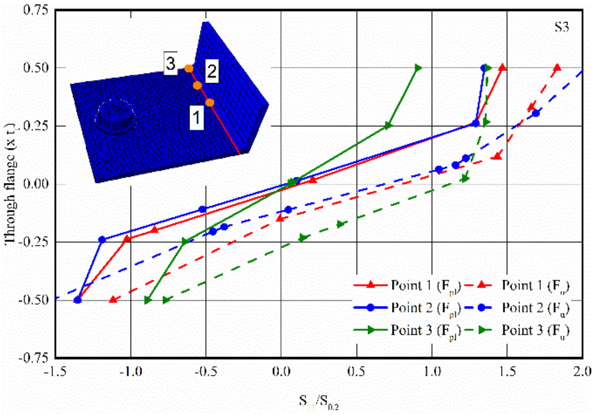

(c) S3

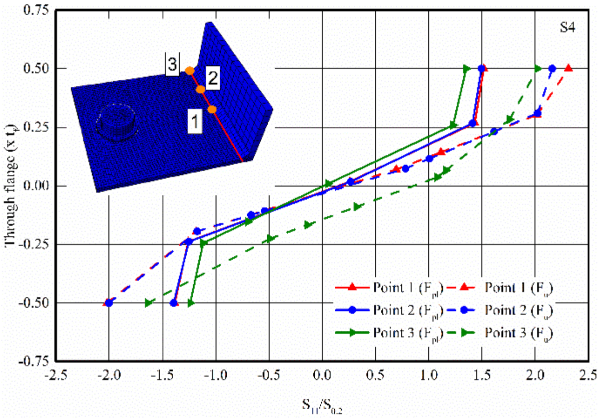

(d) S4

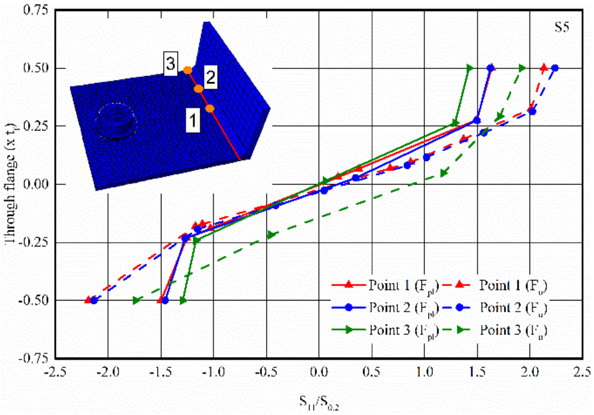

(e) S5

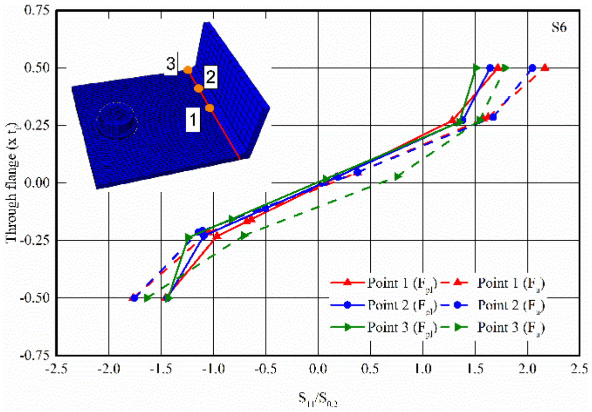

(f) S6

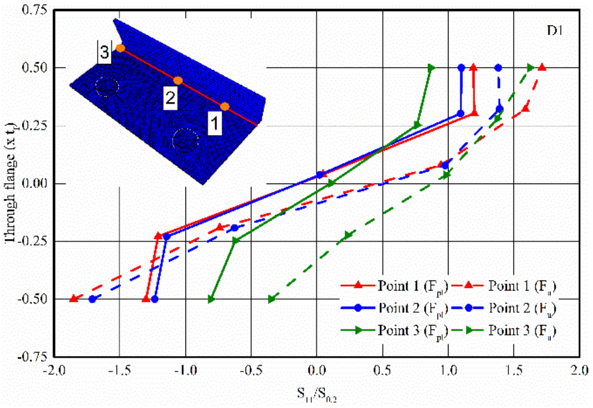

(g) D1

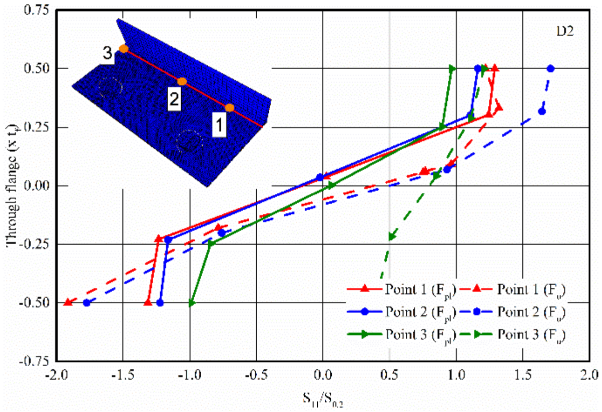

(h) D2

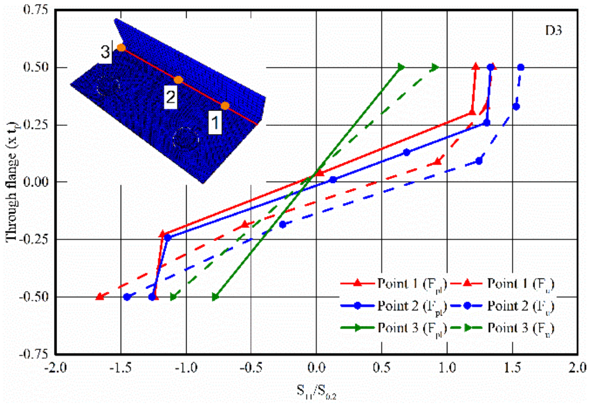

(i) D3

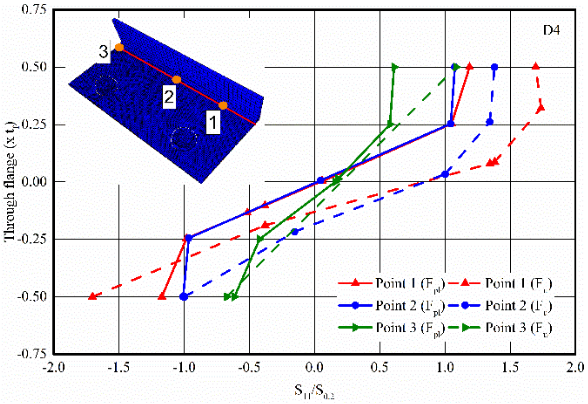

(j) D4

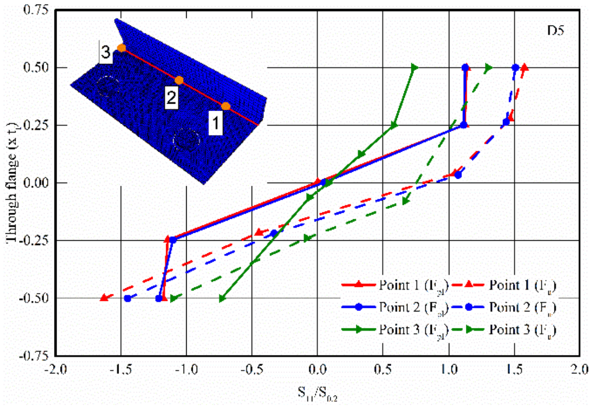

(k) D5

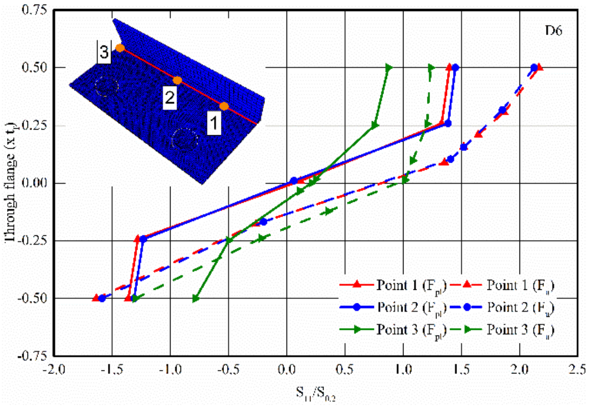

(l) D6

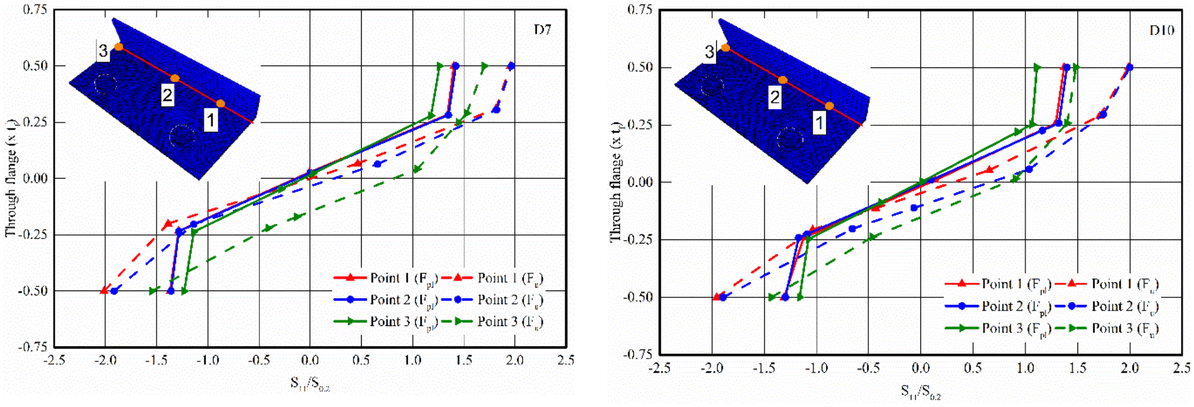

(m) D7 (n) D10

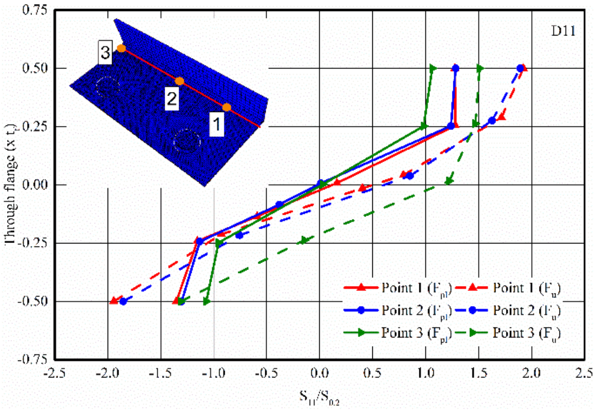

(o) D11

Figure 5.11: The stress distribution through the flange plate thickness.

5.3.4.3 Results of incorporating the bolt fracture

Bolt fracture was included to the FE modelling of S4, S5, D7, D10 and D11 which exhibited severe damage of the bolts using the ductile damage model in ABAQUS. The plastic strain at damage initiation was defined as a function of stress triaxiality according to Equation (5.1), whilst no damage evolution was considered. Hence the time increment at which the damage initiation criterion was fulfilled was obtained and at this time increment the force-displacement curves truncated, as evidenced by the sudden drop exhibited by the red curves in Figure 5.12. This approach eliminates the need for explicit fracture modelling and allows the experimental curves (incoporating damage) to be compared to a modelling approach effectively assuming instantaneous fracture (red curves in Figure 5.12). The force-displacement curves of the numerical models are presented in Figure 5.12, with the blue lines not accounting for bolt fracture and the red ones corresponding to instant fracture when the relevant plastic strain is reached. The results show that the assumption of instant fracture results in conservative results and the final part of the tested curves can not be captured accurately, whilst not considering bolt fracture (blue lines) over estimates the deformations that the specimens can reach and hence the ductility. Hence, the necessity of including damage propogation into the FE model to obtain the load and displacement at failure is highlighted, whilst for design purposes, where a reasonable level of conservatism is necessary, assuming instant fracture is warranted.

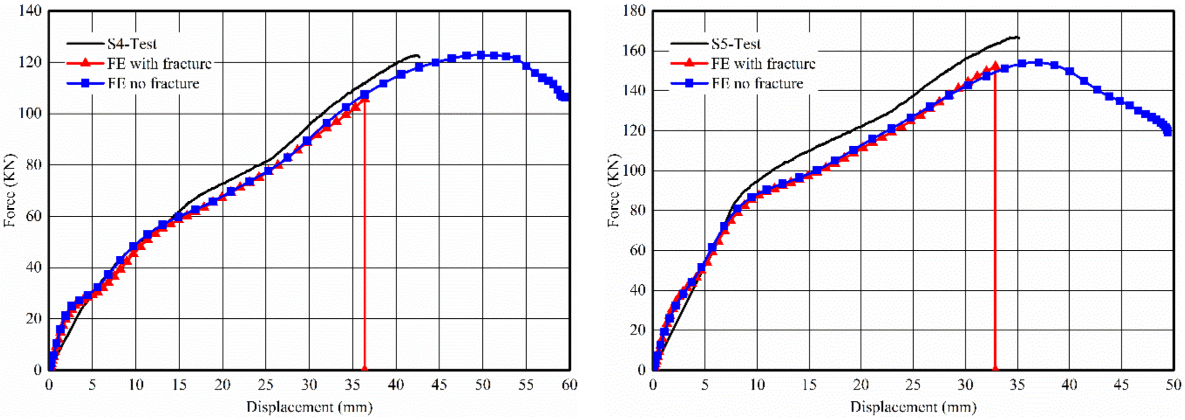

(a) S4 (b) S5

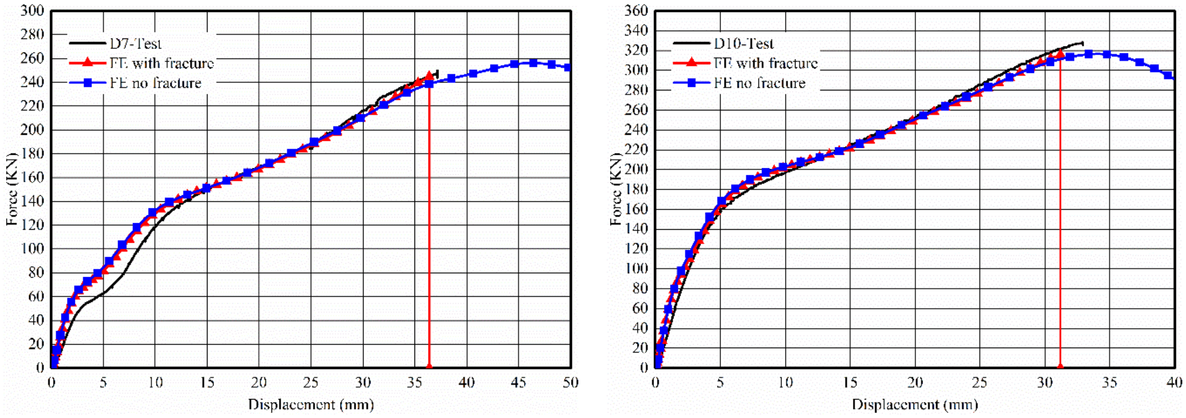

(c) D7 (d) D10

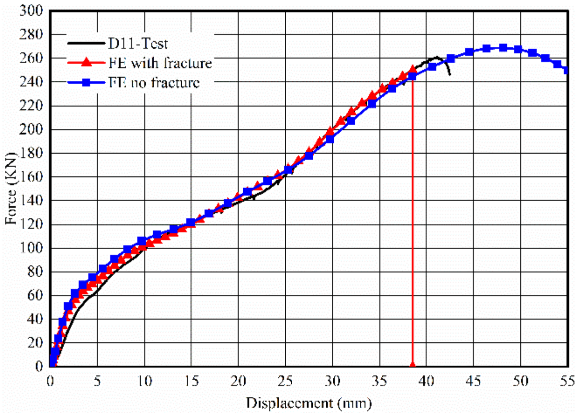

(e) D11

Figure 5.12: The force-displacement curves of FE models with fracture model.

5.4. Parametric study

A parametric study has been conducted in the scope of this project with the aim of quantifying membrane effects and assessing the applicability of relevant predictive equations as discussed in Chapter 6. The modelling assumptions for the parametric analysis follow the ones discussed previously in the validation of the numerical models in Sections 5.2 and 5.3. The parametric studies consider bolted T-stub specimens with a single bolt row only.

5.4.1. FE modelling and assumptions

The FE model for the parametric study of stainless steel bolted T-stubs is constructed based on section 5.3.1 and Figure 5.7. The dynamic explicit solver was utilized as discussed in section 5.3.1 and boundary conditions and loading mechanism remained unchanged. A total of 36 FE models which were created based on the selected parameters in Table 5.17 were performed. The adopted material properties for the austenitic and duplex stainless steels are those reported in Table 5.2, whilst for the ferritic material the properties reported in Table 5.13 for 5mm thick plates are utilised. The predicted plastic and ultimate resistances and corresponding displacements are reported in Table 5.18. The comparison of predicted numerical results with EN 1993-1-8 (2005) is given Chapter 6 in detail, where the membrane effect at high deformations are also quantified and discussed.

Table 5.17: Geometric dimensions of the specimens for the parametric study.

Material	Bolt	$t_f = t_w$	Width	m	n	d_b	h_f
Austenitic	A4-80	3	$b_f = 220$	25	75	16	6
Duplex		6		50	50		
Ferritic		9		75	25		
		12					

Table 5.18: Parametric analysis results of stainless steel bolted T-stubs.

#	Material	n	t_f	m	b_{eff}	b_f	F_{pl}	Δ_{pl}	F_u	Δ_u
1	Austenitic	75	3	25	100	220	24	1.1	103.90	46.69
2	Austenitic	50	3	50	100	220	8.5	1.9	113.69	67.26
3	Austenitic	25	3	75	100	220	4.5	3.2	102.02	72.22
4	Austenitic	75	6	25	100	220	77	0.7	172.63	26.20
5	Austenitic	50	6	50	100	220	33	1.5	132.15	36.28
6	Austenitic	25	6	75	100	220	17	1.2	108.51	49.58
7	Austenitic	75	9	25	100	220	142	0.5	197.59	14.18
8	Austenitic	50	9	50	100	220	71	1	151.87	30.24
9	Austenitic	25	9	75	100	220	39	1.2	111.33	41.25
10	Austenitic	75	12	25	100	220	190	0.3	206.80	8.53
11	Austenitic	50	12	50	100	220	129	0.8	163.15	18.66
12	Austenitic	25	12	75	100	220	77	1.2	120.83	38.49
13	Duplex	75	3	25	100	220	33	1	99.72	30.24
14	Duplex	50	3	50	100	220	14	2.4	108.05	64.86
15	Duplex	25	3	75	100	220	8	3.8	83.88	60.88
16	Duplex	75	6	25	100	220	104	0.4	176.69	22.33
17	Duplex	50	6	50	100	220	48	1.5	137.03	32.99
18	Duplex	25	6	75	100	220	29	2.6	104.19	42.92
19	Duplex	75	9	25	100	220	188	0.4	204.17	8.53
20	Duplex	50	9	50	100	220	108	1.8	157.67	24.89
21	Duplex	25	9	75	100	220	68	2	113.74	41.25
22	Duplex	75	12	25	100	220	208	0.9	219.63	6.97
23	Duplex	50	12	50	100	220	157	1.2	170.71	14.18
24	Duplex	25	12	75	100	220	103	2.3	126.09	41.24
25	Ferritic	75	3	25	100	220	23.5	0.6	74.09	53.15
26	Ferritic	50	3	50	100	220	10	2	76.56	72.55
27	Ferritic	25	3	75	100	220	5.9	3.8	55.96	63.03
28	Ferritic	75	6	25	100	220	78	0.6	158.37	28.87
29	Ferritic	50	6	50	100	220	33.5	1	132.87	41.24
30	Ferritic	25	6	75	100	220	20.5	1.8	121.24	77.95
31	Ferritic	75	9	25	100	220	155	0.5	193.88	15.26
32	Ferritic	50	9	50	100	220	77	1	147.24	31.45
33	Ferritic	25	9	75	100	220	48	1.3	111.21	37.92
34	Ferritic	75	12	25	100	220	195	0.7	205.23	7.73
35	Ferritic	50	12	50	100	220	134	1.1	159.61	19.86
36	Ferritic	25	12	75	100	220	87	1.9	117.49	35.74

5.5. Conclusions

An advanced FE model was developed to simulate the overall behaviour of austenitic and duplex stainless steel bolted T-stubs in tension considering bolt fracture. Thereafter, the numerical simulation of the tests on T-stubs fabricated from EN 1.4003 ferritic stainless steel grade reported in Chapter 4 was performed herein. The numerical study generally details the development of an FE model, which considers the recorded material anisotropy and employs a quasi-static explicit dynamic solution scheme to overcome convergence difficulties. The validation was carried out by comparing the numerical to the experimental results in terms of plastic resistance, ultimate resistance and ultimate displacements, as well as overall load deformation response. Recommendations have been made for the best modelling applications and fundamental strategies for the explicitly modelling of bolt geometry and fracture were reported comprehensively. Parametric study was performed using single bolt row stainless steel T-stubs considering different geometric configurations and three main stainless steel material grades to study the effect of plate thickness, material grade, bolt spacing and flange width on the plastic resistance, ultimate capacity and ductility of joints as well as on the overall response. Following conclusions can be drawn in line with the results reported herein.

- Modelling of the bolt as smooth cylindrical with an effective cross-section area leads to accurate predictions in terms of the plastic force and ultimate force of the T-stubs. Furthermore, the weld toe of the T-stubs needs to be explicitly modelled as not considering it leads to inaccurate results.
- It can be concluded that using quadratic elements instead of linear elements has no significant effect on the obtained numerical ultimate resistance, however the plastic

resistance is less well-predicted when linear elements are employed. In addition, in numerical models using quadratic mesh, it was observed that after the ultimate load is reached, the force drop is sharper than the one with linear elements. The FE model with quadratic elements predicts the plastic force values more accurately and consistently. The mean values of $F_{pl, FEM}$ / $F_{pl, Exp}$ ratios for the type-3 are reported as 0.83 and 0.89 for linear and quadratic elements, respectively.

- The mean value of $F_{pl, FEM}$/ $F_{pl, Exp}$ was equal to 0.86 for the dynamic explicit analysis, which is much better than static with linear mesh configuration and slightly lower than static analysis with quadratic mesh. The mean value of the numerical over experimental ratio in terms of ultimate forces $F_{u, FEM}$/ $F_{u, Exp}$ was equal to 1.00 for all analysis types considered. Furthermore, both the static and the quasi-static explicit dynamic analysis procedure can simulate the stress distribution through the flange thickness accurately.
- The developed FE for the ferritic stainless steel T-stubs simulated the experimental behaviour accurately and failure modes have been predicted with excellent agreement. The effect of incorporating the material anisotropy into the FE model was studied and it was concluded that the plastic force predictions are very accurate and more consistent when material anisotropy is considered.
- The stress distribution through the thickness of the flange at various locations along the length of the T-stub models were obtained at load levels corresponding to the plastic and the ultimate resistance of the T-stub. The obtained results confirmed the observations made in the experimental studies by Yuan *et al.*, (2019) and Chapter 4 regarding the prevailing load transfer mechanism changing form flexural to membrane at high deformations.

Furthermore, the actual stress values at which the plastic resistance load is reached were found to be close to the ultimate tensile stress at the extreme fibres of the T-stubs. It is thus believed that the main source of overstrength observed for T-stubs is not the strain hardening at the developed yield lines but the membrane action (and strain hardening) occurring at high deformation values. This significant reserve strength may be important in enhancing the robustness of structures.

- The developed FE model which explicitly considers fracture provides accurate predictions for the available ductility and fracture of the stainless steel bolted T-stubs in tension. Finally, it was concluded that neglecting the propagation of damage in the FE models leads to conservative predictions for the displacement at fracture. Although the FE model is computationally less costly, it cannot accurately simulate the behaviour of the T-stubs near and after their peak resistance, however provides predictions with a reasonable level of conservatism which is suitable for design purposes.

CHAPTER 6

Design recommendations

6.1. Introduction

In this Chapter, the applicability of the design provisions of EN 1993-1-8 (2005) for the determination of the plastic resistance of stainless steel T-stubs is assessed on the basis of the experimental and numerical results reported herein and collated from the published literature. The provisions for stiffness of T-stubs are not considered given that the Young's modulus of carbon steel is similar to that of stainless steel and hence the material response of stainless steel is identical to that of carbon steel at low strains. Furthermore, it is well-known (Elflah *et al.* 2019 (a)) that the stiffness of joints heavily depends on the inherent imperfections and worksmanship during connection assembly thereby resulting in considerable scatter of the observed response even for nominally identical specimens. In addition to the plastic resistance, the influence of membrane actions, which develop at large deformations, on the structural response of T-stubs is examined. The applicability of predictive equations for the determination of the ultimate resistance of carbon steel T-stubs, recently proposed by Tartaglia *et al.* (2020), is assessed for stainless steel T-stubs. Based on the obtained results, conclusions are drawn and design recommendations are proposed.

6.2. EN 1993-1-8 design provisions for the plastic resistance F_{pl}

The expressions to predict the plastic resistances corresponding to the three failure modes identified in EN 1993-1-8 (2005) for stainless steel bolted T-stubs are given by Equations 6.1-6.3, where all symbols are defined in EN 1993-1-8 (2005).

$$\text{Type-1} \qquad F_{1,Rd} = \frac{(8n - 2e_w)M_{f,1,Rd}}{2mn - e_w(m+n)} \tag{6.1}$$

$$\text{Type-2} \qquad F_{2,Rd} = \frac{2M_{f,2,Rd} + n\Sigma F_{t,Rd}}{m+n} \tag{6.2}$$

$$\text{Type-3} \qquad F_{3,Rd} = \Sigma F_{t,Rd} \tag{6.3}$$

Furthermore, the theoretical relationship between the thickness squared (t_f^2) and plastic resistance of T-stubs is depicted in Figure 6.1. It can be observed that the resistance F_{pl} is proportional to t_f^2 for type 1 and type 2 failure modes, albeit with a different factor of proportionality, however, type-3 failure mechanism is not affected by any change in thickness since it only involves bolt failure.

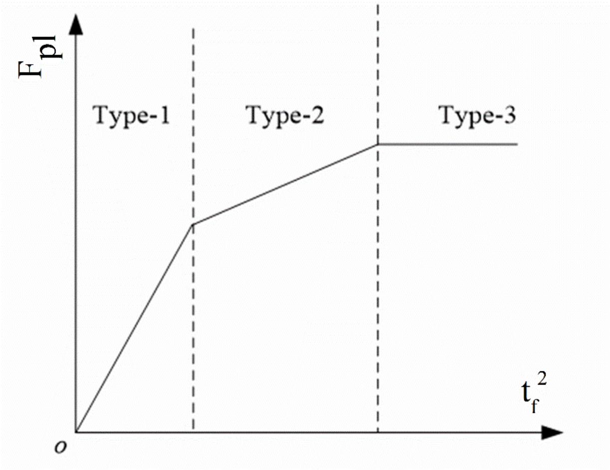

Figure 6.1: Theoretical relationship between F_{pl} and t_f^2 provided in EN 1993-1-8.

6.2.1. Assessment of EN 1993-1-8 for stainless steel T-stubs

All ferritic stainless steel T-stubs failed in mode 1 as predicted by Equation 6.1 and verified both by visual inspection and by the strain gauge readings which indicated large inelastic tensile and compressive strains consistent with the development of plastic hinges. Table 6.1 summarizes the design prediction of EN 1993-1-8 (2005) F_{EC3} according to Equation 6.1 based on the longitudinal tensile 0.2% proof stress, the ratio of the predicted over the experimental plastic resistance and the ultimate deformation at which failure occurred Δ_u, which is a measure of ductility.

The mean value of the predicted over the experimental plastic resistance F_{EC3}/F_{pl} for all specimens is 0.94 with a standard deviation of 0.15. Hence, on average the design predictions of EN1993-1-8 (2005) seem to provide a good estimation of the experimentally obtained plastic resistance, thus verifying the applicability of EN 1993-1-8 (2005) to ferritic stainless steel T-stubs. Based on the experimental results reported by Yuan *et al.* (2019; 2020) for austenitic (1.4301) and duplex (1.4462) stainless steel T-stubs, the applicability of the design provisions of EN 1993-1-8 (2005) for all three stainless steel grades can be assessed.

Table 6.1 Comparison of plastic forces predicted by EN-1993-1-8 with test results.

Specimen	Failure mode	F_{pl}	F_u	Δ_u	F_{EC3}	F_{EC3}/F_{pl}	F_u/F_{pl}	β
S1	1	16.8	102.1	54.0	12.4	0.74	6.1	0.08
S2	1	22.3	111.8	41.0	18.2	0.82	5.0	0.11
S3	1	47	114.3	22.5	41.3	0.88	2.4	0.23
S4	1	48	122.7	42.2	44.1	0.92	2.6	0.23
S5	1	93.5	167.0	34.9	64.8	0.69	1.8	0.46
S6	1	188	227.7	18.4	147.3	0.78	1.2	0.92
D1	1	31	207.5	55.8	31.4	1.01	6.7	0.08
D2	1	46	229.9	43.5	43.6	0.95	5.0	0.11
D3	1	37.5	222.1	59.7	31.4	0.84	5.9	0.09
D4	1	40	220.8	42.8	43.6	1.09	5.5	0.10
D5	1	29	150.5	43.0	31.4	1.08	5.2	0.07
D6	1	36	187.5	41.2	43.6	1.21	5.2	0.09
D7	1	127	249.9	37.2	111.9	0.88	2.0	0.31
D8	1	180	-	-	155.4	0.86	-	0.44
D9	1	105	244.2	42.1	111.9	1.07	2.3	0.26
D10	1	170	328.1	32.9	155.9	0.91	1.9	0.41
D11	1	92	260.9	41.1	111.9	1.22	2.8	0.22
					Mean	0.94		
					St. dev.	0.15		

Table 6.2 summarizes the mean value and standard deviation of the ratio of the predicted over the experimental plastic resistances F_{EC3}/F_{pl}. It can be clearly seen that the codified predictions are overly conservative for austenitic and duplex stainless steel T-stubs whilst they are reasonably accurate for ferritic stainless steel T-stubs. This is attributed to the inferior strain-hardening characteristics of ferritic stainless steels, which do not lead to a significant underestimation of the actual capacity of the T-stubs. In fact, the austenitic stainless steel T-stubs, which possess the most pronounced strain-hardening are the ones for which the design predictions are the most

conservative, whilst the ferritic ones are the least under-predicted with the duplex T-stubs lying in-between.

Table 6.2 Comparison of the mean ratios of $F_{pl,\,EC3}$ / $F_{pl,\,Exp}$ for all three stainless steel grades.

F_{EC3}/F_{pl}	Austenitic	Duplex	Ferritic
Mean	0.70	0.78	0.94
St.dev.	0.06	0.05	0.15

In addition, the parametric study reported in Chapter 5 are considered to assess the EN 1993-1-8 (2005) in terms of plastic resistance predictions. In Table 6.3 the ratio of the plastic resistance predicted based on EN 1993-1-8 (2005) over the numerical one is reported.

The average ratio was 0.80 with a standard deviation of 0.09. The EN 1993-1-8 (2005) provides conservative plastic resistance predictions for stainless steel bolted T-stubs failing in either mode 1 or mode 2.

Furthermore, the numerically obtained plastic force F_{pl} is plotted against the square of the flange thickness t_f^2 for each model of the parametric study in Figure 6.2. It can be concluded that the predicted failure modes based on EN 1993-1-8 (2005) agree well with the plastic force versus t_f^2 behaviours. The curves corresponding to an *m* distance of 50 mm and 75 mm are almost linear with respect to the thickness squared but the ones with 25 mm m distance display a second linear branch which is slightly affected by the change in flange thickness. The change in the slope of the curves corresponds to the change of the failure mode predictions based on EN 1993-1-8 (2005) from mode 1 to mode 2.

Table 6.3 Assessment of EN 1993-1-8 based on parametric study in Chapter 5 section 5.4.

#	Material	n	t_f	m	b_{eff}	b_f	F_{pl}	Δ_{pl}	F_u	Δ_u	Failure mode	$F_{pl,EC3}/F_{pl,FE}$
1	Austenitic	75	3	25	100	220	24	1.1	103.90	46.69	Mode 1	0.54
2	Austenitic	50	3	50	100	220	8.5	1.9	113.69	67.26	Mode 1	0.67
3	Austenitic	25	3	75	100	220	4.5	3.2	102.02	72.22	Mode 1	0.86
4	Austenitic	75	6	25	100	220	77	0.7	172.63	26.20	Mode 1	0.68
5	Austenitic	50	6	50	100	220	33	1.5	132.15	36.28	Mode 1	0.69
6	Austenitic	25	6	75	100	220	17	1.2	108.51	49.58	Mode 1	0.92
7	Austenitic	75	9	25	100	220	142	0.5	197.59	14.18	Mode 1	0.82
8	Austenitic	50	9	50	100	220	71	1	151.87	30.24	Mode 1	0.72
9	Austenitic	25	9	75	100	220	39	1.2	111.33	41.25	Mode 1	0.90
10	Austenitic	75	12	25	100	220	190	0.3	206.80	8.53	Mode 2	0.85
11	Austenitic	50	12	50	100	220	129	0.8	163.15	18.66	Mode 1	0.71
12	Austenitic	25	12	75	100	220	77	1.2	120.83	38.49	Mode 1	0.81
13	Duplex	75	3	25	100	220	33	1	99.72	30.24	Mode 1	0.65
14	Duplex	50	3	50	100	220	14	2.4	108.05	64.86	Mode 1	0.68
15	Duplex	25	3	75	100	220	8	3.8	83.88	60.88	Mode 1	0.81
16	Duplex	75	6	25	100	220	104	0.4	176.69	22.33	Mode 1	0.83
17	Duplex	50	6	50	100	220	48	1.5	137.03	32.99	Mode 1	0.79
18	Duplex	25	6	75	100	220	29	2.6	104.19	42.92	Mode 1	0.89
19	Duplex	75	9	25	100	220	188	0.4	204.17	8.53	Mode 2	0.85
20	Duplex	50	9	50	100	220	108	1.8	157.67	24.89	Mode 1	0.79
21	Duplex	25	9	75	100	220	68	2	113.74	41.25	Mode 1	0.85
22	Duplex	75	12	25	100	220	208	0.9	219.63	6.97	Mode 2	0.89
23	Duplex	50	12	50	100	220	157	1.2	170.71	14.18	Mode 2	0.93
24	Duplex	25	12	75	100	220	103	2.3	126.09	41.24	Mode 2	0.87
25	Ferritic	75	3	25	100	220	23.5	0.6	74.09	53.15	Mode 1	0.66
26	Ferritic	50	3	50	100	220	10	2	76.56	72.55	Mode 1	0.69
27	Ferritic	25	3	75	100	220	5.9	3.8	55.96	63.03	Mode 1	0.79
28	Ferritic	75	6	25	100	220	78	0.6	158.37	28.87	Mode 1	0.80
29	Ferritic	50	6	50	100	220	33.5	1	132.87	41.24	Mode 1	0.82
30	Ferritic	25	6	75	100	220	20.5	1.8	121.24	77.95	Mode 1	0.91
31	Ferritic	75	9	25	100	220	155	0.5	193.88	15.26	Mode 1	0.91
32	Ferritic	50	9	50	100	220	77	1	147.24	31.45	Mode 1	0.80
33	Ferritic	25	9	75	100	220	48	1.3	111.21	37.92	Mode 1	0.88
34	Ferritic	75	12	25	100	220	195	0.7	205.23	7.73	Mode 2	0.87
35	Ferritic	50	12	50	100	220	134	1.1	159.61	19.86	Mode 1	0.82
36	Ferritic	25	12	75	100	220	87	1.9	117.49	35.74	Mode 1	0.86
											Average	0.80
											St. dev	0.09

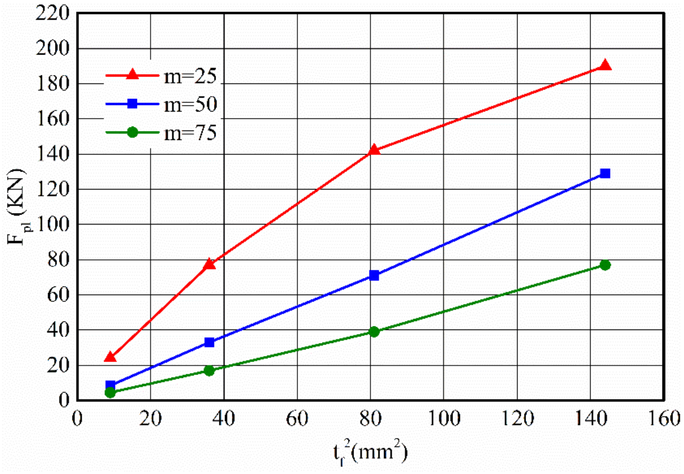

(a) Austenitic T-stubs

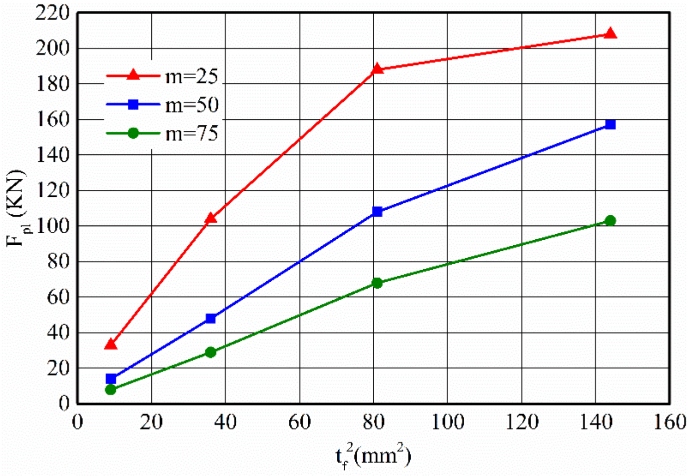

(b) Duplex T-stubs

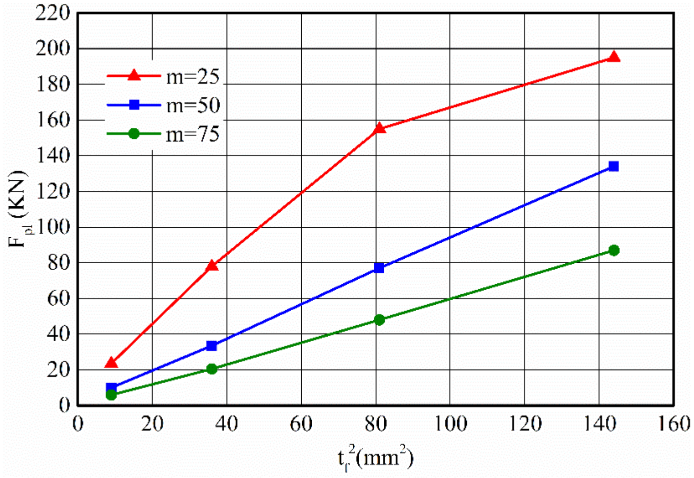

(c) Ferritic T-stubs

Figure 6.2: Relationships between F_{pl} and t_f^2 for parametric study.

6.2.2. Design proposals for stainless steel T-stubs

To provide more accurate resistance predictions for austenitic and duplex stainless steel T-stubs, Yuan *et al.* (2020) recently proposed design formula instead of using $\sigma_{0.2}$ in Equations 6.1-6.3, it is recommended to use $\sigma_{3.0}$. This proposal is based on the fact that stress distributions through the flange thickness corresponding to the plastic resistance were obtained very close to the $\sigma_{3.0}$ which was attributed to the significant strain hardening capacity of the stainless steel T-stubs (Yuan *et al.*, 2020). As reported in Table 6.1, the EN 1993-1-8 (2005) predictions for ferritic stainless steel T-stubs agree well with the test results due to the fact that the stress distributions at the attainment of plastic resistance which was represented in Chapter 5 and in Figure 5.11 are approximating the $\sigma_{0.2}$ of the ferritic stainless steel. Therefore, the proposed design formula by Yuan *et al.* (2020) was applied only to the parametric analysis results of austenitic and duplex grades. The predictions of ferritic stainless steel T-stubs were remained as unchanged. Table 6.4 reports the ratio of the plastic resistances predicted based on proposed formula and provided by FE models.

The average ratio was obtained as 0.93 with a standard deviation of 0.13 which is a significant improvement on the plastic resistance predictions of stainless steel T-stubs. It can be concluded that proposed design formula by Yuan *et al.* (2020) can provide more accurate plastic strength predictions for austenitic and duplex stainless steel and similar conclusions have been drawn by Yuan *et al.* (2020).

Table 6.4: Assessment of proposed design formula by Yuan *et al.* (2020).

#	Material	n	t_f	m	b_{eff}	b_f	F_{pl}	Δ_{pl}	F_u	Δ_u	Failure mode	$F_{pl,prop.}/F_{pl,FE}$
1	Austenitic	75	3	25	100	220	24	1.1	103.90	46.69	Mode 1	0.71
2	Austenitic	50	3	50	100	220	8.5	1.9	113.69	67.26	Mode 1	0.89
3	Austenitic	25	3	75	100	220	4.5	3.2	102.02	72.22	Mode 1	1.14
4	Austenitic	75	6	25	100	220	77	0.7	172.63	26.20	Mode 1	0.89
5	Austenitic	50	6	50	100	220	33	1.5	132.15	36.28	Mode 1	0.91
6	Austenitic	25	6	75	100	220	17	1.2	108.51	49.58	Mode 1	1.21
7	Austenitic	75	9	25	100	220	142	0.5	197.59	14.18	Mode 2	1.07
8	Austenitic	50	9	50	100	220	71	1	151.87	30.24	Mode 1	0.96
9	Austenitic	25	9	75	100	220	39	1.2	111.33	41.25	Mode 1	1.19
10	Austenitic	75	12	25	100	220	190	0.3	206.80	8.53	Mode 2	0.91
11	Austenitic	50	12	50	100	220	129	0.8	163.15	18.66	Mode 1	0.94
12	Austenitic	25	12	75	100	220	77	1.2	120.83	38.49	Mode 1	1.07
13	Duplex	75	3	25	100	220	33	1	99.72	30.24	Mode 1	0.84
14	Duplex	50	3	50	100	220	14	2.4	108.05	64.86	Mode 1	0.87
15	Duplex	25	3	75	100	220	8	3.8	83.88	60.88	Mode 1	1.04
16	Duplex	75	6	25	100	220	104	0.4	176.69	22.33	Mode 1	1.07
17	Duplex	50	6	50	100	220	48	1.5	137.03	32.99	Mode 1	1.02
18	Duplex	25	6	75	100	220	29	2.6	104.19	42.92	Mode 1	1.14
19	Duplex	75	9	25	100	220	188	0.4	204.17	8.53	Mode 2	0.90
20	Duplex	50	9	50	100	220	108	1.8	157.67	24.89	Mode 1	1.02
21	Duplex	25	9	75	100	220	68	2	113.74	41.25	Mode 1	1.10
22	Duplex	75	12	25	100	220	208	0.9	219.63	6.97	Mode 2	0.97
23	Duplex	50	12	50	100	220	157	1.2	170.71	14.18	Mode 2	0.99
24	Duplex	25	12	75	100	220	103	2.3	126.09	41.24	Mode 2	0.97
25	Ferritic	75	3	25	100	220	23.5	0.6	74.09	53.15	Mode 1	0.66
26	Ferritic	50	3	50	100	220	10	2	76.56	72.55	Mode 1	0.69
27	Ferritic	25	3	75	100	220	5.9	3.8	55.96	63.03	Mode 1	0.79
28	Ferritic	75	6	25	100	220	78	0.6	158.37	28.87	Mode 1	0.80
29	Ferritic	50	6	50	100	220	33.5	1	132.87	41.24	Mode 1	0.82
30	Ferritic	25	6	75	100	220	20.5	1.8	121.24	77.95	Mode 1	0.91
31	Ferritic	75	9	25	100	220	155	0.5	193.88	15.26	Mode 2	0.91
32	Ferritic	50	9	50	100	220	77	1	147.24	31.45	Mode 1	0.80
33	Ferritic	25	9	75	100	220	48	1.3	111.21	37.92	Mode 1	0.88
34	Ferritic	75	12	25	100	220	195	0.7	205.23	7.73	Mode 2	0.87
35	Ferritic	50	12	50	100	220	134	1.1	159.61	19.86	Mode 1	0.82
36	Ferritic	25	12	75	100	220	87	1.9	117.49	35.74	Mode 2	0.86
											Average	0.93
											St. dev	0.13

6.3. Prediction of ultimate resistance force F_u

Predictive equations for the determination of the ultimate force of a T-stub were recently proposed by Tartaglia *et al.* (2020) for carbon steel specimens. Its applicability to stainless steel T-stubs is assessed herein based on the reported experimental and numerical results. The proposed predictive equations are given by Equation 6.4-6.6 where $F_{T,1}$ and $F_{T,2}$ are the resistances for failure mode 1 and 2 according to EN 1993-1-8 (2005), whilst $F_{T,LD}$ is an additional force due to the development of membrane action at large deformations. The l_{eff} is the effective length of the T-stub, t_f is the flange thickness, f_u is the ultimate strength of the flange material, $F_{B,R}$ is the bearing resistance calculated based on EN 1993-1-8 (2005). The ratio between the imposed gap opening δ and the distance m is termed as α (Figure 6.3) and ψ is a reduction factor applied to the bolts, which accounts for their reduced tensile strength due to the simultaneous presence of shear force and bending moment.

$$F_T = F_{T,1} + F_{T,LD} \text{ for Mode 1} \tag{6.4}$$

$$F_T = F_{T,2} + F_{T,LD} \text{ for Mode 2} \tag{6.5}$$

$$F_{T,\,LD} = 2 \times \min\left(\frac{l_{eff}}{2} \times t_f \times f_u \times \sin\alpha ; F_{B,\,R} \times \tan\alpha ; F_{t,\,R} \times \psi\right) \tag{6.6}$$

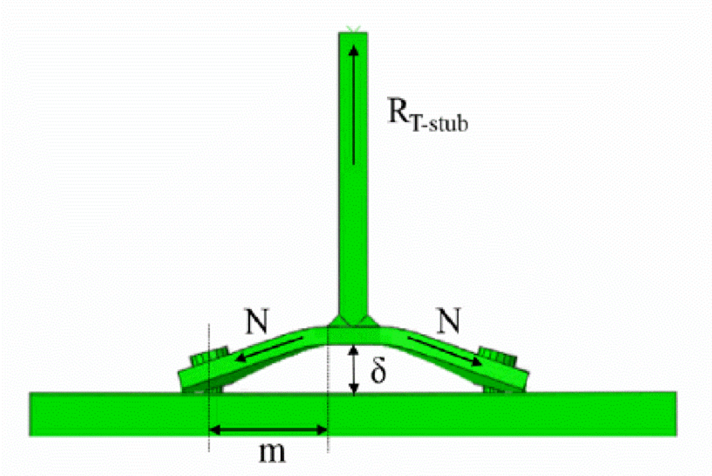

Figure 6.3: Definition of α in a bolted T-stub (Tartaglia *et al.,* 2020).

6.3.1. Determination of overstrength

The relationship between the overstrength and β coefficients was reported in Chapter 4 for the ferritic stainless steel bolted T-stubs. Similarly, the relationships between the overstrength which was previously defined as the ratio of ultimate and plastic resistance and β coefficients are depicted in Figure 6.4 for the parametric analysis results reported in Chapter 5. It was observed that the overstrength increases as β decreases consistently for three types of stainless steels. Similar conclusions were drawn based on the overstrength and β relationships for three stainless steel test results in Chapter 4. The trend in Figure 6.4 supports the idea that there is a clear and solid correlation between the overstrength ratio and β.

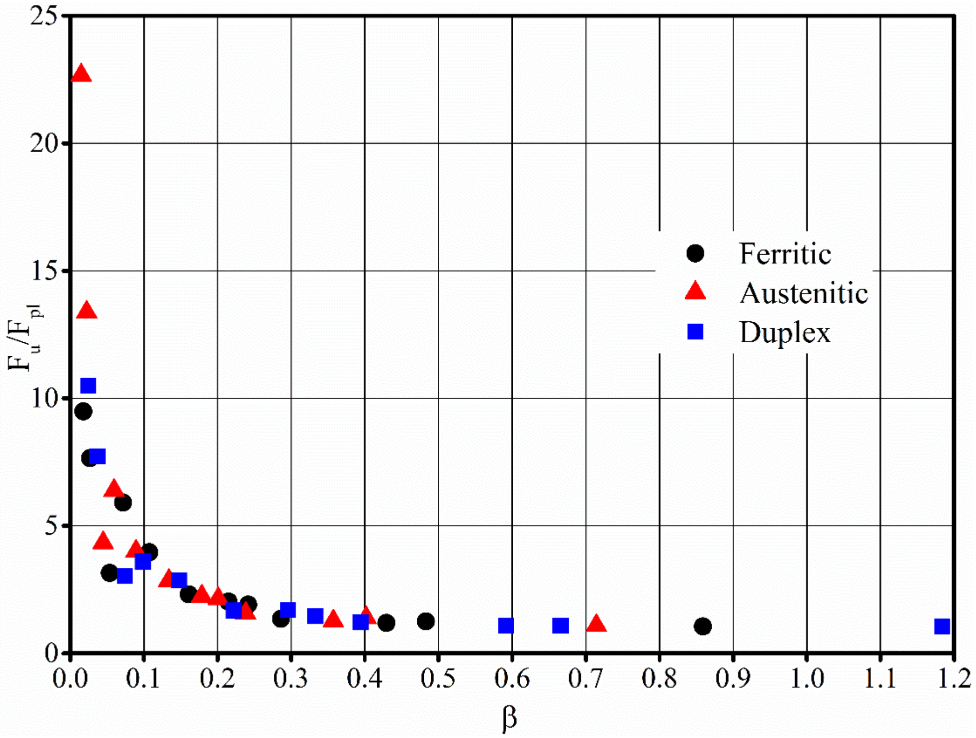

Figure 6.4: The overstrength ratio vs β relationship for parametric analysis.

6.3.2. Ultimate resistance predictions of stainless steel bolted T-stubs

6.3.2.1. Assessment of predictive equations using experimental results

The experimental test results on austenitic and duplex stainless steel bolted T-stubs under monotonic loading reported by Yuan *et al.* (2019; 2020) were used to validate the design formula proposed by Tartaglia *et al.* (2020) to predict the ultimate resistances. A total of 27 bolted T-stubs were considered with three different geometric configuration such as single and double bolt rows named as S and D, respectively. The experimental plastic and ultimate forces and predicted ultimate forces are represented in Table 6.5 with comparisons.

Table 6.5: Assessment of proposed design formula by Tartaglia *et al.* (2020) using available test data for austenitic and duplex stainless steel T-stubs.

#	Material	$F_{pl,Exp.}$	$F_{u, Exp.}$	β	$F_{T,pred.}$	$F_{T,pred} / F_{u,Exp.}$
S1	EN 1.4301	154	200.2	0.48	183.0	0.91
S2	EN 1.4301	85.8	106.8	0.60	112.4	1.05
S3	EN 1.4462	175.7	198.4	0.58	228.8	1.15
S4	EN 1.4462	93.9	108.9	0.61	124.5	1.14
S5	EN 1.4462	87.6	161.6	0.25	150.9	0.93
S6	EN 1.4301	61.8	104.3	0.34	92.1	0.88
S7	EN 1.4462	105.8	175.2	0.33	172.0	0.98
S8	EN 1.4301	131.2	188.0	0.36	157.8	0.84
S9	EN 1.4301	83.3	108.9	0.60	112.5	1.03
S10s	EN 1.4301	51.2	97.3	0.29	74.8	0.77
S11s	EN 1.4301	43.1	136.1	0.11	114.8	0.84
S12s	EN 1.4462	97.3	111.8	0.96	114.5	1.02
S13s	EN 1.4462	79.6	141.8	0.29	142.4	1.00
S14s	EN 1.4462	127.8	140.0	1.65	142.7	1.02
D1	EN 1.4301	211.1	367.5	0.30	286.2	0.78
D2	EN 1.4301	142.2	179.1	0.37	194.7	1.09
D3	EN 1.4462	97.8	260.9	0.18	234.7	0.90
D4	EN 1.4462	254.1	312.5	0.43	344.5	1.10
D5	EN 1.4462	338.7	382.5	0.56	402.5	1.05
D6	EN 1.4301	150.8	306.6	0.20	277.0	0.90
D7	EN 1.4301	104.4	174.3	0.27	167.6	0.96
D8	EN 1.4301	136.2	181.6	0.37	194.3	1.07
D9s	EN 1.4301	63.3	163.1	0.18	123.6	0.76
D10s	EN 1.4301	50.5	224.3	0.06	208.7	0.93
D11s	EN 1.4462	146.8	182.3	0.58	203.3	1.12
D12s	EN 1.4462	244.7	368.4	0.36	358.2	0.97
D13s	EN 1.4462	131.3	194.6	0.38	196.5	1.01
					Average	0.97
					St. dev.	0.11

The proposed expressions in Equations 6.4-6.6 by Tartaglia *et al.* (2020) provide accurate ultimate resistance predictions for austenitic and duplex stainless steel bolted T-stubs. The average ratio of predicted and experimental ultimate force is 0.97 with a standard deviation of 0.11.

In addition, the proposed design formula given in Equations 6.4-6.6 by Tartaglia *et al.* (2020) were employed herein to predict the ultimate resistance of tested ferritic stainless steel bolted T-stubs which were reported in Chapter 4. The predicted ultimate resistance forces are compared with the experimental results in Table 6.6.

Table 6.6: The comparison of the predicted and experimental ultimate resistance forces for ferritic stainless steel bolted T-stubs.

Specimen	Failure mode	$F_{u,\ test}$	β	$F_{u,\ pred.}$	$F_{u,\ pred.}/F_{u,\ test}$
S1	1	102.1	0.08	74.8	0.73
S2	1	111.8	0.11	97.3	0.87
S3	1	114.3	0.23	120.5	1.05
S4	1	122.7	0.23	123.2	1.00
S5	1	167.0	0.46	143.9	0.86
S6	1	227.7	0.92	226.4	0.99
D1	1	207.5	0.08	189.7	0.91
D2	1	229.9	0.11	201.9	0.88
D3	1	222.1	0.09	189.7	0.85
D4	1	220.8	0.10	201.9	0.91
D5	1	150.5	0.07	103.5	0.69
D6	1	187.5	0.09	201.9	1.08
D7	1	249.9	0.31	270.2	1.08
D8	1	-	0.44	-	-
D9	1	244.2	0.26	270.2	1.11
D10	1	328.1	0.41	313.7	0.96
D11	1	260.9	0.22	253.3	0.97
				Mean	0.93
				St. dev.	0.12

The mean value of the ratio of the predicted over the experimental ultimate force is 0.93 with a standard deviation of 0.12, and hence the proposed equations provide satisfactory and consistent predictions for the ultimate resistance of ferritic stainless steel bolted T-stubs failing in mode 1. It should be noted that for all test points considered in Table 6.6, failure was in mode 1, hence Equation 6.4 applied, whilst due to the geometry of the specimens, in all cases the membrane action $F_{T,LD}$ was limited by the strength of the bolts ψ, hence highlighting the importance of the bolt behaviour in the ultimate response of T-stubs.

6.3.2.2. Assessment of predictive equations based on numerical results

To determine the applicability of Equations 6.4-6.6 over a wider range of parameters and failure modes, the parametric numerical study results reported in Chapter 5 and section 5.4 were considered herein. In Table 6.7, the summary of the numerical and predicted ultimate resistance forces are given with the comparison ratios. The average ratio of the ultimate force predicted by the proposed formula over attained by numerical parametric analysis is 1.07 with a standard deviation of 0.19 which indicates a slight overprediction of ultimate resistances of FE models. The predictions agree well with the FE models overall for three types of stainless steels.

Furthermore, Table 6.8 summarizes the average comparison ratios of ultimate resistances including a combination of all the results which were used for validation of predictive equations. The average comparison ratio of the combined experimental and numerical results is 1.01 with a standard deviation of 0.20 which indicates that the proposed equations provide significantly accurate ultimate force predictions for all three stainless steel grade bolted T-stubs.

Table 6.7: Assessment of proposed design formula by Tartaglia *et al.* (2020) using parametric analysis results.

#	Material	n	t_f	m	b_{eff}	b_f	F_u	Δ_u	Failure mode	β	$F_{u,\ pred.}$	$F_{u,pred}/F_{u,FE}$
1	Austenitic	75	3	25	100	220	103.90	46.69	Mode 1	0.04	100.92	0.97
2	Austenitic	50	3	50	100	220	113.69	67.26	Mode 1	0.02	93.64	0.82
3	Austenitic	25	3	75	100	220	102.02	72.22	Mode 1	0.01	80.88	0.79
4	Austenitic	75	6	25	100	220	172.63	26.20	Mode 1	0.18	139.91	0.81
5	Austenitic	50	6	50	100	220	132.15	36.28	Mode 1	0.09	110.78	0.84
6	Austenitic	25	6	75	100	220	108.51	49.58	Mode 1	0.06	103.48	0.95
7	Austenitic	75	9	25	100	220	197.59	14.18	Mode 2	0.40	204.90	1.04
8	Austenitic	50	9	50	100	220	151.87	30.24	Mode 1	0.20	139.36	0.92
9	Austenitic	25	9	75	100	220	111.33	41.25	Mode 1	0.13	122.93	1.10
10	Austenitic	75	12	25	100	220	206.80	8.53	Mode 2	0.71	249.41	1.21
11	Austenitic	50	12	50	100	220	163.15	18.66	Mode 1	0.36	179.36	1.10
12	Austenitic	25	12	75	100	220	120.83	38.49	Mode 1	0.24	150.17	1.24
13	Duplex	75	3	25	100	220	99.72	30.24	Mode 1	0.07	109.46	1.10
14	Duplex	50	3	50	100	220	108.05	64.86	Mode 1	0.04	97.39	0.90
15	Duplex	25	3	75	100	220	83.88	60.88	Mode 1	0.02	70.06	0.84
16	Duplex	75	6	25	100	220	176.69	22.33	Mode 1	0.30	174.07	0.99
17	Duplex	50	6	50	100	220	137.03	32.99	Mode 1	0.15	125.80	0.92
18	Duplex	25	6	75	100	220	104.19	42.92	Mode 1	0.10	113.71	1.09
19	Duplex	75	9	25	100	220	204.17	8.53	Mode 2	0.67	246.97	1.21
20	Duplex	50	9	50	100	220	157.67	24.89	Mode 1	0.33	173.15	1.10
21	Duplex	25	9	75	100	220	113.74	41.25	Mode 1	0.22	145.94	1.28
22	Duplex	75	12	25	100	220	219.63	6.97	Mode 2	1.18	272.99	1.24
23	Duplex	50	12	50	100	220	170.71	14.18	Mode 2	0.59	234.41	1.37
24	Duplex	25	12	75	100	220	126.09	41.24	Mode 2	0.39	177.89	1.41
25	Ferritic	75	3	25	100	220	74.09	53.15	Mode 1	0.05	103.55	1.40
26	Ferritic	50	3	50	100	220	76.56	72.55	Mode 1	0.03	94.79	1.24
27	Ferritic	25	3	75	100	220	55.96	63.03	Mode 1	0.02	44.48	0.79
28	Ferritic	75	6	25	100	220	158.37	28.87	Mode 1	0.21	150.43	0.95
29	Ferritic	50	6	50	100	220	132.87	41.24	Mode 1	0.11	115.40	0.87
30	Ferritic	25	6	75	100	220	121.24	77.95	Mode 1	0.07	106.63	0.88
31	Ferritic	75	9	25	100	220	193.88	15.26	Mode 2	0.48	228.56	1.18
32	Ferritic	50	9	50	100	220	147.24	31.45	Mode 1	0.24	149.76	1.02
33	Ferritic	25	9	75	100	220	111.21	37.92	Mode 1	0.16	113.94	1.02
34	Ferritic	75	12	25	100	220	205.23	7.73	Mode 2	0.86	256.67	1.25
35	Ferritic	50	12	50	100	220	159.61	19.86	Mode 1	0.43	197.85	1.24
36	Ferritic	25	12	75	100	220	117.49	35.74	Mode 2	0.29	162.76	1.39
											Average	1.07
											St. dev	0.19

Table 6.8: Summary of the ultimate resistance predictions by the predictive formula.

$F_{u,pred}/F_{u,FE}$	Austenitic and duplex test results (Yuan *et al.* 2019; 2020)	Ferritic test results (Chapter 4)	Numerical results (Chapter 5)	Overall
Mean	0.97	0.93	1.07	1.01
St. dev.	0.11	0.12	0.19	0.20

6.4. Conclusions

In this chapter, the EN 1993-1-8 (2005) design provisions were assessed considering experimental and numerical studies on ferritic stainless steel bolted T-stubs reported in the scope of the research project herein and existing experimental results in the literature for austenitic and duplex stainless steel bolted T-stubs (Yuan *et al.*, 2019; 2020). The plastic resistance predictions based on EN 1993-1-8 (2005) provided good estimations for ferritic stainless steel bolted T-stubs, since the strain-hardening characteristics of ferritic stainless steels is similar to that of carbon steel. It was also shown that the attained plastic resistance forces from the developed FE models are in a good agreement with EN 1993-1-8 (2005). Moreover, the design proposals which includes the 3.0% proof strength $\sigma_{3.0}$ instead of 0.2% proof strength $\sigma_{0.2}$ for estimating the plastic resistance of austenitic and duplex stainless steels by Yuan *et al.* (2020) were found to offer better plastic resistance predictions than the EN 1993-1-8 (2005) method.

Finally, the proposed expressions for ultimate resistance predictions of bolted T-stubs made of carbon steel by Tartaglia *et al.* (2020) which take into account the effect of membrane actions, were confirmed against the available test data for austenitic and duplex stainless steel bolted T-stubs (Yuan *et al.*, 2019; 2020) and experimental and numerical results on ferritic stainless steel T-stubs in Chapters 4 and 5. The ultimate resistance predictions were obtained with a consistent accuracy for austenitic and duplex stainless steel T-stubs which exhibited failure mode 1 and mode 2 by the proposed formula. Similarly, the proposed predictive model was shown to accurately predict the ultimate resistance of the tested ferritic stainless steel T-stubs. The proposed model was applied to the parametric study and the predictions were satisfactory in overall, yet it overpredicted the ultimate resistances of the T-stubs which exhibited failure mode 2 or very close to the failure mode 3, since originally, the developed equations were intended to be used for T-stubs failing predominantly in mode 1. The overall ratio of predictive ultimate forces and collected data is obtained as 1.01 which clearly shows that the proposed expressions provide remarkably accurate ultimate force predictions for stainless steel bolted T-stubs.

CHAPTER 7

Conclusions and suggestions for future research

7.1. Conclusions

The literature review presented in Chapter 2 has revealed that the studies on stainless steel beam-to-column connections as well as on stainless steel bolted T-stubs have been increasing recently although they remain scarce compared to the investigation on cross-section and member response of stainless steel components. The experimental and numerical studies on full scale stainless steel open beam-to-open column joins (Elflah *et al.*, 2019a; 2019b), beam-to-tubular column joints (Elflah *et al.*, 2019c) and bolted T-stubs (Yuan *et al.*, 2019; 2020) have been conducted using austenitic and duplex stainless steels. Due to the absence of test data on ferritic stainless steel bolted T-stubs, the research project herein has been performed in order to address this knowledge gap in the literature and aiming to develop design rules which can provide accurate and consistent predictions for the plastic and ultimate resistance of ferritic stainless steel connections.

In Chapter 3, 12 tensile tests using duplicate smooth notched specimens manufactured from A4-80 stainless steel bolts, which are commonly used as fasteners in bolted connections, have been performed to obtain the material behaviour, inherent ductility and fracture characteristics of stainless steel bolts as well as their dependance on stress triaxility. An equation which defines the relationship between the plastic strain at fracture initiation to the stress triaxiality has been proposed. It was also observed that the maximum force and strain at fracture strongly depend on the stress triaxiality, with increasing triaxiality leading to higher ultimate force and lower deformation at failure for the identical nominal cross-sections of the same material. Furthermore, the existing models to estimate the fracture initiation for carbon steel (Pavlovic *et al.*, 2013) and stainless steel bolts (Song *et al.*, 2020) have been comperatively assessed. It was concluded that the predictive model by Pavlovic *et al.* (2013) underestimates the ductility of stainless steel bolts and the fracture initiation is reached at relatively higher plastic strains, due to the fundamentally different fracture characteristics of stainless steel and high strength bolts. The strain at fracture which was predicted using the model proposed by Song *et al.*, (2020) for stainless steel bolts were considerably higher than the tested ones in the triaxiality range varies between 0.33 and 0.66. Moreover, an advanced numerical model which contains 2D axisymmetric and 3D advanced finite element models has been developed and calibrated using the test results. The numerical models in which a linear material degradation model with a single damage variable in the form of plastic deformation at fracture were employed replicated the experimental response of all tested specimens remarkably well. Finally, the proposed fracture model was shown to accurately predict the experimental response of bolts under pure tension and a combination of tension and shear (Song *et al.*, 2020), as well as the full moment-rotation response of a flush end plate connection (Elflah *et al.*, 2019), which failed by bolt fracture. The reported modelling strategy regarding the continuation of the curve beyond the ultimate tensile stress (UTS), the proposed fracture initiation criterion incorporating the effect of triaxiality and the displacement at fracture for various mesh sizes reported in Chapter 3 can be used to obtain realistic models of bolted connections or individual bolts where bolt fracture needs to be explictly modelled.

An experimental study on the ultimate behaviour of ferritic stainless steel bolted T-stubs under tension was comprehensively reported in Chapter 4. Testing of 17 ferritic stainless steel bolted T-stubs under monotonic tension was carried out and the plastic and ultimate resistance, the deformation at failure and the failure mechanisms of ferritic T-stubs with single and double bolt rows were obtained. Within the scope of the experimental programme, the material anisotropy exhibited by ferritic stainless steel has been quantified using 5 mm and 10 mm thick coupons extracted in three different directions of the plate material use for the fabrication of the T-stubs. The overstrength exhibited by the T-stubs has been quantified in terms of the ratios of the ultimate over the plastic resistance, which were varying from 1.21 to 6.69, which indicates the considerable reserve capacity of ferritic T-stubs that may be adventageous to mitigate progressive collapse and enhance robustness.

Capter 5 reports an extensive numerical study on stainless steel T-stubs. In the first part, the ultimate behaviour of austenitic and duplex stainless steel T-stubs has been investigated by advanced FE models considering the effect of mesh element type, different bolt modelling techniques and different analysis types such as general static and explicit dynamic. The FE model was validated against the available test data reported by Yuan *et al.* (2019) and modelling recommendations were given in detail. The second part of the numerical study focuses on the ultimate behaviour of ferritic stainless steel bolted T-stubs. The developed FE model was utilised to simulate the response of the tested ferritic stainless steel T-stubs in Chapter 4 and validated against them. The effect of aniostropy was incorporated in the FE models and discussed comprehensively. Finally, the fracture model proposed in Chapter 3 was adopted in some of the FE models of austenitic, duplex and ferritic stainless steel T-stubs. An alternative computationally cheap model incorporating only a fracture initiation criterion was assessed and was found to yield results that lie on the safe side of the epxerimentally observed response, without being too conservative. Hence this alternative model can be used for design purposes.

In Chapter 6, the EN 1993-1-8 (2005) design provisions for the plastic resistance of T-stubs were assessed using the existing experimental data on austenitic, duplex (Yuan *et al.*, 2019; 2020) and ferritic stainless steel test data reported in Chapter 4 as well as the numerical ones generated in Chapter 5. The codified design predictions were found to be appropriate for ferritic T-stubs but overly conservative for austenitic and duplex T-stubs. Moreover, an alternative design approach for austenitic and duplex stainless steel proposed by Yuan *et al.* (2020), which replaces the $\sigma_{0.2}$ with the $\sigma_{3.0}$ to account for the material strain-hardening was assessed and found to lead to considerable improvements relative to the EN 1993-1-8 (2005) predictions for austenitic and duplex T-stubs. Finally, a recently developed formula for the estimaton of the ultimate resistance force of carbon steel T-stubs proposed by Tartaglia *et al.* (2020) was applied to austenitic, duplex and ferritic stainless steel bolted T-stubs. The mean value of the ratio of the predicted over the experimental ultimate force was obtained as 0.99 with standard deviation of 0.11 austenitic and duplex stainless steel T-stubs. The ratio was calculated as 0.93 with standard deviation of 0.12 for ferritic stainless steel T-stubs. Hence, it was concluded that the proposed formula provides satisfactory predictions of ultimate resistance force for austenitic, duplex and ferritic stainless steel bolted T-stubs.

7.2. Recommendations for future research

The reported findings of this research fill a knowledge gap in the litearture on the ultimate behaviour of ferritic stainless steel bolted T-stubs and establish a basis to develop new design methodologies for stainless steel connections as well as explicit modelling of fracture in bolts. Additional research gaps remain and these are listed herefter as suggestions for future research.

1- The methodology of the developed damage model for A4-80 M16 stainless steel bolts can be extended for high strength steel bolts and other steel grades.

2- Fracture properties of austenitic, duplex and ferritic stainless steel plates should be studied to enable the explicit modelling of plate fracture in stainless steel connections.

3- The effect of specimen width and thickness on the material properties of ferritic stainless steel coupons should be studied extensively.

4- The structural behaviour of stainless steel connections as well as T-stubs under cyclic loading needs to be investigated to show the effectiveness of potential application of stainless steels in seismic areas. The high ductility of stainless steel is in theory ideally suited to dissipate energy in seismic applications. Hence, the examination of the cyclic behaviour of stainless steel joints can contribute to quantify potential benefits of adopting stainless steel in connections of earthquake resistant structures.

5- Component based mechanical models for cyclic behaviour of stainless steel joints should be developed which provides a general basis for the design of a stainless steel joint by allowing a simple assessment of the influence of geometrical properties of the joint i.e. bolt diameter, end-plate thickness etc. on the cyclic response.

6- In addition to the cyclic behaviour, the methods of pseudo-dynamic testing, shaking table test, hybrid pseudo dynamic testing and recently developed real time hybrid testing can be used to provide experimental data on structural behaviour of stainless steel joints under seismic loading.

7- The structural response of stainless steel connections under elevated temperatures (i.e. in fire) should be investigated due to the fact that the mechanical behaviour of stainless steels in elevated temperature is considerably different than the room temperature conditions. Hence, the behaviour of stainless steel connections under elevated temperature, fire and traveling fire conditions should be investigated via experimental and numerical research.

8- The structural response of stainless steel bolted T-stubs under high strain rate loading should be investigated to obtain the behaviour of connections under extreme loading, e.g. impact, sudden loss of a column etc. Thus the potential of mitigating progressive collapse in steel buildings by employing stainless steel connections can be investigated.

9- Apart from the T-stubs in tension, the structural behaviour of the idealized components of the stainless steel joints such as the column web panels in shear and the column web in tension and compression should be investigated in line with the component method.

10- The behaviour of the blind bolted stainless steel T-stub connections to unfilled and concrete filled stainless steel hollow section columns under tension should be studied experimentally and numerically. Likewise, cyclic behaviour of the stainless steel open beam to hollow section column with blind bolts should also be studied comprehensively to determine and verify the design rules for stainless steel joints in seismic regions.

11- Alternative design formula to predict the ultimate resistance predictions of stainless steel T-stubs should be developed in order to use the reserve strength capacity which is reported in the scope of this study herein to mitigate progressive collapse and to enhance the robustness.

12- Over recent decades, the efforts on pursuing space exploration and creating the first space hubs and habitats in extra-terrestrial environments have been accelerated. In the perspective of a long vision, there is a demand for civil engineering to broaden the space applications and protect the critical assets such as robots, fuel tanks, power stations and the future inflatable structures from extra-terrestrial hazards. Investigations of stainless steels members and connections under the extreme environmental conditions such as low gravity, vacuum effects, solar winds, seismic occurances (moonquakes) and extreme temperature differences can be a basis for preliminary design rules for the usage of stainless steel structures on the moon and in other extra-terrestrial environments.

13- Finally, the 3D printing technology of structural materials has been rapidly improving for a decade which has a vital role not only for free form design prospects in construction industry but also for extra-terrestrial construction. To investigate the mechanical behaviour of 3-D printed stainless steel members and joints may be beneficial for developing innovative production processes.

References

- ABAQUS (2013) Theory Manual, ver. 6.13, DASSAULT SYSTÈMES SIMULIA CORP Providence, RI, USA.
- Abidelah A, Abdelhamid B, Djamel EK. (2014) Influence of the flexural rigidity of the bolt on the behavior of the T-stub steel connection. Eng Struc 2014;81:181–94.
- Afshan, S. and Gardner, L. (2013) The continuous strength method for structural stainless steel design. Thin-Walled Structures, 68: 42-49.
- Afshan S, Zhao O, Gardner L. (2019) Standardised material properties for numerical parametric studies of stainless steel structures and buckling curves for tubular columns. Journal of Constructional Steel Research 2019; 152:2–11. https://doi.org/10.1016/j.jcsr.2018.02.019.
- Agerskov, H. (1976) High-Strength Bolted Connections Subject to Prying. Journal of the Structural Division, 102, 161-175.

- Agerskov, H. (1977) Analysis of Bolted Connections Subject to Prying. Journal of the Structural Division, 103, 2145-2163.
- AISI (1968) Specification for the Design of Light Gauge Cold-Formed Stainless Steel Structural Members, American Iron and Steel Institute, 1968.
- AISC Design Guide 27 (2013) Structural Stainless Steel. American Institute of Steel Construction.
- Anwar GA, Dinu F, Ahmed M. (2019) Numerical study on ultimate deformation and resistance capacity of bolted t-stub connection. Int J Steel Struct 2019;19(3):970–7.
- AS/NZS 4673 (2001) Cold-formed stainless steel structures, AS/NZS4673. Sydney: Standards Australia.
- Ashraf, M., Gardner, L. and Nethercot, D. (2006) Compression strength of stainless steel cross-sections. Journal of Constructional Steel Research, 62: (1-2): 105-115.
- Baddoo, N.R. (2008) Stainless steel in construction: A review of research, applications, challenges and opportunities. Journal of Constructional Steel Research, 64: (11): 1199-1206.
- Bai Y., Wierzbicki T. (2008) A new model of metal plasticity and fracture with pressure and Lode dependence. International Journal of Plasticity; 24(6): 1071-1096.
- Bai Y., Teng X., Wierzbicki T. (2009) On the application of stress triaxiality formula for plane strain fracture testing. Journal of Engineering Materials and Technology; 131(2): 021002.

- Baniotopoulos, C.C. (1994), On the Numerical Assessment of the Separation of the Separation Zones in Semirigid Column Base Plate Connections, Structural Engineering & Mechanics - An International Journal 2 (3) 1-15.
- Baniotopoulos, C.C. (1995), On the Separation Process in Bolted Steel Splice Plates, Journal of Constructional Steel Research 32 15-35.
- Baniotopoulos, C.C., Abdalla, K.M. & Panagiotopoulos, P.D. (1994), A Variational Inequality and Quadratic Programming Approach to the Separation Problem of Steel Bolted Brackets, Computers & Structures 53 (10) 983-991.
- Baniotopoulos, C.C. & Abdalla, K.M., (1995), Sensitivity Analysis Results on the Separation Problem of Bolted Steel Column-to Column Connections, International Journal of Solids & Structures 32 (2) 251-265.
- Bao W, Jiang J, Yu Z, Zhou X. (2019) Mechanical behavior of high-strength bolts in T-stubs based on moment distribution. Eng Struct 2019;196:109334.
- Bao Y. (2003) Prediction of ductile crack formation in uncracked bodies. PhD thesis, Massachusetts Institute of Technology.
- Bao Y., Wierzbicki T. (2004) On fracture locus in the equivalent strain and stress triaxiality space. International Journal of Mechanical Sciences; 46:81-98.
- Bao Y., Wierzbicki T. (2005) On the cut-off value of negative triaxiality for fracture. Engineering Fracture Mechanics; 72(7): 1049-1069.
- Becque, J, Oyawoye, A, Guadagnini, M, Huang, S. (2014) Notched Strip Tensile Tests to

Determine Yield Characteristics of Stainless Steel. Journal of Engineering Mechanics 2014;140:04013007.

- Becque J., Rasmussen K.J.R. (2009a). Experimental investigation of local-overall interaction buckling of stainless steel lipped channel columns. Journal of Constructional Steel Research 65(8-9): 1677-1684
- Becque J., Rasmussen K.J.R. (2009b). A numerical investigation of local–overall interaction buckling of stainless steel lipped channel columns. Journal of Constructional Steel Research 65(8-9): 1685-1693.
- Beg, D., Zupančič, E. & Vayas, I. (2004) On the rotation capacity of moment connections. Journal of Constructional Steel Research, 60, 601-620.
- Bock M., Gardner L., Real E. (2015). Material and local buckling response of ferritic stainless steel sections. Thin-Walled Structures 89: 131-141.
- Bouchair A, Averseng J, Abidelah A. (2008) Analysis of the behaviour of stainless steel bolted connections. *J Constr Steel Res*;64:1264–74. doi:10.1016/j.jcsr.2008.07.009.
- Bridgman P.W. (1964) Studies in large plastic flow and fracture. Cambridge, MA: Harvard University Press.
- BS EN ISO 6892-1:2009, (2009) British Standard: Metallic Materials - Tensile Testing. Part 1: Method of Test at Ambient Temperature, The Standards Policy and Strategy Committee.
- Bu, Y., Wang, Y. and Zhao, Y. (2019) Study of stainless steel bolted extended end-plate

joints under seismic loading. *Thin-Walled Structures*, 144: 106255. doi:10.1016/j.tws.2019.106255.

- Cai, Y. and Young, B. (2014a) Behavior of cold-formed stainless steel single shear bolted connections at elevated temperatures. Thin-Walled Structures, 75: 63-75.
- Cai, Y. and Young, B. (2014b) Structural behavior of cold-formed stainless steel bolted connections. Thin-Walled Structures, 83: 147-156.
- Cashell K.A., Baddoo N.R. (2014). Ferritic stainless steels in structural applications. Thin-Walled Structures 83: 169-181.
- Chaboche J.L. (1987) Continuum damage mechanics: Present state and future trends. Nuclear Engineering and Design; 105(1): 19-33.
- Coelho, A. G. (2004) Characterization of the ductility of bolted end plate beam-to-column steel connections. PhD, Fac. de Ciencias e Tecnologia da Univ. de Coimbra.
- Coelho, A. M. G., Bijlaard, F. S. K., Gresnigt, N. & Simões Da Silva, L. (2004) Experimental assessment of the behaviour of bolted T-stub connections made up of welded plates. Journal of Constructional Steel Research, 60, 269-311.
- Coelho, A. M. G., Bijlaard, F. S. K., Simões Da Silva, L. (2004) Experimental assessment of the ductility of extended end plate connections. Engineering Structures; 26(9): 1185-1206.
- Coelho, A. M. G., Bijlaard, F. S. K. (2006) Experimental behaviour of high strength steel end-plate connections. Journal of Constructional Steel Research; 63(9): 1228-1240.

- Coelho, A. M. G., Silva, L. S. D. & Bijlaard, F. S. K. (2006a) Ductility analysis of bolted extended end plate beam-to-column connections in the framework of the component method. Steel and Composite Structures, 6, 33-53.
- Coelho, A. M. G., Silva, L. S. D. & Bijlaard, F. S. K. (2006b) Finite-Element Modelling of the Nonlinear Behavior of Bolted T-Stub Connections. Journal of Structural Engineering, 132, 918-928.
- Crisfield M.A., Wills J. (1988) Solution strategies and softening materials. Computer methods in applied mechanics and engineering; 66(3): 267-289.
- Culache G., Byfield M. P., Ferguson N. S., Tyas A. (2017) Robustness of Beam-to-Column End-Plate Moment Connections with Stainless Steel Bolts Subjected to High Rates of Loading, Journal of Structural Engineering; 143: 04017015.
- D'Aniello M., Cassiano D., Landolfo R. (2016) Monotonic and cyclic inelastic tensile response of European preloadable gr10.9 bolt assemblies. Journal of Constructional Steel Research; 124: 77-90.
- De Matteis G, Mandara A, Mazzolani FM. (2000) T-stub aluminium joints: influence of behavioural parameters. Comput Struct 2000;78(1–3):311–27.
- Demonceau, J.F., Weynand, K., Jaspart, J.P., Müller C., (2010) Application of Eurocode 3 to steel connections with four bolts per horizontal row, Proceedings of the SDSS'Rio 2010 Conference 2010, pp. 199–206 , Rio de Janeiro.
- Elflah, Mohamed A Hussaen (2018). Structural behaviour of stainless steel bolted beam to

column joints. University of Birmingham. Ph.D.

- Elflah M, Theofanous M, Dirar S, Yuan HX. (2019a) Behaviour of stainless steel beam-to column joints—Part 1: Experimental investigation. *J Constr Steel Res*;152:183–93.
- Elflah M, Theofanous M, Dirar S. (2019b) Behaviour of stainless steel beam-to-column joints—Part 2: Numerical modelling parametric study. *J Constr Steel Res* ;152:194–212.
- Elflah M, Theofanous M, Dirar S, Yuan H. (2019c) Structural behaviour of stainless steel beam-to-tubular column joints. Engineering Structures ;184:158–75. https://doi.org/10.1016/j.engstruct.2019.01.073.
- EN 10088-2 (2005). Stainless steels – Part 2: Technical delivery conditions for sheet/plate and strips of corrosion resisting steel for general purposes. CEN.
- EN 1993-1-4:2006+A1:2015 (2015) Eurocode 3: Design of Steel Structures–Part 1.4: General Rules–Supplementary Rules for Stainless Steels, CEN.
- EN 1993-1-8 (2005) Eurocode 3: Design of steel structures – Part 1-8: Design of joints. CEN.
- Errera, S.J., Popowich, D.W. and Winter, G. (1974) Bolted and welded stainless steel connections. ASCE J Struct Div, 100: (ST6): 1279-1296.
- Faella, C., Piluso, V. & Rizzano, G. (1995) Reliability of Eurocode-3 Procedures for Predicting Beam-to-Column Joint Behaviour. Third International Conference on Steel and Aluminium Structures. Istanbul: Bogazici University Bebek.
- Faella, C., Piluso, V. & Rizzano, G. (1996a) Experimental analysis of T-stub assemblies

with snug tightened or pretensioned bolts. Rapporto N.73. Italy: Dept. of Civ. Engrg., Univ. of Salerno.

- Faella, C., Piluso, V. & Rizzano, G. (1996b) Some proposals to improve EC3-Annex J approach for predicting the moment-rotation curve of extended plate connections. Costruzioni Metalliche, 48, 15-31.
- Faella, C., Piluso, V. & Rizzano, G. (1998) Experimental Analysis of Bolted Connections: Snug versus Preloaded Bolts. Journal of Structural Engineering, 124, 765-774.
- Faella, C., Piluso, V. & Rizzano, G. (2000) Structural Steel Semirigid Connections: Theory, Design, and Software, CRC Press.
- Faralli A. C, Tan P.J, Latour M, Rizzano G. (2018) Finite Element Analysis of Bolted T-Stubs Undergoing Large Displacement: A Preliminary Study. Open Construct Build Tech J. 2018;12(Suppl-1, M10):170-176.
- Francavilla AB, Latour M, Piluso V, Rizzano G. (2015) Simplified finite element analysis of bolted T-stub connection components. Eng Struct 2015;100:656–64.
- Fransplass H, Langseth M, Hopperstad OS. (2011) Tensile behaviour of threaded steel fasteners at elevated rates of strain. International Journal of Mechanical Sciences;53: 946-57.
- Gao, J. D., Yuan, H. X., Du, X. X., Hu, X. B. & Theofanous, M. (2020) Structural behaviour of stainless steel double extended end-plate beam-to-column joints under monotonic loading. Thin-Walled Structures 151, 106743, doi: 10.1016/j.tws.2020.106743.

- Gardner, L. (2005) The use of stainless steel in structures. Progress in Structural Engineering and Materials, 7: (2): 45-55.
- Gardner, L. (2008). The continuous strength method. Proceedings of the Institution of Civil Engineers - Structures and Buildings, 161, 127-133.
- Gardner, L. and Theofanous, M. (2008) Discrete and continuous treatment of local buckling in stainless steel elements. Journal of Constructional Steel Research, 64: (11): 1207-1216.
- Gardner, L., and Nethercot, D. A. (2004a) Experiments on stainless steel hollow sections. Part 1: Material and cross-sectional behaviour. J. Constr. Steel Res., 60, 1291–1318.
- Gardner, L., and Nethercot, D. A. (2004b) Numerical modelling of stainless steel structural components—A consistent approach. J. Struct. Eng., 130_10_, 1586–1601.
- Gardner, L., and Nethercot, D. A. (2004c) Stainless steel structural design: A new approach. Struct. Eng., 82_21_, 21–28.
- Gardner L., Bu Y. Theofanous M. (2016). Laser-welded stainless steel I-sections: Residual stress measurements and column buckling tests. Engineering Structures 127: 536-548.
- Grimsmo E.L., Aalberg A., Langseth M, Clausen A.H. (2016) Failure modes of bolt and nut assemblies under tensile loading. Journal of Constructional Steel Research; 126: 15–25.
- Guo W., Dong H., Lu M., Zhao X. (2002). The coupled effects of thickness and delamination on cracking resistance of X70 pipeline steel. International Journal of Pressure Vessels and Piping 79(6): 403–412.

- Gurson A.L. (1977) Continuum theory of ductile rupture by void nucleation and growth: Part I – yield criteria and flow rules for porous ductile media. Journal of Engineering Materials and Technology; 99(1): 2-15.

- Hill, R. (1953). “A new method for determining the yield criterion and plastic potential of ductile metals.” J. Mech. Phys. Solids, 1(4), 271–276.

- Hradil P., Talja A., Real E., Mirambell E., Rossi B., (2013) Generalized multistage mechanical model for nonlinear metallic materials, Thin-Walled Structures. 63–69. doi:10.1016/j.tws.2012.10.006.

- International Iron & Steel Institute (2005) Sustainability report of the world steel industry. Brussels: IISI.

- ISO 68-1:1998 ISO (1998) general purpose screw threads – Basic profile – Part 1: Metric screw threads. International Organization for Standardization.

- Jaspart, J.-P. (1991) Study of the semi-rigid behaviour of beam-to-column joints and of its influence on the stability and strength of steel building frames. PhD, University of Liège.

- Jaspart, J.-P. (1997) Contributions to recent advances in the field of steel joints. Column bases and further configurations for beam-to-column joints and column bases. Agrégé en sciences de l'ingénieur, Université de Liège.

- Jaspart, J.-P. & Maquoi, R. (1995) Effect of bolt preloading on joint behaviour. First European Conference on Steel Structures. Athens, Greece.

- Jia L-J, Kuwamura H. (2014) Ductile Fracture Simulation of Structural Steels under

Monotonic Tension. Journal of Structural Engineering;140: 04013115.

- Kanvinde A.M., Deierlein G.G. (2007) Finite element simulation of ductile fracture in reduced section pull-plates using micromechanics-based fracture models. Journal of Structural Engineering; 133:656-664.
- Kato, B. & Mcguire, W. (1973) Analysis of T-Stub Flange-to-Column Connections. Journal of the Structural Division, 99, 865-888.
- Kim, T.S. and Kuwamura, H. (2007) Finite element modelling of bolted connections in thin-walled stainless steel plates under static shear. Thin-Walled Structures, 45:(4): 407-421.
- Kim, T.S., Kuwamura, H. and Cho, T.J. (2008) A parametric study on ultimate strength of single shear bolted connections with curling. Thin-Walled Structures, 46: (1): 38-53.
- Kim, T.S. and Kuwamura, H. (2011) Numerical investigation on strength design and curling effect of mechanically fastened joints in cold-formed austenitic stainless steel. Materials and Design, 32: (7): 3942-3956.
- Kontoleon, M., Mistakidis, E.S., Baniotopoulos, C.C. & Panagiotopoulos, P.D. (1999), Parametric Analysis of the Structural Response of Steel Base Plate Connections, Computers & Structures 71, 87-103.
- Kontoleon, M. J. & Baniotopoulos, C. C. (2000), Computational Aspects on the Frictional Unilateral Contact Problem Arising on Steel Base Plate Connections, Computers & Structures 78, 303-309.

- Kuwamura, H. and Isozaki, A. (2002) Ultimate behavior of fastener connections of thin stainless steel plates. Study on light-weight stainless steel structures part 4. Journal of Structural and Construction Engineering, (556): 159-166.
- Latour M, and Rizzano G. (2012) Experimental Behavior and Mechanical Modeling of Dissipative T-Stub Connections. J. Struct. Eng. 2012;138(2):170-182.
- Latour M, Rizzano G, Santiago A, Da Silva LS. (2014) Experimental analysis and mechanical modeling of T-stubs with four bolts per row. J Constr Steel Res 2014;101:158–74.
- Lemaitre. A (1985) Continuous Damage Mechanics Model for Ductile Fracture. Journal of Engineering Materials and Technology; 107: 83–89.
- Li D., Uy B., Wang J., Song Y. (2020) Behaviour and design of high-strength Grade 12.9 bolts under combined tension and shear. Journal of Constructional Steel Research; 174: 106305.
- Liew, A. and Gardner, L. (2015) Ultimate capacity of structural steel cross-sections under compression, bending and combined loading. Structures, 1: 2-11.
- Ling Y. (1996) Uniaxial true stress-strain after necking. AMP Journal of Technology; 5: 37-48.
- Liu, Y., Malaga-Chuquitaype, C. and Elghazouli, A.Y. (2012b) Response and component characterisation of semi-rigid connections to tubular columns under axial loads. Engineering structures, 41: 510-532.

- Mann, A. P. & Morris, L. J. (1979) Limit Design of Extended End-Plate Connections. Journal of the Structural Division, 105, 511-526.
- Manninen, T. (2010). SAFSS Deliverable WP1, Task 1.3: Characterization of Stress–Strain Behaviour. Outokumpu Tornio Works, Tornio Research Centre, 2010 (available at www.steel-stainless.org/media/1186/safss-01-03.pdf)
- Manos G.C., Theofanous M., Katakalos K. (2014) Numerical simulation of the shear behaviour of reinforced concrete rectangular beam specimens with or without FRP-strip shear reinforcement. Advances in Engineering Software; 67: 47-56.
- Mirambell, E., and Real, E. (2000) On the calculation of deflections in structural stainless steel beams: An experimental and numerical investigation. J. Constr. Steel Res., 54, 109–133.
- Mistakidis, E,S., Baniotopoulos, C.C., Bisbos C.D. & Panagiotopoulos P.D. (1997), Steel T-Stub Connections under Static Loading: An Effective 2-D Numerical Model, Journal of Constructional Steel Research 44 (1-2) 51-67.
- Mistakidis, E.S., Baniotopoulos, C.C. & Panagiotopoulos, P.D. (1998), An Effective Two-Dimensional Numerical Model for the Analysis of a Class of Steel Connections, Computational Mechanics 21 363-371.
- Nair, R. S., Birkomoe, P. C. & MUNSE, W. H. (1974) High strength bolts subject to tension and prying. Journal of the Structural Division, 100.
- Nethercot, D. A. & Zandonini, R. (1989) Structural connections. Stability and strength.

Chapter 2. Methods of prediction of joint behaviour: beam-to-column connections, Jason Consultants SA.

- Packer, J. A. & Morris, L. J. (1977) A limit state design method for the tension region of bolted beam-column connections. The Structural Engineer, 5, 446-458.
- Pavlović M, Marković Z, Veljković M, Buđevac D. (2013) Bolted shear connectors vs headed studs behaviour in push-out tests. Journal of Constructional Steel Research; 88:134-49.
- Piluso, V., Faella, C. & Rizzano, G. (2001a) Ultimate Behavior of Bolted T-Stubs. I: Theoretical Model. Journal of Structural Engineering, 127, 686-693.
- Piluso, V., Faella, C. & Rizzano, G. (2001b) Ultimate Behavior of Bolted T-Stubs. II: Model Validation. Journal of Structural Engineering, 127, 694-704.
- Quach W. M., Teng J. G., Chung K. F. (2008) Three-Stage Full-Range Stress-Strain Model for Stainless Steels, Journal of Structural Engineering. 134 1518–1527. doi:10.1061/(ASCE)0733-9445(2008)134:9(1518).
- Ramberg W, Osgood W R (1943) Description of stress–strain curves by three parameters, Technical Note No. 902.
- Rasmussen, K. J. R., Burns, T., Bezkorovainy, P., and Bambach, M. R. (2003) Numerical modelling of stainless steel plates in compression. J. Constr. Steel Res., 59, 1345–1362.
- Ribeiro J, Santiago A, Rigueiro C, Da Silva L.S. (2015) Analytical model for the response of T-stub joint component under impact loading. J. Constr. Steel Res. 2015;6:23-34.

- Ribeiro J, Santiago A, Rigueiro C, Barata P, Veljkovic M. (2016) Numerical assessment of T stub component subjected to impact loading. Eng Struct 2016;106:450–60.
- Rice JR, Tracey DM. (1969) On the Ductile Enlargement of Voids in Triaxial Stress Fields. J Mech Phys Solids; 17:201–17.
- Rossi B. (2010a). Mechanical behavior of ferritic grade 3Cr12 stainless steel-Part 1: Experimental investigations. Thin-Walled Structures 48(7): 553-560.
- Rossi B. (2010b). Mechanical behavior of ferritic grade 3Cr12 stainless steel-Part 2: Yield locus and hardening laws. Thin-Walled Structures 48(7): 540-552.
- Rossi, B. (2014) Discussion on the use of stainless steel in constructions in view of sustainability. Thin-Walled Structures, 83: 182-189.
- Ryan, I. (1999) Development of the use of stainless steel in construction. WP 4.2, ECSC Project No. 7210-SA, 327.
- Salih, E.L., Gardner, L. and Nethercot, D.A. (2010) Numerical investigation of net section failure in stainless steel bolted connections. Journal of Constructional Steel Research, 66: (12):1455-1466.
- Salih, E.L.M. (2010) Analysis and design of stainless steel bolted connections. Department of Civil and Environmental Engineering Imperial College London. PhD thesis.
- Salih, E.L., Gardner, L. and Nethercot, D.A. (2011) Bearing failure in stainless steel bolted connections. Engineering structures, 33: (2): 549-562.
- Salih, E.L., Gardner, L. and Nethercot, D.A. (2013) Numerical study of stainless steel

gusset plate connections. Engineering structures, 49: 448-464.

- Santos AF, Santiago A, Latour M, Rizzano G. Da Silva L.S. (2020) Response of friction joints under different velocity rates. J Constr Steel Res 2020.
- Schafer B.W., Ojdrovic R.P., Zarghamee M.S. (2000) Triaxiality and fracture of steel moment connections. Journal of Structural Engineering; 126(10): 1131-1139.
- SEI/ASCE-8-02 (2002) Specification for the design of cold-formed stainless steel structural members. American Society of Civil Engineers (ASCE).
- Shaheena M.A., Foster A.S.J., Cunningham L.C., Afshan S. (2020) Behaviour of stainless and high strength steel bolt assemblies at elevated temperatures - A review. Fire Safety Journal; 113: 102975.
- Song, Y. & Uy, B. and Wang, J. (2019) Numerical analysis of stainless steel-concrete composite beam-to-column joints with bolted flush endplates. *Steel and Composite Structures*. 33. 975-994. 10.12989/scs.2019.33.1.975.
- Song Y., Wang J., Uy B., Li D. (2020) Experimental behaviour and fracture prediction of austenitic stainless steel bolts under combined tension and shear. Journal of Constructional Steel Research; 166: 105916.
- Stamatopoulos GN, Ermopoulos JC. (2010) Influence of the T-stub flexibility on its strength. Int J Steel Struct 2010;10(1):73–9.
- Swanson, J. A. (1999) Characterization of the Strength, Stiffness, and Ductility Behavior of T-stub Connections. PhD, School of Civil and Environmental Engineering, Georgia

Institute of Technology.

- Swanson, J. A. & Leon, R. T. (2000) Bolted Steel Connections: Tests on T-Stub Components. Journal of Structural Engineering, 126, 50-56.
- Swanson, J. A. & Leon, R. T. (2001) Stiffness Modelling of Bolted T-Stub Connection Components. Journal of Structural Engineering, 127, 498-505.
- Swanson, J. A., Kokan, D. S., Leon, R. T. (2002) Advanced finite element modelling of bolted T-stub connection components, J. Constr. Steel Res. 58 (2002) 1015–1031.
- Talja, A. and Torkar, M. (2014) Lap shear tests of bolted and screwed ferritic stainless steel connections. Thin-Walled Structures, 83: 157-168.
- Tartaglia, R.; D'Aniello, M.; Zimbru, M. (2020) Experimental and numerical study on the T-Stub behaviour with preloaded bolts under large deformations. Structures 2020, 27, 2137–2155.
- Thornton, W. A. (1985) Prying action – a general treatment. Engineering Journal AISC, 22, 67-75.
- Trattnig G, Antretter T, Pippan R. (2008) Fracture of austenitic steel subject to a wide range of stress triaxiality ratios and crack deformation modes. Engineering Fracture Mechanics;75(2): 223–35.
- Tvergaard V., Needleman A. (1984) Analysis of the cup-cone fracture in a round tensile bar. Acta Metallica; 32(1): 157-169.
- Verma P, Sudhakar Rao G, Srinivas NCS, Singh V. (2017) Rosette fracture of modified

9Cr–1Mo steel in tension. Materials Science and Engineering: A;683:172–86. https://doi.org/10.1016/j.msea.2016.12.011.

- Van der Merwe, P. (1987) Development of design criteria for ferritic stainless steel cold-formed structural members and connections. University of Missouri-Rolla, USA.
- Wang, J., Uy, B. and Li, D. (2019) Behaviour of large fabricated stainless steel beam-to-tubular column joints with extended endplates, *Steel Compos. Struct., Int. J.,* 32(1), 141-156. https://doi.org/10.12989/scs.2019.32.1.141
- Wang, Z., Tizani, W. and Wang, Q. (2010) Strength and initial stiffness of a blind-bolt connection based on the T-stub model. Engineering structures, 32: (9): 2505-2517.
- Wang, Z.-Y. and Wang, Q.-Y. (2016) Yield and ultimate strengths determination of a blind bolted endplate connection to square hollow section column. Engineering Structures, 111: 345-369.
- Weynand, K., Jaspart, J.-P. and Steenhuis, M. (1996) The stiffness model of revised annex j of Eurocode 3. Connections in steel structures III. Elsevier 441-452.
- Wierzbicki T., Bao Y. Lee Y.-W., Bai Y. (2005) Calibration and evaluation of seven fracture models. International Journal of Mechanical Sciences; 47(4-5): 719-743.
- Winter, G. (1956) Tests on bolted connections in light gage steel. Journal of the Structural Division, 82: (2): 1-25.
- Yee, Y. L. & Melchers, R. E. (1986) Moment-Rotation Curves for Bolted Connections. Journal of Structural Engineering, 112, 615-635.

- Yidu B., Wang Y., Zhao Y. (2019) Study of stainless steel bolted extended end-plate joints under seismic loading. Thin-Walled Structures; 144: 106255.
- Yuan HX, Hu S, Du XX, Yang L, Cheng XY, Theofanous M. (2019) Experimental behaviour of stainless steel bolted T-stub connections under monotonic loading. *J Constr Steel Res*;152:213–24.
- Yuan HX, Gao JD, Theofanous M, Yang L, Schafer BW (2020a) Initial stiffness and plastic resistance of bolted stainless steel T-stubs in tension. Journal of Constructional Steel Research 2020;173:106239. https://doi.org/10.1016/j.jcsr.2020.106239.
- Yuan HX, Hu S, Du XX, Yang L, Cheng XY, Theofanous M. (2020b) Corrigendum to "Experimental behaviour of stainless steel bolted T-stub connections under monotonic loading", J. Constr. Steel Res. 172 (2020), 105860.
- Zhao M.S., Lee C.K., Chiew S.P. (2016) Tensile behavior of high performance structural steel T-stub joints. Journal of Constructional Steel Research; 122: 316-325.
- Zhu X, Wang P, Liu M, Tuoya W, Hu S. (2017) Behaviors of one-side bolted T-stub through thread holes under tension strengthened with backing plate. J Constr Steel Res 2017;134:53–65.
- Zoetemeijer, P. (1974) A Design Method for the Tension Side of Statically Loaded, Bolted Beam-to-Column Connections.
- Zoetemeijer, P. (1990) Summary of the Research on Bolted Beam-to-column Connections, TU Delft, Faculteit der Civiele Techniek.